

SINGLE-PHOTON GENERATION FROM DEFECTS AND MANIPULATION WITH NANOSTRUCTURES

**A Thesis Submitted to
the Graduate School of Engineering and Sciences of
İzmir Institute of Technology
in Partial Fulfillment of the Requirements for the Degree of
DOCTOR OF PHILOSOPHY
in Materials Science and Engineering**

**by
Elif ÖZÇERİ İYİKANAT**

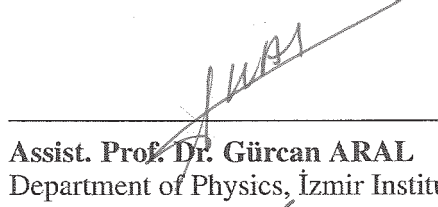
**December 2019
İZMİR**

We approve the thesis of **Elif ÖZÇERİ İYİKANAT**

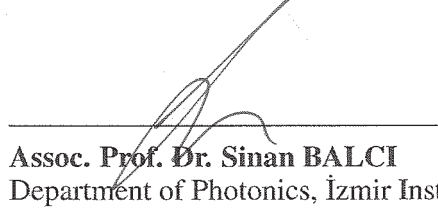
Examining Committee Members:



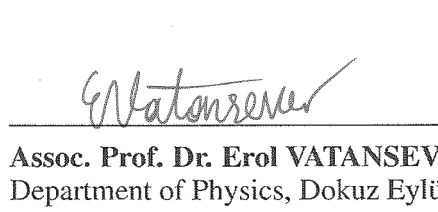
Assist. Prof. Dr. Enver TARHAN
Department of Physics, İzmir Institute of Technology



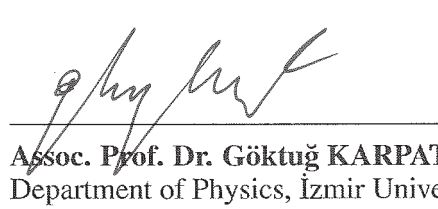
Assist. Prof. Dr. Gürcan ARAL
Department of Physics, İzmir Institute of Technology



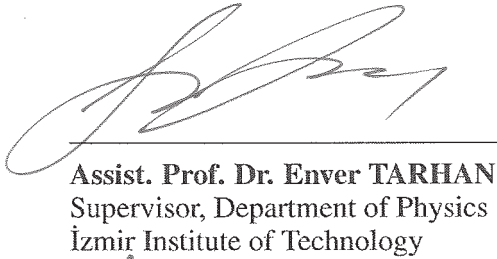
Assoc. Prof. Dr. Sinan BALCI
Department of Photonics, İzmir Institute of Technology



Assoc. Prof. Dr. Erol VATANSEVER
Department of Physics, Dokuz Eylül University

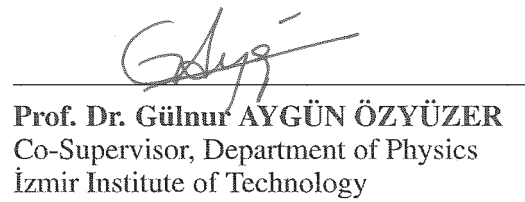


Assoc. Prof. Dr. Göktuğ KARPAT
Department of Physics, İzmir University of Economics

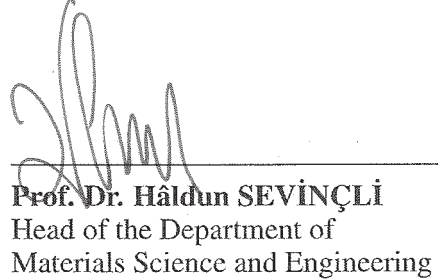


Assist. Prof. Dr. Enver TARHAN
Supervisor, Department of Physics
İzmir Institute of Technology

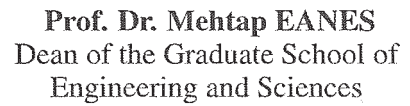
20 December 2019



Prof. Dr. Gülnur AYGÜN ÖZYÜZER
Co-Supervisor, Department of Physics
İzmir Institute of Technology



Prof. Dr. Hâldun SEVİNÇLİ
Head of the Department of
Materials Science and Engineering



Prof. Dr. Mehtap EANES
Dean of the Graduate School of
Engineering and Sciences

ACKNOWLEDGMENTS

Firstly, I would like to express my gratitude to my advisor Assist. Prof. Dr. Enver Tarhan for being always enthusiastic, helpful, and inspirational, teaching me how to approach to problems, and much more. Without his support, kindness and invaluable advises, I would never have been able to complete this thesis. The writing of the name of a respected scientist like him on this thesis will give me life-long pride. I would also like to thank Assoc. Prof. Dr. Sinan Balcı for his guidance and giving me a chance to work with him. He always trusted me and encouraged me throughout this study. I could not have completed this PhD without his support. His honest personality and humanity will set an example for me all my life.

I would also like to thank my co-advisor Gülnur Aygün Özyüzer for her support. I would like to thank my committee members Erol Vatansever and Göktuğ Karpat. In particular, I would like to thank Gürcan Aral who supported and trusted me without hesitation. Moreover, I would like to thank my deceased ex-advisor Assoc. Prof. Dr. Yusuf Selamet who had a huge influence on me, not only in terms of scientific methodologies, but also as in diligence, passion and dedication. I will always feel his good heart.

When it comes to thank my friends, first of all, I want to thank my lab-mate and my best friend Nahit Polat for his continued support and encouragement. I feel very lucky to have him in my life. I would like to thank Zebih Çetin for his friendship with his unique style. I would like to thank Gülsüm Efsun Tekneci for supporting me with her priceless friendship in my last days. Additionally, I would like to thank Sinem İşbilen and Senem Duman, who are always with me in my life and who I love as much as my sisters.

Through my entire life, I have encountered many problems, many challenges both personally and academically. There were such cases that I faced gender discrimination, unjust decisions, unethical behaviors regardless of my studies. Yet, I have never stopped believing in working, studying and as a proud woman, I never let the light of science fade in me. I would like to thank Oğul Başol who is there for me through these years and will continue to be thereafter. I would like to thank my all family members who have always been my side, especially Işıl and Ertan Özçeri. I would also like to thank Sezgin Uçal for making me taste the most delicious food in the world, during my student life.

Lastly, I thank my husband Fadıl for his endless support. During this thesis, I could not overcome the difficulties I had without his faith and love. You are the best spouse that ever existed, and I love you with my entire heart forever.

ABSTRACT

SINGLE-PHOTON GENERATION FROM DEFECTS AND MANIPULATION WITH NANOSTRUCTURES

Single-photon sources are essential components for several applications in the field of quantum information technologies, such as quantum cryptology and quantum computation. To this aim, efficient generation and detection of single-photons are the crucial to be achieved. Among single-photon sources that are extensively studied in the literature, defect centers in solid are very promising due to their room temperature operation and their stability. The aim of this thesis is to generate single photons at room temperature and control their optical properties by nanostructures.

Single-photon emission from TMDCs originates from localized weakly bound excitons at cryogenic temperatures due to their small exciton binding energies. However, room temperature SP emission from WS_2 can be obtained by creating WO_3 defects. In our study, room temperature emission from defects in WO_3 was investigated. Density functional theory calculations showed that the source of the emission can be oxygen defects. Additionally, the emission was brightened by plasmonic gold nanoparticles.

Furthermore, defects in two-dimensional (2D) hexagonal boron nitride (hBN) is offered as an efficient room temperature SPS. HBN is a wide bandgap 2D material, in which defect centers create discrete energy level to generate single photons. In our study, reversible single-photon emission control from defects in hBN was demonstrated by Förster-like resonance energy transfer between the single-photon emitter and a graphene layer. To this aim an ionic liquid based device structure was used.

ÖZET

KUSURLARDAN TEK-FOTON ÜRETİMİ VE NANOYAPILARLA MANİPÜLASYONU

Tek-foton kaynakları, kuantum kriptolojisi ve kuantum hesaplama gibi kuantum bilgi teknolojileri alanındaki çeşitli uygulamalar için temel bileşendir. Bu amaçla, tek-fotonların verimli bir şekilde üretilmesi ve tespit edilmesi çok önemlidir. Literatürde yoğun olarak incelenen tek-foton kaynakları arasında, katı ortamlardaki kusur merkezleri, oda sıcaklığındaki çalışmaları ve stabiliteyi nedeniyle oldukça ümit vericidir. Bu tezin amacı oda sıcaklığında tek-foton üretmek ve optik özelliklerini nanoyapılarla kontrol etmektir.

TMDC'lerden lokalize zayıf bağlanmış eksitonlardan kaynaklanan tek-foton emisyonu düşük eksiton bağlanma enerjileri nedeniyle krayojenik sıcaklıklarda gözlenir. Bununla birlikte, WS_2 'den oda sıcaklığında tek-foton emisyonu, WO_3 kusurları yaratılarak elde edilebilir. Çalışmamızda, WO_3 'teki kusurlardan oda sıcaklığı emisyonu incelenmiştir. Yoğunluk fonksiyonel teorisi hesaplamaları, emisyon kaynağının oksijen kusuru olabileceğini göstermiştir. Ek olarak, emisyon şiddeti plazmonik altın nanoparçacıkları ile artırıldığı gösterilmiştir.

Ayrıca, iki boyutlu altıgen bor nitrürdeki (hBN) kusurlar, verimli bir oda sıcaklığı tek-foton kaynağıdır. HBN, kusur merkezlerinin tek-foton üretmek için kesikli enerji seviyesi oluşturduğu geniş bir bant aralığına sahip bir malzemedir. Çalışmamızda, hBN'deki kusurlardan tersinir olarak tek-foton ışınması kontrolü, kaynak ile bir grafen katmanı arasındaki Förster benzeri rezonans enerji transferi ile gösterilmiştir. Bu amaçla iyonik sıvı bazlı bir cihaz yapısı kullanılmıştır.



Dedicated to my grandmother and grandfather

TABLE OF CONTENTS

LIST OF FIGURES	x
LIST OF TABLES	xx
CHAPTER 1. INTRODUCTION	1
CHAPTER 2. THEORETICAL BACKGROUND OF LIGHT-MATTER INTERACTION	5
2.1. Statistical Classification of Light	5
2.2. Correlation Functions	8
2.2.1. First Order Correlation Function	8
2.2.2. Second Order Correlation Function	9
2.2.3. The Hanbury Brown-Twiss Experiment.....	13
2.3. Interaction of light with a Defect Center: Two-Level Model	16
2.4. Three-Level Model	22
2.5. Electronic Absorption and Emission in Defect Centers	25
2.5.1. Zero-Phonon Line and Phonon Side Band	26
2.5.2. Line shape of ZPL and PSB	30
2.6. Photoluminescence Properties of Single Photon Emission.....	31
2.6.1. Single Photon Emission Efficiency	31
2.6.2. Polarized Fluorescence of Single Photon	33
2.6.3. Time-Correlated Single Photon Counting.....	35
2.7. Interaction Between the Emitter and Different Materials	37
2.7.1. Fluorescence Brightening: Plasmon Effect	37
2.7.2. Fluorescence Quenching: Förster Resonance Energy Transfer	41
2.7.2.1. Near-Field Dipole-Dipole Interaction	42
2.7.2.2. Near-Field Dipole-Graphene Interaction	47
CHAPTER 3. EXPERIMENTAL TECHNIQUES	51
3.1. Raman Spectroscopy and Micro-Photoluminescence Setup	51
3.1.1. Two-dimensional Photoluminescence Mapping	54

3.1.2. Temperature Dependent PL Measurements	54
3.2. Hanbury Brown-Twiss Interferometer Setup	54
3.2.1. Lifetime Measurements	59
3.3. Scanning Electron Microscopy	60
CHAPTER 4. STRUCTURAL AND SPECTROSCOPIC CHARACTERIZATION	
OF THE MATERIALS	62
4.1. Tungsten Di-sulfide (WS_2)	62
4.2. Tungsten Three-oxide (WO_3)	67
4.3. CVD-grown Graphene	71
4.3.1. Transfer of Graphene onto a Desired Substrate	71
4.4. Hexagonal Boron Nitrite (hBN)	75
4.4.1. Defect Creation by Electron Beam Irradiation in Bulk hBN	77
4.4.2. Transfer of CVD-grown hBN onto a Silicon-based	
Substrate	77
4.4.3. Sample Preparation	79
4.5. Summary	83
CHAPTER 5. SINGLE PHOTON EMISSION FROM DEFECTS IN WO_3 AND	
PLASMON EFFECT	84
5.1. Single Photon Emission from Defects in WS_2	86
5.2. Single Photon Emission from Defects in WO_3	89
5.3. First Principles Calculations on Oxygen Defect in WO_3	96
5.3.1. Structural and Electronic Properties of WO_3	97
5.3.2. Vibrational Properties of WO_3	98
5.3.3. Structural and Electronic Properties of Oxygen Vacancy in	
WO_3	100
5.4. Low Temperature Optical Characteristics of WO_3	100
5.4.1. Low Temperature Raman Spectroscopy Analyses of WO_3	101
5.4.2. Photoluminescence Analyses of Defects in WO_3 at Low	
Temperatures	105
5.5. Single Photon Emission Enhancement by Gold Nanoparticles	107
5.5.1. Statistical Analyses of Emission Enhancement	110
5.6. Summary	111

CHAPTER 6. ENERGY TRANSFER BETWEEN A SINGLE PHOTON	
EMITTER IN HBN AND GRAPHENE: QUENCHING EFFECT ...	114
6.1. Irreversible Energy Transfer: Static Quenching.....	115
6.1.1. Energy Transfer from a Single Emitter to Single Layer	
Graphene	116
6.1.2. Energy Transfer from a Single Emitter to Three Layer	
Graphene	122
6.1.3. Influence of Transition Rates	129
6.1.4. Lifetime Measurements of Static Quenching	135
6.2. Reversible Energy Transfer: Active Quenching	135
6.2.1. Device Structure.....	139
6.2.2. The Effect of Ionic Liquid	140
6.2.3. Demonstration of Active Quenching	141
6.2.4. Summary	141
CHAPTER 7. CONCLUSIONS	144
REFERENCES	146

LIST OF FIGURES

<u>Figure</u>	<u>Page</u>
Figure 2.1. Statistical difference among light sources. (a) An example of bunched light with (b) its $g^{(2)}(\tau) = 2$. (c) An example of coherent light with (d) its $g^{(2)}(\tau) = 1$. (e) An example of antibunched light with (f) its $g^{(2)}(\tau) = 0$. For all types of light sources $g^{(2)}(\tau \rightarrow \infty) = 1$	12
Figure 2.2. The schematic representation of Hanbury-Brown-Twiss interferometer setup. Sides 1 and 2 are for incoming photons to beam splitter (BS) while site 3 and 4 are for the outgoing ones. The corresponding photon annihilation operators are given where D1 and D2 are detectors.	14
Figure 2.3. Schematic representation of interaction between a two-level system and a classical single mode electromagnetic field.	17
Figure 2.4. Schematic representation of a three-level system.	22
Figure 2.5. Second order correlation function, $g^{(2)}(\tau)$, calculated for $k_{12} = 0.001$ is the black line, $k_{12} = 0.1$ is the red line and $k_{12} = 1$ is the blue line.	24
Figure 2.6. (a)Excitation of a basic two level system and transition from ground state E_0 to higher excited energy level E_1 and its different vibrational levels $\nu = 0, 1, 2, 3$. (b) Schematic absorption spectrum of different transitions which have different energies and intensities. (c) Schematic emission spectrum of different transitions which have different energies and intensities.	26
Figure 2.7. (a) Schematic representation of the energy diagram of an electronic transition with phonon coupling and, (b) Schematic representation of the absorption and fluorescence spectra.	28
Figure 2.8. A representative room temperature photoluminescence spectrum that shows a ZPL at 623.9 nm and a PSB. To see the ZPL-PSB energy difference the ZPL is plotted to zero energy.	29
Figure 2.9. (a) The effect of k_{23} on emission efficiency. (b) the effect of k_{23} on second order correlation function.	33
Figure 2.10. The relation of excitation laser polarization and single photon emission intensity. The red line corresponds to zero minimum intensity, $I_B = 0$, condition without background effects. The dashed blue line represents the effect of non zero $I_B \neq 0$	34

<u>Figure</u>	<u>Page</u>
Figure 2.11. Time-Correlated Single Photon Counting. (a) Measurement of the time difference between excitation laser pulse and emitted single photon, $\Delta t = t_{pulse} - t_{sp}$. (b) The accumulated single photons with respect to detection time differences creates a histogram and a decay curve.	36
Figure 2.12. Calculated nonradiative decay rates for an emitter with emission wavelengths 610 nm by FDTD method. The diameter of gold particle is fixed as 30 nm. The orientation of the emitter which behaves like a dipole is represented in the inset.	41
Figure 2.13. Non-radiative energy transfer process between a donor (D) and an acceptor (A).	42
Figure 2.14. Energy transfer efficiency with respect to the distance between D and A, r , and Förster radius, R_0 . The x-axis is normalized distance r/R_0	45
Figure 2.15. (a) The orientation factor, κ^2 , and the relative directions of the D and A dipole moments. (b) The examples for three different values of κ^2 with respect to relative dipole moment directions.	46
Figure 2.16. FRET rate and distance between the quantum dot and graphene relation. The distance was controlled by the thickness of dielectric material (MgO) (Federspiel et al. (2015)).	48
Figure 2.17. (a) Near-field interaction between point dipoles as donor dipole and acceptors. The non-radiative decay rate is related to r^{-6} .(b) Near-field interaction between a point dipole as donor and two dimensional graphene surface as acceptor. In this case, the non-radiative decay rate is related to r^{-4}	49
Figure 2.18. Single photon emission by a three level system and energy transfer to graphene with rate equations.	50
Figure 3.1. Raman Spectroscopy and Micro-Photoluminescence setup is shown. ...	52
Figure 3.2. At the left the two dimensional PL maps of the same dropcasted hBN flakes cluster are plotted with respect to different wavelengths which are shown at the right. In the maps, the spectrum which has the maximum intensity at the chosen wavelengths are seen as the brightest pixels (yellow). The plotted maps with respect to different wavelengths show the emission originates from localized points in the cluster. On the right panel, the coordinates of these pixels are written with respect to the maps.	55

<u>Figure</u>	<u>Page</u>
Figure 3.3. Linkam THMS600, heating and cooling microscope stage (Linkam (2016)).	56
Figure 3.4. Hanbury Brown-Twiss interferometer (HBT) setup is used to measure correlation function and excited state lifetime.	57
Figure 3.5. (a) A ZPL obtained from a defect center in hBN and its PSB are shown. (b) The photon correlation measurement result of HBT interferometer of this ZPL is shown. The dip is below 0.2 at zero delay time which means that a SP emission is measured. (c) Power dependent photon correlation measurement results with respect to saturation power.	58
Figure 3.6. Second order correlation measurement performed by pulsed laser.	59
Figure 3.7. (a) Excitation polarization dependent PL intensity of a single photon emission. (b) PL spectra extracted from the polarization dependency series in (a) for the degree of maximum and minimum intensities. (c) Excitation power dependent PL intensity of a single photon emission. (d) Lifetime measured at 20 MHz frequency. Black dots are the experimental statistics and the line is theoretical fit. Excited state lifetime was calculated by this exponential fit curve.	61
Figure 4.1. Schematic representation of two dimensional structure of WS ₂ . (a) Top view, (b) side view. Blue atoms represent Tungsten and yellow atoms Sulfur.	63
Figure 4.2. Optical microscope images of dropcasted WS ₂ particles on a SiO ₂ /Si substrate. (a) low and (b) high concentration region.	65
Figure 4.3. The dropcasted hBN sample preparation from solution. For WS ₂ and WO ₃ samples, SiO ₂ /Si substrates were used.	66
Figure 4.4. (a) Schematic representation of the atomic displacements of two adjacent layers in WS ₂ . (b) Raman spectra of asgrown (red) and annealed (blue) WS ₂ samples.	67
Figure 4.5. Schematic representation of WO ₃ structure with different phases. (a) Monoclinic crystal structure of room temperature, (b) simple cubic, (c) tetragonal, (d) monoclinic structure of low temperature, (e) triclinic, and (f) orthorhombic crystal structures. The spheres of green and red colored represent Tungsten and Oxygen atoms, respectively (Wang et al. (2011); Di Valentin et al. (2013)).	68
Figure 4.6. Optical microscope images of dropcasted WO ₃ particles on a SiO ₂ /Si	

<u>Figure</u>	<u>Page</u>
substrate. (a) low and (b) high concentration region.	69
Figure 4.7. Raman spectra of asgrown (red) and annealed (blue) WO ₃ samples.	70
Figure 4.8. Schematic representation of two dimensional structure of graphene.	71
Figure 4.9. hBN transfer procedure from Cu foil to a Si-based substrate	72
Figure 4.10. Sticking of the graphene/photoresist on glass substrate homogeneously by heating on a hotplate is observed from backside of the glass. (a) After the first 4 steps the Cu foil etched graphene/photoresist. (b) The fifth step of the transfer procedure, put on the substrate. (c) heating on hotplate to slightly liquefaction of the Photoresist. (d) Too much heat, (e) too low heat, (f) appropriate temperature $\cong 80^{\circ}\text{C}$ with fully sticking on substrate.	73
Figure 4.11. (a) On the left before immersed in acetone the photoresist/graphene on glass are shown. On the right after removing the acetone the graphene on glass is seen by slight contrast difference. (b) The Raman spectrum of the transferred graphene layer on the glass substrate.	74
Figure 4.12. The optical images of the transferred graphene layers are given with (a) low, (b) appropriate and (c) high hot plate temperatures.	75
Figure 4.13. (a) The optical image of graphene that transferred by the optimized conditions. (b) Raman spectra belong to single layer graphene and Si. (c) The optical image of graphene transferred at high hot plate temperature on the substrate. (d) Raman spectra of graphene with intense defect signals.	76
Figure 4.14. Schematic representation of defect types in hBN. (a) Boron vacancy, (b) nitrogen vacancy and (c) an antisite crystallographic defect.	77
Figure 4.15. (left top) the SEM image of an hBN flake before electron beam irradiation, (left bottom) after electron beam irradiation, (right) after treatment the hBN raman and an emission from defect center in hBN is seen from PL spectra.	78
Figure 4.16. (a) HBN flakes in solution. (b) Commercial single layer hBN grown on Cu foil. (c) SEM image of single layer hBN on Cu foil (Graphene-supermarket (2016)).	79
Figure 4.17. After hBN transfer from Cu foil to a silicon substrate Raman Spectrum of the shown images were taken by 633 nm laser. The optical contrast is seen on the optical images, but the hBN Raman signal could not	

<u>Figure</u>	<u>Page</u>
observed. The Raman spectra were collected from the colored dots on the images and plotted with the same colors shown on images.	80
Figure 4.18. (a) Optical image of a hBN flake by 50x magnification (b) Raman shifts of silicon substrate and hBN as well as zero-phonon line emission with phonon sidebands from a single defect.	81
Figure 4.19. The Raman active modes of graphene, 2D and G are seen in spectrum. In the inset optical image of graphene and an hBN is shown.	82
Figure 4.20. (a) Photoresist on graphene and Cu foil immersed into the acid solution to dissolve Cu foil. (b) Photoresist on graphene is placed onto the Si substrate which already have a layer of graphene and heated on hot-plate. (c) Two layer graphene transferred on Si substrate is seen with some wrinkles and holes.	82
Figure 5.1. (a) Optical image of a WS ₂ . The red circle represents the laser exposure spot where the spectra are recorded. (b) Excitation power dependent intensities. (c) Excitation power dependent spectra. The intensities are increasing by increased power.	85
Figure 5.2. (a) Optical microscope image of as-grown WS ₂ flake. (b) Unstable single photon emission shown in red frame.	87
Figure 5.3. (a) Raman Spectra of Si substrate and annealed WS ₂ are shown. (b) Optical image of a WS ₂ flake on Si substrate.	88
Figure 5.4. (a) The Photoluminescence spectra were recorded from three individual spots. The black line belongs to the spectrum of monolayer WS ₂ (Tran et al. (2017)). (b) Second order correlation measurement results. (c) Photoluminescence spectrum taken from the green point on (d). The spectra were recorded by 514 nm CW excitation. (d) Optical image of a WS ₂ flake on Si substrate.	89
Figure 5.5. Photoluminescence spectra from a defect center in annealed WS ₂ flake on Si substrate were recorded by 514 nm (above) and 488 nm (below) excitation wavelengths.	90
Figure 5.6. The excitation polarization and emission intensity of defect center.	91
Figure 5.7. (a) Optical microscopy image of a typical WO ₃ flake on Si substrate. The colored dots represent the points where the same colored spectrum shown in (b) were recorded. (b) WO ₃ PL spectra recorded from four different points of the flake. (c) The green spectrum in (b) which has	

<u>Figure</u>	<u>Page</u>
humidity peaks, excited by 514 nm laser (green) and 488 nm laser (purple).	92
Figure 5.8. (a) The Photoluminescence spectra were recorded from three individual spots. The black line belongs to the spectrum of monolayer WS ₂ (Tran et al. (2017)). (b) PL spectrum from an annealed WO ₃ flake on Si substrate. The data in yellow frame is very similar to the yellow data which was reported in literature from WS ₂	93
Figure 5.9. Single photon emission (ZPL) from a localized defect center in WO ₃ and its phonon side bands.	94
Figure 5.10. (a) 2D PL map and (b) optical microscopy image of the WO ₃ flake on Si substrate. (c) Excitation (black) and emission (red) polarization dependent intensity variation. (d) Excitation power dependent intensity variations of the single photon emission (red) and Si Raman (black).	95
Figure 5.11. The room temperature monoclinic structural model of WO ₃	97
Figure 5.12. The electronic band dispersion of RT-WO ₃ . Red lines belong to calculations performed by GGA, and blue lines refer to HSE06 approximation added.	98
Figure 5.13. Experimental Raman spectrum of RT-monoclinic WO ₃ and calculated Raman activities are shown with black and red lines, respectively.	99
Figure 5.14. On the left, top views of an oxygen vacancy defect structure in 2x2x1 supercell, and on the right partial density of states (PDOS) of RT-WO ₃ with oxygen vacancy defect structures are given. On the left, the structures of (a) O vacancy along \vec{b} and (b) \vec{a} directions are shown. The black atoms are the removed oxygen atoms.	101
Figure 5.15. Temperature dependent Raman spectra of an annealed WO ₃ flake. (a) Raman spectra were recorded by 150 gr/mm and (b) by 600 gr/mm.	102
Figure 5.16. Temperature dependent Raman spectra of an annealed WO ₃ flake. (a) Raman spectra were recorded by 150 gr/mm and (b) the selected spectra.	103
Figure 5.17. Temperature dependent Raman spectra of an annealed WO ₃ flake. (a) Raman spectra were recorded by 600 gr/mm and (b) the selected spectra.	104
Figure 5.18. Excitation polarization dependent PL intensity from two different defect centers in annealed WO ₃ flakes. PL spectra were recorded by 150	

<u>Figure</u>	<u>Page</u>
gr/mm and 514 nm excitation source. At the right the optical microscope images of the flakes are shown.	106
Figure 5.19. Temperature dependent Photoluminescence spectra from two different defect center in annealed WO ₃ flakes. PL spectra were recorded by 150 gr/mm and 514 nm excitation source.	107
Figure 5.20. Reflection spectra for various annealing (a) temperatures and (b) durations.	108
Figure 5.21. PL spectra recorded from a WO ₃ flake (blue) and about 1 μm distance away from the defect center in WO ₃ flake (green) shown in the inset. Intensities of the spectra are for 1 sec exposure counts. The green spectrum is shown to clearly understand that there is no background effect of gold nanoparticles.	109
Figure 5.22. (a) After gold nanoparticle deposition, the excitation power dependent intensity variation of an emission. The circles represent the intensities of the emission and the dots are intensities of Si Raman signals extracted from the same spectra. The solid lines are theoretical fits. (b) The low power excited emission intensity decrease after exposure to a high power to obtain the saturation curve of the power series.	110
Figure 5.23. (a) Before (black) and after (red) gold nanoparticle deposition, the excitation power dependent intensity variation of the emission from same defect center. The circles represent the intensities of the emission and the solid lines are theoretical fits. (b) the optical image of the WO ₃ flake before the gold nanoparticle deposition. (c) Excitation (red) and emission (black) polarization dependent intensity variation of the emission. The solid lines are theoretical fits	111
Figure 5.24. (a) Before (black) and after (red) gold nanoparticle deposition, the excitation power dependent intensity variation of the emission are shown. The circles represent the intensities of the emission and the solid lines are theoretical fits.	112
Figure 6.1. (a) Schematic of the studied sample structure is shown with the drop-casted hBN flakes (yellow) and defect centers (red dots). A single layer graphene (black line) is transferred on top. Excitation by a 532 nm CW laser (green) and the emission (colored) in visible spectrum depend on the emission wavelength are shown by arrows. (b) A single defect is il-	

<u>Figure</u>	<u>Page</u>
	illustrated as a three-level system. The non-radiative energy transfer rate is k_{FR} . The band structure of graphene near the K point is seen with Fermi level, E_F 116
Figure 6.2.	(a) Optical microscope image (left) and the PL map of the same bulk hBN with a bright and localized emission from a single defect (right). (b) Room temperature PL spectra of the defect shown in the map before (black) and after (red) graphene transfer. 117
Figure 6.3.	The relation between excitation polarization and emission intensity of defect center with before (black) and after (red) graphene transfer shows linearly polarized emission. 118
Figure 6.4.	Excitation power dependent of ZPL and the Silicon Raman peak intensities extracted from the same spectra before (black) and after (red) graphene transfer for the same defect. 120
Figure 6.5.	To identify the single photon character of the emission observed at 610 nm from a localized point in the hBN the second order photon correlation experiment was performed by HBT setup. (a) The extracted excited state and metastable state lifetimes from the fit are on the order of 1.65 ns and 1.55 μ s. (b) The antibunching dip is seen and it is below the value of 0.5 which is the threshold value to identify a single photon emitter. 121
Figure 6.6.	Bare, one layer, two layer and three layer graphene transferred onto hBN flake are given respectively. Red dots show the (laser beam) defect center position on the flake. 123
Figure 6.7.	A single photon emission at 697 nm is seen from bottom to up bare, one layer, two layer and three layer graphene transferred onto emitter are shown. On the left raw spectra and on the right intensity corrected in terms of Si Raman peak spectra are shown. The orange lines belong to fit curves of the peaks. The calculated FWHM, intensity and shift values are also given in each spectrum. The black arrows show the quenching rates. 124
Figure 6.8.	A SP emission at 697 nm is corrected by normalizing the Si Raman signal intensity. The inset shows the normalized intensity variation of the emission with respect to the layer number of graphene. 125
Figure 6.9.	A single photon emission at 740 nm is seen from bottom to up bare,

one layer, two layer and three layer graphene transferred onto emitter cases are shown. They are corrected with respect to Si Raman signals. On the left the spectra are plotted linearly normalized. On the right the spectra are plotted logarithmically normalized. The orange lines belong to fit curves of the peaks. The calculated FWHM, intensity and shift values are also given in each spectrum. The orange arrows show the quenching percentages. To see clearly the energy difference between PSB and ZPL center, the ZPL center plotted on zero in purpose. 127

- Figure 6.10. (a) A SP emission at 656 nm (D656) next to the Silicon Raman peak at 654.6 nm and its quenching after each graphene layer transfer are observed with 600 gr/mm grating. (b) The PL spectra of D656 are shown by 150 gr/mm with G and 2D bands of graphene. (c) Quenching of another defect emitting at 653 nm (D653) is shown. (d) Quenching rate of both defects as a function of graphene layer. 128
- Figure 6.11. (a) Excitation power dependent $g^{(2)}(\tau)$ for the ZPL at 610 nm after graphene layer transfer. (b) The parameters calculated from $g^{(2)}(\tau)$ fits, a , τ_1 and τ_2 129
- Figure 6.12. Schematic representation of the de-shelving model with higher lying states from the excited states. 132
- Figure 6.13. (a) The constant rate model and (b) de-shelving model rate equations are used to fit experimental power series of before and after graphene coupling 134
- Figure 6.14. (a) Optical microscopy image of the hBN flake cluster. (b) excitation polarization versus emission intensity (c) PL spectra of before (black) and after (red) graphene transfer show emission quenching. (d) Excitation power versus emission intensity. (e) Lifetime measured at 50 MHz frequency. Black dots are the experimental statistics of before graphene and the line is one order fit. The red dots belong to after graphene statistics. 136
- Figure 6.15. (a) Excitation power versus emission intensity. (b) PL spectra of before (black line), after one layer graphene transfer (red line) and after a second layer graphene (blue line) transfer. (c) Lifetime measured at 50 MHz frequency. Black dots are the experimental statistics of before graphene and the line is one order fit. The red dots belong to after 1

layer graphene statistics and the blue dots refer to after a second layer graphene transfer. 137

Figure 6.16. Energy band diagrams of the pristine, n-doped and p-doped graphene with their Fermi levels. 138

Figure 6.17. (a) Schematic representation of the Fermi level shifting of graphene by gate voltage and energy transfer restriction. (b-c) Schematic representation of the designed device for reversible fluorescence quenching of SPE. (d) The used device in the experiments. 139

Figure 6.18. The background effect of ionic liquid. The left panel includes the Raman spectra of Si substrate, solution 1 (Sol01)/Si and glass/(Sol01)/Si. The right panel shows the background of another solution (Sol03). 140

Figure 6.19. (a) After three layer graphene (3 L GR) are placed on hBN individually, PL intensity variation of the SP emission at 725 nm with respect to gate voltages are shown. (b) The effect of alteration of the gate voltage on PL intensity of ZPL at 725 nm. (c) The excitation polarization dependent ZPL emission intensity under 1.4 V gate voltage. 142

LIST OF TABLES

<u>Table</u>	<u>Page</u>
Table 2.1. Characteristic properties of the second order correlation function at zero or any delay time value, $g^{(2)}(\tau)$, with respect to statistical classification of light.	10
Table 6.1. The extracted rates for before and after graphene coupling with respect to constant rate model (CRM) and de-shelving model (DSM).	133



CHAPTER 1

INTRODUCTION

Single photon (SP) sources are important for various practical applications such as quantum information processing, quantum computers, quantum communication, metrology, and medical applications (Nielsen (2000)). In principle, any single stable quantum system such as an isolated atom or a molecule can be regarded as a SP source. However, in practice, to achieve such an isolation is very hard to or sometimes impossible. For that matter, usually, point defects in solid materials such as diamond, ZnO, and SiC have been extensively used and studied as SP sources (Kurtsiefer et al. (2000); Neitzke et al. (2015); Gordon et al. (2013)). The best traditional SP sources are nitrogen vacancies in diamond (NV centers). Even though NV center in diamond is extensively researched and used it has several drawbacks such as; room temperature luminescence is very weak, diamond is very expensive and it is hard to control its properties. Research on other materials such as ZnO and SiC is very active. However, SP luminescence spectra from defects of these materials are very broad and not very stable (Choi et al. (2014)).

To achieve more stable and intense luminescence at room temperature (RT) alternative SP sources are under intense investigation. Recently, most commonly studied alternative materials are transition metal dichalcogenides (TMDCs) with layered structures (Tran et al. (2017)), lead halide perovskite quantum dots (PQDs) (Utzat et al. (2019)), graphene quantum dots (Zhao et al. (2018)), gallium nitride (GaN) (Berhane et al. (2018)), and hexagonal boron nitride (hBN) (Tran et al. (2015)). In such materials, the origin of the emission over a wide temperature range (from cryogenic to RT) generally results from discrete energy levels of the defect (color) centers (point defects) within the band gap of a host material (Wong et al. (2015)). Therefore, the emission can be observed in a very broad spectral range from the ultraviolet to the visible spectral region (Tran et al. (2016)).

Two dimensional (2D) materials, on the other hand, offer a fascinating platform for quantum-optic researches. Internal reflections of photons from a SP emitter embedded in a monolayer are suppressed more than those from an SP emitter in a bulk material, which leads to better light yield efficiency than those in a bulk material. Another advantage of SP sources in 2D materials is their ability to couple with plasmonic structures and cavities which leads to enhanced or quenched luminescence, thus, providing a control mechanism for the intensity of SP emission. The thickness of the host has a remarkable

importance for the applications based on the coupling to plasmonic tips (such as that of an atomic force microscope) or to plasmonic gap cavities, which requires nanometre-scale proximity. Such a coupling is usually quite difficult for SP emitters in bulk crystals due to their thicknesses being much more than tens of nanometers.

The most investigated SP emitting 2D materials are TMDCs such as MoSe₂, MoS₂, WSe₂ and WS₂, which are widely studied for use in many optoelectronic applications (Srivastava et al. (2015)). TMDCs have unique band structure features. For example, the conduction and valence band edges of monolayered crystals are located at the K points (K valley) in their hexagonal Brillouin zone (Dong et al. (2017)). Spin-orbit coupling splits the valence band electrons with different spins into two subbands (spin up and spin down bands) which leads to spin dependent selection rules for transitions between conduction and valence bands. In addition, the ability to observe strong Zeeman shifts is important in potential photon indistinguishability applications (Aharonovich et al. (2016)). The SP emission in monolayered TMDCs originates from localized (Frenkel), weakly bound excitons (Tonndorf et al. (2015)). To increase the stability of the emission, excitons can be trapped into potential wells by vacancy defects, impurity atoms, or local stresses (Raj and Tripathi (2019); Rosenberger et al. (2019)). However, SP emission in these materials can only be observed at very low temperatures due to their small exciton binding energies. This problem greatly restricts their practical applications (Aharonovich et al. (2016)). For that reason, current research activities on these materials are mainly focused on obtaining SP emission at higher temperatures, possibly at RT. In a recent study, for example, it was reported that interaction of TMDCs with plasmonic nano-cavities leads to SP emission at 160 K (Luo et al. (2019)). Another method of obtaining SP emission at high temperatures, as high as RT, is based on creating covalently bound oxygen or sp³ defects in a host material such as carbon nanotubes (He et al. (2017); Ma et al. (2015)). In a more recent study, using this approach (i.e. introducing oxygen defects), SP emission at RT was observed from WO₃ defects which occurred after thermal annealing of a WS₂ host (which is a TMDC material) (Tran et al. (2017)). Hence, for the first time a TMDC material was shown to exhibit SP emission at RT.

In this study, defects in WO₃ were investigated as room temperature SP sources. Inhomogeneous spectral distribution can be controlled by annealing of the materials. In addition to that multi-photon emission can be reduced in the same way. Efficient and stable luminescence at RT was obtained from localized single defect centers of annealed WO₃. Then, the structural and optical characteristics of observed localized emission from WO₃ were explained. We carried out a density functional theory (DFT) based first princi-

ple computational approach to understand the nature of such a SP center. We tried oxygen vacancies as the most possible cause for such a defect since its formation is energetically probable. We calculated the energy states for oxygen vacancies in a host WO_3 material yielding localized states in the band gap with energy levels consistent with the observed photoluminescence (PL) energies from annealed WO_3 samples.

Furthermore, to increase the brightness of the emissions at RT we introduced gold nanoparticles as plasmonic resonators which exhibit weak coupling with the individual color centers at distances of a few nanometers (Nguyen et al. (2018); Iff et al. (2018); Hoang et al. (2016)). After introduce gold nano particles near WO_3 samples (usually in the form of flakes), emission intensity enhancement, as much as 5 times, was clearly observed. These results are promising for future applications of SP emitters in WO_3 for both TMDC hosts in terms of integrated nanophotonics and plasmonic devices. Our results contribute to the understanding of the nature of defects as room temperature SP emitters in WO_3 .

Among the stable 2D materials, hBN has attracted a great deal of attention as a room temperature SP source (Tran et al. (2015, 2016)). It is a wide band gap (5.9 eV) insulator. Recent studies show that hBN is a very promising candidate for quantum information technologies, medical applications, quantum communication, and optoelectronic applications. Localized defect centers in hBN have discrete energy states in the band gap, very much like atomic energy levels, hence, emit SPs. Its wide bandgap allows the emissions distributed across a large energy range exceeding 500 meV (Museum et al. (2008)). SP emission from bulk hBN is observed from optically active defect centers without any pretreatment (Martínez et al. (2016)). Thus, potential applications of SP emission from hBN has attracted many researches. For example, research on the application of hBN as a SP source to the field of quantum key distribution begun only very recently, in 2016. A major disadvantage of a 2D material, such as hBN, as a SP source is that the emitters are exposed to the environment conditions and are easily affected by them which deteriorate device performance over time. Hence such materials are need to be covered with protecting transparent layers.

In this thesis, reversible fluorescence quenching of SP emission in hBN at RT has been studied. Firstly, SP emission from some defects in hBN was investigated. Then, a single layer graphene was placed on hBN at a near field distance to the SP emitters. The analyses of optical characteristics of particular SP emitters before and after graphene transfer were carried out in detail. Förster-like resonance energy transfer between a particular SP emitter and the graphene layer were investigated in terms of the number of

coupled graphene layers. Furthermore, reversible modulation of the SP emission quenching by an applied gate voltage was demonstrated by a custom designed ionic liquid-based device structure.

The thesis is structured as follows. Chapter 2 is devoted to the theoretical background of light-matter interaction which includes the characteristics of SP emission from defects. In Chapter 3, experimental techniques and methods used in this thesis were described in detailed. In Chapter 4, the structural and spectroscopic properties of the materials used in this study were investigated. Chapter 5 gives the analyses and results of optical characterizations of room temperature SP emission from the defects in WO_3 which were further investigated by theoretical calculations. Brightness enhancement results due to plasmonic gold nano particles are also given. In Chapter 6, SP emission from defects in hBN was investigated in detail with a theoretical background. After that, energy transfer mechanism between an emitter in hBN and graphene was studied. Finally, a reversible on-off control mechanism via a gate voltage was shown for the emission from a SP source using a device structure. Chapter 7, summarizes the results of our studies.

CHAPTER 2

THEORETICAL BACKGROUND OF LIGHT-MATTER INTERACTION

In this chapter, a brief introduction is given about the theoretical background of photon statistics and light-matter interaction on the basis of a simple two-level system with an extension to a three-level systems. Absorption-emission processes and photoluminescence characteristics of defects are explained. Furthermore, interaction of a single photon source with various nanostructures are examined. Fluorescence brightening by plasmonic nanoparticles and quenching by Förster Resonance Energy Transfer (FRET) mechanism are discussed. The results of the fluorescence experiments carried out in this thesis could be analyzed in the light of this background.

2.1. Statistical Classification of Light

Most light sources show fluctuations in the intensity and phase of the emitted light. Due to nature of sources such fluctuations are almost impossible to avoid. The most stable beam of light with a constant intensity is perfectly coherent. Such a beam of light has light waves whose electric field \vec{E} can be expressed in terms of a single sine function with a definite angular frequency ω and a wave vector \vec{k} in the direction of propagation with a constant amplitude \vec{E}_0 as

$$\vec{E}(x, t) = \vec{E}_0 \sin(kx - \omega t + \phi) \quad (2.1)$$

for a light wave propagating along x direction only, where ϕ is a constant phase (depending on initial conditions). According to classical electromagnetic theory, intensity of light (I) is proportional to the square of the time averaged electric field. Classical expression of electric field of light can be given as

$$\vec{E}(\vec{r}, t) = \int \vec{E}_k(\vec{r}, t) d\vec{k}, \quad (2.2)$$

the sum (integral) of all possible monochromatic components containing all possible frequencies (Jackson (1998)).

$$\vec{E}_k(\vec{r}, t) = \vec{E}_k^* e^{-i\omega_k t + i\vec{k}\cdot\vec{r}} + \vec{E}_k e^{i\omega_k t - i\vec{k}\cdot\vec{r}}, \quad (2.3)$$

where k indicates a particular mode (monochromatic component) corresponding to a particular wave vector \vec{k} whose amplitude is inversely proportional to the wavelength λ of that mode ($k = 2\pi/\lambda$). In quantum mechanics, however, light intensity is proportional to photon flux, i.e. the number of photons, per given area with a definite photon energy of $\hbar\omega$. In quantum electrodynamics, the proper account of light interaction with matter (especially with electrons of atoms) require the quantization of electric and magnetic fields of light (photons). Since electric and magnetic fields behave similarly we will consider the electric field only. The generalized quantized electric (electromagnetic) field operator is expressed as the following (Paul (1982); Wysin (2011)):

$$\hat{\vec{E}}(\vec{r}, t) = \int \hat{\vec{E}}_k(\vec{r}, t) d\vec{k}. \quad (2.4)$$

The constituent field operators in the momentum space (k-space) are expressed in the symmetrical form as

$$\hat{\vec{E}}_k(\vec{r}, t) = \hat{\vec{E}}_k^+ + \hat{\vec{E}}_k^-, \quad (2.5)$$

where the positive (+) and negative (−) field operators are given as

$$\hat{\vec{E}}_k^+ = i\sqrt{\frac{2\pi\hbar\omega_k}{V}}\epsilon_k(\hat{a}_k e^{-i\omega_k t + i\vec{k}\cdot\vec{r}}), \quad (2.6)$$

$$\hat{\vec{E}}_k^- = -i\sqrt{\frac{2\pi\hbar\omega_k}{V}}\epsilon_k(\hat{a}_k^\dagger e^{i\omega_k t - i\vec{k}\cdot\vec{r}}), \quad (2.7)$$

respectively. Here \hat{a} and \hat{a}^\dagger are photon annihilation and creation operators (Paul (1982); Wysin (2011)). In the following parts of this thesis, for single mode electromagnetic field the mode label k will be omitted. For a photon state $|n\rangle$ the following well known eigen

equations hold for field quantization:

$$\hat{a}|n\rangle = \sqrt{n}|n-1\rangle, \quad (2.8)$$

$$\hat{a}^\dagger|n\rangle = \sqrt{n+1}|n+1\rangle, \quad (2.9)$$

where all elements of the bases $|n\rangle$ forms a complete set. One can easily show that $\hat{a}^\dagger\hat{a}|n\rangle = n|n\rangle$, hence $\hat{a}^\dagger\hat{a}$ is called the number operator.

For a perfectly coherent light, flux should be time independent with no fluctuations. That means the average number of photons emitted from a coherent source in a time interval Δt must be time independent provided Δt is much longer than life times of excited states of light emitting sources. In practice, such a perfectly coherent beam of light with no intensity fluctuations can be approximated by a monochromatic laser field. In reality, one can not expect the same number of photons for any given time interval Δt even from the most stable light source. There will always be fluctuations in the number n of the photons reaching a detector from a coherent light source for a duration longer than life times of sources, but not too long. The probability of counting n photon from such a source for a definite time interval is given in terms of Poisson distribution (Fox (2006)):

$$P_P(n) = \frac{\bar{n}^n}{n!} e^{-\bar{n}}, \quad (2.10)$$

where \bar{n} is the average photon count. Thus, the photon counting obeys Poisson statistics with a standard deviation Δn ($\Delta n = \sqrt{\bar{n}}$).

Furthermore, there are other classical light sources that has larger intensity fluctuations in time and resulting larger photon number fluctuations than constant intensity sources. The most known form of these sources is thermal light. Statistics of such photons are called super-Poissonian ($\Delta n > \sqrt{\bar{n}}$) and the probability function for a single mode of this kind of field which follows Bose-Einstein distribution, is given as (Fox (2006))

$$P_{BE}(n) = \frac{\bar{n}^n}{(1 + \bar{n})^{n+1}}. \quad (2.11)$$

Finally, a third possibility exist where intensity or photon number fluctuations in time may be smaller than that for a perfectly coherent light, that is; $\Delta n < \sqrt{\bar{n}}$. Obviously,

this type of light is more stable than coherent light. A single photon source is a good example for such a light source since such a source, under a continuous excitation (such as due to irradiation), will emit a stream of photons with a well defined time interval between consecutively emitted photons defined by the life times of the excited states of the source. The statistics of light from such a source obeys the so called sub-Poissonian statistics. The nature of sub-Poissonian light is completely quantum electrodynamical rather than classical. As expected, the detection of this kind of light is very difficult due to extremely weak intensities that are suppressed by optical losses. Thus, the observation of single photons became possible only after the development of single photon sensors such as photomultiplier counters and avalanche photon diodes (APD).

2.2. Correlation Functions

In order to explain the properties of the measured photon counting statistics for coherent light in the classical perspective, correlation functions are defined. The quantum mechanical definition for the coherence function of order n is (Benson (2009))

$$G^{(n)}(\mathbf{r}_1 t_1, \dots, \mathbf{r}_n t_n; \mathbf{r}_{n+1} t_{n+1}, \dots, \mathbf{r}_{2n} t_{2n}) = \langle E^-(\mathbf{r}_1 t_1) \dots E^-(\mathbf{r}_n t_n) E^+(\mathbf{r}_{n+1} t_{n+1}) \dots E^+(\mathbf{r}_{2n} t_{2n}) \rangle, \quad (2.12)$$

where $\langle \dots \rangle$ indicates the time average, n being the number of sources. We can see that spacial and temporal positions of strongly correlated electric fields will be very close to each other within a given temporal or spacial period. To obtain the coherence time and length of radiation from a single source in classical terms the normalized first order correlation function can be used.

2.2.1. First Order Correlation Function

The simplest case of first order coherence is observed, for example, from a Young's Double Slit experiment. In the classical case, the electric field $\vec{E}_1(t)$ and $\vec{E}_2(t+\tau)$ of light waves coming from two coherent sources 1 and 2 are superpositioned and the net intensity I is proportional to the square of the net field vector where the averages are taken over a period and in terms of photons these equations represent photon fluxes:

$$\begin{aligned}
I &\propto \langle |\vec{E}_1(t) + \vec{E}_2(t + \tau)|^2 \rangle \\
&= \langle |\vec{E}_1(t)|^2 \rangle + \langle |\vec{E}_2(t + \tau)|^2 \rangle + 2\text{Re}\langle \vec{E}_1(t)\vec{E}_2(t + \tau) \rangle.
\end{aligned} \tag{2.13}$$

The last term in this equation indicates a first order correlation between the electric fields from the sources 1 and 2 with time dilations of t and $t + \tau$ between them, respectively, (where the phase difference is due to τ only). The first order correlation function is defined as the normalized first order coherence function:

$$g^{(1)}(\tau) = \frac{\langle \vec{E}_1(t)\vec{E}_2^*(t + \tau) \rangle}{\langle |\vec{E}_1(t)|^2 \rangle}. \tag{2.14}$$

Quantum mechanical expression for the first order correlation function at the same space position is given as

$$g^{(1)}(\tau) = \frac{\langle E^-(t)E^+(t + \tau) \rangle}{\sqrt{\langle E^-(t)E^+(t)E^-(t + \tau)E^+(t + \tau) \rangle}}. \tag{2.15}$$

In terms of creation and annihilation operators for a single mode coherent light (such as laser light) one can show that above equation becomes:

$$g^{(1)}(\tau) = \frac{\langle a^\dagger(t)a(t + \tau) \rangle}{\langle a^\dagger a \rangle}. \tag{2.16}$$

In a Young's Double Slit experiment, one can define whether light source is monochromatic or not. One can also determine the coherence length. However, the statistical properties of photons cannot be understood from such an experiment. In other words, first order correlation experiments cannot distinguish between the states of light with the same spectral distribution but different photon number distribution. For example, the field intensity of a single photon state and a coherent state with $\bar{n} = 1$ are the same.

2.2.2. Second Order Correlation Function

To distinguish photon statistics and define the single photon character first order correlation function is not sufficient. To study states having the same spectral distribu-

tion but with different photon statistics one needs to consider the second order coherence function. The normalized second order correlation function, $g^{(2)}(\tau)$, gives the probability of detecting a second photon at a time $t + \tau$ after detecting a first photon at an earlier time t at a common space position r (Fox (2006)):

$$g^{(2)}(\tau) = \frac{\langle E^-(t)E^-(t+\tau)E^+(t+\tau)E^+(t) \rangle}{\langle E^-(t)E^+(t) \rangle^2} = \frac{\langle I(t+\tau)I(t) \rangle}{\langle I(t) \rangle^2}. \quad (2.17)$$

It is obvious that the second order correlation function gives the intensity correlation of two different sources instead of electric field correlation. Since intensity is proportional to photon number flux, this function is clearly related to photon statistics. Since photon statistics of a single photon source is different from the others, hence, we clearly need to use the second order correlation function to understand the statistics of such a source.

Table 2.1. Characteristic properties of the second order correlation function at zero or any delay time value, $g^{(2)}(\tau)$, with respect to statistical classification of light.

Light Source	Property	Comments
Classical	$g^{(2)}(0) \geq 1$ $g^{(2)}(0) \geq g^{(2)}(\tau)$	Bunched (thermal light)
Perfectly Coherent	$g^{(2)}(0) = 1$	No bunching (laser light)
Non-classical	$g^{(2)}(0) < 1$ $g^{(2)}(0) < g^{(2)}(\tau)$	Anti-bunched (single photon source)

In the quantum field theory perspective, properties of photon statistics are better understood when one uses photon annihilation (\hat{a}) and creation (\hat{a}^\dagger) operators instead of field operators E^- and E^+ (Loudon (2000)). For a single mode electric field, using equations (2.6) and (2.7) second order correlation function becomes:

$$g^{(2)}(\tau) = \frac{\langle \hat{a}^\dagger(t)\hat{a}^\dagger(t+\tau)\hat{a}(t+\tau)\hat{a}(t) \rangle}{\langle \hat{a}^\dagger(t)\hat{a}(t) \rangle^2}. \quad (2.18)$$

In the zero time delay ($\tau = 0$) case, for a classical field, considering the randomness of the classical field the function can be bounded by the Cauchy-Schwarz inequality

as following (Gerry and Knight (2004)):

$$\langle I(t) \rangle^2 \leq \langle I(t)^2 \rangle \rightarrow g^{(2)}(0) \geq 1. \quad (2.19)$$

In the case of a general time delay (τ), one can show that

$$\langle I(t)I(t + \tau) \rangle \leq \langle I(t) \rangle^2, \quad (2.20)$$

which means

$$g^{(2)}(\tau) \leq g^{(2)}(0). \quad (2.21)$$

These results mean that, if a light source has a time varying (time dependent) intensity; when a photon at $t = 0$ was detected, the probability of detecting another photon in a duration at an earlier time is greater than that for the same duration but at a later time. As a result, one observes more number of photons within the first time interval (τ) compared to later time intervals of the same duration. Thus, $g^{(2)}(0) > 1$ is called bunched light. In this case, we expect $g^{(2)}(\tau)$ decrease with (τ) which will reach unity for very large (τ) values.

On the other hand, consider a light source that has a constant (time independent) intensity. If there is no intensity fluctuations, light source is perfectly coherent and monochromatic. In this case, it is clear that, for a zero delay time or a general time delay, $g^{(2)}(\tau)$ will be equal to unity. This means that the probability of detecting of a photon is the same for all values of delay time, τ , regardless of any previous emission. Such a probabilistic event is a general property of the Poissonian statistics. In other words, for a perfectly coherent light, time intervals between consecutively emitted photons from the same light source is random. A coherent state is defined by eigenfunction of the photon annihilation operator, $|\alpha\rangle$ (Gerry and Knight (2004)). In that case time characteristic of the second order correlation function can be expressed as following:

$$g^{(2)}(0) = g^{(2)}(\tau) = \frac{\langle \alpha | \hat{a}^\dagger \hat{a}^\dagger \hat{a} \hat{a} | \alpha \rangle}{\langle \alpha | \hat{a}^\dagger \hat{a} | \alpha \rangle^2} = \frac{|\alpha|^4}{|\alpha|^4} = 1. \quad (2.22)$$

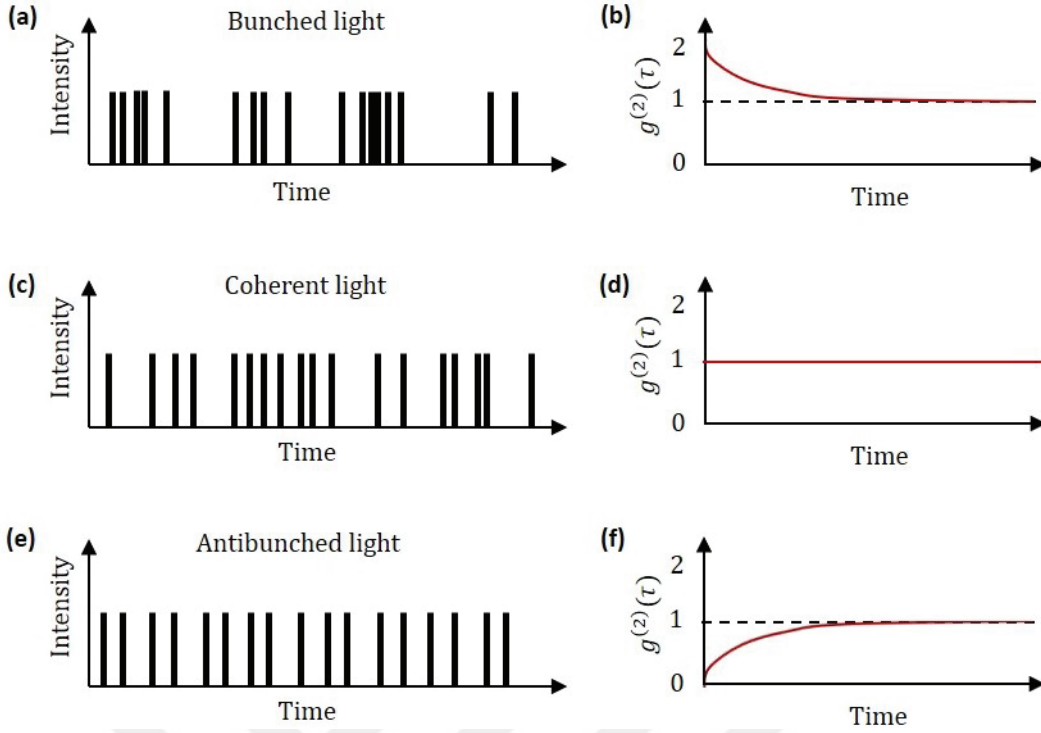


Figure 2.1. Statistical difference among light sources. (a) An example of bunched light with (b) its $g^{(2)}(\tau) = 2$. (c) An example of coherent light with (d) its $g^{(2)}(\tau) = 1$. (e) An example of antibunched light with (f) its $g^{(2)}(\tau) = 0$. For all types of light sources $g^{(2)}(\tau \rightarrow \infty) = 1$.

For a sub-Poissonian light, whereas, the eigen states are photon number states (Fock states) $|n\rangle$. Thus, one can find the second order correlation function with no time delay as

$$g^{(2)}(0) = \frac{\langle n | \hat{a}^\dagger \hat{a}^\dagger \hat{a} \hat{a} | n \rangle}{\langle n | \hat{a}^\dagger \hat{a} | n \rangle^2} = 1 - \frac{1}{\langle n \rangle} \quad (2.23)$$

(Gerry and Knight (2004)). It is seen that $g^{(2)}(0) < 1$ for any number state, in particular $g^{(2)}(0) = 0$ for a single photon state $|1\rangle$ since $\hat{a}|n\rangle = c|n-1\rangle = c|0\rangle = 0$. In general, fluctuations in the character of a source obeying sub-Poissonian statistics may cause an increased number of photon counts in the shorter time durations. Then, for a nonclassical light source the following inequality holds:

$$1 - \frac{1}{\langle n \rangle} \leq g^{(2)}(0) < 1. \quad (2.24)$$

For a single photon source, $g^{(2)}(0) = 0$ means that there will be longer time intervals between each observed photon counting events. In this case, the probability of detection of a second photon after detecting the first one is smaller for smaller values of τ and increases up to unity with time. This, $g^{(2)}(\tau) > g^{(2)}(0)$, type of light is called antibunched light. This light is incompatible with Eq.(2.19) and (2.20) hence, it has no classical counterpart, in other words, it is purely due to the quantum nature of light (Kimble et al. (1977)). According to the type of light, the value of $g^{(2)}(\tau)$ varies $g^{(2)}(\tau) < 1$, $g^{(2)}(\tau) = 1$ and $g^{(2)}(\tau) > 1$ for antibunched, coherent and classical (bunched) light, respectively. This is shown in Fig.2.1.

As we discussed earlier, for a perfect single photon source, $n = 1$ and the second-order correlation function is $g^{(2)}(\tau = 0) = 0$. Thus, for an ideal single photon the probability to detect two photons at the same time is zero. After a certain time delay the photon is emitted and then the system can be re-excited to emit a second photon. In particular, for a two state system the excited state corresponds to $n = 2$. In that case $g^{(2)}(\tau = 0) = 0.5$. In general, the source is either in the ground state or in the excited state, one can say

$$0 < g^{(2)}(\tau = 0) < 0.5. \quad (2.25)$$

2.2.3. The Hanbury Brown-Twiss Experiment

An experimental method to measure the second order correlation function $g^{(2)}(\tau)$ for a single photon source employs an intensity interferometer. Such an interferometer was first used by R. Hanbury Brown and R. Q. Twiss in 1954 (Brown and Twiss (1954)) to measure the angular diameter of radio stars. A schematic diagram of a Hanbury Brown and Twiss (HBT) interferometer is given in Fig.2.2. In that setup, light from a common source splits into a reflected and a transmitted beams via a beam splitter. Then, both light beams are detected at the same distance r from the beam splitter. Thus, correlation in such a setup will only be measured in terms of fluctuations in time between the two beams.

The photon antibunching using an HBT interferometer set up was exhibited for the first time in 1977 (Kimble et al. (1977)). Upon impinging on a 50:50 beam splitter (BS) incident light beam splits into two parts; reflected and transmitted beams with equal intensities. To detect the intensity correlation in time, two photon counting detectors D1 and D2 detecting the photons in the transmitted and reflected beams, respectively,

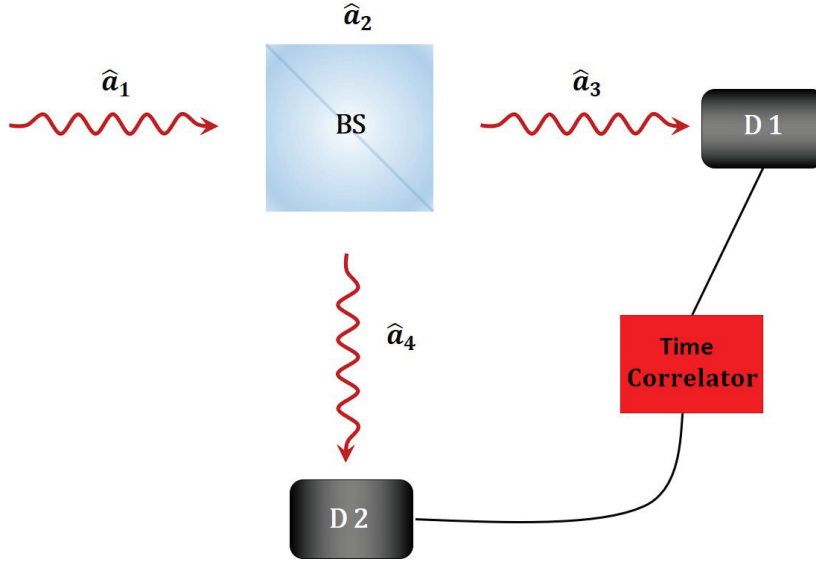


Figure 2.2. The schematic representation of Hanbury-Brown-Twiss interferometer setup. Sides 1 and 2 are for incoming photons to beam splitter (BS) while site 3 and 4 are for the outgoing ones. The corresponding photon annihilation operators are given where D1 and D2 are detectors.

are placed at equal distances from the BS. These detected counts are multiplied by one another in a time correlator. The integrated value of the product in a sufficiently long time period gives the measured intensity fluctuation. In the classical approach we can write down the electric fields for the reflected (E_r) and transmitted (E_t) as a fraction for incoming field E_0 : Thus: $E_t = TE_0$ and for the reflected one: $E_r = RE_0$.

In quantum mechanical approach, since the second order correlation function for a light source is defined in terms of annihilation (\hat{a}) and creation (\hat{a}^\dagger) operators, we must express the transmitted and reflected electric field operators as such. Since BS transmits a portion T (transmission coefficient) of the original field and reflects a portion R (reflection coefficient), the same is true for the corresponding creation and annihilation operators for transmitted and reflected light fields. However, in the quantum mechanical view one must include a zero state incoming field (null field) on the side 2 of the BS in order to account for the proper vacuum fluctuations. Thus, the following equations must hold for annihilation operators corresponding to the transmitted (index 3) and reflected (index 4) photons:

$$\hat{a}_3 = T\hat{a}_1 + R\hat{a}_2, \quad (2.26)$$

$$\hat{a}_4 = \mathbf{R}\hat{a}_1 + \mathbf{T}\hat{a}_2. \quad (2.27)$$

In general the complex numbers R and T can be frequency dependent. Usually, beam splitters do not absorb any photon. Thus, energy conservation for the photons must hold. For a monochromatic light source, then, the following relations can be written:

$$|\mathbf{R}|^2 + |\mathbf{T}|^2 = 1, \quad (2.28)$$

$$\mathbf{R}\mathbf{T}^* + \mathbf{R}^*\mathbf{T} = 0. \quad (2.29)$$

As shown in Fig.2.2, the incoming field state, $|\phi\rangle$, is defined by the index 1, the other input side; by the index 2. The total incoming light is $|\phi\rangle|0\rangle$ where the number zero in the ket notation means no photon. Using equations (2.26) and (2.27) the output mean photon numbers are

$$\begin{aligned} \langle n_3 \rangle &= \langle 0 | \langle \varphi | \hat{a}_3^\dagger \hat{a}_3 | \varphi \rangle | 0 \rangle \\ &= \langle 0 | \langle \varphi | |\mathbf{R}|^2 \hat{a}_1^\dagger \hat{a}_1 + \mathbf{R}^* \mathbf{T} \hat{a}_1^\dagger \hat{a}_2 + \mathbf{T}^* \mathbf{R} \hat{a}_2^\dagger \hat{a}_1 + |\mathbf{T}|^2 \hat{a}_2^\dagger \hat{a}_2 | \varphi \rangle | 0 \rangle \\ &= |\mathbf{R}|^2 \langle n_1 \rangle, \end{aligned} \quad (2.30)$$

$$\langle n_4 \rangle = |\mathbf{T}|^2 \langle n_1 \rangle, \quad (2.31)$$

where first equation gives the total number of photons detected by D1 while the other is that detected by D2 for a long enough time. The mean input photon number n_1 is given as

$$\langle n_1 \rangle = \langle \varphi | \hat{a}_1^\dagger \hat{a}_1 | \varphi \rangle. \quad (2.32)$$

Then, the measured intensity correlation for the reflected and transmitted photons can be found in terms of the mean value of the product of output photon number operators n_3 (for transmitted light) and n_4 (for reflected light). Using $[\hat{a}, \hat{a}^\dagger] = \hat{a}\hat{a}^\dagger - \hat{a}^\dagger\hat{a} = 1$, and energy conservation relations (equations (2.28-31)), this correlation can be obtained as the following (Chunlang (2007)):

$$\begin{aligned}
\langle n_3 n_4 \rangle &= \mathbf{R}^* \mathbf{R} \mathbf{T}^* \mathbf{T} \langle \varphi | \hat{a}_1^\dagger \hat{a}_1 \hat{a}_1^\dagger \hat{a}_1 | \varphi \rangle + \mathbf{R}^* \mathbf{T} \mathbf{R}^* \mathbf{T} \langle \varphi | \hat{a}_1^\dagger \hat{a}_1 | \varphi \rangle \\
&= |\mathbf{R}|^2 |\mathbf{T}|^2 \langle \varphi | \hat{a}_1^\dagger \hat{a}_1 \hat{a}_1 \hat{a}_1^\dagger - \hat{a}_1^\dagger \hat{a}_1 | \varphi \rangle \\
&= |\mathbf{R}|^2 |\mathbf{T}|^2 \langle \varphi | \hat{a}_1^\dagger \hat{a}_1^\dagger \hat{a}_1 \hat{a}_1 | \varphi \rangle.
\end{aligned} \tag{2.33}$$

Finally, combining Eq.(2.30), (2.31) and (2.33) the normalized second order correlation function can be written as

$$g_{3,4}^{(2)}(\tau) = \frac{\langle n_3 n_4 \rangle}{\langle n_3 \rangle \langle n_4 \rangle} = \frac{\langle \hat{a}_1^\dagger \hat{a}_1^\dagger \hat{a}_1 \hat{a}_1 \rangle}{\langle \hat{a}_1^\dagger \hat{a}_1 \rangle^2} = g_1^{(2)}(\tau). \tag{2.34}$$

As clearly seen, measuring the detected counts by two different detector in HBT setup and multiplying by one another in a time correlator we can measure the second order correlation function of the incoming light.

In an HBT experiment, if the fluorescence source is a true single photon source, only one detector can record a signal at any time t . The second order correlation function refers to the probability that two detectors measure more than one photon at the same time. For a single photon source this probability must be equal to zero. One of the detectors, D1, detect a photon at time t_1 the other detector, D2, detect another photon at time t_2 , and the time difference between the two closest detection times is $\Delta t = t_1 - t_2 = \tau$. Thus, τ will be zero if the probability of detecting two photon at the same time is zero. The HBT time correlation experiment must be carried out over a time period which should be long enough to obtain a time correlation histogram. Considering that a single photon source will emit a single photon in a natural life time, such a duration must span many life times of the source. The experimental description of $g^{(2)}(\tau)$ can be given as

$$g^{(2)}(\tau) = \frac{N_c(t)}{I_3 I_4 \Delta t T}, \tag{2.35}$$

where $N_c(t)$ is the number of count coincidences, I_3 and I_4 are intensities (average number of photons per unit time interval of the measurement) of the detected signal from paths 3 and 4, respectively (Fig.2.2). The time resolution is Δt and T is the total time period of the signal detection in HBT experiment. To sum up, the second order correlation function is measured by HBT experiment consisting the setup a beam splitter, two SP sensitive detectors and a time correlator.

2.3. Interaction of light with a Defect Center: Two-Level Model

In this thesis, defect centers in the WS_2 , WO_3 , and hBN host materials have been studied as single photon sources. We will now characterize the statistical properties of single photon emitted from such defects along with the related second order correlation functions. The simplest case of a single photon emitter is given by a two level model. In such a system, there are two states only, that are; a ground state $|g\rangle$ and an excited state $|e\rangle$ with corresponding energy eigenvalues E_g and E_e , respectively. A schematic representation of the non-resonantly driven model, when a single mode classical electromagnetic field interacts with the system, is shown in Fig. 2.3. The emitter is excited by an electric field with a frequency ω_i and a fluorescent light with a frequency ω is generated. Usually, $\omega_i > \omega$, and extra energy of the excited system is lost via a vibrational relaxation process reducing it down to energy E_e . Then, the excited system emits a photon with energy $\hbar\omega$ equal to the energy difference between the excited and the ground states.

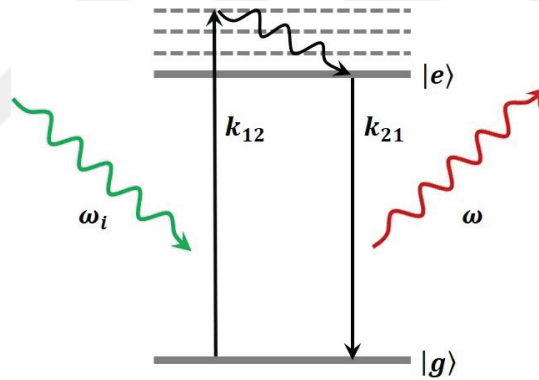


Figure 2.3. Schematic representation of interaction between a two-level system and a classical single mode electromagnetic field.

In quantum perspective, Hamiltonian operator of the two-level system is given as (MIT OpenCourseWare (2006))

$$\hat{H}_A = E_e|g\rangle\langle e| + E_g|e\rangle\langle g|. \quad (2.36)$$

The raising operator, $\hat{\sigma}_+ = |e\rangle\langle g|$, generates a transition from the ground to the excited

state and lowering operator, $\hat{\sigma}_+^\dagger = |g\rangle\langle e|$, transition from the excited state to the ground state. Both are non-Hermitian operators. In physical terms, after interaction with the excitation laser the system in the ground state ($|g\rangle$) absorbs one photon and excited into an internal energy level (usually vibronic) in the excited state, where it quickly relaxes to the lowest energy level in the excited state $|e\rangle$. The system then decays to the ground state by spontaneous emission of a single photon (the average time the system spends in the excited state is called the life time of that state). Such excitation and emission transitions can be understood in terms of an electric dipole transition in the first order approximation for the disturbed medium atoms. (that is; when the electric field of the incident light is reasonable weak, or in the case of point defects, the wavelength of the field is much longer than the size of the emitter, the change in the total energy (Hamiltonian) of the system is linearly proportional to the disturbing field, (higher order terms in electric field can be ignored)). Thus, the total Hamiltonian of the system can be written as the sum of the Hamiltonian of the two level system and an interaction Hamiltonian (Gerry and Knight (2004)):

$$\hat{H} = \hat{H}_A + \hat{H}_I. \quad (2.37)$$

The interaction Hamiltonian in the (electric) dipole approximation is (Gerry and Knight (2004)):

$$\hat{H}_I = -\hat{\vec{d}} \cdot \hat{\vec{E}}(\vec{x}_A, t), \quad (2.38)$$

where $\hat{\vec{d}}$ is the (electric) dipole moment operator and $\hat{\vec{E}}(\vec{x}_A, t)$ is the electric field operator (MIT OpenCourseWare (2006)). Since the transition is either from ground state to excited state (ge) or vice versa (eg) both absorption (ge) and emission (eg) must be accounted for. Thus dipole operator includes both transitions as following (MIT OpenCourseWare (2006)):

$$\hat{\vec{d}} = \vec{d}_{eg}|g\rangle\langle e| + \vec{d}_{ge}|e\rangle\langle g|, \quad (2.39)$$

where \vec{d}_{eg} and \vec{d}_{ge} are corresponding classical electric dipole moments. The electric field operator can also be cast into a more symmetric form:

$$\hat{\vec{E}}(\vec{x}_A, t) = \frac{1}{2}(E_0 e^{i\omega t} \hat{\vec{e}}_p + E_0^* e^{-i\omega t} \hat{\vec{e}}_p^*), \quad (2.40)$$

where $\hat{\vec{e}}_p$ is polarization vector of the monochromatic electromagnetic wave.

Due to interaction with light the atomic states are not in pure quantum mechanical states. This means that interaction picture (Heisenberg's matrix mechanics) is more suitable for such systems. In particular, the second order correlation function can be obtained via the matrix algebra of quantum mechanics. In that case, the equation of motion of a system is expressed in terms of a density operator $\hat{\rho}$ which includes a mixture of quantum states. For N dimensional Hilbert space of state vectors $|\varphi_j\rangle$ it is given as

$$\hat{\rho} = \sum_j^N p_j |\varphi_j\rangle \langle \varphi_j|, \quad (2.41)$$

where p_j are probabilities for each state j . For a two state system, density matrix elements can be solved numerically under its most general conditions. In the matrix formalism of the density operator, the diagonal elements are populations of the excited and ground states, ρ_{22} and ρ_{11} , respectively. To simplify the notations, the excited state and the ground state populations will be described by ρ_2 and ρ_1 , respectively, while the off-diagonal elements (ρ_{12} and ρ_{21}) represent the coherence. The time evolution of the density matrix can be described in the interaction picture by following master equation in the Lindblad form (Yamamoto and Imamoglu (1999)):

$$\dot{\hat{\rho}} = \frac{1}{i\hbar} [\hat{H}_I, \hat{\rho}] + L(\hat{\rho}), \quad (2.42)$$

where $L(\hat{\rho})$ includes the sum of all possible transition operators of the system. In fact, Eq.(2.42) is a generalization to Heisenberg's equation of motion in the interaction picture when the system is disturbed by environmental variables, here in our case, the exciting light. The dynamics of such a system can be understood from the solutions of Eq.(2.42) and carried out. The solutions give a set of coupled differential equations (See page 243 in the book "Introductory Quantum Optics" by Gerry and Knight (2004)) that are the Bloch equations first obtained for the magnetic resonance. The solutions of these equations give the populations and coherence for an idealized two-level system. The excited state population can be easily solved by considering the initial conditions, $\rho_1(t =$

$\rho_{11}(t=0) = 1, \rho_{22}(t=0) = 0, \rho_{21}(t=0) = 0, \rho_{12}(t=0) = 0$, meaning the emitter is in the ground state initially. The second order correlation function is defined by (Kurtsiefer et al. (2000))

$$g^{(2)}(\tau) = \frac{\rho_{22}(\tau)}{\rho_{22}(\tau \rightarrow \infty)}, \quad (2.43)$$

which is the possibility of detecting a photon emitted from a single source is directly proportional to the excited state population normalized by its steady state value.

One can now calculate $g^{(2)}(\tau)$ from Eq.(2.43) where the population density matrix elements are found from matrix algebraic approach in the Heisenberg formalism using Bloch equations. However, such calculations are lengthy and complicated. On the other hand, in the case of slowly varying weak fields, classical rate equations can produce the same results as those found from Bloch equations (Kimble et al. (1986)). Accordingly, in the interaction process as described by Fig.2.3, the relaxation time from higher levels to excited state $|e\rangle$ is very short and negligible. For a two level system of states 1 (ground state $|g\rangle$) and state 2 (excited state $|e\rangle$), the change of the population of the state 1 and state 2 depends on the populations of the states 1 and 2 in the following manner (Novotny and Hecht (2006)):

$$\frac{d\rho_1}{dt} = -k_{12}\rho_1 + k_{21}\rho_2, \quad (2.44)$$

$$\frac{d\rho_2}{dt} = k_{12}\rho_1 - k_{21}\rho_2. \quad (2.45)$$

In Eq.(2.44), k_{12} is the excitation or pump rate (absorption rate) coefficient from state 1 to state 2 and k_{21} is the decay (emission) rate from state 2 to state 1. Thus, Eq.(2.44) gives the change in the population of the state 1 in terms of excitation to state 2 (which decreases the state 1 population) and a transition from state 2 to state 1 (2nd term in Eq.(2.44) which increases the population of state 1. The rate equation (Eq.(2.45)) for the state 2 is interpreted likewise. The sum of the population densities of states 1 and 2 is now conserved; $\rho_1 + \rho_2 = 1$. This immediately implies that; $\dot{\rho}_1 + \dot{\rho}_2 = 0$. Under these conditions the differential equations can be solved to obtain the excited state population. In particular, in the long time limit the population density of the excited state is found to be (Novotny and Hecht (2006))

$$\rho_2(\infty) = \frac{k_{12}}{k_{12} + k_{21}}. \quad (2.46)$$

As discussed previously, raising operator, $\hat{\sigma}_+$, generates a transition from the ground to the excited state while lowering operator, $\hat{\sigma}_+^\dagger$, generates a transition from the excited to the ground state. The excited state population corresponds to the expectation value of these operators. The definition of $g^{(2)}(\tau)$ in Eq.(2.46) can now be written in terms of these operators as we already showed before in Eq.(2.18),

$$g^{(2)}(\tau) = \frac{\langle \hat{\sigma}_+^\dagger(t) \hat{\sigma}_+^\dagger(t+\tau) \hat{\sigma}_+(t+\tau) \hat{\sigma}_+(t) \rangle}{\langle \hat{\sigma}_+^\dagger(t) \hat{\sigma}_+(t) \rangle^2}. \quad (2.47)$$

To obtain the $g^{(2)}(\tau)$, we can first calculate the operator products at $(t+\tau)$ by the quantum regression theorem. According to this theorem the expectation value of an operator \hat{O} at a time $(t+\tau)$ is related to the expectation value of a set of operators $\hat{O}_i(t)$ at time t (Loudon (2000)):

$$\langle \hat{O}(t+\tau) \rangle = \sum_i \alpha_i(\tau) \langle \hat{O}_i(t) \rangle. \quad (2.48)$$

Using these relation one can solve the rate equations to obtain $\rho_2(t+\tau)$ in terms of $\rho_2(t)$

$$\begin{aligned} \rho_2(t+\tau) &= \frac{k_{12}}{k_{12} + k_{21}} [1 - e^{-\tau/\tau_0}] + \rho_2(t) e^{-\tau/\tau_0} \\ &= \frac{1}{k_{12} + k_{21}}, \end{aligned} \quad (2.49)$$

combining these with regression theorem and using the relation of $\langle \hat{\sigma}_+^\dagger(t) \hat{\sigma}_+^\dagger(t) \hat{\sigma}_+(t) \hat{\sigma}_+(t) \rangle = 0$,

$$\begin{aligned} \langle \hat{\sigma}_+^\dagger(t) \hat{\sigma}_+^\dagger(t+\tau) \hat{\sigma}_+(t+\tau) \hat{\sigma}_+(t) \rangle &= \frac{k_{12}}{k_{12} + k_{21}} [1 - e^{-\tau/\tau_0}] \langle \hat{\sigma}_+^\dagger(t) \hat{\sigma}_+(t) \rangle \\ &\quad + e^{-\tau/\tau_0} \langle \hat{\sigma}_+^\dagger(t) \hat{\sigma}_+^\dagger(t) \hat{\sigma}_+(t) \hat{\sigma}_+(t) \rangle \\ &= \frac{k_{12}}{k_{12} + k_{21}} [1 - e^{-\tau/\tau_0}] \langle \hat{\sigma}_+^\dagger(t) \hat{\sigma}_+(t) \rangle \\ &\quad + e^{-\tau/\tau_0} \langle \hat{\sigma}_+^\dagger(t) \hat{\sigma}_+(t) \rangle. \end{aligned} \quad (2.50)$$

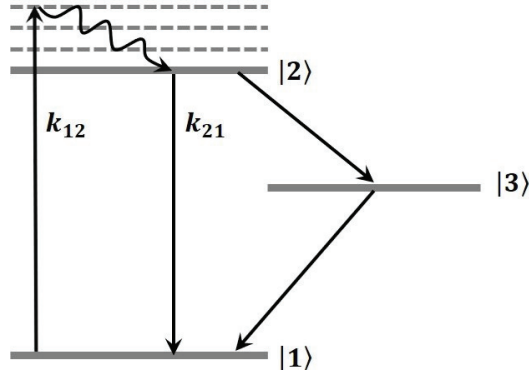


Figure 2.4. Schematic representation of a three-level system.

As clearly seen the average of the operator product is equal to excited state population in equilibrium. Finally we obtain that

$$\langle \hat{\sigma}_+^\dagger(t) \hat{\sigma}_+(t) \rangle = \frac{k_{12}}{k_{12} + k_{21}} = \rho_2(\infty). \quad (2.51)$$

Substituting the Eq.(2.50), (2.51) into (2.43) the second order correlation function, $g^{(2)}(\tau)$, of a defect center modeled by a two level system can be derived as

$$g^{(2)}(\tau) = 1 - e^{-\tau/\tau_0}, \quad (2.52)$$

where the emitted photons are separated by τ_0 constant of the system.

2.4. Three-Level Model

The real defects can often have additional levels called as shelving states and these states decreases the efficiency by introducing additional intensity fluctuations. A three-level system involves ground state $|1\rangle$, the excited state $|2\rangle$ and one intermediate state (shelving state) $|3\rangle$ with a longer lifetime. A schematic diagram of such a three-level system is given in Fig.2.4. For the same reason given in the discussion of two level states, the second order correlation function can be derived from the classical rate equations as we did before. The transition rates between the states are indicated by arrows. Here, k_{12}

and k_{21} denote the pump rate and the spontaneous decay rate from ground state to the excited state and vice versa. Photons emitted via the radiative transition k_{21} are detected in a usual experimental setup. The excited three level system first decays from the excited state to the shelving state with a decay rate constant k_{23} and relaxes back to the ground state at a rate k_{31} . These transitions including the shelving state are considered as non-radiative. Additionally, a transition from shelving state to excited state is also possible with a rate k_{32} . However, this transition may be observable or effective under strongly pumping of the system (strong field intensities). In general, the transitions from the shelving state to other states have ignorable effects. In some conditions, the shelving state can trap electrons and the populations and no photons are detected on the radiative transition k_{21} .

The rate equations for the three level model can be extended from Eq. (2.44) and (2.45), neglecting all coherence,

$$\frac{d\rho_1}{dt} = -k_{12}\rho_1 + k_{21}\rho_2 + k_{31}\rho_3, \quad (2.53)$$

$$\frac{d\rho_2}{dt} = k_{12}\rho_1 - k_{21}\rho_2 - k_{23}\rho_2, \quad (2.54)$$

$$\frac{d\rho_3}{dt} = k_{23}\rho_2 - k_{31}\rho_3, \quad (2.55)$$

where ρ_i , with $i = 1, 2, 3$, are the populations of the three energy levels. Assuming the system to be in the ground state at $t = 0$ ($\rho_1(0) = 1, \rho_2(0) = \rho_3(0) = 0$) and that the sum over all populations $\rho_1 + \rho_2 + \rho_3 = 1$, the analytical solution of these differential equations yields the population of the excited state $\rho_2(t)$,

$$\rho_2(\infty) = \frac{k_{12}}{(1 + \frac{k_{23}}{k_{31}})k_{12} + k_{21} + k_{23}}. \quad (2.56)$$

According to Eq.(2.43) the second order correlation function for a three level model can be calculated with τ_1 and τ_2 which are the excited and metastable state lifetimes, respectively as following:

$$g^{(2)}(\tau) = 1 - (1 + a)e^{-|\tau|/\tau_1} + ae^{-|\tau|/\tau_2}, \quad (2.57)$$

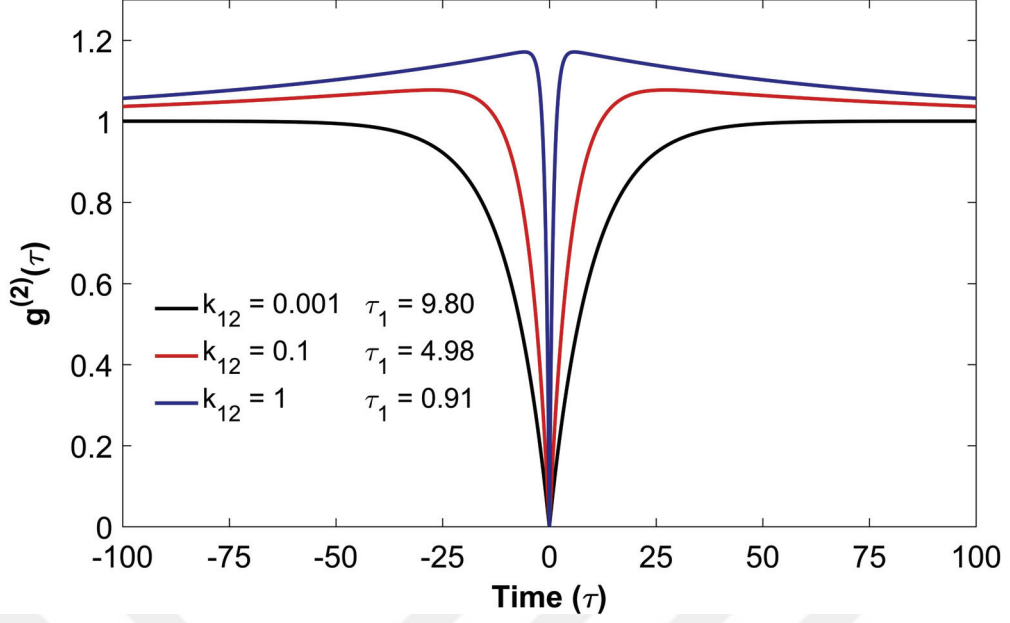


Figure 2.5. Second order correlation function, $g^{(2)}(\tau)$, calculated for $k_{12} = 0.001$ is the black line, $k_{12} = 0.1$ is the red line and $k_{12} = 1$ is the blue line.

The parameters of the Eq.(2.57) are given by

$$\tau_{1,2} = 2/(A \pm \sqrt{A^2 - 4B}), \quad (2.58)$$

$$A = k_{12} + k_{21} + k_{23} + k_{31}, \quad (2.59)$$

$$B = k_{12}k_{23} + k_{12}k_{31} + k_{21}k_{31} + k_{23}k_{31}, \quad (2.60)$$

$$a = \frac{1 - \tau_2 k_{31}}{k_{31}(\tau_2 - \tau_1)}. \quad (2.61)$$

The main contribution to antibunching is the second term in the right hand side of Eq.(2.57) when the delay times close to zero. The bunching due to the third term in Eq.(2.57) takes effect at longer delay time values. The parameter a represents the effect of the shelving state. If $a = 0$, the $g^{(2)}(\tau)$ function for three level model reduces to the $g^{(2)}(\tau)$ function of the two level system. $g^{(2)}(\tau)$ is plotted as a function of delay time τ_2 for several excitation pump rates and excited state life times in Fig.2.5. Fig.2.5 shows that the second order correlation function strongly depends on the pump rate k_{12} . The function is calculated

for $k_{12} = 0.001$ (black line), $k_{12} = 0.1$ (red line) and $k_{12} = 1$ (blue line). The other rate parameters used in the calculation are: $k_{21} = 0.1$, $k_{23} = 0.001$ and $k_{31} = 0.01$. As seen from the figure, the increased pump rate shrinks the width of the dip at zero delay time. According to Eq.(2.57) the width of this dip corresponds to τ_1 . The calculated τ_1 values for the given rate constants are 9.80 (black curve), 4.98 (red curve), and 0.91 (blue curve). The increased pump rate also causes bunching and this corresponds to τ_2 . The τ_2 values for each black, red, and blue lines are 99.89, 90.52 and 84.50, respectively.

2.5. Electronic Absorption and Emission in Defect Centers

A single photon emitting defect which consists of discrete energy levels is also called as a color center due to the observed wavelength of the non-absorbed or reflected light. A photon of the incoming light can be absorbed by the system (defect center) if its energy is equal to or greater than the energy difference between two electronic levels of the system, that are E_0 and E_1 for the lower (ground) and the upper (excited) states, respectively. In the case of the absorption of a photon by a defect bound electron, the electron absorbs the momentum and energy of the photon (hence photon is annihilated) and jumps to a higher energy level with a different momentum. Strictly speaking, during the interaction the defect center is disturbed by the photon, hence, the new quantum states are slightly different from those of the non-interacting case which can be accounted for the time depended perturbation theory. For small enough excited fields the defect preserves its undisturbed quantum states, hence, the electron jumps into one of these states when the defect is excited. Since the defect center is located in the much larger ensemble of the atoms of the host, when possible, it loses some of the extra energy it gained to mostly vibrations of the surrounding atoms (thermal relaxation) which is a nonradiative process. Thus, if the electron is in a vibrational level of the defect in an excited state it goes down to the lowest vibronic energy level of the excited state from where it decays back to the ground state by emitting a photon with an energy equals to the energy difference between the excited and ground states. The average time electron remains in the excited state is called the life time of that state. These processes are shown in Fig.2.6. A two level electronic system with a ground state of energy E_0 and an excited state of energy E_1 along with their sub vibronic energy levels of $\nu = 0, 1, 2, 3$ are given in the figure. According to the figure, an incident photon of energy $\hbar\omega_i$ is absorbed by an electron in the ground state from where it jumps to one of the vibronic energy levels of the excited state. After thermal relaxation to the lowest possible vibronic level of the excited state it will make a

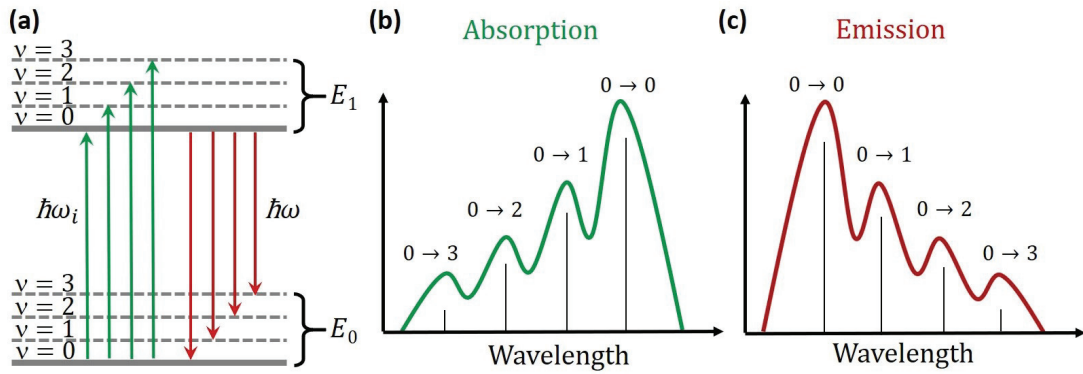


Figure 2.6. (a) Excitation of a basic two level system and transition from ground state E_0 to higher excited energy level E_1 and its different vibrational levels $\nu = 0, 1, 2, 3$. (b) Schematic absorption spectrum of different transitions which have different energies and intensities. (c) Schematic emission spectrum of different transitions which have different energies and intensities.

radiative transition to one of the vibronic levels of the ground state emitting a photon with energy $\hbar\omega$. A set of four possible absorption and emission process are indicated by green and red arrows Fig.2.6, respectively.

The probability of these transitions define the intensity of observed absorption spectra and are defined by Franck-Condon principle which states that the transitions will occur without changing nuclear positions or the surrounding environment. This is justified for low intensity light as mentioned earlier. The similar discussions are valid for the emission spectrum of transitions from zero vibrational level $\nu = 0$ of the excited state E_1 to any vibrational levels $\nu = 0, 1, 2, 3$ of ground state E_0 . To figure out the probability of the transitions for a single photon emitting defect, Franck-Condon principle need to be explained.

2.5.1. Zero-Phonon Line and Phonon Side Band

An electron in the ground state makes a transition to an excited state when a defect center is excited. In this process, not only spatial wave function but also the charge distribution around the defect center is changed. This changes the equilibrium coordinates of the adjacent nucleus. The electron-phonon coupling, hence, combines the movement of the lattice and electronic transitions of the defect (Davies (1981)). In this coupling

scheme, in general, for several vibrational modes the excited state energy V_e is given by

$$V_e = E_e + \frac{1}{2} \sum_i m_i \omega_i^2 Q_i^2 + \sum_i a_i Q_i + \sum_{i,j} b_{ij} Q_i Q_j, \quad (2.62)$$

where E_e is the excited state's electronic energy and ω is the vibrational mode frequency. The effective mass corresponding to the mode is m . Q is the displacement of the nuclei from their equilibrium coordinates. The term of aQ denotes linear electron-phonon coupling, while the last term bQ^2 describes quadratic electron-phonon coupling. The vibration in the ground and excited state does not have to be around an exact equilibrium point, which corresponds to the linear term. The quadratic term reveals the changes in the bond strengths and the vibrational frequencies in the excited state.

A schematic representation of the energy diagram of an electronic transition for a lattice coupled defect center is shown in Fig.2.7 (a). The upward transitions (green arrows) represent an absorption of a photon by a defect electron in the ground state (with energy E_0) with the lowest vibronic state ($\nu = 0$) to the first excited electronic state (with energy E_1) with a vibronic (phonon) level indicated with the phonon quantum number $\nu = 2$. Then, the electron in the excited state minimizes its energy (relaxes) to the lowest vibronic state by emitting phonons whose total energy will be equal to $2\hbar\omega$ (that is, creating two phonons each with energy $\hbar\omega$). This relaxation occurs in a very short time period of a few ps. Finally, it decays back to a vibronic level in the electronic ground state (red arrow in Fig.2.7 (a)) by emitting a photon whose energy equals the energy difference between initial and final energies of the electron. According to the Frank-Condon principle the probability (hence intensity) of a transition increases with increasing overlap between the vibronic wave functions in the ground and excited states of the defect center. Note that according to the argument given above, due to slight changes in the nuclei positions of the host atoms, their phonon (vibronic) wave functions are also shifted accordingly in the configurational (positional) space. Hence, the intensity distribution of transitions between the ground and excited states will depend strongly on the degree of overlaps between the vibronic wave functions of the excited and ground states as indicated in Fig.2.7.

For the shown case, the largest wave function overlap (and the largest transition probability) takes place when the excitation photon energy is equal to the energy difference between the two electronic states and two quanta of lattice vibrational mode energies ($E_{0,\nu=0} \rightarrow E_{1,\nu=2}$). For this reason the maximum absorption probability and corresponding maximum intensity in the absorption spectrum is obtained between these states. The

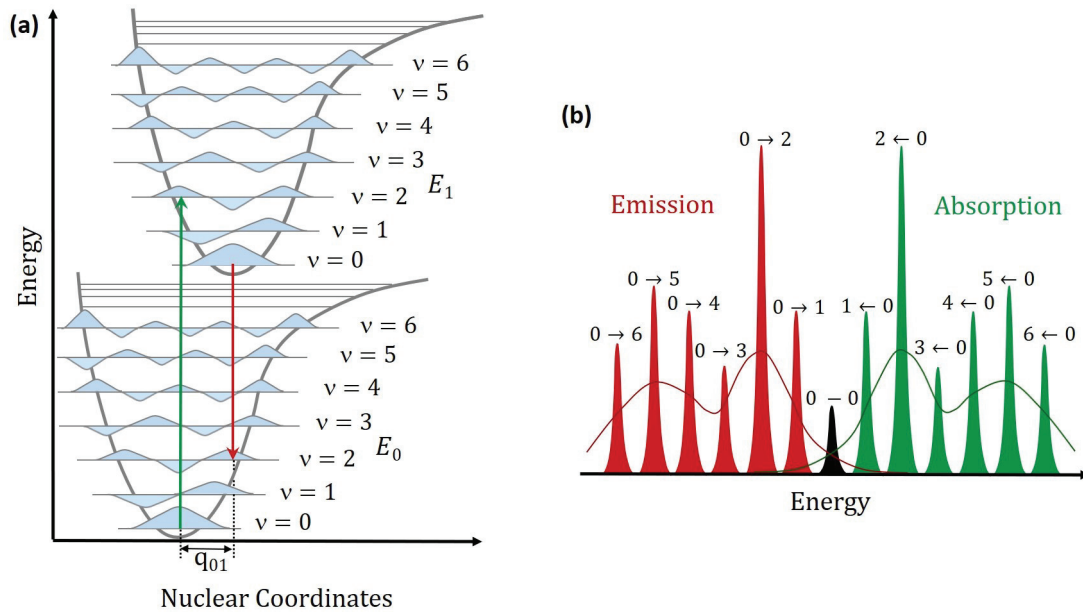


Figure 2.7. (a) Schematic representation of the energy diagram of an electronic transition with phonon coupling and, (b) Schematic representation of the absorption and fluorescence spectra.

other transitions from zero vibrational level $\nu = 0$ of the ground state to $\nu = 0 \rightarrow 0$ and $\nu = 0 \rightarrow 1$ have their own intensities in the absorption spectra which is defined by the degree of the overlap of corresponding vibronic wave functions in both electronic states (see Fig.2.7 (b)). In Fig.2.7 the most probable and most intense transition is the $0 \rightarrow 2$ transition both in absorption and in emission which means the overlap of vibrational wave functions in these two electronic states are maximum (see Fig.2.7 (a)), whereas in Fig.2.6 (b) the most probable and most intense transition is $0 \rightarrow 0$. This study focuses on the transitions between discrete level systems, defects in host materials. The $0 \rightarrow 0$ transition is called the zero phonon line (ZPL) which defines a single photon emission or absorption. We will focus on the emission processes since the aim of this thesis is to identify and characterize single photon emitters. Other possible transitions also participate the emission with the energy difference equal to the energy difference between two closest vibrational levels of the system. These transitions are called as phonon side band (PSB). An observed ZPL and accompanying PSB of a defect center in hBN (hexagonal boron nitride) is given in Fig.2.8 as an example. The PSB is displaced from ZPL to higher frequencies in absorption and to lower frequency in emission, where the frequency difference indicates various phonon energies. The frequency shift of phonon side bands from the ZPL in hBN is about 1369 cm^{-1} ($\sim 170 \text{ meV}$) which incidentally corresponds to the

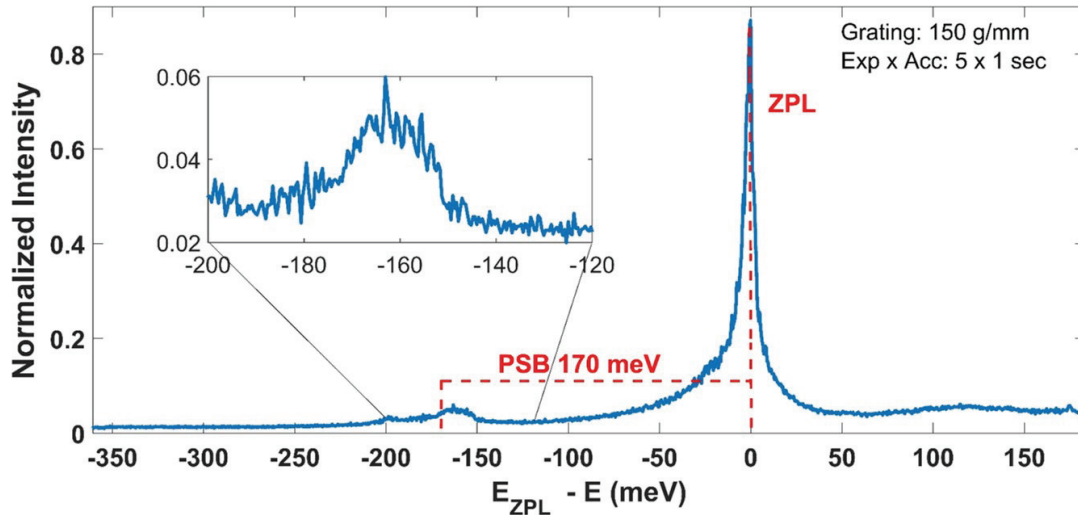


Figure 2.8. A representative room temperature photoluminescence spectrum that shows a ZPL at 623.9 nm and a PSB. To see the ZPL-PSB energy difference the ZPL is plotted to zero energy.

main phonon mode of the hBN lattice as observed in the IR absorption and Raman spectroscopies. A typical room temperature SP emission spectrum from a defect center in hBN is shown in Fig.2.8. The ZPL is observed at 623.9 nm. Note that the energy scale is given relative to the ZPL energy. Furthermore, a phonon side band (PSB) doublet is also seen in the inset. The energy difference between the ZPL and its PSB is around 170 meV which is equal to the energy of main phonon mode of the hBN as confirmed by its Raman spectrum.

A strong ZPL than phonon side bands means that $0 \rightarrow 0$ transition is dominant. In addition all phonon side bands are almost equally displaced from the ZPL. This confirms that vibrational potential energy is parabolic in the configuration space. Thus it is safe to say that mode is well described by a quantum harmonic oscillator for the phonon states is applicable. Second approximation is that the harmonic oscillator potential is equal in both ground and the excited states. This approximation, called linear coupling (two equally shaped parabolic potentials and by equally spaced phonon energy levels in both states). The third approximation is that only the zero level ($\nu = 0$) lattice vibration is excited from ground state. This is known as the low temperature approximation. In that way, the electronic transitions do not result from any of the higher vibrational levels. Incidentally, the room temperature energy for $T = 300$ K corresponds to an energy of 26 meV. For any phonon energies much larger than this low temperature approximation holds.

Experimentally, the linear electron-phonon coupling can be expressed by the Debye-Waller factor (DW) or the Huang-Rhys factor factor (S). The definition of the Huang-Rhys factor is division of the integrated luminescence intensity of the ZPL (I_{ZPL}) to the total integrated luminescence intensity of the defect center (I_{Tot}) (Gaebel et al. (2004)) as following (Walker (1979)):

$$\frac{I_{ZPL}}{I_{Tot}} = \exp(-S). \quad (2.63)$$

The Huang-Rhys factor also can be understand as an indicator of the most probable vibration assisted transition. The most probable luminescence transition then makes the optically active defect center to the vibrational energy level with $n = S$ phonon in the ground state. This transition shows the maximum of the emission band (discussion following Ref. Walker (1979)).

2.5.2. Line Shape of ZPL and PSB

The ZPL line shape is Lorentzian (Loudon (2000)) and according to the Heisenberg uncertainty principle its width is determined by the excited state lifetime τ . The natural line width (full width at half maximum, FWHM), without the influence of the lattice, is $FWHM = 1/\tau$. The non-radiative decays due to lattice phonons decreases the excited state lifetime. Thus, one can accept the excited state lifetime is equal to τ at absolute zero. Above the absolute zero, thermal motions affect the local environment and shift the energy of the electronic transition. This increases the FWHM. Thus, the relation of ZPL width is expressed as $FWHM \geq 1/\tau$. The spectral line width of the transitions including vibrational transitions is wider because of the fast (\sim ps) relaxation rates. A narrow line width of a ZPL and its broad PSB are shown in Fig. 2.8. The PSB line shape conforms to Poisson distribution because of it consists of a discrete number of events, electronic transitions with phonons, during a certain time interval. However, above the absolute zero, the probability of exciting more than one photon is higher and the PSB line shape approximates to a Gaussian distribution.

Additionally, the environmental fluctuations cause dephasing and spectral diffusion with additional time described by T . In this case, the spectral line width broadens by $FWHM = 1/\tau + 2/T$. In order to reduce these additional fluctuations and reach the FWHM at absolute zero, the samples must be cooled down to cryogenic temperatures. In

this way, phonon scattering events are reduced and line broadening is prevented.

2.6. Photoluminescence Properties of Single Photon Emission

The emission rate of the single photon source depends on the excitation pump rate (excitation laser power) and the excitation polarization angle. In this section these dependencies will be explained.

2.6.1. Single Photon Emission Efficiency

Assuming that the transition rates are constant due to the fast vibrational relaxations ($\sim ps$), the pump rate of the emitting system affects the emission efficiency linearly, that is

$$k_{12} = \alpha P, \quad (2.64)$$

where k_{12} is the pump rate, P ; the excitation power of the field, and α ; a constant. The effect of the pump rate on $g^{(2)}(\tau)$ was discussed in the preceding section and this effect was demonstrated for several values of the pump rate in Fig.2.5. In addition, all quantities involving the pump rate, k_{12} , are also affected by the excitation power such as excited state population, ρ_2 . The photon emission rate measured for a power value P is related to the excited state population at steady state, $\rho_2(\infty)$, as given in Eq. (2.46). This emission rate is proportional to the measured intensity, $I(P)$, for that excitation power. The steady state population of the excited state for a two level model is calculated from Eq.(2.46). Rewriting the equation by combining Eq.(2.64) gives the following:

$$\rho_2(\infty)k_{21} = \frac{k_{21}\alpha P}{\alpha P + k_{21}} = \frac{k_{21}P}{P + \frac{k_{21}}{\alpha}} = \frac{k_{21}P}{P + P_{sat}} = I_{\infty} \frac{P}{P + P_{sat}}, \quad (2.65)$$

where P_{sat} is the constant saturation power of the emitting two level system. The emission rate (measured intensity) reaches to a constant k_{21} value when the excitation power P is much larger than the saturation power P_{sat} . Thus at this limit the emission rate becomes

equal to the steady state intensity, I_∞ .

The two level model is the most simplified model. In most cases the defect center has additional states, which are called "shelving states" which causes a reduction in the emission efficiency. For a three level model, such as the one discussed in the preceding section, the rate equations are already given by equations Eq.(2.53-55) with their solution for the excited state population given by Eq.(2.56). This the emission rate conditions for the there level model using steady state population of the excited state Eq.(2.56) as following:

$$\begin{aligned}
 \rho_2(\infty)k_{21} &= \frac{k_{21}\alpha P}{\left(1 + \frac{k_{23}}{k_{31}}\right)\alpha P + k_{21} + k_{23}} \\
 &= \frac{k_{21}k_{31}}{k_{23} + k_{31}} \frac{P}{P + \frac{k_{21}k_{31} + k_{23}k_{31}}{(k_{23} + k_{31})\alpha}} \\
 &= I_\infty \frac{P}{P + P_{sat}}, \tag{2.66}
 \end{aligned}$$

where

$$I_\infty = k_{21} \frac{k_{31}}{k_{23} + k_{31}} \tag{2.67}$$

is related to k_{21} similar to two level model.

The detected photons from the emitting system are related to the radiative transition rate k_{21} . Thus, the value of k_{21} directly affects the emission efficiency. This can be deduced from the description of I_P and I_∞ . It is clearly seen from Eq.(2.65) and (2.66) that I_∞ depends linearly on k_{21} . The rates k_{23} and k_{31} , which include the shelving state transitions are non-radiative, and affect the saturation emission rate, I_∞ . However, their influence on the efficiency is much smaller than that of k_{12} and k_{21} . In fact k_{31} has the smallest affect on the efficiency which can usually be ignored in the denominator of Eq.(2.67). Then it is more important to see the effect of the ratio k_{23}/k_{31} on the emission efficiency and $g^{(2)}(\tau)$. Fig.2.9 gives the emission rate as a function of power for various ratios of k_{23}/k_{31} . In the calculation all other rates were kept constant as $k_{12} = 0.001$, $k_{21} = 0.1$ and $k_{31} = 0.01$. The increased k_{23} causes to observe decreased saturation emission intensity. In Fig.2.9 (b), $g^{(2)}(\tau)$ for the same rates were also plotted. In the figure increasing k_{23} causes to observe bunching and decreased τ_1 and antibunching width.

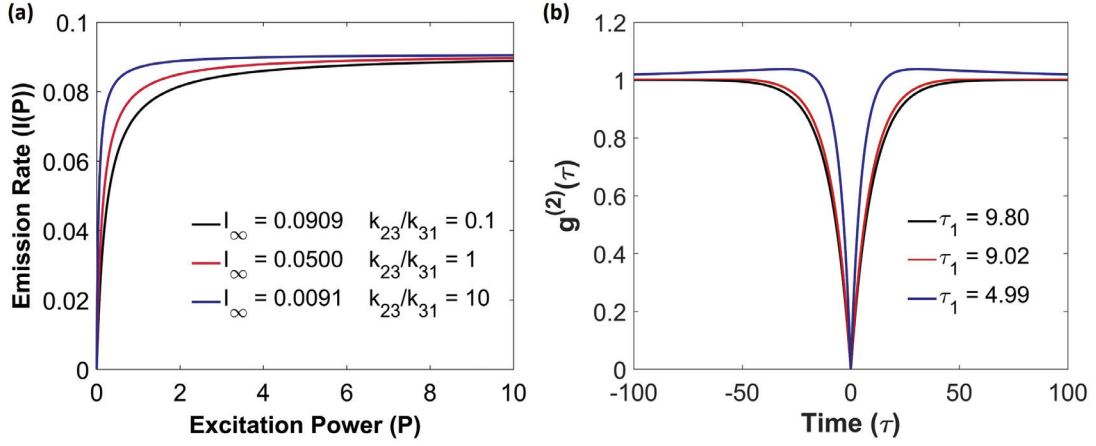


Figure 2.9. (a) The effect of k_{23} on emission efficiency. (b) the effect of k_{23} on second order correlation function.

2.6.2. Polarized Fluorescence of Single Photon

It is well known that according to the uncertainty principle, two canonical conjugate observables can not be measured at the same time. Polarization of a photon and the diagonal basis are the important examples to such observables and they play an important role in quantum information technologies. Furthermore, polarization properties of photons are directly related to the emitting sources. Excitation polarization of a dipole (as a discrete-level system) defines its emission intensity behavior. In this study, the polarization characteristics of observed single photon emission will be studied. The polarization is described as the direction of the electric field component of light propagating in \mathbf{k} direction. The polarization of the field can be described in the most general form as the following:

$$\mathbf{E}_{\mathbf{x},t} = (E_1 \mathbf{e}_1 + E_2 \mathbf{e}_2) e^{i\mathbf{k}\cdot\mathbf{x} - i\omega t}, \quad (2.68)$$

where the \mathbf{e}_1 and \mathbf{e}_2 are the directions of polarization vectors to the \mathbf{k} vector. The electric field vector E_0 can be resolved into two rectangular components i.e $E_0 \cos(\theta)$ and $E_0 \sin(\theta)$. The analyzer of the system transmits only one component which is parallel to its transmission axis while the other component being absorbed. Therefore, the intensity

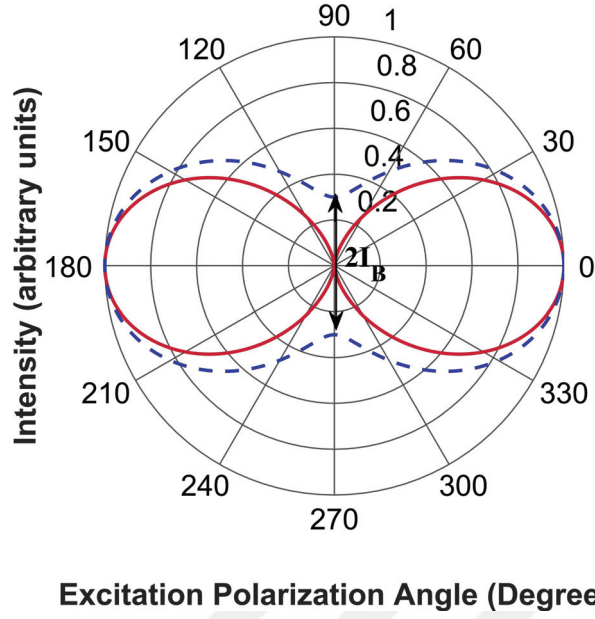


Figure 2.10. The relation of excitation laser polarization and single photon emission intensity. The red line corresponds to zero minimum intensity, $I_B = 0$, condition without background effects. The dashed blue line represents the effect of non zero $I_B \neq 0$.

of the emission transmitted by the analyzer will be

$$I = I_B + I_0 \cos^2(\theta + \theta_{offset}), \quad (2.69)$$

where I_B and $I_B + I_0$ are the minimum and maximum values of the emission intensity. θ corresponds to excitation polarization angle and θ_{offset} is the angle corresponds to the maximum emission intensity. In this study, this equation is used to fit the calculated polarization dependency to the experimental data. Fig.2.10 gives two different intensity distributions for all possible polarization angles with two different background intensities. In a polarization measurement set up, the background intensity which is defined as a minimum intensity of the emission, I_B is observed in the figure as a gap in the middle with blue dashed line. Additionally, the polarization degree of the emitter is defined by its visibility which is defined as the following:

$$V = \frac{I_{max} - I_{min}}{I_{max} + I_{min}} = \frac{I_0}{I_0 + 2I_B}, \quad (2.70)$$

where I_{max} and I_{min} are the maximum and minimum intensities, respectively.

In this study, polarization measurements of emitted single photons was performed by a half-wave plate which changes the excitation field polarization and the angle between the field and emitter dipoles. The observed intensity of the emission is maximum when the angle between the two dipoles is equal to 90° . The minimum is observed at 0 degree. In that way, the polarization property of the emitter was characterized.

2.6.3. Time-Correlated Single Photon Counting

Single photon emission can be obtained from single atom defects such as a host atom vacancy, interstitial, or anti-site defects. When such a defect is excited, for example by some incident radiation, it will loose the extra energy by emitting a photon as it goes back down to its excited state. The emitted photon energy will be equal to the energy difference between the excited and ground state energies. The electron then absorbs another photon, upon a continuous incident excitation radiation, then the whole process repeats. At each excitation-emission cycle a single photon will be emitted. Usually the excited electron spends a time in the excited state which is equal to the life time of that state which is called fluorescence lifetime as well. For most photoluminescence (or fluorescence) events this life time is in nanoseconds, albeit it can be as long as milliseconds or even seconds (in that case it is called phosphorescence). For the usual nanosecond life time excitations we can carry out time-correlated single photon counting.

Fig.2.3 and Fig.2.6 (a) give schematic representation of absorption and emission processes. These can be described by the following energy processes in that order (Akhtar (2010)):

$$E_0 + \hbar\omega_i \rightarrow E_1, \quad (2.71)$$

$$E_1 \rightarrow E_0 + \hbar\omega. \quad (2.72)$$

In a single photon emission experiment one can excite a defect either with continuous wave laser or a pulse laser. The time span of the pulse at its full width at half maximum (FWHM) must be much shorter than the excited state life time in order to account for the excited life time as the difference between the excitation time and the emission time of the defect. On the other hand, the time difference between two pulses should be at least

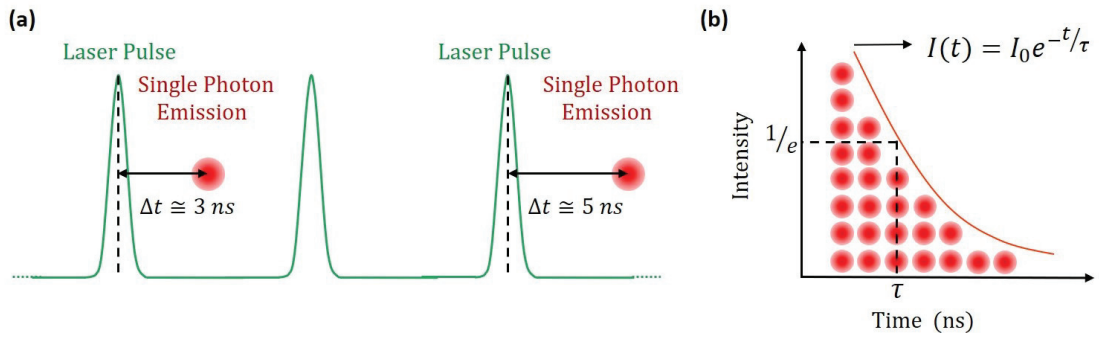


Figure 2.11. Time-Correlated Single Photon Counting. (a) Measurement of the time difference between excitation laser pulse and emitted single photon, $\Delta t = t_{pulse} - t_{sp}$. (b) The accumulated single photons with respect to detection time differences creates a histogram and a decay curve.

several times longer than the excited state life time so that all the de-excitation process will be completed. Statistically, we can define the lifetime of an excited system when the population of the excited state electrons decay to $1/e$ of the initial (right after the excitation time of the pulse) excited state population of the system. This lifetime refers to the average time of a defect (discrete level system) stays in its excited state before emitting a single photon. This relaxation is described by

$$I(t) = I_0 e^{-t/\tau}, \quad (2.73)$$

where I_0 is the initial intensity (or maximum count value) of emission which relaxes with time t . At the same time more than one single photon source can be excited. In this case, another exponential term is added to Eq.2.73. Instead of intensities, the relaxation can be described by populations and the decay rate k as the following (Novotny and Hecht (2006)):

$$k = \frac{1}{\tau}. \quad (2.74)$$

The time difference between two consecutive laser pulses are equal and each pulse recorded as t_{pulse} . As shown in Fig.2.11 (a), also emitted single photons are recorded as t_{sp} . The time difference between consecutive laser pulse and single photon emission

$\Delta t = t_{pulse} - t_{sp}$ is recorded. Such a single photon time-count (that is a Δt value for each count of a single photon) measurements are repeated many times consecutively for a duration much larger than the expected life time of the excited state, until a statistical histogram of accumulated counts for each observed Δt value, that is histogram of counts, are obtained. A schematic representation of such a histogram is given in Fig.2.11 (b) where, for example the total count for time τ is about four in that particular example, this number is $1/e$ of the initial count I_0 which can be found by extrapolating the curve given by Eq.(2.73) to $t = 0$. Note that equation Eq.(2.73) is fitted to the experimental counts by adjusting I_0 and τ . Hence these are treated as fitting parameters.

The most important constrain of the measurement is that the probability of detecting a single photon per laser pulse should be less than 1. In other words, after excitation by a single pulse there should be either one or zero photon count until the next pulse hits.

2.7. Interaction Between the Emitter and Different Materials

Single photons sources are used in many applications such as quantum computing and quantum communication. To advance such technologies, not only bright, stable, and controllable single photon sources are needed but also they must be well integrated with their environments in a designed system so that their properties, such as brightness, lifetime, and detectibility, will have a good mach with the system requirements. The most known methods involve integration of SP sources with cavities of different shape and sizes, coupling with plasmonic nanoparticles, and designing hybrid structures. In this study, the emission from defects in WO_3 is coupled with Au nanoparticles to enhance the emission (which is called the "plasmonic nanoantenna effect"). Furthermore, the single photon emission from defects in hBN is coupled with graphene to observe emission quenching by a mechanism called "Förster-like resonance energy transfer".

2.7.1. Fluorescence Brightening: Plasmon Effect

Metallic nanoparticles can be used to enhance the emission from a material in close proximity due to the enhanced resonance effect of the plasmon oscillations with incident electromagnetic field. The free electrons in metallic material under an external electromagnetic field, collectively oscillate at the same frequency of the external field which is called "plasma oscillation". This oscillation is in resonance when frequencies

of restoring forces and the exciting external field are nearly the same. The oscillating electrons are described as quasi-particles in plasma (free electron gas). These quantized quasi-particles are called plasmons. The simplest explanation of forced plasma oscillations are due to Drude model. In the Drude model, electrons are independent from each other (that is, they do not interact) oscillating with the same frequency, and they feel the same restoring forces. In that case, the equation of motion of an electron under the effect of a driving force due to an external harmonic electromagnetic field $E = E_0 e^{-i\omega t}$ is given by the following equation:

$$m\ddot{\mathbf{x}} + m\gamma\dot{\mathbf{x}} = -e\mathbf{E}_0 e^{-i\omega t}, \quad (2.75)$$

where m and e are the effective mass and charge of the electron. The damping term γ arises from the collisions of electrons mainly with the lattice phonons. The solution $x(t)$ of Eq.2.75 gives the position of the electrons as a function of time. Then one can write down the electric dipole moment associated with such an electron as $\mathbf{d} = e\mathbf{x}$. For n such electrons per unit volume the electric polarization vector is defined as $\mathbf{P} = n\mathbf{d}$. In the weak field approximation polarization is linearly proportional to \mathbf{E} ; that is $\mathbf{P} = \epsilon_0\chi\mathbf{E}$ where χ is electric susceptibility while ϵ_0 being electric permittivity of the empty space. The electric displacement vector is given as $\mathbf{D} = \epsilon\mathbf{E} = \epsilon_0\mathbf{E} + \mathbf{P}$, from which dielectric constant is obtained as

$$\epsilon(\omega) = 1 - \frac{\omega_p^2}{\omega^2 + i\gamma\omega}, \quad (2.76)$$

where $\omega_p = \sqrt{\frac{ne^2}{\epsilon_0 m}}$ is the plasma frequency (natural oscillation frequency) of the free electron gas. For high field frequencies the damping term can be ignored in the dielectric function. However, in this case photons will have large enough energy to create substantial inter-band transitions which should be taken into account by adding a resonance term in Eq.2.75 which is known as the Drude-Lorentz model.

Plasmon (also called a plasmon polaritons) in a bulk material are called "volume plasmons" while those at the surface are named as "surface plasmons". Conductors involving large concentration (n) of free electrons (such as metals) limit the penetration depth of the external electromagnetic field. For an absorptive medium incident light intensity falls of exponentially with the length of the light path x in the material as $I = I_0 e^{-\alpha x}$

where α is called the "absorption coefficient" and depends on the free charge density n . For a metallic conductor $n \approx 10^{22} \text{cm}^{-3}$ which sets the plasma frequency in the ultraviolet region of the electromagnetic spectrum while a typical penetration depth (for which $I = I_0 e^{-1}$) will be a few nanometers for a visible light.

At a metal-insulator junction boundary such as that of a thin metallic film on a dielectric substrate, the collective oscillations of the electrons on the surface (that are surface plasmons or surface plasmon polaritons) propagate along the interface between the metal and its dielectric surrounding. Solving the boundary conditions at the interface the wavevectors in the z-direction (perpendicular to the surface) can be obtained. Combining the dielectric function relation for the high frequencies, the surface plasmon frequency can be found as $\omega_{SP} = \omega_P / \sqrt{2}$. Then, the dispersion relation of this surface plasmon can be found as

$$k_{SP} = \frac{\omega}{c} \sqrt{\frac{\varepsilon_d \varepsilon_m}{\varepsilon_d + \varepsilon_m}}, \quad (2.77)$$

where ε_d and ε_m are the dielectric functions of the insulator and the metal, respectively. Both energy (frequency) and wavevector (momentum) need to be conserved at the same time for surface plasmons, but this cannot be achieved by directly illuminating the metal surface with light. Additionally, the model does not satisfy at high frequencies. However, there are studies to excite surface plasmons using specifically designed prisms or gratings (Novotny and Hecht (2006)).

The geometry (size and dimensions) of a metal affects the motion of surface plasmons. The oscillations in metal nanostructures are limited within the boundaries and are called localized surface plasmons. In contrast to surface plasmons, localized surface plasmons do not have momentum and by an appropriate excitation energy the electrons can be excited (Mie (1908)). In the quasi-static limit spherical nanoparticles with diameters $d \ll \lambda$, external electric field as well as the induced dipoles are considered to be static. Solving Maxwell's equations for such a dipole the polarizability $\alpha = \varepsilon_0 \chi$ can be found as

$$\alpha(\lambda) = 4\pi r^3 \frac{\varepsilon(\lambda) - \varepsilon_d(\lambda)}{\varepsilon(\lambda) + 2\varepsilon_d(\lambda)}, \quad (2.78)$$

where a being the radius of the nanoparticle. Accordingly, the maximum polarizability is observed when $\varepsilon(\lambda) \approx -2\varepsilon_d(\lambda)$, which is called the "Fröhlich condition". The induced dipole moment in the spherical particle is

$$\mathbf{p} = 4\pi\epsilon_0\epsilon_m a^3 \frac{\epsilon_d - \epsilon_m}{\epsilon_d + 2\epsilon_m} \mathbf{E}_0. \quad (2.79)$$

The superposition of the external field and the induced dipole field is

$$\mathbf{E}_{out}(\mathbf{r}) = \mathbf{E}_0 + \frac{3\mathbf{n} \cdot \mathbf{p} - \mathbf{p}}{4\pi\epsilon_0\epsilon_m} \frac{1}{r^3}, \quad (2.80)$$

where \mathbf{n} is the unit vector \mathbf{r}/r . However, the particles that have diameters >20 nm obey these considerations without any quantization and surface effects (Link and El-Sayed (2003)). In this study, to enhance the luminescence signal we used Au nanoparticles whose diameters are larger than 20 nm.

In crystalline solids, size, shape, structure, and orientation affect the emission by enhancement or quenching. Fluorescence properties of an excited material nearby a metallic nanoparticle are affected from the changes in the excitation field, transition rates and angular distribution of the emission with additional nonradiative channels. The radiative decay rate (γ_r) is modulated by the scattered field E_s from the nanoparticle dipoles. Some of the excitation energy of a photon source is transferred to a nanoparticle in close proximity, creating a nonradiative decay channel. In classical approach, the transferred energy induced currents dissipates into heat by resistivity of the metal nanoparticle. This nonradiative decay rate is given as (Schietinger (2012))

$$\gamma_{nr} = \frac{1}{2} \int_V \sigma(\omega) |\mathbf{E}|^2 d\mathbf{r}, \quad (2.81)$$

where $\sigma(\omega)$ is the conductivity of metal nanoparticle. As seen the decay rates depend on the distance between the emitter and nanoparticle. The nonradiative decay rates with respect to the distance between the emitter and the surface of gold nanoparticle can be calculated by Lumerical simulations with the finite-difference time-domain (FDTD) method package and are shown in Fig.2.12 (Lumerical Solutions, Inc. (2019)). The calculated decay rate dependency is for the emission wavelength of 610 nm which is the most common in our experiments of this thesis study. The gold nanosphere diameter was fixed as 30 nm to be the same for our experiments in this thesis study. The dipole polarization is parallel to the vertical axis as shown in the inset.

At this point, it is necessary to express that the enhancement of the nonradiative and radiative decay rates are much higher when the coupling with the sphere is much

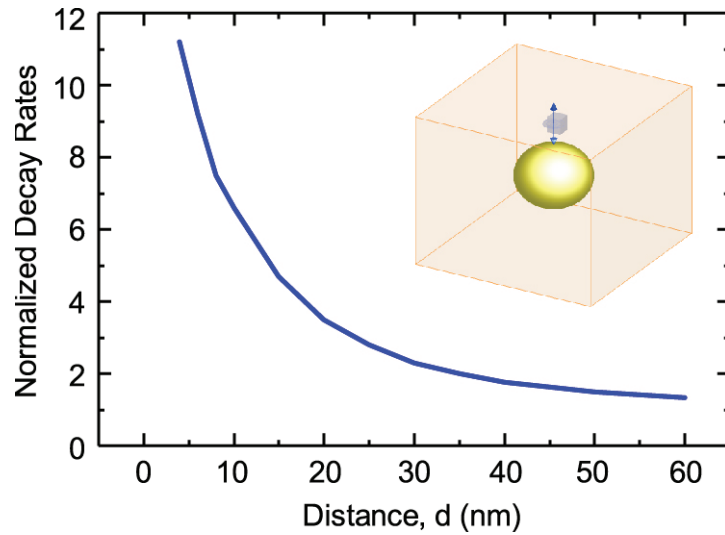


Figure 2.12. Calculated nonradiative decay rates for an emitter with emission wavelengths 610 nm by FDTD method. The diameter of gold particle is fixed as 30 nm. The orientation of the emitter which behaves like a dipole is represented in the inset.

larger. This occurs closer to the plasmon resonance wavelength which is defined by the size of the nanoparticle. However, this is opposite when the dipole orientation is horizontal (Schietinger (2012)). In summary, the observation of the emission enhancement in close proximity to the metal nanoparticle surface depends on the distance to the surface of the particle, size of the particle and the relative orientation of the dipole.

2.7.2. Fluorescence Quenching: Förster Resonance Energy Transfer

Single photon emission can be quenched via transfer of energy to a nearby material by a non-radiative process. This kind of energy transfer is called non-radiative Förster-like resonance energy transfer (FRET). Energy is transferred from what is called a donor (D) to an acceptor (A). In principle, D and A can be two atoms, molecule, or dipoles. Non-radiative energy transfer occurs without photon emission by interaction between D and A at distances smaller than the wavelength λ of the exciting light. Fig.2.13, gives a schematic representation of radiative and non radiative process where k_{21} is the radiative, k_{FRET} is non-radiative decay rate. The distance between D and A is the most important parameter defining the strength of the nanradiative decay. The energy transfer can also occur by electron exchange if D-A separation is less than 1 nm which is called

"Dexter transfer" and it is due to overlap of the electron wave functions of D and A. Usually FRET occurs when in near field zone when the distance between D and A is in the range; $1 < d < 10nm$, which is called the "near field zone". The distance dependency of FRET provides a useful tool which can be exploited in a wide variety of applications such as sensing, etc.. There are reported studies in literature, on the distance dependency of FRET rate for a graphene and fluorescent emitter such as molecules (Gaudreau et al. (2013)), single nitrogen-vacancy center in a nanodiamond (Tisler et al. (2013), Reserbat-Plantey et al. (2016)), single quantum dots (Ajayi et al. (2014)), TMDCs (Goodfellow et al. (2016)).

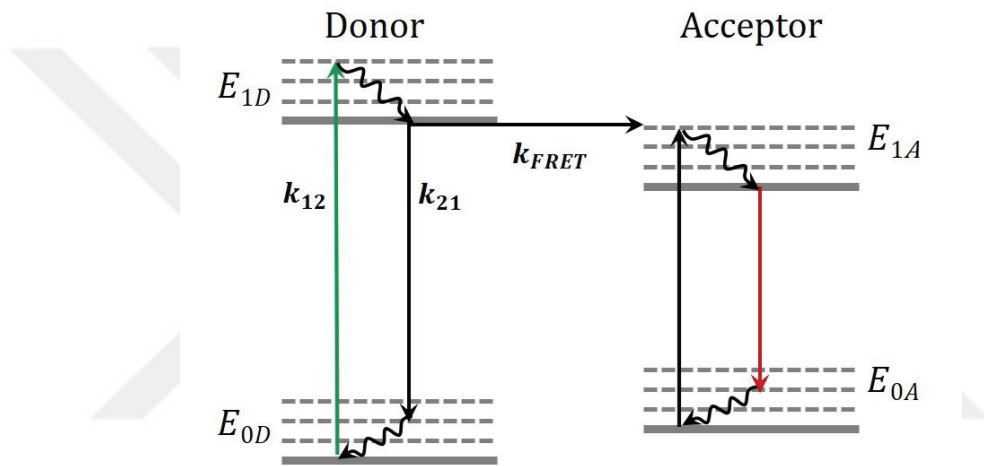


Figure 2.13. Non-radiative energy transfer process between a donor (D) and an acceptor (A).

In this study, a single photon emitting defect center in hBN and a graphene layer as a two dimensional material will be used as D and A, respectively. We shall assume that the internal structures of the materials are not affected by the D-A interactions. Therefore, processes such as electron transfer and molecular binding are not considered. The non-radiative transfer of energy from a single photon source to graphene causes quenching of the emission. Such a quenching is called as static quenching. On the other hand, using an ionic liquid based device structure, the transferred energy rate can be modulated by electrically and reversibly. This kind of quenching is called active quenching. That way, a single photon emission can be modulated gradually and can even be turned on and off like a switch. To figure out the working principle of this graphene-hybrid nano-device a brief theoretical discussion is given below.

2.7.2.1. Near-Field Dipole-Dipole Interaction

In classical perspective, energy transfer between D and A can be understood in terms of an interaction between an initially oscillating dipole (D) and a static dipole (A). The energy transfer occurs when a resonance condition is achieved, that is, both dipoles should oscillate more or less with the same frequency. However, in quantum perspective an electron in D and another in A are in their own states and energy transfer involves a form of wave function overlap. This energy transfer can first be understood in classical approach by considering electric field of an oscillating dipole (Govorov et al. (2016)):

$$E(r, t) = \frac{p(t - \frac{r}{c})}{4\pi\epsilon_0} \left\{ [3(\mathbf{n} \cdot \mathbf{d})\mathbf{n} - \mathbf{d}] \left(\frac{1}{r^3} - \frac{ik}{r^2} \right) + [(\mathbf{n} \cdot \mathbf{d})\mathbf{n} - \mathbf{d}] \frac{k^2}{r} \right\} \quad (2.82)$$

where p is the time dependent electric dipole moment, \mathbf{n} ; unit vector from D to A direction, \mathbf{d} ; unit vector along the donor dipole moment, k equals $\frac{\omega}{c}$ and r is the distance from the dipole. The electric field is always perpendicular to \mathbf{n} . Since radiation is from a point source it creates spherical waves.

In the energy transfer process, the donor's radiated power P_D and the acceptor's absorbed power P_A are related as the following:

$$P_A = \left(\frac{6\pi\epsilon_0^2 c^4 \sigma}{p_0^2 \omega^4} E_0^2 \right) P_D, \quad (2.83)$$

where p_0 is the electric dipole moment amplitude, σ is absorption cross section of the A. E_0 is the electric field amplitude and orientation averaging gives its square as following (Govorov et al. (2016)):

$$E_0^2 = 2 \left(\frac{p_0}{4\pi\epsilon_0} \right)^2 \left(\frac{k^4}{3r^2} + \frac{k^2}{3r^4} + \frac{1}{r^6} \right). \quad (2.84)$$

Combining these equations yields

$$P_A = \frac{\sigma}{4\pi r^2} \left[1 + \left(\frac{\lambda}{2\pi r} \right)^2 + 3 \left(\frac{\lambda}{2\pi r} \right)^4 \right] P_D. \quad (2.85)$$

Since FRET occurs in near field zone, that is the distance d between D and A is from 1 to 10 nm. then it is safe to say $r \ll \lambda$. Thus, neglecting the first and second terms on the right hand side of Eq.(2.85) the absorbed power of A becomes

$$P_A = \frac{3\sigma}{64\pi^5} \left(\frac{\lambda^4}{r^6} \right) P_D. \quad (2.86)$$

This relation can be expressed in terms of transfer rate k_{FRET} and radiative rate k_r , by dividing both sides to $h\nu$ and using molar absorption coefficient ε_A (Govorov et al. (2016)):

$$k_{FRET} = k_r \left(\frac{3ln10\varepsilon_A\lambda^4}{64\pi^5 N_A n^4} \right) \frac{1}{r^6}, \quad (2.87)$$

where N_A is the Avogadro's number and n is the refractive index of the medium. This equation can be generalized as the following when the exciting light has a spectral distribution of wavelengths:

$$k_{FRET} = \frac{1}{\tau_0} \left(\frac{Q_D 3ln10}{64\pi^5 N_A n^4} \right) \frac{1}{r^6} \int_0^\infty F_D(\lambda) \varepsilon_A(\lambda) \lambda^4 d\lambda, \quad (2.88)$$

$$R_0^6 = \frac{9000ln10\kappa^2 Q_D}{128\pi^5 N_A n^4} J(\lambda), \quad (2.89)$$

$$k_{FRET} = \frac{1}{\tau_0} \left(\frac{R_0}{r} \right)^6, \quad (2.90)$$

where quantum yield of donor is $Q_D = k_r \tau_0$ related to the donor's non-interaction lifetime τ_0 . R_0 is called as Förster radius (Förster (1948); Forster (1951)) which is the distance when energy transfer efficiency is equal to 50% of the total efficiency as shown in Fig.2.14. The energy transfer efficiency, E_{FRET} , can be described as the transfer rate k_{FRET} divided by the total decay rate ($k_{FRET} + 1/\tau_0$) with Eq.(2.90) the efficiency is

$$E_{FRET} = \frac{k_{FRET}}{k_{FRET} + \tau_0^{-1}} = k_{FRET} \tau_0, \quad (2.91)$$

$$E_{FRET} = \frac{R_0^6}{R_0^6 + r^6}, \quad (2.92)$$

where τ_0 is the lifetime of the donor without interaction and τ_D is the lifetime with interaction. One of the other parameters in Eq.2.89 is the spectral overlap of D emission and

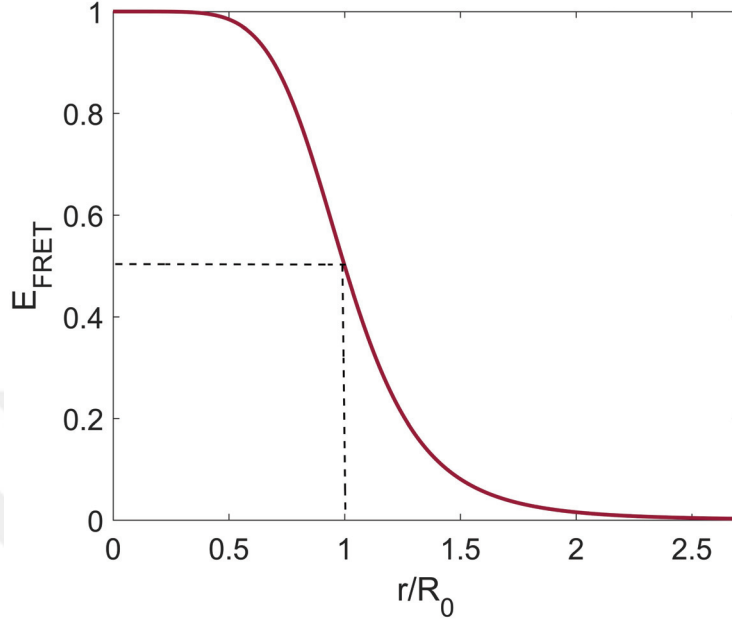


Figure 2.14. Energy transfer efficiency with respect to the distance between D and A, r , and Förster radius, R_0 . The x-axis is normalized distance r/R_0 .

A absorption, $J(\lambda)$. The overlap integral can be described as a function of wavelength, wavenumber, or frequency. Orientation factor, κ^2 takes into account the relative dipole moment positions of D and A:

$$\kappa^2 = (\cos\theta_{DA} - 3\cos\theta_D\cos\theta_A)^2, \quad (2.93)$$

where \hat{d} and \hat{a} are unit vector along the D dipole and A dipole, respectively. The unit vector \hat{r} is the along the line from D to A. According to the Fig.2.15, this relative value is $0 \leq \kappa^2 \leq 4$. The angle between D dipole moment and \hat{r} is θ_D and $\hat{d} \cdot \hat{r} = \cos\theta_D$. Similarly, the angle between A dipole moment and \hat{r} is θ_A and $\hat{a} \cdot \hat{r} = \cos\theta_A$. The angle between D and A dipole moments is $\theta_{DA} = \hat{d} \cdot \hat{a}$.

In quantum mechanical perspective, anti-symmetrized wave functions of the initial and final states of the system are defined for donor excited state and acceptor ground state

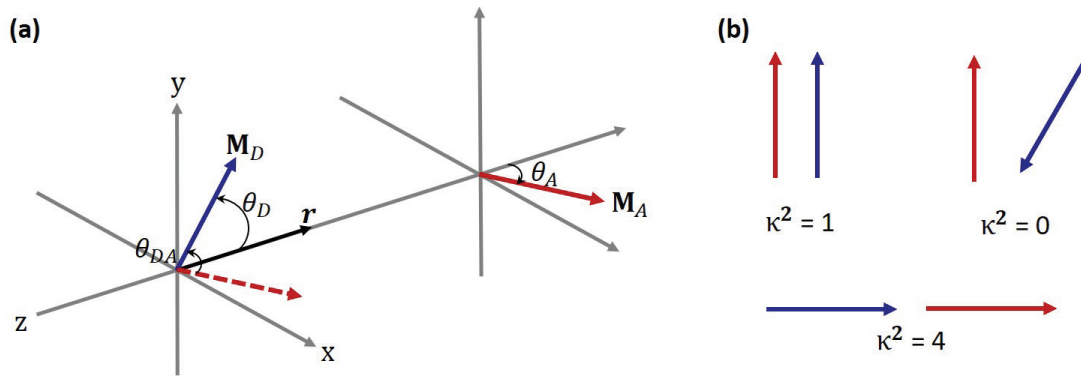


Figure 2.15. (a) The orientation factor, κ^2 , and the relative directions of the D and A dipole moments. (b) The examples for three different values of κ^2 with respect to relative dipole moment directions.

case as Ψ_i and for donor ground state and acceptor excited state case as Ψ_f . The total Hamiltonian of the system is $\hat{H} = \hat{H}_D + \hat{H}_A + \hat{H}_I$ where \hat{H}_I is the perturbation term and also given in Eq.2.38. Using the initial and final states the interaction matrix can be described by

$$U = \langle \Psi_i | \hat{H}_I | \Psi_f \rangle, \quad (2.94)$$

where U consists of Coulombic term, U_C and Exchange term, U_E . The exchange term arises from exchange of spin and space coordinates of exchanging electrons on D and A. Thus, this term contributes when the separation distance between D and A short enough to overlap their electron clouds. In this study, the separation distance between the D and A is always longer than a few nm's. Thus, exchange term does not contribute. Coulombic term arises due to the dipole moments of D and A.

$$U_C = \frac{\mathbf{M}_D \cdot \mathbf{M}_A}{r^3} - \frac{(\mathbf{M}_A \cdot \mathbf{r})(\mathbf{M}_D \cdot \mathbf{r})}{r^5}, \quad (2.95)$$

$$U_C = 5.04 \frac{|\mathbf{M}_D| |\mathbf{M}_A|}{r^3} (\cos\theta_{DA} - 3\cos\theta_D \cos\theta_A). \quad (2.96)$$

In quantum mechanical perspective, the photon emission at a random time by an

excited system can not be known, however its probability can be calculated by *Fermi's Golden Rule*. The rule describes the photon emission rate by dipole matrix element of transition from an initial state ($|i\rangle$) to a final state ($|f\rangle$), M_{if} , and density of optical modes (photonic mode density) $\rho(\nu_{if})$ at frequency of ν_{if} given from the energy difference between two states $\Delta E_{if} = h\nu_{if}$,

$$\Gamma_{if} \propto |M_{if}|^2 \rho(\nu_{if}). \quad (2.97)$$

The rule clearly reveals that an emitter is affected by the properties of its surrounding with respect to its optical properties. Accordingly, using *Fermi's Golden Rule* the energy transfer rate k_{FRET} can be given as the following (Novotny and Hecht (2006)):

$$k_{FRET} = \frac{2\pi}{\hbar} |U|^2 \rho, \quad (2.98)$$

where ρ is the density of interacting initial and final states which is related to the overlap integral between the emission and absorption spectra of D and A, respectively. The $1/r^6$ relation arises from square of the interaction potential of the system.

2.7.2.2. Near-Field Dipole-Graphene Interaction

Graphene was the first 2D material to be investigated for nonradiative energy transfer from the vicinity emitters (Gaudreau et al. (2013), Chen et al. (2010), Ajayi et al. (2014)). Fluorescent nanomaterials and graphene coupling exhibits strong photoluminescence quenching (~ 70 -fold) (Chen et al. (2010)). Furthermore, the effective Förster radius of graphene acceptor was considered to be 11–16 nm (Guzelturk and Demir (2016)) due to its large absorption cross-section ($> 10^5 \text{ cm}^{-1}$). The exceptionally large Förster radius allows graphene for long-range couplings ($> 20 \text{ nm}$). Additionally, the zero band gap of graphene leads interband transitions without frequency dependence. This makes graphene an exciting material for an extremely wide range of nanoemitters. There are variety of reports on FRET-based graphene hybrid nanomaterials such as nanocrystals (Federspiel et al. (2015); Guzelturk and Demir (2016); Yu et al. (2015)), dye molecules (Kim et al. (2010); Treossi et al. (2009)), nitrogen-vacancy centers (NVCs) in diamond (Tisler et al. (2013)). The exceptional fluorescence quenching ability of graphene also widely

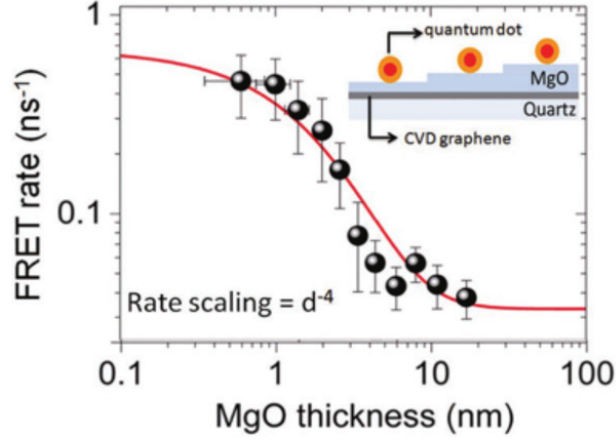


Figure 2.16. FRET rate and distance between the quantum dot and graphene relation. The distance was controlled by the thickness of dielectric material (MgO) (Federspiel et al. (2015)).

used in applications such as biosensors (Tang et al. (2010); Wang et al. (2011)), nanoposition sensor (Mazzamuto et al. (2014)) and fluorescence quenching microscopy (Stöhr et al. (2012)).

The emission from donor quenches with the rate of r^{-4} (Fig.2.16) for two dimensional materials (Swathi and Sebastian (2009); Kim et al. (2010); Federspiel et al. (2015)) due to the plane-like structure of graphene as an acceptor. Optical emission intensity of donor quenches by $\approx k_{rad}/(k_{rad} + k_{nonrad} + k_{FRET})$ like near-field dipole-dipole interaction (Federspiel et al. (2015)). Thus, we need to modify the energy transfer rate model based on the interaction between two point dipoles which is derived by Eq.2.90 for a model for the interaction between a point dipole and two dimensional surface. This modification was showed by Wolber and Hudson (1979) and also nicely summarized by Tabernig (2018). According to these studies the Eq.2.90 is integrated over a plane to derive the energy transfer rate from point dipole to plane (graphene) with polar coordinates r and ϕ :

$$\begin{aligned}
 k_{FRET} &= \frac{R_0^6}{\tau_0} \int_0^\infty \int_0^{2\pi} \frac{r'}{(R(r, r'))^6} dr d\phi \\
 &= \frac{R_0^6}{\tau_0} \int_0^\infty \int_0^{2\pi} \frac{r'}{(\sqrt{r^2 + r'^2})^6} dr d\phi \\
 &= \frac{R_0^6}{\tau_0} \cdot \frac{\pi}{2r^4}, \tag{2.99}
 \end{aligned}$$

where $R(r, r')$ is the distance between the point dipole and an infinitesimally small dipole on the plane. The energy transfer rate obtained by modification for graphene-like plane acceptors by r^{-4} distance dependency. The schematic systems of interacting two dipole and dipole-graphene are shown in Fig. 2.17.

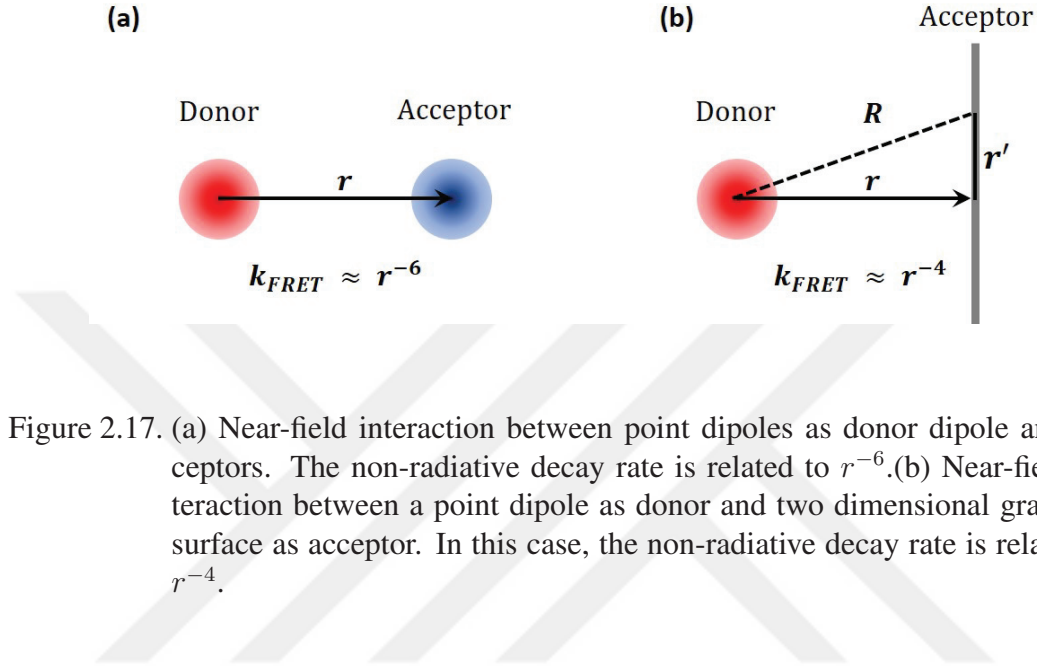


Figure 2.17. (a) Near-field interaction between point dipoles as donor dipole and acceptors. The non-radiative decay rate is related to r^{-6} . (b) Near-field interaction between a point dipole as donor and two dimensional graphene surface as acceptor. In this case, the non-radiative decay rate is related to r^{-4} .

In Fig. 2.18, the single photon emission emission from a three level system and its energy transfer to graphene is shown schematically. The differential equations of time dependent population change of the system was given in Eq.2.53. The interaction of this kind of three level system with graphene includes non-radiative decay rate k_{FRET} from the excited state to graphene. There is possibility to exist this kind of decay from metastable level to graphene, but this has very little effect which is negligible . Thus the population changes of the system under interaction can be shown by

$$\frac{d\rho'_1}{dt} = -k_{12}\rho'_1 + (k'_{21} + k_{FRET})\rho'_2 + k'_{31}\rho'_3, \quad (2.100)$$

$$\frac{d\rho'_2}{dt} = k_{12}\rho'_1 - (k'_{21} + k_{FRET})\rho'_2 - k'_{23}\rho'_2, \quad (2.101)$$

$$\frac{d\rho'_3}{dt} = k'_{23}\rho'_2 - k'_{31}\rho'_3. \quad (2.102)$$

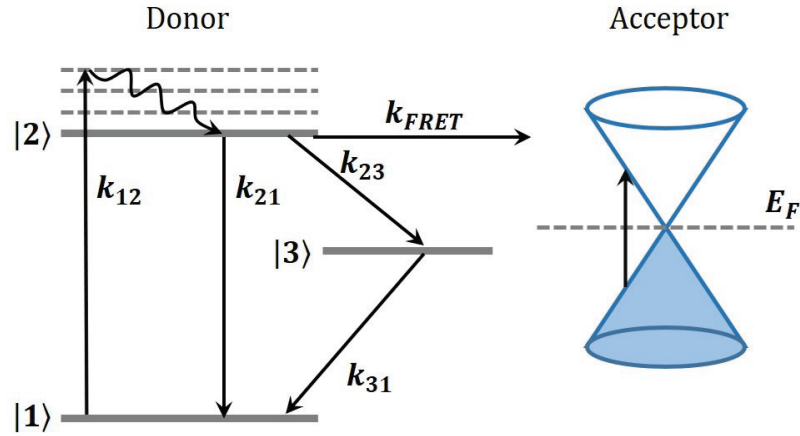


Figure 2.18. Single photon emission by a three level system and energy transfer to graphene with rate equations.

The relaxation rate without interaction k_{21} , k_{23} and k_{31} change due to a non-radiative contribution under interaction such that $k'_{21} + k_{FRET}$, k'_{23} and k'_{31} , respectively. When steady-state population is constant $d\rho/dt = 0$ without interaction, summation of the differential equations of population changes of the system is equal to 1. However, under interaction it must be less than 1. The decay rates decreases due to FRET decay rate, but the rates k_{23} and k_{31} have negligible effects as discussed in Neu (2012).

CHAPTER 3

EXPERIMENTAL TECHNIQUES

Optical techniques play a crucial role in the study of defects which are single photon sources. In this thesis, we employed three important optical experimental techniques namely, Raman spectroscopy, Micro-Photoluminescence (μ -PL) spectroscopy, and Hanbury Brown-Twiss (HBT) interferometry. Raman spectroscopy was used mainly to study the phonon modes of the host and the vibrational modes of the defects along with their interactions with the host phonons. PL spectroscopy was first used to study the fluorescence from the defect centers. Then, emission characteristics of a single photon source was also studied by μ -PL spectroscopy. The third optical technique, HBT interferometry, was used to obtain $g^2(\tau)$ data where either a continuous or a pulsed laser excitation was employed. Additionally, lifetime measurements were carried out with the same HBT setup as described below.

3.1. Raman Spectroscopy and Micro-Photoluminescence Setup

The samples used in this study are characterized both optically and structurally by confocal microscopy, Raman and PL spectroscopy. In the study, a microscope is used to focus excitation laser light to a small spot (about a micron in diameter) which allowed us to obtain signals from a single defect center. We were able to utilize the same Raman setup for both PL and Raman measurements. A generalized schematic diagram of our PL/Raman setup is given in Fig.3.1. Necessary modifications to the given setup were done for specific measurements when needed.

A continuous-wave (CW) HeNe laser source with a 633 nm wavelength excitation was used for most PL and Raman applications. The setup includes additional excitation sources such as a Melles-Griot Ar-Ion laser with 514 nm and 488 nm wavelength emissions, a Coherent Verdi V6 laser with 532 nm wavelength, and a 483 nm pulsed-laser (PiL048X) with a maximum 120 MHz repetition rate and a 60 ps pulse width. For Raman measurements, light from the laser was focused on the sample by the objective of an Olympus BX51 microscope. The scattered light from the sample was collected by the same objective in the back-scattering geometry. After passing through a beamsplitter

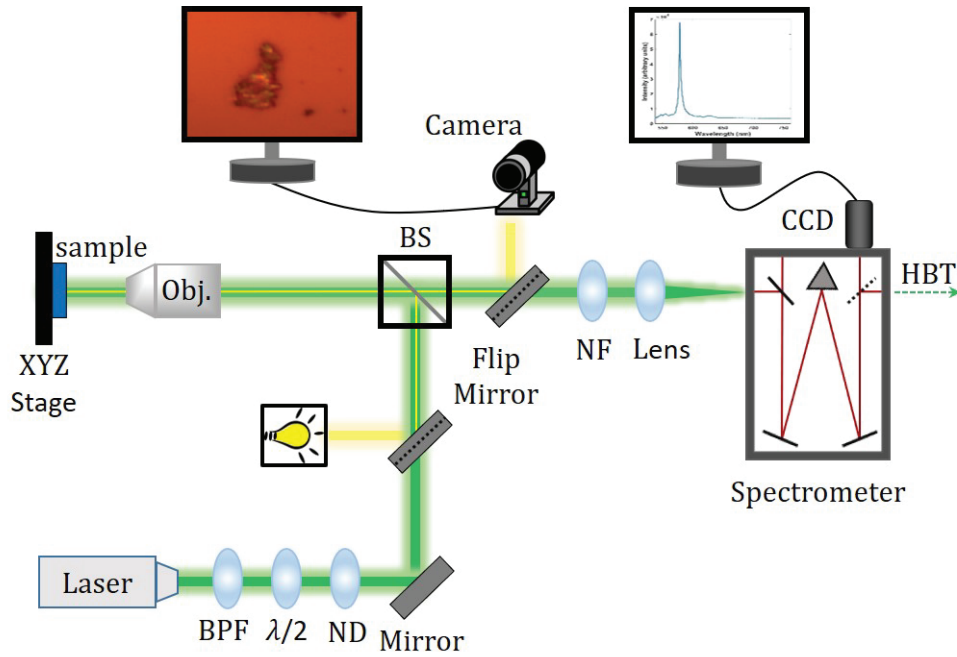


Figure 3.1. Raman Spectroscopy and Micro-Photoluminescence setup is shown.

(BS) and a notch filter (NF), the scattered light was focused onto the entrance slit of a 750 mm focal length monochromator (Princeton Instruments, ACTON SP2750, with a grating turret including three interchangeable holographic gratings of 150, 600, and 1800 grooves/mm). After spectral deconvolution at the grating the spectra was collected by a multichannel high resolution CCD detector (ProEM-EMCCD, containing 1600 (horizontal) x 200 (vertical) pixels with a maximum resolution of 0.3 cm^{-1}).

Photoluminescence experiments are carried out either in free space or by using fibers. Some of the experiments were performed by directing the laser beam in free-space as in the case of Raman measurements described earlier. After leaving the laser, the beam first passed through a band-pass filter (BPF) to filter out all radiation except the one at the emission wavelength with a spectral range $\lambda_{laser} \pm 5 \text{ nm}$. As going along the laser beam path, then, a half wave plate ($\lambda/2$) was used to alter the polarization state of the excitation light to characterize the polarization dependence of the emission. Next, a wheel of neutral density (ND) filters was placed to control the excitation power. Then, the laser beam passed through a 50:50 non-polarizing beam splitter (BS) or a dichroic mirror to be directed to the objective of the BX51 microscope system as seen in the Raman setup Fig.3.1. High numerical aperture (NA) 50x (0.75 NA) and 100x (0.90 NA) objectives and a Mitutoyo Plan Apo Infinity Corrected objective with long working distance, 50x (0.55

NA) were used in the Microscope system to focus the laser onto the sample. The long working distance objectives were used for device experiments and the low temperature experiments which shall be described in detail later in this chapter. After the laser light exciting the sample, the luminescent light was collected with the same objective lens in the back-scattering geometry and separated from the excitation beam using a 50:50 non-polarizing beam splitter (BS) or a dichroic mirror. A white light source (integrated to the microscope) was used to obtain the real time view and image of the sample surface via an integrated camera. An initial flip mirror was placed on the beam path before the BS to direct the light from a white light source onto the sample while a second flip mirror after BS was used to direct the reflected light from the sample onto the camera. The Rayleigh component in the reflected light from the sample as well as the laser light reflected from the BS was filtered out with a notch filter (NF) with a 17 nm absorption band centered at the laser wavelength. The filtered PL emission was, then, either focused onto the entrance slit of a monochromator (ACTON SP2750, Princeton Instruments) for spectral analysis or directed to the HBT setup for photon correlation experiments. (For some experiments light was directed onto the HBT setup at an exit slit of the monochromator via a flip mirror placed before the CCD detector as shown in the Fig.3.1). After spectral separation from a proper grating set the light was detected at the entrance slit of the monochromator by the multichannel EMCCD detector.

After reaching the monochromator, the light was detected on an array CCD detector. The signal detected in the CCD was digitized as electrical data, and transferred to the controlling computer for analysis. An S&I TriVista program was used both for controlling the experiment (setting up some parameters such as choosing filters, laser light calibration etc. and starting and finishing the data collection) and for analyzing the collected data. Our samples were mounted on a high-precision XYZ moving stage. The position of the focused laser beam on the sample was controlled precisely by the Tri-Vista software which was also monitored by the integrated camera in real time. The positional accuracy of the XYZ stage was in the submicron level. Thus, we were able to focus the laser beam onto very small (submicron) sized particles as well as on to a specific defect centers emitting single photon radiation. In this way, for example, Raman and PL measurements from the same predetermined points were obtained before and after graphene transfer or gold nanoparticle deposition for comparative analyses (to be discussed in detail). We also employed a second setup for PL and photon correlation experiments very similar to the one described above. In this setup, a Shamrock750 spectrometer with 750 mm focal length with a selectable choice of a set of three gratings of 150, 600 and 1800

gr/mm with an array CCD detector (Newton920 with 1024x255 pixels) was used and the data was collected and analyzed by a home-made LabVIEW program.

3.1.1. Two-dimensional Photoluminescence Mapping

We studied the point defects in dropcasted flake clusters on Si-based substrates for single photon sources. We were able to obtain a two dimensional map of such defects via XYZ stage in our PL/Raman setup. Scans were carried out step by step first along X then Y direction over a predetermined region of the sample. The step size along both X and Y directions were $0.25 \mu\text{m}$, Thus, at each step a PL spectrum was collected from a spot with an area of $0.25 \times 0.25 \mu\text{m}^2$. After completion of all PL measurements from every spot on the chosen area of the sample, the spacial distribution of a particular emission wavelength of a single photon source produced a two dimensional image of that defect in the chosen area. Thus, by means of the micro-PL mapping, the PL spectra of several defects were analyzed from a single map data. Fig.3.2 gives such a PL maps obtained from some chosen areas of a drapcasted hBN sample on a Si substrate. The maps show the two dimensional distribution of the single photon radiation which was seen as an intense peak in the PL spectrum of a chosen spot on the side.

3.1.2. Temperature Dependent PL Measurements

A Linkam THMS600 stage was used to perform temperature dependency measurements of PL and Raman signals. The stage, shown in Fig.3.3, was mounted on the XYZ stage under a long working distance objective of the BX51 microscope. The temperature of the samples placed in the chamber of the Linkam stage was controlled in a wide range from $+300 \text{ }^\circ\text{C}$ to $-196 \text{ }^\circ\text{C}$. Cooling below room temperature (RT) was achieved via vaporized nitrogen from a liquid nitrogen (LN2) reservoir while heating over RT was obtained by electrical currents under the sample mount in the chamber. Before cooling with LN2, the chamber was evacuated via a pump to prevent ice formation on the sample as well as on the optical window of the stage. However the pump noise introduced vibrations to the chamber which caused fluctuations in the position of the sample. This limited the exposure time to a few seconds for low temperature experiments.

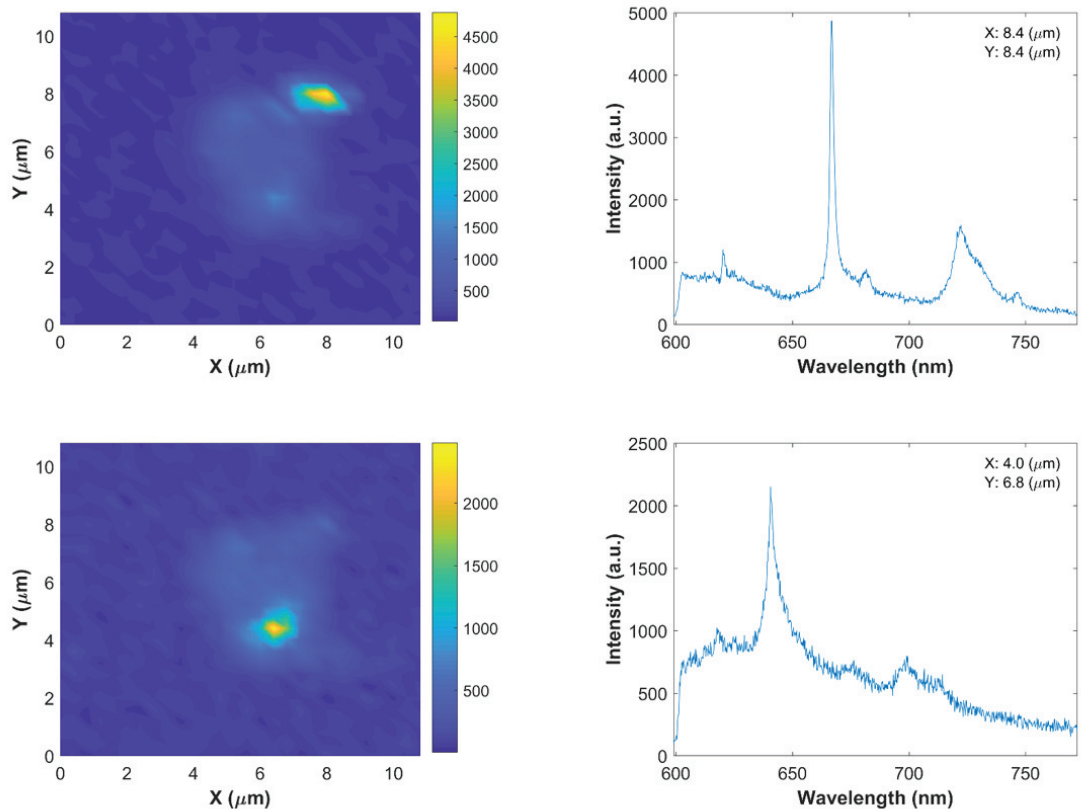


Figure 3.2. At the left the two dimensional PL maps of the same dropcasted hBN flakes cluster are plotted with respect to different wavelengths which are shown at the right. In the maps, the spectrum which has the maximum intensity at the chosen wavelengths are seen as the brightest pixels (yellow). The plotted maps with respect to different wavelengths show the emission originates from localized points in the cluster. On the right panel, the coordinates of these pixels are written with respect to the maps.



Figure 3.3. Linkam THMS600, heating and cooling microscope stage (Linkam (2016)).

3.2. Hanbury Brown-Twiss Interferometer Setup

For the second order correlation function measurements, the spectrally filtered emission was directed to an HBT interferometer setup. Depending on the type of experiment, the emission from a single photon source was directed on to the detectors either over a pair of split fiber cables or over a free-space optical setup. A generalized diagram for the setup is shown in Fig.3.4. The setup consists of a 50:50 non-polarizing BS and two single photon counting avalanche photo diodes (APD). A time digital converter module (Excelitas SPCM-AQRH) was used to convert the detection time of the photons. Then, the histogram as a function of delay time (τ) was obtained as the number of photons for the difference of any two given detection time t_1 and t_2 ($\tau = t_1 - t_2$).

The correlation function, which obtained from the histogram of the experimental setup, ($g^{(2)}(\tau)$) is used to determine whether the emitted radiation from the sample has a single-photon character by correlating the photon measurement times of the APDs (t_1 for the first and t_2 for the second). If the radiation comes in SP (from a SP source), each photon will be reflected or passed through the beam splitter with a 50% probability. Thus, If a source emits one photon at a time only one of the APD's should detect a photon at any time. The process was explained in the preceding chapter. The excited state lifetime measurements were also carried out using the same HBT setup shown in Fig.3.4.

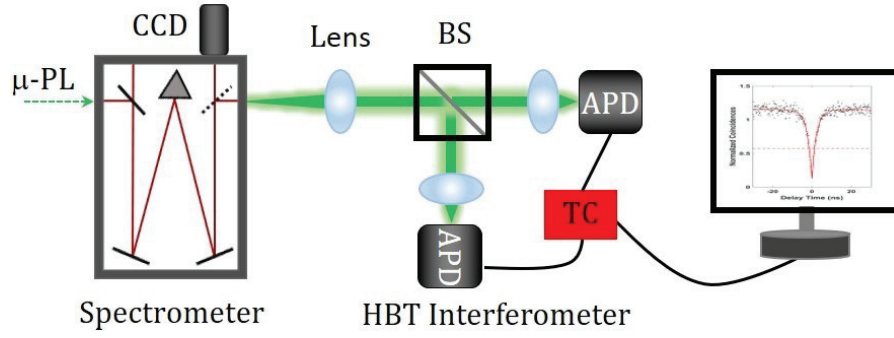


Figure 3.4. Hanbury Brown-Twiss interferometer (HBT) setup is used to measure correlation function and excited state lifetime.

Photon correlation measurements were performed by both continuous wave (CW) and pulsed laser excitation. We were able to measure the second order correlation function of the for a particular single photon emission in both way. Fig.3.5 (a) shows a typical single photon PL emission from a defect center in hBN while the second order correlation function measurements of the same defect center are given in Fig.3.5 (b) and (c). The correlation function $g^{(2)}(\tau = 0)$ measurements obtained with a CW-excitation gives a dip at zero time delay. Experimentally, the value of $g^{(2)}(\tau)$ at zero time delay should be between 0 and 0.5 to be able to identify the defect center as a single photon source as described in theoretical chapter in detailed. Under the ideal conditions $g^{(2)}(\tau = 0)$ must be equal to zero. In reality, it is never zero due to background effects. On the other hand, the width of the deep, which is inversely related to the decay rate, is affected from the excitation power and increasing power leads to bunching. The effect of the pump rate on the delay time is given by the the following equation:

$$\tau_1 = \frac{1}{\Gamma + W_p}, \quad (3.1)$$

where Γ is the spontaneous decay rate while $\Gamma + W_p$ is the effective pump rate, ideally $\Gamma \gg W_p$. Fig. 3.5 (c) shows a typical excitation power and correlation function dependency of the single photon emission from a defect center in hBN.

In Fig.3.6, the correlation function measurement of a particular defect obtained using a pulsed laser excitation is shown. A series of peaks are separated by from each other with a repetition. We notice that the peak around zero time delay was depressed. The relative area of the central peak compared to other peak areas is about 0.35 indicating

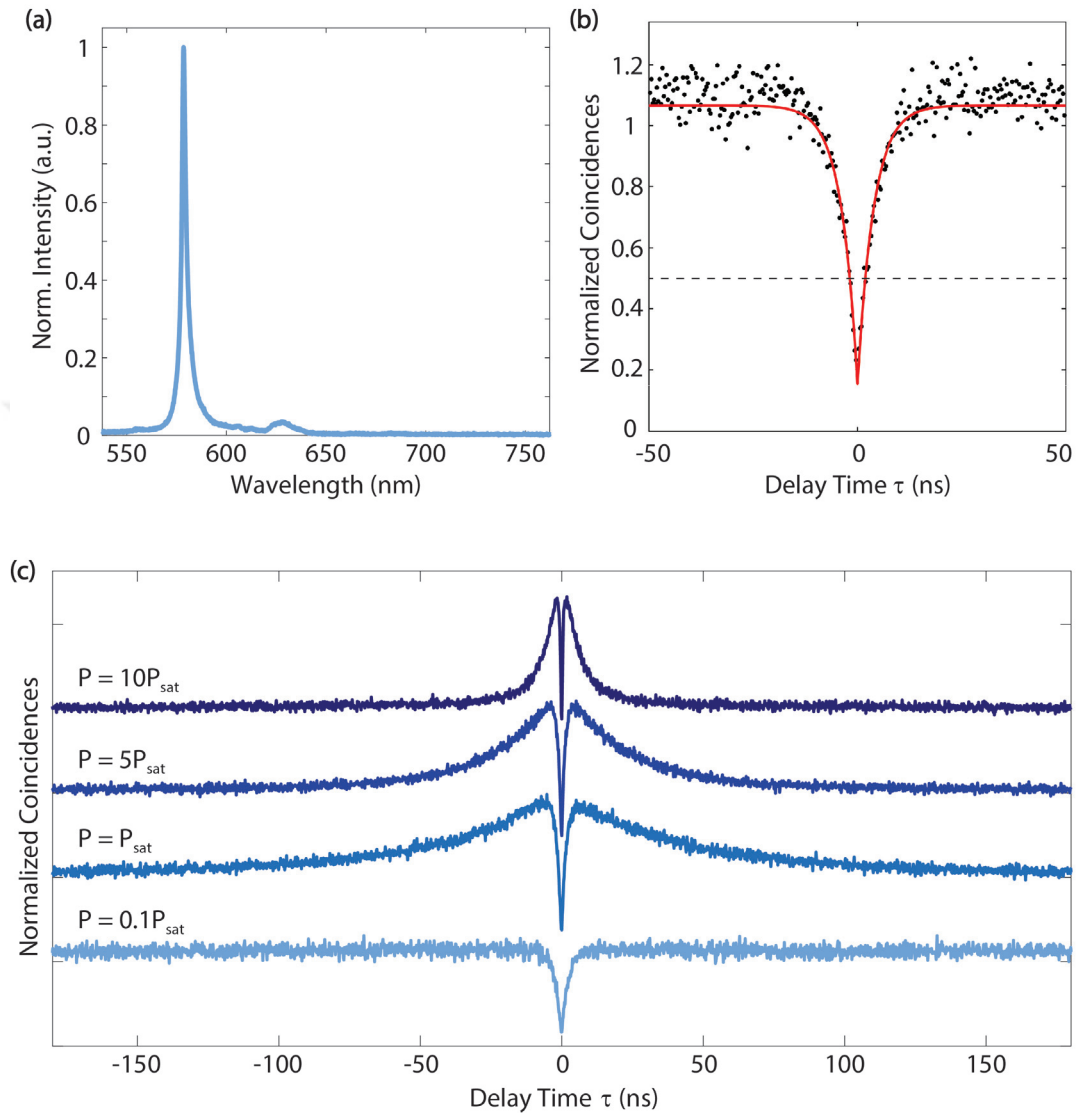


Figure 3.5. (a) A ZPL obtained from a defect center in hBN and its PSB are shown. (b) The photon correlation measurement result of HBT interferometer of this ZPL is shown. The dip is below 0.2 at zero delay time which means that a SP emission is measured. (c) Power dependent photon correlation measurement results with respect to saturation power.

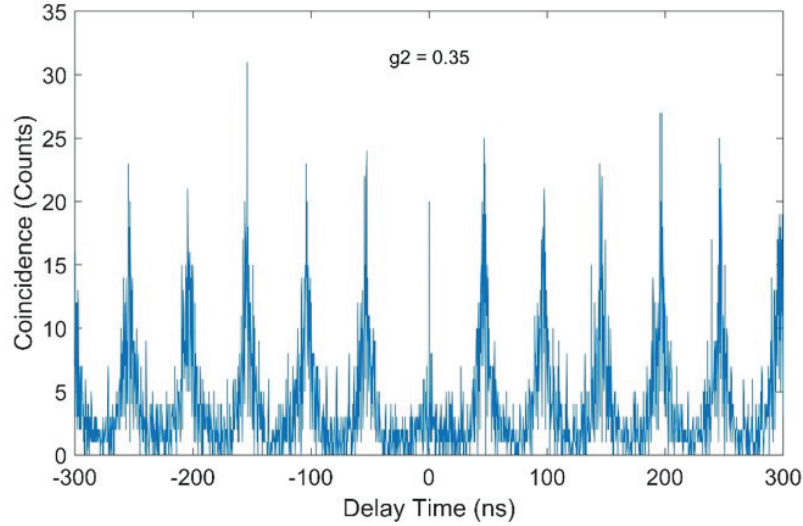


Figure 3.6. Second order correlation measurement performed by pulsed laser.

that the source emits single photons. The pulse frequency of the exciting laser (not the emitted radiation frequency) was 20 MHz corresponding to a period of 50 ns which is equal to the peak separation in the measurement given in Fig.3.6.

3.2.1. Lifetime Measurements

To measure the excited state lifetime a 483 nm pulsed-laser (PiL048X) with a maximum 120 MHz repetition rate and a 60 ps pulse width was used. The average decay time of an emitter's excited state which is defined as the time interval (t_0) between an excitation pulse and the subsequent photon count was measured and plotted as a histogram, as shown in Fig.3.7. For life time measurements the same HBT setup given in Fig.3.4 was used employing only one of the APD detectors. The number of the photons decays exponentially with the delay time. The temporal decay rate can be given by an exponential decay probability function:

$$P(t) \cong 1/\tau e^{-t/\tau}, \quad (3.2)$$

where $\tau = 1/\gamma$ corresponds to the lifetime of the excited state. Hence, the excited state life time is equal to the average delay time when the photon count reaches the 1/e of the

maximum photon count (almost no time delay count). Strictly speaking for a time delay t_0 being very close to zero, the number of detected photons will be zero because of the finite response time of the detector which is seen as a sharp decrease in the photon counts when τ is very close to zero (see Fig.3.7 (d)).

In Fig.3.7, the single photon characteristics of an emission from defect centers in hBN are shown. Fig.3.7 (a) gives polarization dependency of the SP emission, while power dependency and lifetime measurements were given in Fig.3.7 (c) and (d). Fig.3.7 (b) shows the quenching of the single photon emission after a graphene transfer on the defect. The stable emitter is excited with both 532 nm CW laser and 483 nm pulsed laser. The lifetime is calculated from the trace of the histogram as shown in Fig.3.7 (d).

3.3. Scanning Electron Microscopy

The ability to create optically active defect centers artificially is of crucial importance for the SP-based applications. Various processes have been studied to generate SPs. Most of them are based on the implantation of foreign atoms (gas, powder or solid catalyst film) during the growth of the host material by CVD (Rabeau et al. (2005); Naydenov et al. (2009)). In this study, we focused on one of the ex-situ defect creation methods, that is, electron beam irradiation by Scanning Electron Microscopy (SEM).

Generally, SEM was used to obtain magnified images by scanning a sample on a Si-based substrate with a high energy beam of electrons. In an SEM system an electron gun produces a high energy (keV) electron beam which is directed to the sample by electromagnetic fields (acting as lenses in optical sense). When the beam strikes the sample it interacts with the sample. This interaction frees some of the sample electrons, called the secondary electrons (SE), some of the will backscatter (backscattered electrons (BSE)). When an electron is knocked out from an inner full shell of the sample, a downward transition of an electron from a higher electronic shell will create a characteristic X-ray, Depending on the sample the deflected and ejected electrons from the sample will create current signals. Different types of detectors are used to collect and convert these signals into a two dimensional image on the screen. In this study, a Quanta FEG 250 SEM system was used to create defects in commercial bulk hBN pieces on Si-based substrate. The irradiation was performed by 20 keV energy electrons for 5-20 min durations.

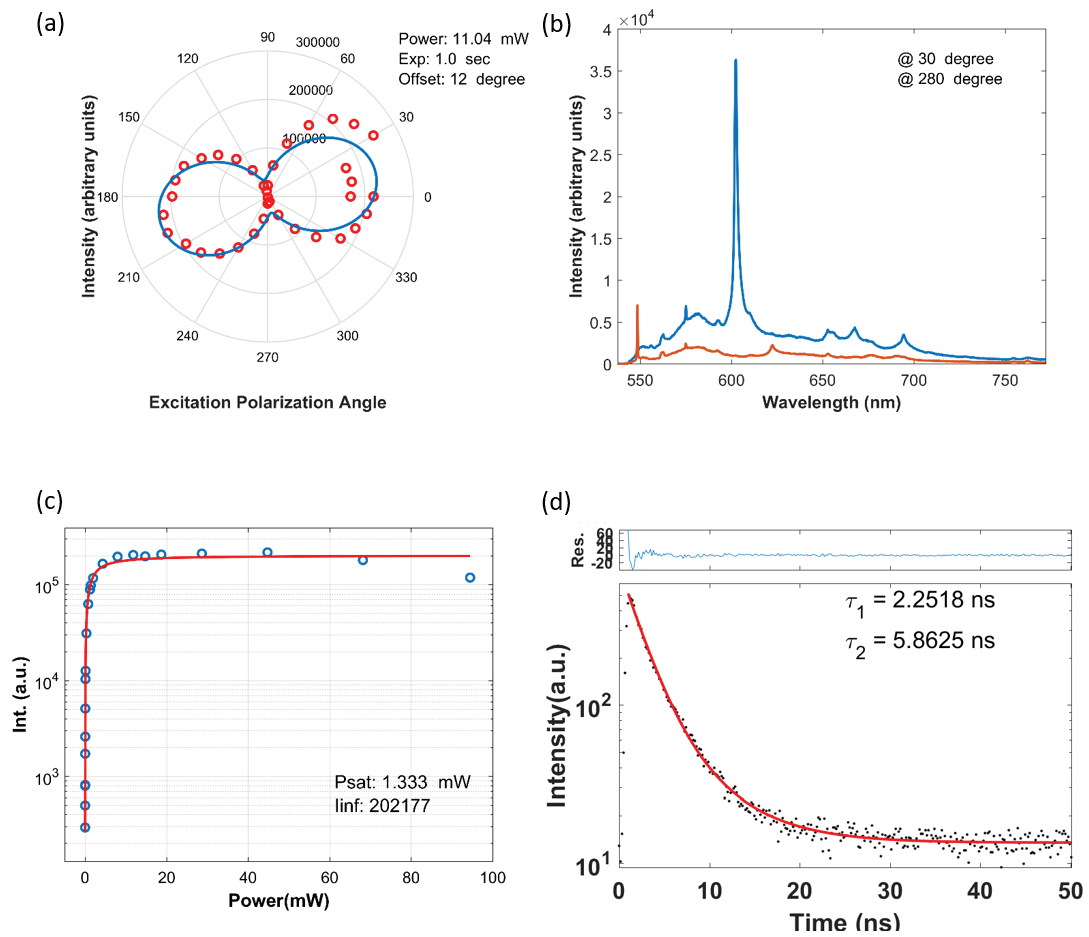


Figure 3.7. (a) Excitation polarization dependent PL intensity of a single photon emission. (b) PL spectra extracted from the polarization dependency series in (a) for the degree of maximum and minimum intensities. (c) Excitation power dependent PL intensity of a single photon emission. (d) Lifetime measured at 20 MHz frequency. Black dots are the experimental statistics and the line is theoretical fit. Excited state lifetime was calculated by this exponential fit curve.

CHAPTER 4

STRUCTURAL AND SPECTROSCOPIC CHARACTERIZATION OF THE MATERIALS

In this chapter, the structural and optical properties, relating to our studies, of all materials investigated in this study, namely, WS₂, WO₃, graphene, and hBN, are given in some detail. Furthermore, experimental techniques and material methods employed in this study, such as the transfer procedure of 2D materials onto desired substrates and single photon source material preparation, are also given. For the generation of single photon sources, defects in the bulk hBN were created by electron beam irradiation. Even though the emission from these defects was of single photon in character, it was not stable to carry out consistent set of required experiments such as polarization and power dependencies and photon correlation experiments (using HBT setup).

To solve the stability problem, we first tried CVD-grown hBN samples as single photon sources. A CVD-grown hBN layer was first placed on a silicon substrate, then Raman and PL measurements were carried out. However, the dominant Raman signal of hBN around 1369 cm⁻¹ could not be observed which indicated a structural deformation. In our final try, hBN was transferred onto Si substrates via dropcast method as described in detail later in this chapter. This method produced stable single photon sources suitable for all the required analyses and characterizations.

4.1. Tungsten Di-sulfide (WS₂)

There are many types of single photon sources besides defect centers with energy levels in the band gap of a host material, such as localized (Frenkel) excitons (Jiandong Qiao et al. (2019)). In particular, localized excitons can be seen in transition metal dicalcogen (TMDC) alloys such as MoSe₂, MoS₂, WSe₂ and WS₂. The general structure of a TMDC alloy is MX₂, M being a transitional metal element and X being a Group-VI chalcogen element, such as S and Se. The band gap energy of a typical TMDC is less than 2.5 eV (about 500 nm), making them suitable for defect and band gap related luminescence investigations. TMDCs may have a multi or monolayer crystal structure.

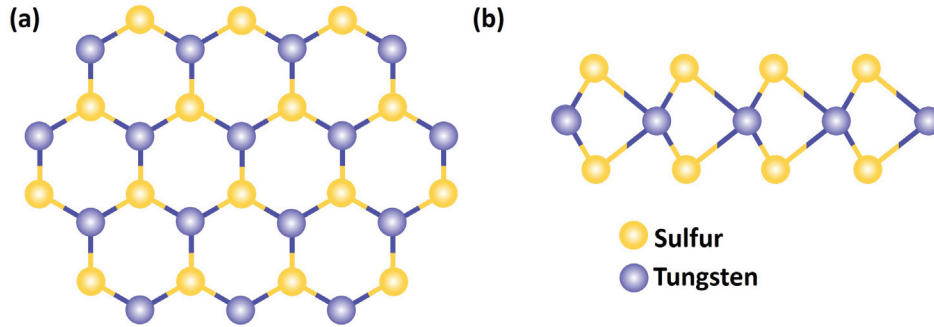


Figure 4.1. Schematic representation of two dimensional structure of WS_2 . (a) Top view, (b) side view. Blue atoms represent Tungsten and yellow atoms Sulfur.

Similar to graphene, there are strong covalent bonds between atoms in a layer and weak van der Waals interaction between individual layers. As an example, the monolayered crystal structure of WS_2 is shown in Fig.4.1 with top (a) and side (b) views. A single layer of WS_2 consists of one metal atom layer with a 6-fold in-plane coordination in the middle of two trigonal chalcogenide atom layers which are packed in hexagonal form.

Physical properties of TMDC's are of great importance due to a direct energy gap in the semiconductor range as well as high carrier mobilities, thus making them suitable for many semiconductor applications. Tailoring their electronic and optical properties for specific applications are on going research activities in the scientific community. The band edges of the monolayers are located at the corners of the hexagonal Brillouin region (K valley). Both valence and conductive bands have a large spin splitting with oppositely marked K^+ and K^- valleys, coupling spins and valley degrees of freedom. The optical transition selection rules permit valley selective excitations of excitons via circularly shifting the polarization of exciting light. In addition, strong Zeeman splittings can be observed in potential photon indistinguishability applications (Aharonovich et al. (2016)). Opto-electronic device applications of these materials are of interest due to the spin-valley coupling of tightly bound excitons and their possible new functionality (Dong et al. (2017)). Finally, many interesting properties of hybrid structures of TMDCs with graphene and other functional materials offer great potential for new developments in electronic and nano-optical technologies.

In semiconductor materials, photoluminescence spectra due to conduction-valence band transition are caused by electron-hole recombinations in a strongly bound non-localized (Mott-Wannier) excitons. On the other hand, recombination radiation from the

excitons localized at a defect point (Frenkel exciton) exhibit single photon nature (Tonndorf et al. (2015); Perebeinos (2015)). The binding energies of localized excitons are much higher than free excitons which shifts the position of the ground state down towards the middle of the energy gap leading to sharp recombination peaks in their PL spectra. Excitons can be attached to impurity atoms or trapped in potential wells caused by vacancy defects, structural defects or local stresses (Rosenberger et al. (2019)). In the literature, it was reported that excitons are mostly trapped at the defects on the edges of monolayer TMDC flakes due to local potential well formations. These wells are deep enough for stable excitonic PL emissions (Raj and Tripathi (2019)). In addition to natural defect formations to trap Frenkel excitons, hand made traps can also be formed by creating local stresses via nanoindentations at the surface of a semiconductor. In a recent study, such local nanoindentations were formed by submerging the tip of an atomic force microscope (quantum calligraphy) into a WSe₂ layer (Rosenberger et al. (2019)).

Ideally, at cryogenic temperatures, the recombination radiation for a well localized exciton with a mid-gap energy state must give a very sharp luminescence peaks. However, with increasing temperature such peak widths exhibit substantial broadening mainly due to acoustic phonon scattering. In contrast, the ionization energy of free excitons in many materials are only a few meV, hence their shallow ground state exhibit a strong coupling with conduction and valence band electronic states causing broader PL peaks and the discrete excitonic levels required for single-photon emission disappear when the temperature rises above 20-35 K ($k_{BT} = 26$ meV at room temperature). Therefore, free excitons can only exhibit single photon luminescence at cryogenic temperatures down to 5 K. For opto-electronic applications single photon emission must be in the visible range of electromagnetic spectrum. However, the gap energy of TMDC's are too small to create mid-gap defect states which can have excitonic luminescence in the visible range. Also the defect states in them are not deep enough for stable single photon emission. Hence they cannot be used as single photon sources (Aharonovich et al. (2016)). In a study, regional stresses were created to trap excitons and to increase emission stability at temperatures up to 60 K (Rosenberger et al. (2019)). In another study, the interaction of TMDCs with plasmonic nano-cavities increased the observation temperature of single-photon radiation to 160 K (Luo et al. (2019)). Alternatively, single photon emission was observed in the ultraviolet spectral region at room temperature from carbon nano-tubes, creating covalently bound oxygen or sp^3 defects (He et al. (2017); Ma et al. (2015)).

In the study of such alternative materials, it is important to obtain stable and bright radiation at room temperature (Chakraborty et al. (2015); Srivastava et al. (2015)). In a

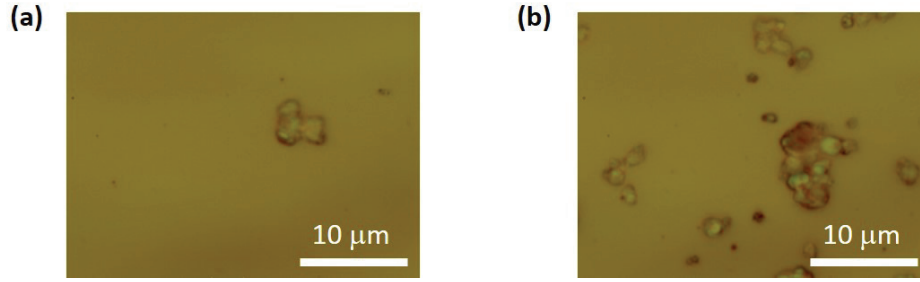


Figure 4.2. Optical microscope images of dropcasted WS_2 particles on a SiO_2/Si substrate. (a) low and (b) high concentration region.

recent study, it has been reported that multi-layer WS_2 emits single photons after thermal annealing (Tran et al. (2017)). The reason for this was interpreted as the occurrence of WO_3 defects as a result of annealing. The researchers claimed that these defects entrap excitons and deepen their ionization energies, hence, creating sharp excitonic levels in the energy gap. Based on the claims set forth by Tran et al. (2017), we have investigated WS_2 and WO_3 as candidates for room temperature single photon sources. Indeed the emission characteristics from the defects in our WO_3 samples showed strong single phonon characteristics. Hence, for the first time we were able to confirm that a TMDC material can also produce single photons at room temperature. This evidence creates the necessity of new studies in this field.

In this study, WS_2 was purchased in powder form from Sigma-Aldrich with $2\mu m$ particle size and 99% purity. Powder was mixed with equal amount of DI-water and ethanol to obtain $\sim 5mg/L$ concentration. This solution was stirred with a vibrator for 10 minutes and dropcasted on a clean SiO_2/Si substrate. Then we let the liquid solvent evaporate by itself until the samples were completely dry. The Fig.4.2 shows optical microscope images of dropcasted WS_2 particles on a SiO_2/Si substrate. This preparation method produced a non-homogeneous distribution of WS_2 particles on the substrate surface. In Fig.4.2 (a), a low-concentration and in (b) a high-concentration region of particles are shown. The preparation is very similar to the illustration in Fig.4.3 which is given for hBN samples.

Raman spectrum of a multi-layered WS_2 sample gives two first-order Raman modes; $E_{2g}^1(\Gamma)$ and $A_{1g}(\Gamma)$ at the Brillouin zone center. Additionally, a zone-edge mode at the M point is seen as the longitudinal acoustic mode $LA(M)$. These are due to in-plane joint movements of the atoms with periodic compression and expansions of the lattice. In

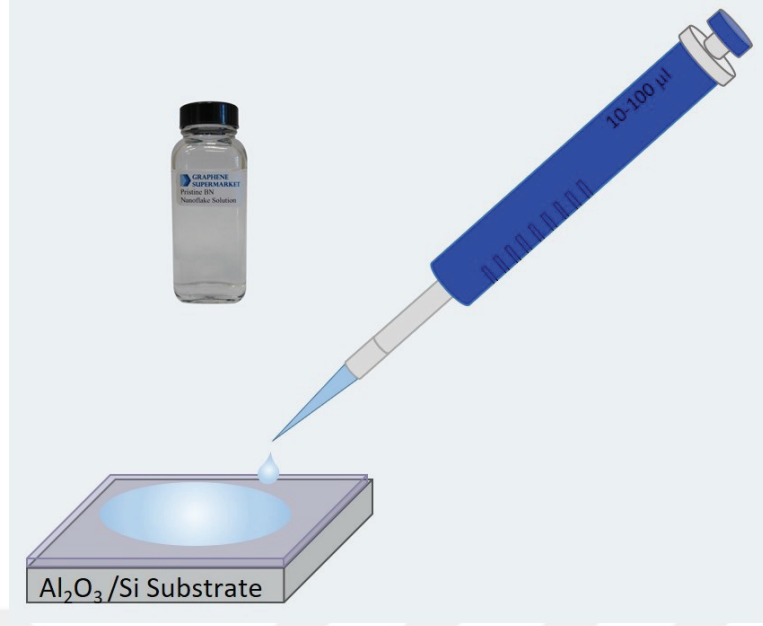


Figure 4.3. The dropcasted hBN sample preparation from solution. For WS₂ and WO₃ samples, SiO₂/Si substrates were used.

Fig.4.4 (a), the atomic displacements of $E_{2g}^1(\Gamma)$, and the $A_{1g}(\Gamma)$ modes are given. The dashed line refers to the weak inter-layer van der Waals interaction.

Raman spectroscopy can not exactly determine the number of layers. However, the layer number is predicted by the intensity ratio of $I_{E_{2g}^1(\Gamma)}/I_{A_{1g}(\Gamma)}$ which is greater than 1 for a single layer and less than 1 for more than 3-layers of WS₂ that are bound together by van der Waals forces (Berkdemir et al. (2013)). When the number of layer decreases the Raman intensity of the $A_{1g}(\Gamma)$ mode decreases as well which means the inter-layer phonon restoring forces get weaker with decreasing number of layers. The three first-order modes of $E_{2g}^1(\Gamma)$, $A_{1g}(\Gamma)$, and $LA(M)$ and a second-order mode $2LA(M)$ are observed at 356 cm^{-1} , 418 cm^{-1} , 176 cm^{-1} and 352 cm^{-1} , respectively in the Raman spectra of such layers. The second-order disorder mode becomes highly intense under 514 nm excitation wavelength and overlaps with $E_{2g}^1(\Gamma)$ mode (Berkdemir et al. (2013); Iqbal et al. (2016)).

In this study, the dropcasted WS₂ samples were used after annealing at $550\text{ }^\circ\text{C}$ for 30 minutes to increase the stability of defects to enhance the single photon emission characteristics. After annealing, however, in addition to WS₂ phonon modes, we also observed the phonon modes of WO₃ in the Raman spectra of these samples as shown in Fig.4.4 (b). The peak at 520 cm^{-1} is the fundamental phonon mode of silicon coming

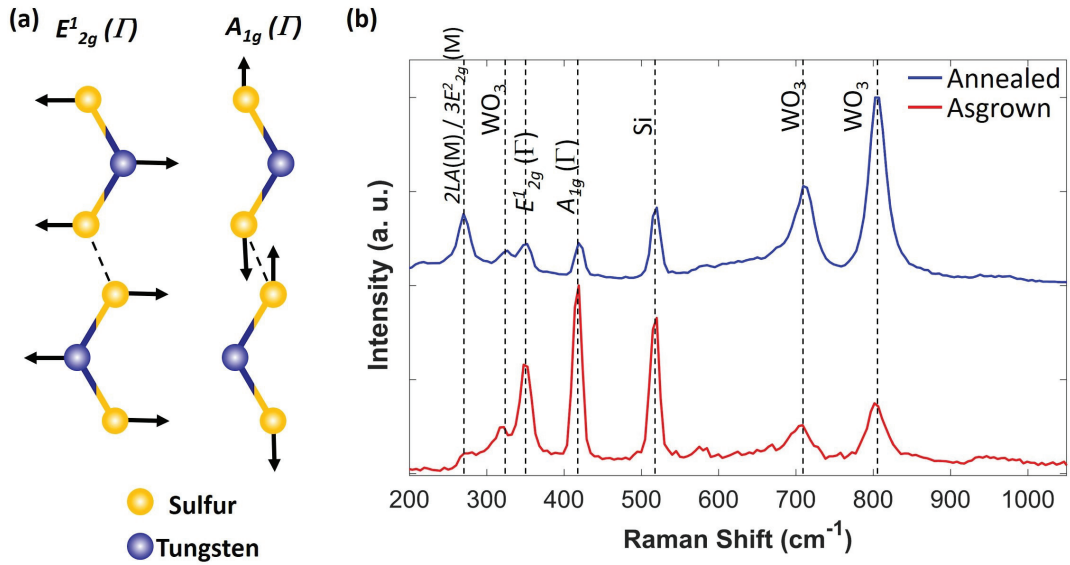


Figure 4.4. (a) Schematic representation of the atomic displacements of two adjacent layers in WS_2 . (b) Raman spectra of asgrown (red) and annealed (blue) WS_2 samples.

from the substrate. The occurrence of this mode indicates that the WO_3 film is very thin on the Si substrate. As seen, the $E_{2g}^1(\Gamma)$ and $A_{1g}(\Gamma)$ modes of WS_2 are at 352.5 cm^{-1} and 419 cm^{-1} , respectively. The Raman mode at 270.1 cm^{-1} could be a difference mode, namely $2LA(M) - 3E_{2g}^2(M)$ mode of WS_2 or WO_3 (or a combination of both). The intensity of this peak noticeably increases after annealing. The annealing process also intensifies the Raman peaks at 326.7 cm^{-1} , 709.4 cm^{-1} and 807.5 cm^{-1} . These modes are in fact Raman active phonon modes of WO_3 , which will be explained in the next section. After annealing, oxide defects in the WS_2 increases. But most importantly, as a part of this thesis work, we were able to observe single photon emission from WO_3 defect centers. We observed that, annealing increased intensity of single photon emission as well indicating an increase in the emitter concentration due to annealing.

4.2. Tungsten Three-oxide (WO_3)

In a recent study, it has been reported that single photon emission from WS_2 can be observed at room temperature albeit it is due to defects in WO_3 which is formed in WS_2 (Tran et al. (2017)). The authors considered two possibilities for the source of single photons in WS_2 : either WO_3 defects trap the excitons shifting their binding energies to

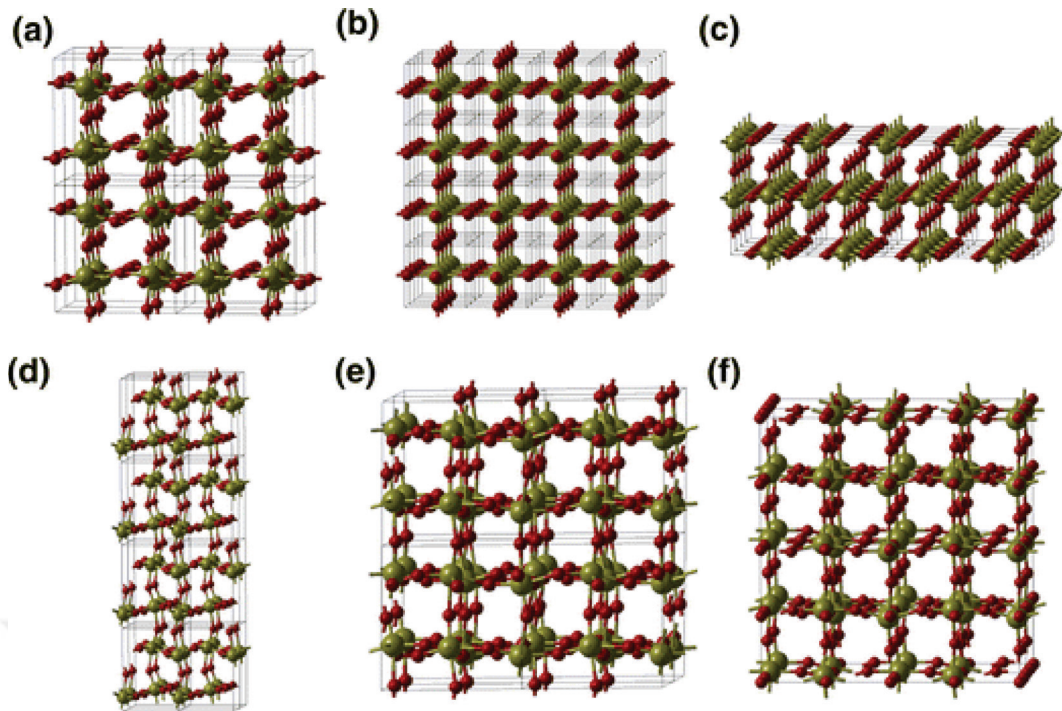


Figure 4.5. Schematic representation of WO_3 structure with different phases. (a) Monoclinic crystal structure of room temperature, (b) simple cubic, (c) tetragonal, (d) monoclinic structure of low temperature, (e) triclinic, and (f) orthorhombic crystal structures. The spheres of green and red colored represent Tungsten and Oxygen atoms, respectively (Wang et al. (2011); Di Valentin et al. (2013)).

deeper levels in the band gap of WS_2 or localized defects with mid-gap discrete energy levels in WO_3 are the source of single photons. This study confirms that single photon emission can be observed at room temperature from a TMDC. To identify the source of the single photon emission reported by these researchers, we studied both WS_2 and WO_3 , separately. Our WS_2 samples did indeed show single photon emission characteristics as reported in the Tran et al. (2017). But, the PL emission from our WO_3 samples show strong single photon characteristics, to our knowledge, this is the first observation of single photon emission from a WO_3 material. The similar single photon emission characteristics with that of WS_2 clearly show that the single photon emission originates from WO_3 but not WS_2 itself.

WO_3 has a wide variety of applications in optical electronics such as smart electronic devices, optical memories and flat panel information displays (Ramana et al. (2006)). Most importantly, WO_3 can be used in chemical sensors via functional activity to various gases (Djerad et al. (2004)). The crystal structure of WO_3 at room temperature is mon-

oclinic as illustrated in Fig.4.5 (a). Annealing at 550 °C leads to hexagonal phase, but it reversibly transformed to monoclinic phase when temperature reaches to room temperature again (Ramana et al. (2006)). WO_3 has different phases under different temperature conditions which are also shown in Fig.4.5. According to the reports, the simple cubic phase structure is the least stable one (Wang et al. (2011)). According to experimental studies, the phase transitions of WO_3 are low temperature monoclinic ϵ -phase from 5 to 278 K, triclinic δ -phase from 248 to 290-300 K, monoclinic γ -phase from 290-300 to 600 K, orthorhombic 600 to 1010 K and tetragonal up to the melting point 1746 K (Cazzanelli et al. (1999a)). The band gap of WO_3 affects from the structure. According to the experimental measurements such as optical absorption (González-Borrero et al. (2010); Granqvist (2000)) and photocurrent (Hodes et al. (1976)), the band gap varies between 2.5 and 3.2 eV.

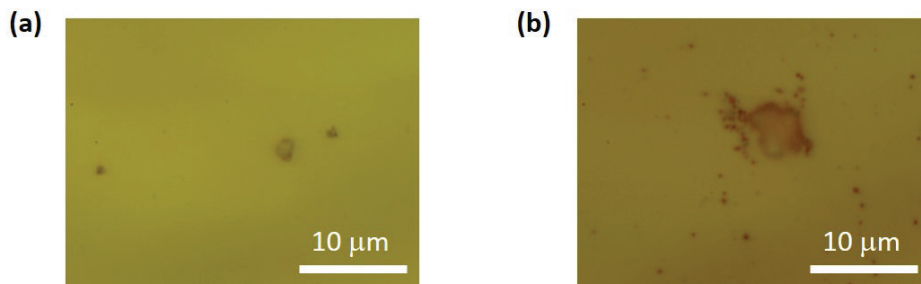


Figure 4.6. Optical microscope images of dropcasted WO_3 particles on a SiO_2/Si substrate. (a) low and (b) high concentration region.

In this study, WO_3 was obtained in the powder form from Sigma-Aldrich with 99.9% purity. The sample preparation method is the same as that for the WS_2 samples given earlier. The WO_3 powder was mixed with equal amount of DI-water and ethanol to obtain $\sim 5\text{mg/L}$ concentration. This solution was vibrated for 10 min and dropcasted on a clean SiO_2/Si substrate, then we let the liquid solution evaporate in the ambient condition. As for WS_2 samples, WO_3 particles was spread on the substrate inhomogeneously. Fig.4.6 (a) shows a region with a high concentration of WO_3 particles while Fig.4.6 (b) shows a low-concentration region. The preparation was similar to the illustration in Fig.4.3 which is for hBN sample preparation. Annealing was also carried out for a set of samples to improve their emission characteristics.

Raman spectrum of a room temperature WO_3 sample gives peaks associated with

the phonons of monoclinic phase (m-phase) (Pecquenard et al. (1998); Daniel et al. (1987)). Fig.4.7 shows typical Raman measurement results of as grown and annealed WO_3 samples. A set of for peaks observed in the spectra clearly indicate the characteristic phonon modes of m phase- WO_3 . The Raman active modes observed at 715 cm^{-1} and 807 cm^{-1} originate from antisymmetric and symmetric stretching vibration modes assigned by $\nu(\text{W-O-W})$ and $\nu(\text{O-W-O})$, respectively (Daniel et al. (1987); Xu et al. (2015)). Other Raman active modes observed at 272 cm^{-1} and 326 cm^{-1} are due to the bending vibrational modes $\delta(\text{O-W-O})$ (Daniel et al. (1987); Xu et al. (2015)). Annealing at $550 \text{ }^\circ\text{C}$ causes more intense Raman peaks indicating the formation of more oxygen-ion vacancies which also changes the optical band gap (Flores-Mena et al. (2012)).

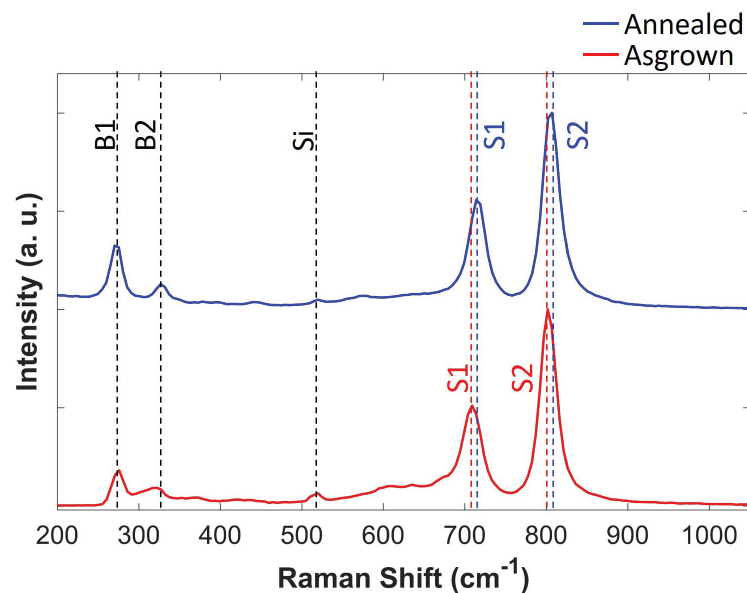


Figure 4.7. Raman spectra of asgrown (red) and annealed (blue) WO_3 samples.

Our Raman analysis of asgrown and annealed WO_3 are shown in Fig.4.7 as red and blue lines, respectively. The peak at 520 cm^{-1} comes from the substrate indicating the fundamental phonon mode of Si. It can be observed because WO_3 is very thin. The Raman peaks of bending vibrational modes are observed at 275.5 cm^{-1} (B1) and 326.9 cm^{-1} (B2) while the stretching vibration modes of asgrown WO_3 are observed at 708.9 cm^{-1} (S1 red) and 801.9 cm^{-1} (S2 red). However, stretching vibration modes of annealed samples are observed at 714.1 cm^{-1} (S1 blue) and 807.2 cm^{-1} (S2 blue) indicating a clear redshift for the annealed samples which is due to the increase in compressive residual

stress (Flores-Mena et al. (2012)). The shifting to lower wavenumbers can occur with the increase of tensile stress (Flores-Mena et al. (2012)).

4.3. CVD-grown Graphene

Graphene is a monolayer of carbon atoms with a honeycomb structure of hexagons. It is the first material experimentally produced and observed in that structure which is atomically thin and almost transparent (Novoselov et al. (2005)). The structure of a single layer graphene is shown in Fig.4.8 with honeycomb-bonded carbon atoms. A single layer graphene absorbs about 2% of incident light (Nair et al. (2008)). Graphene has very high charge carrier mobility (Bolotin et al. (2008)). It has a gapless electronic band structure which leads to frequency-independent efficient interband transitions. These properties makes it an excellent candidate for coupling with fluorescent nanomaterials (Chen et al. (2010)).

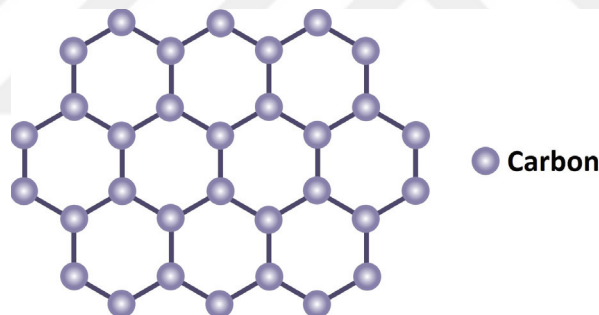


Figure 4.8. Schematic representation of two dimensional structure of graphene.

Such couplings leads to reduction (quenching) in the PL emission intensity of the nanomaterials. This quenching is due to the interaction of nanoparticles with graphene. Some of the excited electrons in the nanoparticles transfer their energies to the valence band electrons of graphene generating electron-hole pairs in graphene. This phenomenon is known as Förster-like Resonance Energy Transfer. In this study, graphene is placed at a near field distance to a single photon emitter (a point defect) in hBN. The optical analyses before and after graphene transfer on the emitter shows static quenching of the PL emission.

4.3.1. Transfer of Graphene onto a Desired Substrate

Single layers of graphene are synthesized on a smooth Cu foil (Mitsui mining and smelting co.) by CVD in a quartz tube which was heated up to 1035 °C under 100 s.c.c.m. H₂ flow. After the temperature was stabilized at 1035 °C flow rate, 10 s.c.c.m. H₂ and 85 s.c.c.m. CH₄ were supplied into the tube simultaneously. The partial pressures of H₂ and CH₄ were 3 and 1.5 Torr, respectively. After 10 minutes of growth at this temperature, the tube was cooled down to room temperature under a 100 s.c.c.m. H₂ flow rate.

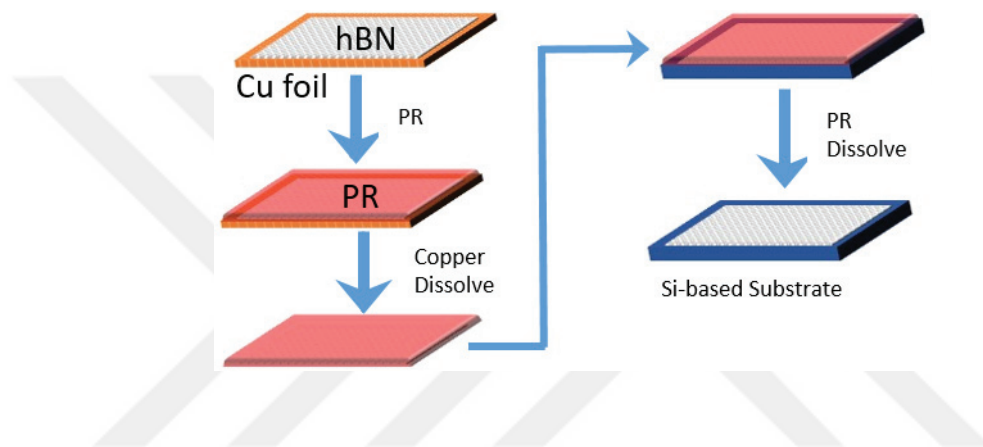


Figure 4.9. hBN transfer procedure from Cu foil to a Si-based substrate

The single layer graphene must be transferred onto a desired substrate to perform the experiments. In the study, a transfer procedure which was reported in the studies of Kocabas Research Group (Polat et al. (2015)) was used for all CVD-grown samples. The brief steps of the procedure are:

1. Dropcast photoresist (S1813) onto the foil and put into the furnace heated up to 60°C for 12-24 hours
2. Etch the Cu foil in H₂O₂:HNO₃:HCL:H₂O solution
3. Rinse the sample by DI and dry it by nitrogen gas
4. Take onto a cleaned Si-based substrate
5. Put them on a hot plate at 80°C during 5-10 min
6. Immerse in acetone
7. Immerse in isopropanol
8. Dry the film by nitrogen gas

The process was optimized for each step. In order to etch Cu foil also Fe₃Cl₂ could be

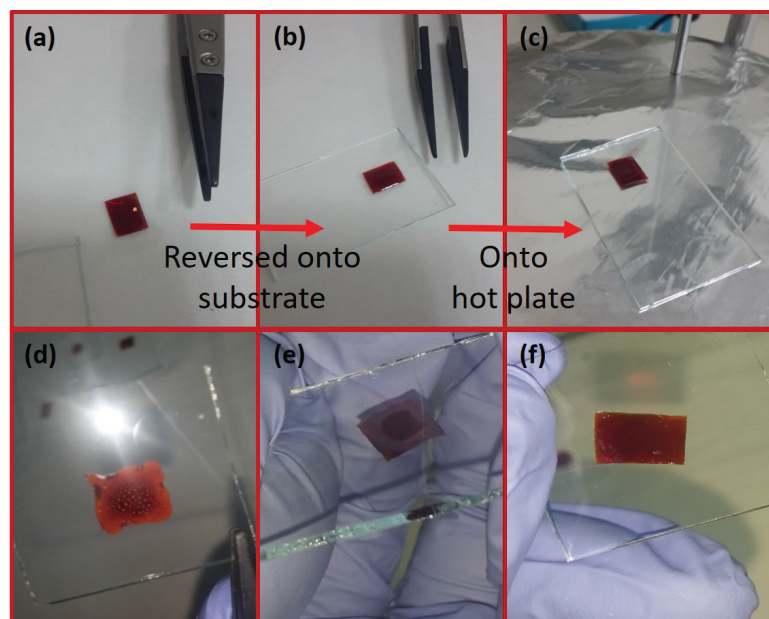


Figure 4.10. Sticking of the graphene/photoresist on glass substrate homogeneously by heating on a hotplate is observed from backside of the glass. (a) After the first 4 steps the Cu foil etched graphene/photoresist. (b) The fifth step of the transfer procedure, put on the substrate. (c) heating on hotplate to slightly liquefaction of the Photoresist. (d) Too much heat, (e) too low heat, (f) appropriate temperature $\cong 80^{\circ}\text{C}$ with fully sticking on substrate.

used. The most important step is heating on the hot plate to stick on the substrate homogeneously. We need to get rid of unwanted preexisting defects created by transfer procedure such as grain boundaries and edges. Because in the study, the single photon emitting defect centers are investigated. Thus, it is very important to succeed an irreproachable and easily replicable transfer procedure. To that aim first we tried the transfer procedure by glass substrate to observe the backside of the glass and photoresist as shown in the Fig.4.10, to confirm homogeneous spread. Then, we performed the procedure by CVD-grown graphene and hBN by silicon substrate.

Fig.4.10 shows the cleaned and etched Cu foil. Then, graphene/photoresist was placed on the glass with the graphene in between the substrate and photoresist (b). The sample was heated on a hotplate to slightly liquefy the photoresist (c). Too much heat ($\gg 80^{\circ}\text{C}$) causes a quick burn of the photoresist (d). Too low heat ($\ll 80^{\circ}\text{C}$) causes partial sticking on the substrate (e). However, the appropriate heating temperature ($\cong 80^{\circ}\text{C}$) results in a full sticking on the substrate. The Raman spectrum of a graphene layer which was transferred on a glass substrate is shown in Fig.4.11. The three most dominant

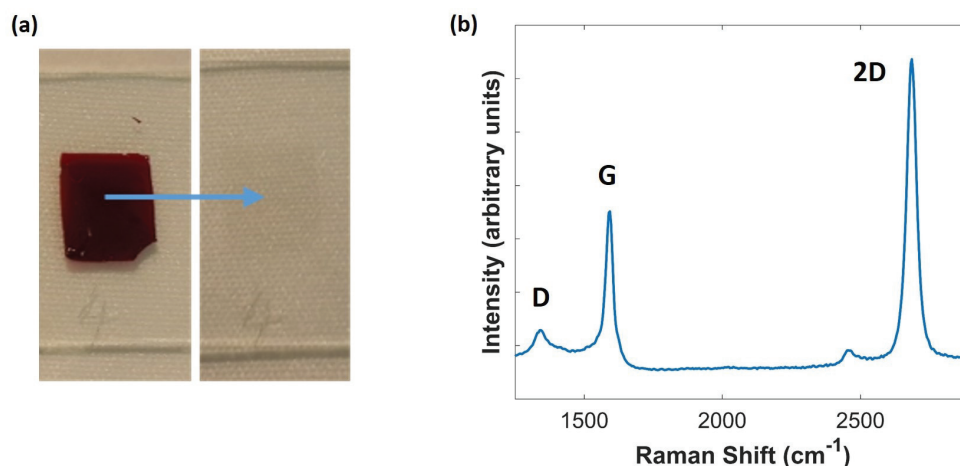


Figure 4.11. (a) On the left before immersed in acetone the photoresist/graphene on glass are shown. On the right after removing the acetone the graphene on glass is seen by slight contrast difference. (b) The Raman spectrum of the transferred graphene layer on the glass substrate.

Raman peaks observed at 1339 cm^{-1} , 1589 cm^{-1} and 2686 cm^{-1} correspond to D, G, and 2D vibrational modes of graphene, respectively. The relative intensity of I_{2D}/I_G is about 0.5 which is an indicator of a single layer graphene structure.

The transfer procedure is also optimized for silicon substrates. We used a few degrees lower and higher temperatures than those used for glass substrates to get a complete and homogeneous sticking on the silicon substrate. The optical microscope images of the transferred samples are shown in Fig.4.12 for low (a), appropriate (b), and high (c) heating temperatures. Only for the heating temperature at about 80°C , full sticking on the substrate is observed. In that case even the edges of a graphene layer was seen very sharp (Fig.4.12).

Lower heating temperatures cause peeling off the transferred flakes from the substrate. Higher heating temperatures, on the other hand, cause burned regions. Additionally, as seen from Fig.4.13 (c, d) the defect-related signal of graphene (D peak), is noticeably more intense than the one that transfer process was performed at appropriate temperature (a, b). Thus, we concluded that the most suitable heating temperature was 80°C heating for 10 min. After that, the substrate was immersed in acetone to dissolve the photoresist which was followed by a few minutes rinse with isopropanol. Then the samples were dried by nitrogen gas as described earlier. In Fig.4.13 (b) and (d), the three most dominant Raman signals observed at 1339 cm^{-1} , 1589 cm^{-1} and 2686 cm^{-1} correspond to D, G and 2D signals of graphene, respectively.

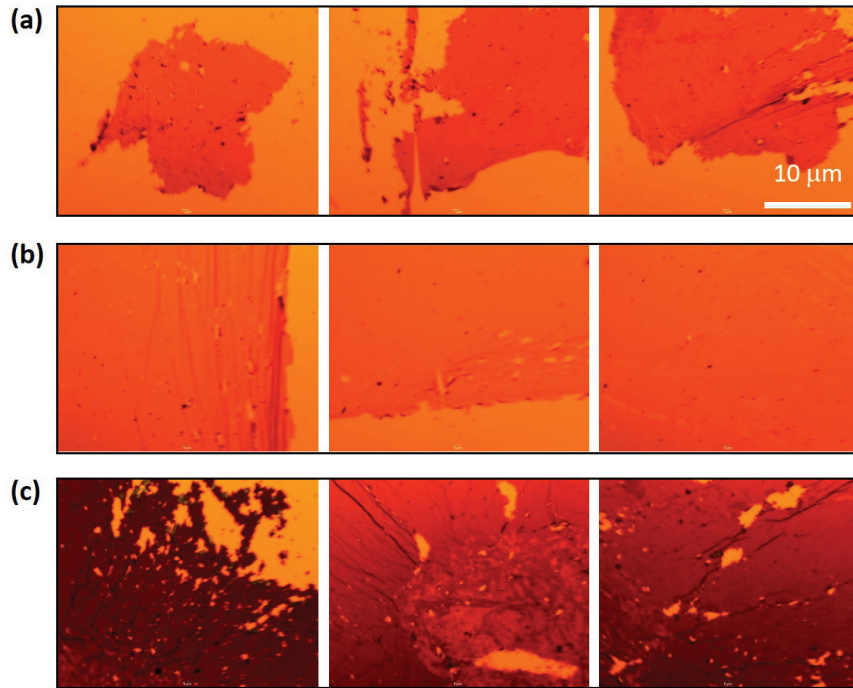


Figure 4.12. The optical images of the transferred graphene layers are given with (a) low, (b) appropriate and (c) high hot plate temperatures.

4.4. Hexagonal Boron Nitrite (hBN)

2D materials offer a promising platform for quantum-optic technologies. Among them hexagonal boron nitride (hBN) has attracted a great deal of attention due to its structural similarities with graphene (Song et al. (2010), Shi et al. (2010)). It is a wide band gap (5.9 eV) insulator. Defect studies reported in the literature mostly comprise of the effects of vacancies and impurity and adsorption atom effects on its electronic and magnetic properties (Liu and Cheng (2007)). Additionally, in 2004, it was discovered that the origin of the luminescence from deformed hBN samples was excitons, and in 2007, it was reported that such defects in hBN were the source of ultraviolet light at room temperature (Kubota et al. (2007), Watanabe et al. (2004), Watanabe et al. (2006)). These developments indicate that hBN is a promising candidate for quantum information technologies, medical applications, quantum communication, and optoelectronic applications.

According to the reports, the luminescence in hBN at about 4 eV originates from impurities, and the one at 5.5 eV originates from stacking faults (Kubota et al. (2007), Watanabe et al. (2006), Museur et al. (2008)). It was found out that the defect centers

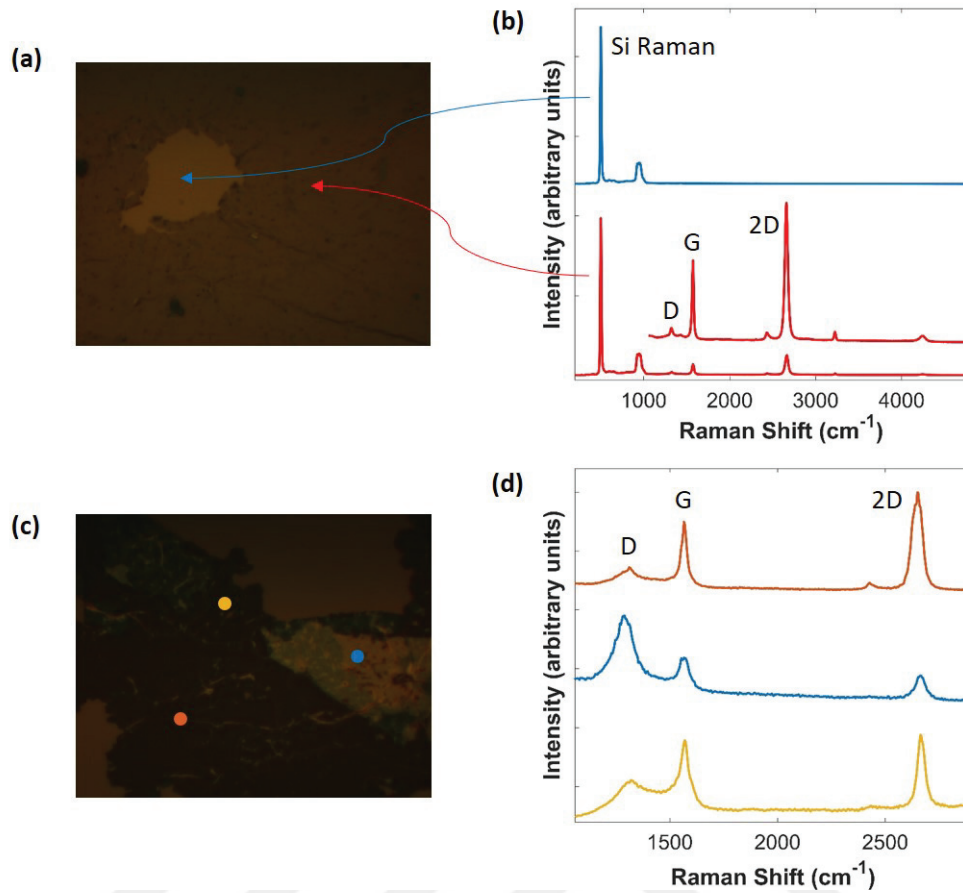


Figure 4.13. (a) The optical image of graphene that transferred by the optimized conditions. (b) Raman spectra belong to single layer graphene and Si. (c) The optical image of graphene transferred at high hot plate temperature on the substrate. (d) Raman spectra of graphene with intense defect signals.

in hBN create discrete energy levels within the bandgap which these behave like atomic energy levels and can be used to generate SPs. Emitters in hBN are associated with boron vacancies (V_B), nitrogen vacancies (V_N), and antisite crystallographic defect ($N_B V_N$) of the lattice, as shown in Fig.4.14. The PL emission observed at 623 nm is thought to be coming from an antisite complex, $N_B V_N$ (Holmes et al. (2014)). Its wide bandgap allows the emissions distributed across an energy range that exceeds 500 meV (Museum et al. (2008)). SP emission from bulk hBN is observed from its optically active defect centers without any pretreatment (Martínez et al. (2016)). However, SP emission from TMDCs such as MoS₂, WSe₂, are obtained at low temperatures, $\sim 5K$. Besides, these materials have gap energies of about 1.3 eV and this obstruct to measure the small excitation. However, defect centers in hBN emits SPs at room temperature.

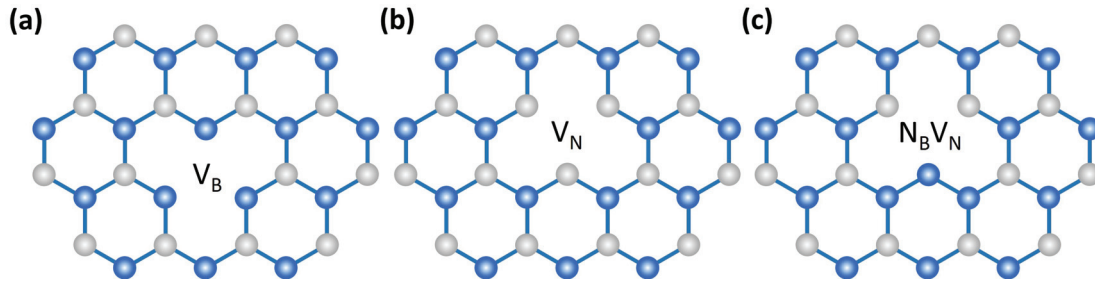


Figure 4.14. Schematic representation of defect types in hBN. (a) Boron vacancy, (b) nitrogen vacancy and (c) an antisite crystallographic defect.

4.4.1. Defect Creation by Electron Beam Irradiation in Bulk hBN

In this study, we wanted to create defect centers by electron beam irradiation to obtain single photon emissions with similar optical properties. Theoretical simulations have demonstrated that boron vacancies act as acceptor whereas boron interstitials or nitrogen vacancies are electron donors (Attacalite et al. (2011); Orellana and Chacham (2001)). Therefore, native or intentionally generated vacancy-interstitial pairs, or the interaction between different kinds of vacancies, could be compatible with the observed donor-acceptor character of the broadband emission. We tried to create defects in hBN by electron beam irradiation in SEM according to the procedures given in the literature. In Fig.4.15, SEM image of an irradiated hBN flake and its PL emission spectrum are shown. In our experiments, electron beam irradiation was performed by 20 keV energy during 20 min. Any stable emission could not be observed for lower exposure times such as 5, 10 and 15 min.

In our experiments, the electron beam irradiation method to create defect centers was a very promising one-step process which does not require a post annealing treatment. The process is very useful. However, there are no reports about whether the electron beam creates new defects or activates preexisting defects that are present in asgrown hBN. Thus, further studies are needed to determine the effect of electron beam irradiation process on creating SPSs in hBN. Additionally, observed emissions were stable just for a few seconds. Therefore, in this thesis we decided to continue with existing optically active defect centers in hBN.

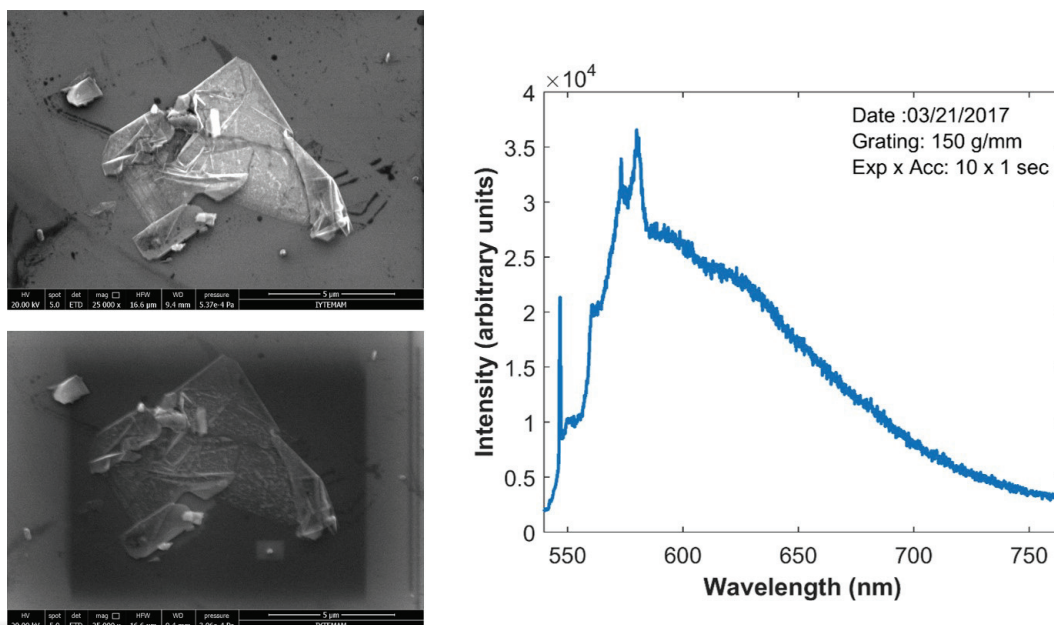


Figure 4.15. (left top) the SEM image of an hBN flake before electron beam irradiation, (left bottom) after electron beam irradiation, (right) after treatment the hBN raman and an emission from defect center in hBN is seen from PL spectra.

4.4.2. Transfer of CVD-grown hBN onto a Silicon-based Substrate

HBN was supplied in multi/single layer forms on copper foil and dispersed in ethanol/water solution from graphene supermarket (Fig.4.16). Commercial single or a few layer hBN films are grown by chemical vapor deposition (CVD) on copper foils as shown in Fig.4.16 (b) and (c). The SEM image shows hBN as wrinkles on top of the copper foil.

The optimized graphene transfer procedure was used to transfer CVD-grown hBN onto silicon substrate as well. Samples were prepared using the main procedure steps with heating temperature of 80°C and lower and higher temperatures were also tried. The samples were analyzed by optical microscopy and Raman spectroscopy after the transfer procedure. Substrates have a 60 nm-thick Al_2O_3 oxide layer to see the optical contrast of hBN on the substrate (Gorbachev et al. (2011)). The optical contrast difference on the silicon substrate was clearly observed, but we could not observe the hBN peak in its Raman spectrum that was expected at about 1369 cm^{-1} (Fig. 4.17).

The multi/single layer hBN Raman signal could not be observed by different ex-

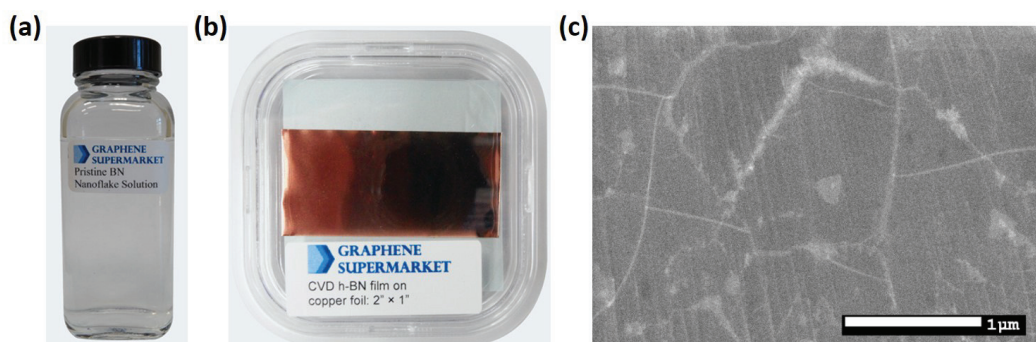


Figure 4.16. (a) HBN flakes in solution. (b) Commercial single layer hBN grown on Cu foil. (c) SEM image of single layer hBN on Cu foil (Graphene-supermarket (2016)).

citation lasers, 532 nm, 488 nm and 633 nm. Fig. 4.17 represents the data collected by 633 nm laser using a 600 gr/mm grating in the monochromator. The thin layers of hBN have very weak Raman signal due to its wide band gap of 5.9 eV. Thus, we need to use a UV laser source, which, unfortunately, does not exist in our set up. This work was first focused on the defects in multi/single layers of hBN as sources of single photons which were needed to make graphene-hybrid nanodevices. However, since we were unable to observe the Raman signal and the single photon emission from the defects was not stable, we changed our sample preparation method. Instead of producing defect intentionally in our lab we used commercially purchased hBN flakes in ethanol/water solution. It was also recently reported that single layer hBN exhibits broad and weak ZPL spectrum whereas multilayer hBN has very narrow and sharp single photon emission (Tran et al. (2015)).

4.4.3. Sample Preparation

A solution containing 1-5 monolayer thick hBN flakes with 50-200 nm lateral-size was purchased (Fig.4.16 (a)) from the company Graphene Supermarket. The solution was dropped directly on a clean substrate and dried in ambient conditions. The preparation is illustrated in Fig.4.3. The substrate had ~ 60 nm Al_2O_3 oxide layer to see the optical contrast of hBN on the substrate (Gorbachev et al. (2011)). These samples were not annealed after dropcasting, because most of the ZPLs which were observed from the hBN flakes were very stable at room temperature. However, most of the reported studies involve annealing processes at about 550 °C for 30 min.

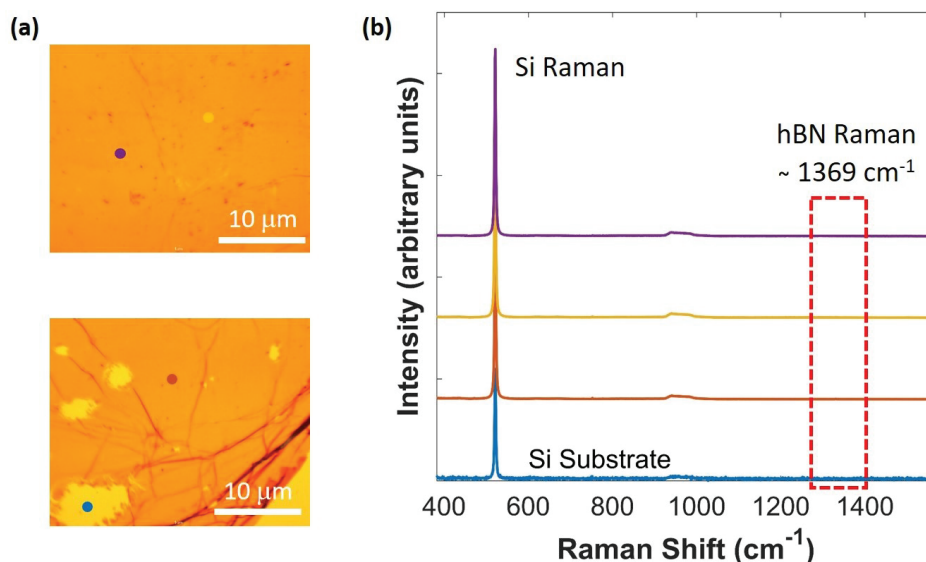


Figure 4.17. After hBN transfer from Cu foil to a silicon substrate Raman Spectrum of the shown images were taken by 633 nm laser. The optical contrast is seen on the optical images, but the hBN Raman signal could not be observed. The Raman spectra were collected from the colored dots on the images and plotted with the same colors shown on images.

In this study, the single photon emission was observed optically active defect centers of hBN flakes. In a typical emission spectrum, the Raman signal of phonons of hBN and Si substrates always accompany the single photon (ZPL) emission along with a PSB peak as seen in Fig.4.18. In figure (b), the peaks at 430 cm^{-1} , 520 cm^{-1} , 1369 cm^{-1} , 1720 cm^{-1} and 2849 cm^{-1} correspond to a ZPL originating from a defect center under laser beam, Si Raman signal, hBN Raman signal, PSB $\sim 160\text{ meV}$ away from the ZPL and a secondary PSB $\sim 160 + 140\text{ meV}$ away from the ZPL, respectively.

After observing strong and stable single photon ZPL emission from hBN, a graphene layer was transferred on the hBN flake to observe a static quenching of the single photon emission by Förster resonance energy transfer. Thus, depending on the distance between the defect center in hBN and the graphene layer, the emission energy was non-radiatively transferred to the graphene layer. Analyses of these experiments are based on the graphene Raman signals, D, G and 2D, besides hBN and Si Raman signals. In Fig.4.20, the inset is an optical image of the graphene layer on hBN flake. As seen, hBN is under the graphene edge, thus half of it is under the graphene and the other half is not. The spectrum includes peaks at 520 cm^{-1} , 1369 cm^{-1} , 1589 cm^{-1} and 2686 cm^{-1} 3300 cm^{-1} which are Si Raman signal, hBN Raman signal, D and G Raman signals of

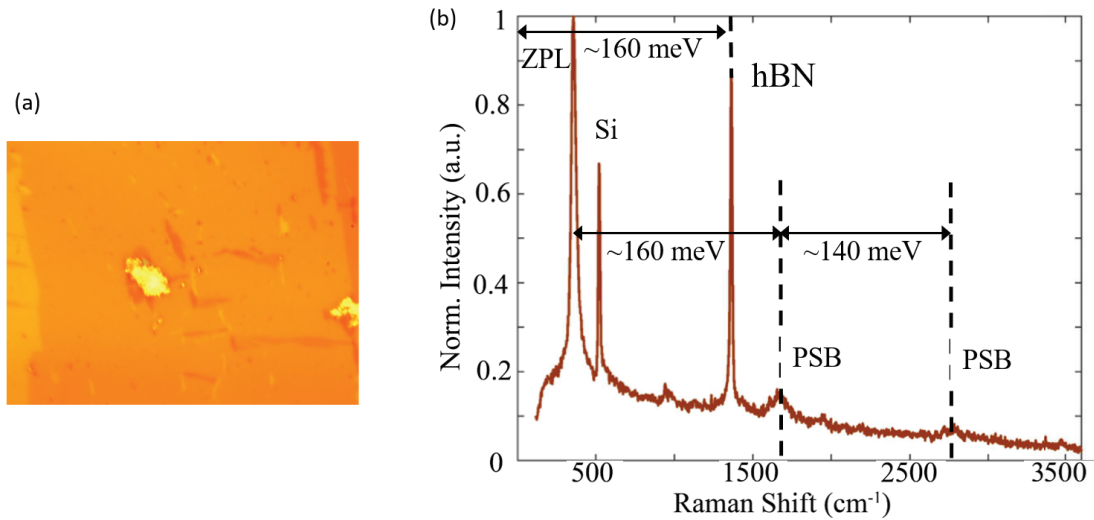


Figure 4.18. (a) Optical image of a hBN flake by 50x magnification (b) Raman shifts of silicon substrate and hBN as well as zero-phonon line emission with phonon sidebands from a single defect.

graphene layer, respectively. The last peak is a ZPL from a defect center.

First we analyzed the optically active defect centers in hBN flakes. We recorded the coordinates of the position of defects on the substrate on a XYZ scanning table under the microscope of our Raman/PL set up. The coordinates of a defect center under the laser beam were adjusted for the observation of most intense ZPL peak. We identified about 50 different defect centers from different hBN flakes on the same substrate, a thin graphene layer was transferred by using the transfer procedure explained in the previous sections. All the pre-analyzed defect centers were analyzed again with under the same optical conditions and exposure times. In that way, we compared the data before and after graphene transfer to observe the quenching of the single photon emission. For some of the samples, this cycle was repeated by a second and a third layer graphene. In Fig.4.20, a second layer graphene transferred sample is shown, representatively. On the edges the first and second layer can be differentiated by contrast difference.

We compared the effect of graphene near a defect center on observed ZPL emission from a defect centers in an hBN flake. However, it is known that the stress of the graphene due to the hBN flake height and thickness leads to break the graphene and causes wrinkles around the flakes. This affects the structural and optical properties of graphene and coupling efficiency with the emission.

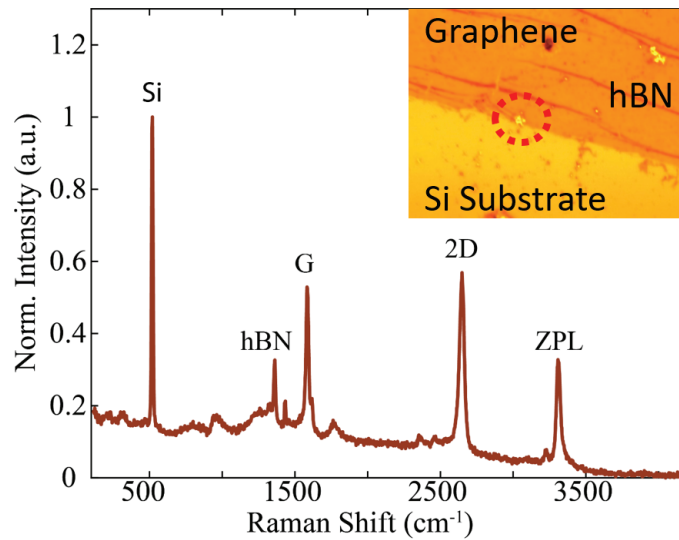


Figure 4.19. The Raman active modes of graphene, 2D and G are seen in spectrum. In the inset optical image of graphene and an hBN is shown.

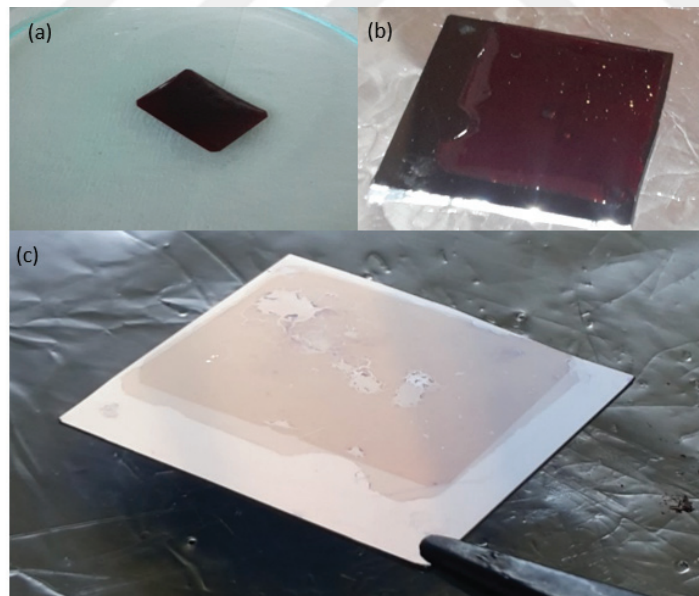


Figure 4.20. (a) Photoresist on graphene and Cu foil immersed into the acid solution to dissolve Cu foil. (b) Photoresist on graphene is placed onto the Si substrate which already have a layer of graphene and heated on hotplate. (c) Two layer graphene transferred on Si substrate is seen with some wrinkles and holes.

4.5. Summary

In this chapter, the experimental setup including Raman spectroscopy, photoluminescence and Hanbury Brown Twiss interferometry is explained. The general spectroscopic characteristics of WS_2 and WO_3 samples used in the study were also examined with their preparation techniques in detail. After that, optimization of a general 2D material transfer procedure was carried out. 2D materials are generally grown by a CVD technique on Cu foils. To integrate them with electronic chip applications as in optoelectronics, photonics etc. They need to be transferred from Cu foil to a suitable substrate, most generally a Si-based one. In this work, we optimized a successful transfer procedure for graphene. We characterized the graphene before and after its transfer by optical microscope and Raman microscope. This procedure can be used for other 2D materials that have similar layered structure with graphene. Thus the procedure was performed on a few layers of hBN grown on Cu foil by CVD, although optical contrast is observed the Raman signal of hBN by 532 nm and 633 nm laser excitations could not be observed. This is because of the wide bandgap of hBN (~ 5.9 eV). Thus, dropcasted hBN flakes were used in this study. The general spectroscopic characteristics of hBN and hybrid graphene-hBN samples were also examined along with their preparation techniques as well.

CHAPTER 5

SINGLE PHOTON EMISSION FROM DEFECTS IN WO₃ AND PLASMON EFFECT

Alternative room temperature single photon sources are under intense investigation such as transition metal dichalcogenides (TMDCs) as layered materials (Tran et al. (2017)), lead halide perovskite quantum dots (PQDs) (Utzat et al. (2019)), graphene quantum dots (Zhao et al. (2018)), and gallium nitride (GaN) (Berhane et al. (2018)). The origin of the emission over a wide temperature range from cryogenic to room temperature generally results from discrete energy levels generated by the defect (color) centers within the band gap of the material (Wong et al. (2015)). Therefore, the emission can be observed in a wide spectral range from the ultraviolet to the visible region (Tran et al. (2016)). So far, defects in materials such as diamond, ZnO, SiC and hBN have been extensively studied (Kurtsiefer et al. (2000); Neitzke et al. (2015); Gordon et al. (2013)). However, spectral diffusion of the observed emission from defects in hBN limits the photon coherence time, which increases the minimum line widths obtained in the photoluminescence measurements and makes the sequential photon emissions to be indistinguishable (Sontheimer et al. (2017)). Therefore, investigation of alternative materials has been accelerated in recent years. Among these, the most investigated materials are TMDCs such as MoSe₂, MoS₂, WSe₂ and WS₂, which are widely studied for use in many optoelectronic applications (Srivastava et al. (2015)). TMDCs have unique band structure features with a large bandgap, non-equivalent valleys and adjustable optical properties (Dong et al. (2017)). In addition, the ability to observe strong Zeeman shifts is important in potential photon indistinguishability applications (Aharonovich et al. (2016)). The observed single photon emission is due to localized (Frenkel), weakly bound excitons (Tonndorf et al. (2015)). Excitons can be trapped into potential wells as a result of vacancy defects, impurity atoms, or local stresses, thereby increasing radiation stability (Raj and Tripathi (2019); Rosenberger et al. (2019)). Due to the small exciton binding energy of these materials, single photon emission can be observed at cryogenic temperatures only which limits their practical applications (Aharonovich et al. (2016)). However, a study has been reported on increasing the single photon emission temperature up to 160 K by interaction of TMDCs with plasmonic nano-cavities (Luo et al. (2019)). Another method of observing single

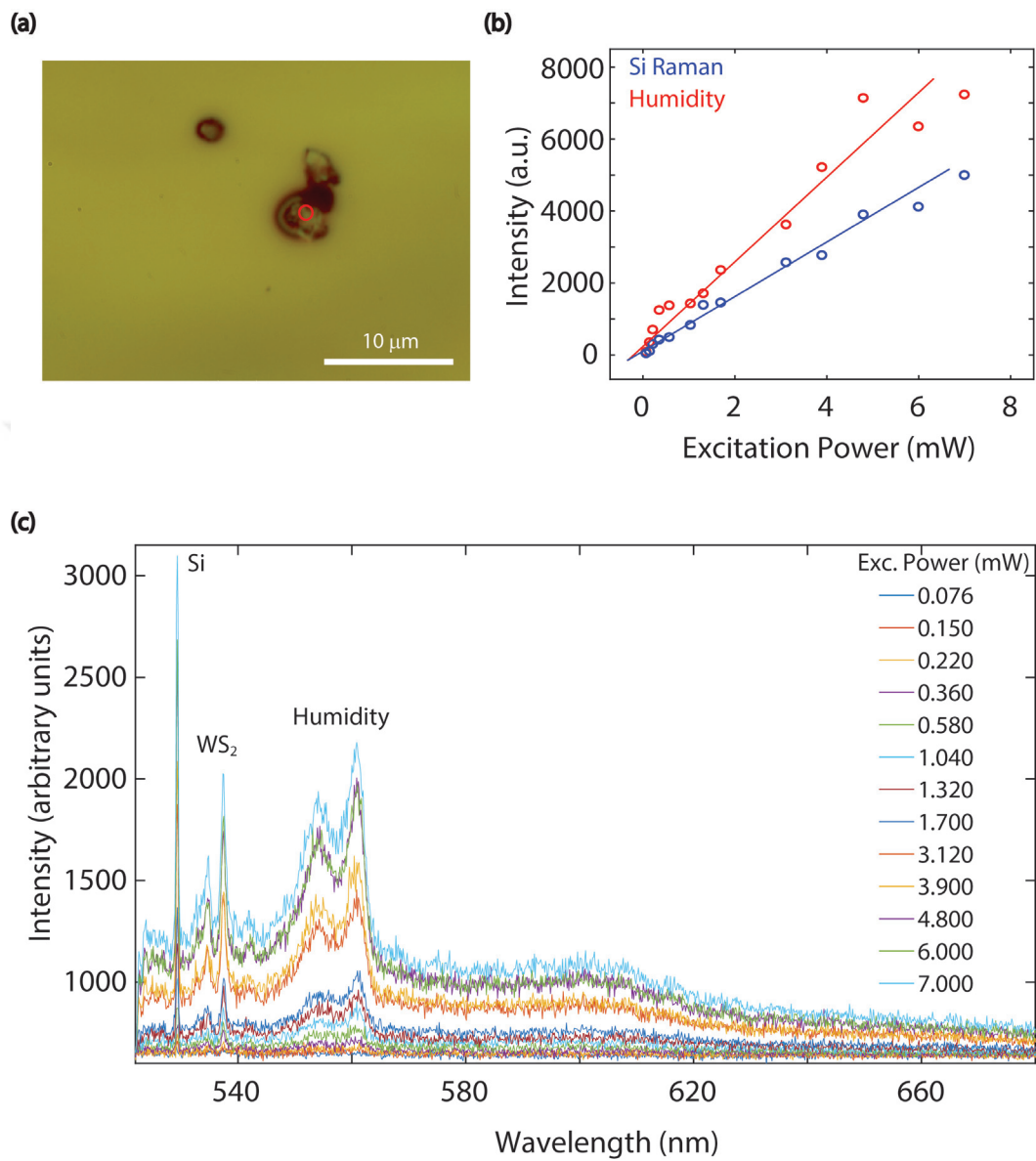


Figure 5.1. (a) Optical image of a WS₂. The red circle represents the laser exposure spot where the spectra are recorded. (b) Excitation power dependent intensities. (c) Excitation power dependent spectra. The intensities are increasing by increased power.

photon emission at room temperature is creating covalently bound oxygen or sp^3 defects (He et al. (2017); Ma et al. (2015)). Accordingly, in a recent study, it was reported that single photon emission was observed from WO_3 defects occurred after thermal annealing of WS_2 (Tran et al. (2017)). It is seen that TMDCs can be a single-photon source at room temperature and the necessity of new studies in this field has been demonstrated.

In this study, first it is clarified that the main source of the room temperature emission is defects in WO_3 itself, not the trapped excitons of WS_2 host material. We showed that efficient and stable fluorescence at room temperature is obtained from localized single defect centers of annealed WO_3 . Then, the structural and optical characteristics of observed localized emission from WO_3 are studied. To increase the brightness and detectability of the emission we introduce gold nanoparticles as plasmonic resonators for weakly coupling with the individual color centers (Nguyen et al. (2018); Iff et al. (2018); Hoang et al. (2016)). The resulting emission enhancement which is about $\sim 10^5$ times, can be clearly demonstrated. The results are promising for the future applications of single photon emitters in WO_3 for both TMDC hosts and integrated nanophotonic and plasmonic devices. To further clarify the source of the single photons in WO_3 , we also carried out a computational investigation of the most promising color center candidates using a density functional theory (DFT) approach. We were able to obtain a good agreement between the experimental observations and DFT computations for the characteristics of defect states in WO_3 . Our results contribute to a better understanding of source of the room temperature emission from the defect centers in WO_3 .

5.1. Single Photon Emission from Defects in WS_2

The dropcasted WS_2 samples were prepared on SiO_2/Si substrates according to the procedure given in the previous chapter. First, a single photon analysis was carried out on as-grown (before annealing) samples. Optical image of a typical WS_2 flake on a Si substrate is shown in Fig.5.1 (a). The red circle indicates the laser exposure spot on the flake from where the data were collected. Fig.5.1 (b) shows emission spectra of the same flake taken from three different spots. As we see, there are two peaks besides the characteristic Raman peaks of WS_2 and Si substrate, which correspond to the OH-O and W-OH bond vibrations observed at 554 nm ($\sim 1405 \text{ cm}^{-1}$) and 561 nm ($\sim 1630 \text{ cm}^{-1}$), respectively. These peaks are not of single photon emission but they originate from humidity related bonds (Misra et al. (2015)).

To avoid confusion, the excitation power dependency of the spectra were recorded

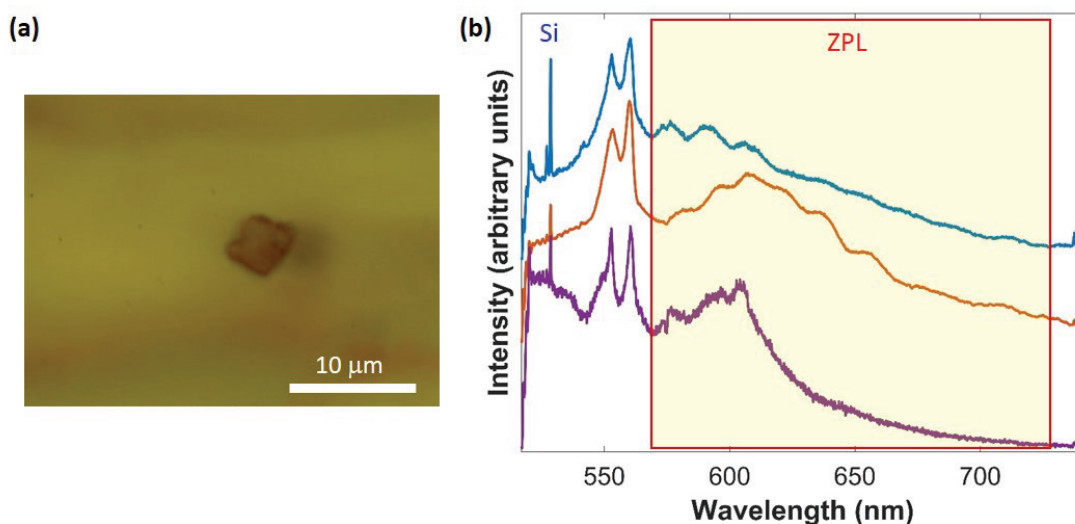


Figure 5.2. (a) Optical microscope image of as-grown WS_2 flake. (b) Unstable single photon emission shown in red frame.

as shown in Fig.5.1 (b-c) where a 514 nm excitation laser was used. Peak intensities plotted with respect to the excitation power must saturate if the light is due to a PL emission originating from the defect levels in the band gap of WS_2 while the intensities of Raman peaks increase linearly with no saturation. However, as seen in Fig.5.1 (c), the peak intensities increase linearly for both the humidity (blue dots) and the Si substrate (red dots) related peaks. Thus, it can be concluded that these peaks are Raman signals but not photoluminescence originating from defect states.

The peaks recorded from an as-grown WS_2 flake which is shown in Fig.5.2 (a) were observed from the defect centers in the flake and they were very unstable and indistinguishable (Fig.5.2 (b)). It was clearly understood that these peaks (encircled by a red frame), were a combination of peaks at different wavelengths ranging from 570 nm to 800 nm. During the measurement the line shapes of these peaks were changing instantly. Thus, we concluded that it is not possible to carry out further analyses on these samples to characterize these peaks to confirm their single photon behavior. To improve the stability we decided to anneal the samples at 550 °C for 30 min (which were found out as the optimum parameters for stability after a brief survey of a range of temperature and duration parameters) to stabilize the defect structures giving rise to single photon emission. Annealing is a common method to obtain stabilized emission from defect centers. The results of Raman spectroscopy measurements after annealing the dropcasted WS_2 flakes are

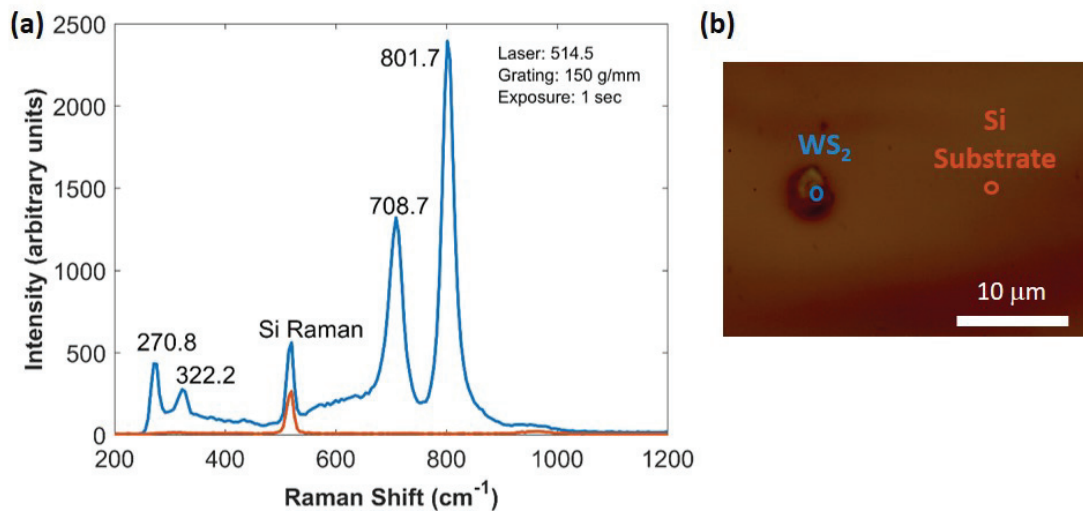


Figure 5.3. (a) Raman Spectra of Si substrate and annealed WS₂ are shown. (b) Optical image of a WS₂ flake on Si substrate.

shown in Fig.5.3 (a) which were recorded from the green point in the optical microscope image in (d).

Fig.5.4 (a) shows an emission spectrum of such annealed samples (S1, S2 and S3) each with a different ZPL transition (Tran et al. (2017)) while the second order correlation measurements shown in Fig.5.4 (b) clearly indicate their single photon nature. After annealing, the emission spectra of our samples were similar to those reported in the literature. An example of such a spectrum is given in Fig.5.4 (c) for an annealed sample which was collected from the green spot shown in Fig.5.4 (d). The observed Raman peaks in Fig.5.4 (c) are those of WS₂. Fig.5.5 gives the emission spectra of the same sample spot for two different excitation wavelengths of the Ar laser in our set up namely, 524 and 488 nm lines. The spectra were plotted in the absolute energy scale to see the Raman modes shifting with the excitation wavelength while PL signals remaining stationary due to their energies depending only on the energy differences between the excited and the ground states of the defects with no dependency on the exciting photon energy (as long as it is big enough for such an excitation). The broad PL peak in the highlighted region is very similar to the red peak shown in Fig.5.4 (a). The vertical dashed lines indicates the positions of the Si Raman signal which was observed at 528.12 nm with 514 nm laser while at 500.7 nm with 488 nm excitation wavelength (both of which correspond to about 520 cm⁻¹ Raman shift).

The linearly polarized emission behavior is another indication of the single pho-

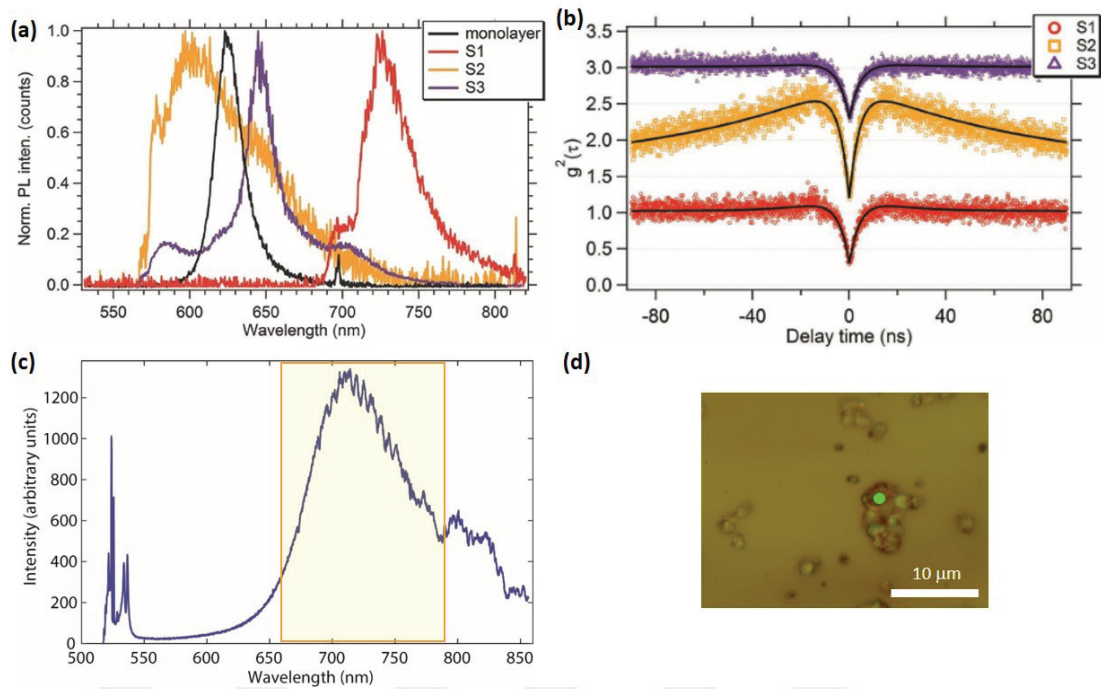


Figure 5.4. (a) The Photoluminescence spectra were recorded from three individual spots. The black line belongs to the spectrum of monolayer WS_2 (Tran et al. (2017)). (b) Second order correlation measurement results. (c) Photoluminescence spectrum taken from the green point on (d). The spectra were recorded by 514 nm CW excitation. (d) Optical image of a WS_2 flake on Si substrate.

ton emission. Polarization dependencies were obtained for both excitation polarization and emission polarization measurements. The excitation polarization dependency of the intensity of a single photon emission peak is shown in Fig.5.6. Each data point in the figure was obtained from the maximum intensity position of a PL spectrum of the same defect at a polarization angle of the incident light.

5.2. Single Photon Emission from Defects in WO_3

After a series of comprehensive studies with WS_2 , it was necessary to show that PL emissions indeed originate from WO_3 defect phases in WS_2 flakes as reported in the literature Tran et al. (2017) based on their XPS analyses. For that reason, we carried out similar studies on annealed WO_3 flakes as well. The annealing were carried out at 550 °C for 30 minutes (which is the same as that for the WS_2 samples).

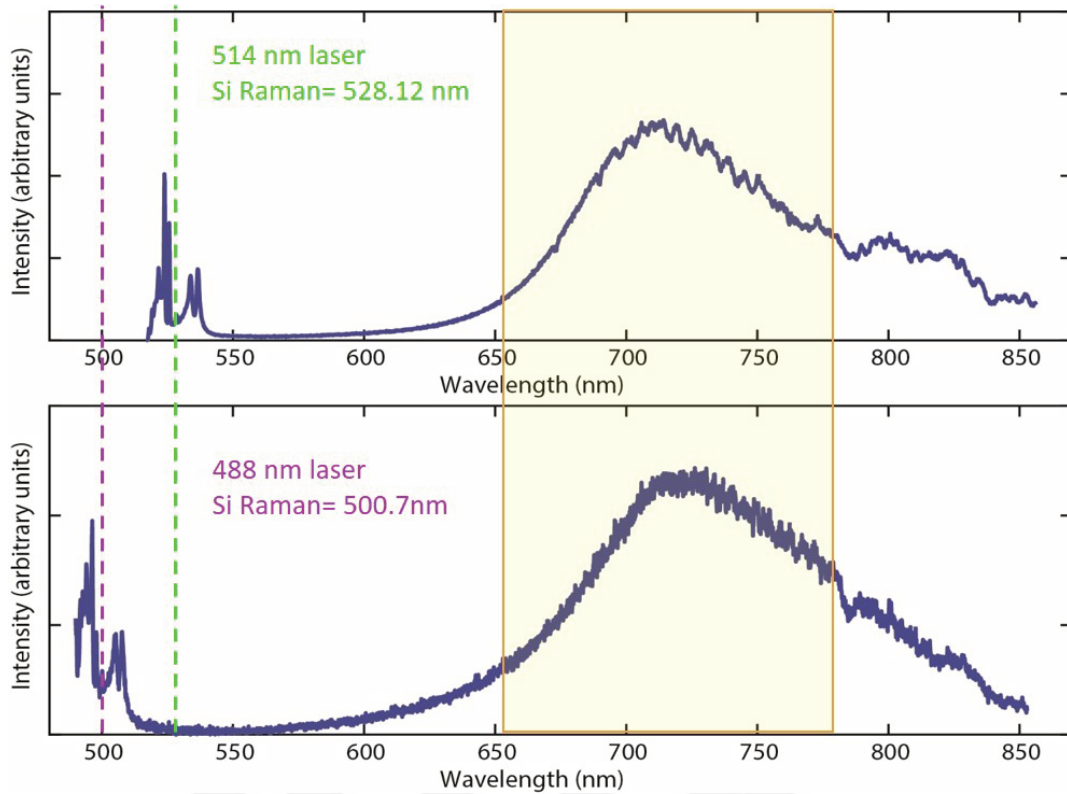


Figure 5.5. Photoluminescence spectra from a defect center in annealed WS₂ flake on Si substrate were recorded by 514 nm (above) and 488 nm (below) excitation wavelengths.

A typical WO₃ flake on Si substrate is shown in Fig.5.7 (a). The green dot indicates the laser exposure spot on the flake where the data was taken from. As seen in Fig.5.7 (b), the green spectrum recorded from the flake in (a) has two peaks besides the Raman peaks of the WO₃ flake and the Si substrate. These are Raman peaks corresponding to the OH-O and W-OH bond vibrations observed at 554 nm ($\sim 1405 \text{ cm}^{-1}$) and 561 nm ($\sim 1630 \text{ cm}^{-1}$), respectively. As before, they are humidity related peaks with no single photon nature (Misra et al. (2015)). The other colored spectra were recorded from different flakes which do not show humidity peaks. The spectra in Fig.5.7 (b) were recorded using the 514 nm laser. To prove the humidity peaks are indeed Raman signals but not PL, we also used the 488 nm excitation. The spectra of the same spot for both excitations is shown in Fig.5.7 (c). Clearly all Raman peaks follow the exciting laser energy while PL emission remains stationary on the absolute energy scale. Hence the above mentioned humidity peaks are indeed Raman peak not originating from any defect states.

A PL spectrum recorded from an annealed WO₃ flake on a Si substrate is shown

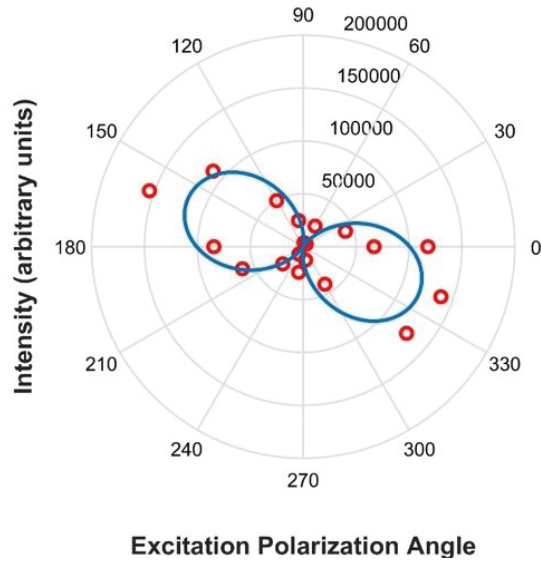


Figure 5.6. The excitation polarization and emission intensity of defect center.

in Fig.5.8 (b). The yellow highlighted broad peak is very similar to the yellow PL peak in Fig.5.8 (a) reported by Tran et al. (2017) from annealed WS_2 samples. The dotted yellow arrow shows the similar two peaks which are the yellow data in (a) and the data in yellow frame (b). The Ref. Tran et al. (2017) claims that the broad and bright peaks originate from WO_3 defect phases in annealed WS_2 . In contrast, the data recorded in our studies were directly taken from WO_3 flakes (such as that given in Fig.5.8 (b)). Hence, our measurements taken directly from WO_3 confirms the claim of Ref. Tran et al. (2017). That indeed the reported single photon emission comes from the defects in WO_3 but not from WS_2 . By comparing the yellow spectrum of Fig.5.8 (a) and our data in Fig.5.8 (b) we can identify the small peak on the left edge of the PL emission in Fig.5.8 (a) as a humidity peak as mentioned above.

The phonon side band (PSB) transitions associated with the single photon emission (ZPL) have energy differences equal to the energy difference between the vibrational levels of the system. These are four dominant phonon modes of WO_3 observed at 99.5 meV, 88 meV, 40 meV and 33.6 meV in their Raman spectra and called as phonon side bands (PSBs). In Fig.5.9, we identified the positions of these PSBs. Even though these PSBs do not show well resolved peaks they cause broadening a broadening in the PL signal.

Optical properties of the broad and bright emission from a defect center in WO_3 flake (Fig.5.8 (b)) was analyzed and shown in Fig.5.10. The two dimensional PL map

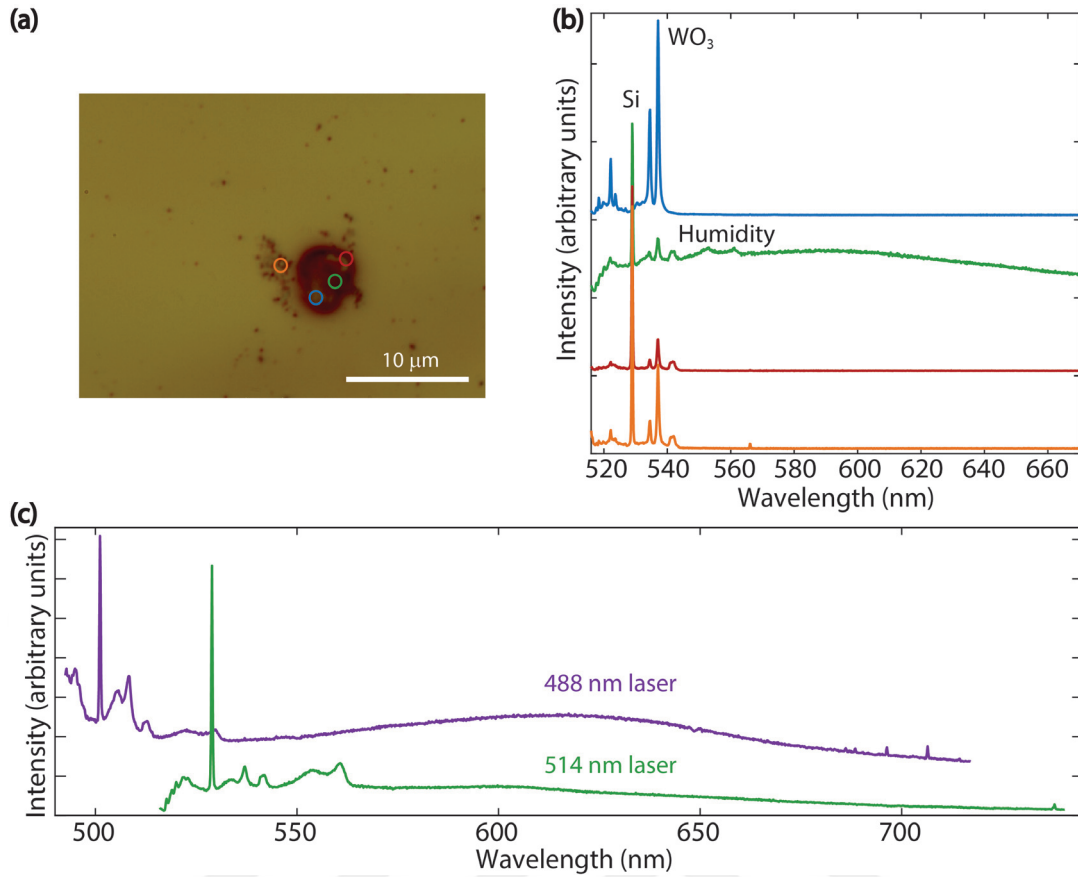


Figure 5.7. (a) Optical microscopy image of a typical WO_3 flake on Si substrate. The colored dots represent the points where the same colored spectrum shown in (b) were recorded. (b) WO_3 PL spectra recorded from four different points of the flake. (c) The green spectrum in (b) which has humidity peaks, excited by 514 nm laser (green) and 488 nm laser (purple).

of the WO_3 flake and its optical microscope image are shown in Fig.5.10 (a) and (b), respectively. The brightest (most intense PL) spot on the map refers a localized emission from a single defect center. Furthermore, dipole properties of the emission was also characterized in terms of excitation (black) and emission (red) polarization dependencies (Fig.5.8 (c)) at room temperature. The linear polarization dependency indicates single dipole behavior. The experimental data can be fitted to a theoretical calculation given by the following equation for a linearly polarized light (Fig.5.8 (c), solid lines):

$$I = I_B + I_0 \cos^2(\theta + \theta_{offset}) \quad (5.1)$$

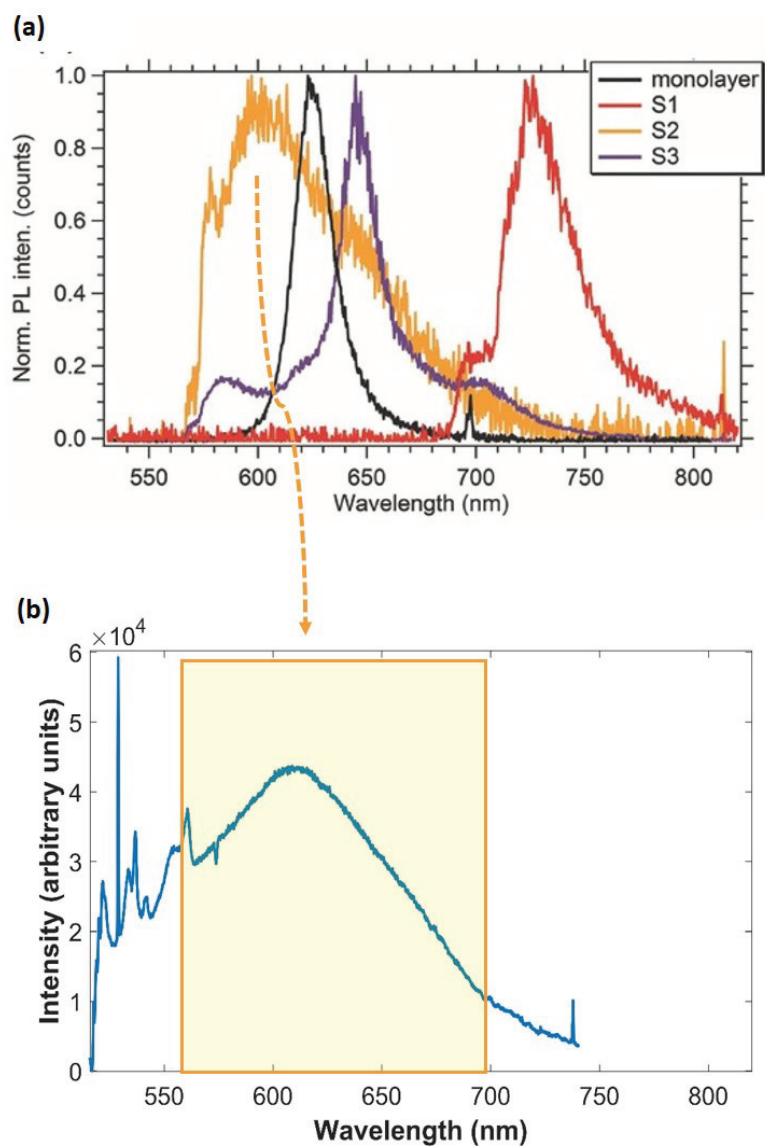


Figure 5.8. (a) The Photoluminescence spectra were recorded from three individual spots. The black line belongs to the spectrum of monolayer WS₂ (Tran et al. (2017)). (b) PL spectrum from an annealed WO₃ flake on Si substrate. The data in yellow frame is very similar to the yellow data which was reported in literature from WS₂.

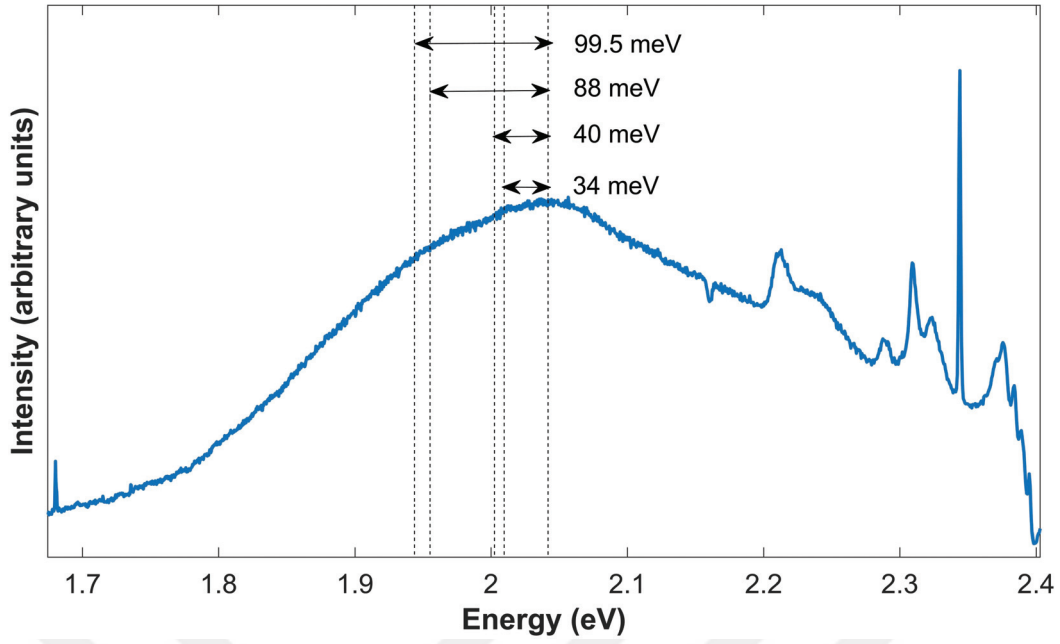


Figure 5.9. Single photon emission (ZPL) from a localized defect center in WO_3 and its phonon side bands.

where I_B and $I_B + I_0$ are the minimum and maximum values of the PL intensity, θ corresponds to excitation polarization angle and θ_{offset} is the angle corresponds to the maximum emission intensity. The spectra which were used to extract the polarization versus emission intensity relation graph in Fig.5.8 (c) were recorded under the saturation excitation power value which is less than 1 mW.

Additionally, the excitation power versus emission intensity saturation relation is seen in Fig.5.8 (d). The red and black dots belong to experimental data and the solid lines extracted from the theoretical fits using the relation which was described in Chapter 2 in detailed,

$$I = I_{\infty} \frac{P}{P_{sat} + P} \quad (5.2)$$

where I_{∞} , P_{sat} are the emission rate and excitation power at saturation, respectively. The spectra which were used to extract the excitation power versus emission intensity relation shown in Fig.5.8 (d) were recorded under the excitation polarization of maximum intensity. The position of the laser spot on the sample was optimized via the XYZ stage control to observe the maximum intensity of the emission. Silicon Raman peak intensities

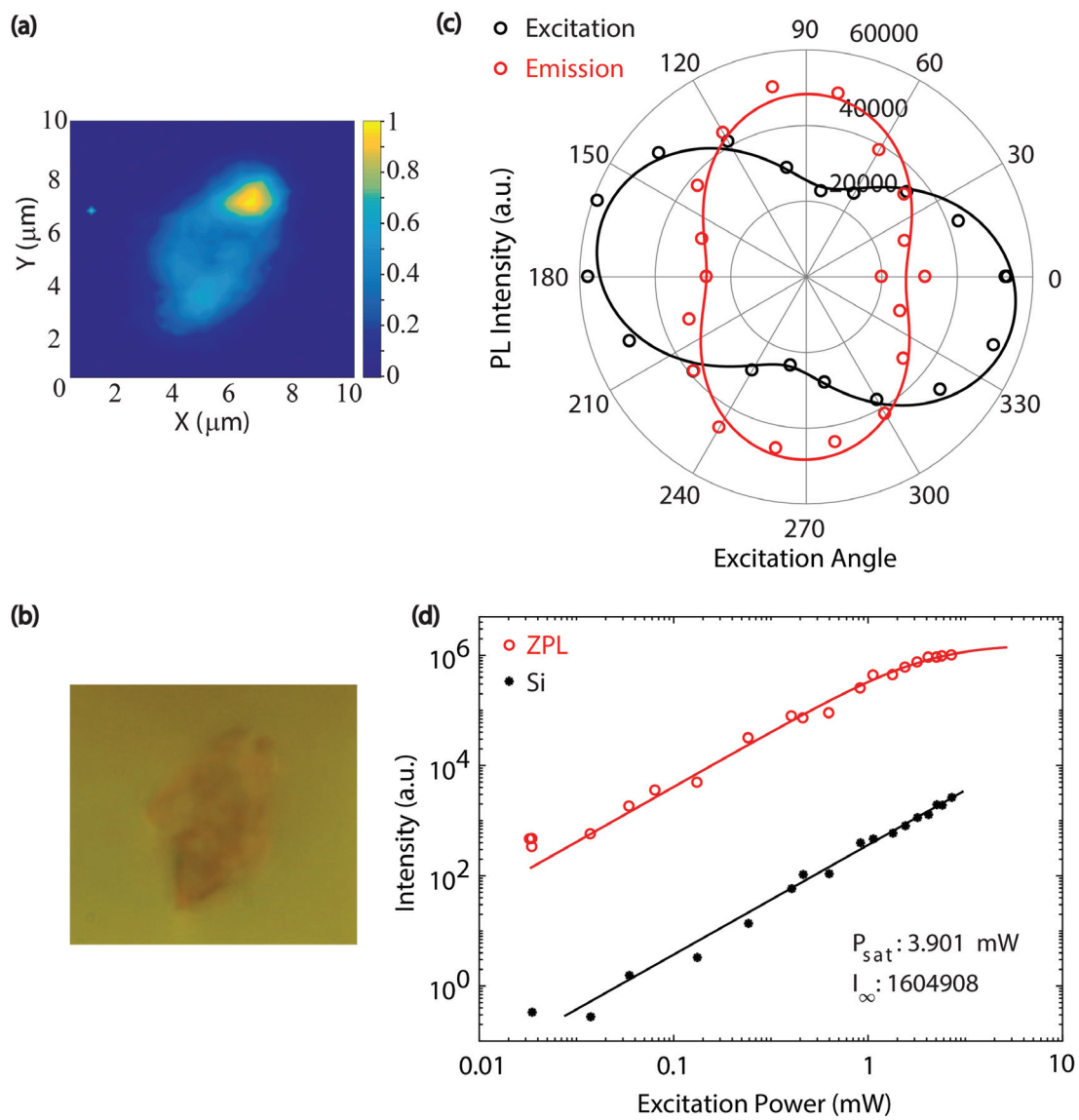


Figure 5.10. (a) 2D PL map and (b) optical microscopy image of the WO_3 flake on Si substrate. (c) Excitation (black) and emission (red) polarization dependent intensity variation. (d) Excitation power dependent intensity variations of the single photon emission (red) and Si Raman (black).

were extracted from the same spectra recorded for each excitation power values. The Si Raman intensities are linearly increasing, while the emission intensities saturates after excitation power of 3.9 mW. This is another indication of the emission obtained from discrete energy states in the band gap of WO_3 .

5.3. First Principles Calculations on Oxygen Defect in WO_3

The structural properties of WO_3 has important effect on electronic and optical properties. To better understand and explain the structural, electronic, optical properties and defects for a many-electron system, density functional theory (DFT) calculations are very useful and common method. In that way, to solve the Schrödinger equation and obtain the wave function of the system some approximations must applied. Then, the allowed energy states of the system also can be determined.

The Born-Oppenheimer approximation which was put forward by Max Born and J. Robert Oppenheimer in 1927 (Born and Oppenheimer (1927)), reduces the number of degrees of freedom hence reducing the computation time greatly. In this approximation since the mass of nuclei are greater than that electron's, the nuclei are assumed to be static and classical particles. After that the interaction between the electrons should be reduced from N -electron system to one central electron system. To that aim one of the approximations methods is the DFT method. In this method, electron density which has three degrees of freedom is a function of space and time. Hence, the dimension of N the interacting electron, $3N$, can be reduced to 3. This approach mainly makes the calculations easier.

The electron density based theorem was formulated by Hohenberg and Kohn in 1964 (Hohenberg and Kohn (1964)). According to their theorem, all of the ground state properties of a system can be determined by electron density and the total ground state energy of the system is a functional of the density. The Schrödinger equation of the system is described by these approximations and the total energy is obtained in terms of ion-electron potential energy, ion-ion potential energy, electron-electron energy, kinetic energy and the exchange-correlation energy. The kinetic energy, and the exchange-correlation energy are the most difficult terms to calculate. Thus, these are the key factors in DFT. The interaction of two electrons is described by an anti-symmetric total wave function which produces an exchange energy. The exchange energy is defined by Pauli exclusion principle. To define exchange energy there are various functional approximations. The most known ones are Local Density Approximation (LDA) and Generalized Gradient Approx-

imation (GGA). LDA assumes the exchange correlation energy is uniform and electron gas of the density for each part of system is divided into infinitesimal volumes (Ceperley and Alder (1980)). However, LDA is not a good approximation for rapidly varying electron densities. Within GGA approximation, gradient of the electron density is included to deal with these systems. The total energy functional is defined by both electron density and its gradient which are called semi-local functionals (Perdew et al. (1996)).

In this section, the emission which was characterized as single photon emission by excitation polarization and power dependent intensity behavior is also explained by DFT calculations. Based on the results of our DFT calculations we can confidently claim that the observed single photon emission in WO_3 originates from defect states within the band gap of WO_3 .

5.3.1. Structural and Electronic Properties of WO_3

In order to determine the single photon emission originating from in-gap defect states, the DFT based first-principles calculations were performed for WO_3 crystal with and without oxygen defects. It is well known that oxygen vacancies are the most common

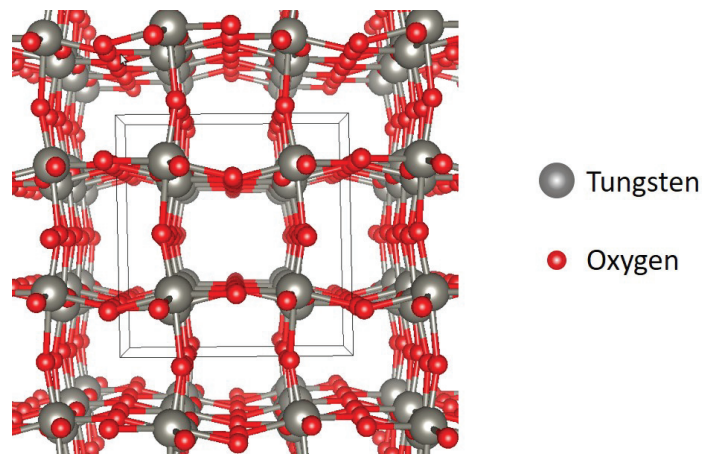


Figure 5.11. The room temperature monoclinic structural model of WO_3 .

form of native defects in any oxide compounds. As discussed in the previous sections, WO_3 crystal structure has several phases depending on the temperature range (Matthias and Wood (1951); Diehl et al. (1978); Loopstra and Boldrini (1966); Cazzanelli et al.

(1999b); Kehl et al. (1952)). In this thesis study, the experimental observations were performed mostly at room temperature. Thus, the DFT based calculations were also performed for room temperature phase of WO_3 which is monoclinic crystal structure (RT- WO_3) with space group $\text{P2}_1/\text{n}$. Fig.5.11 illustrates optimized atomic structure of the crystal. The unit cell contains 8 tungsten and 24 oxygen atoms. The lattice parameters a , b , c and β are found to be 7.53 Å, 7.68 Å, 7.83 Å, and 90.3, respectively. Additionally, Bader charge analysis indicates that each tungsten atom donates 0.9 e to oxygen atoms.

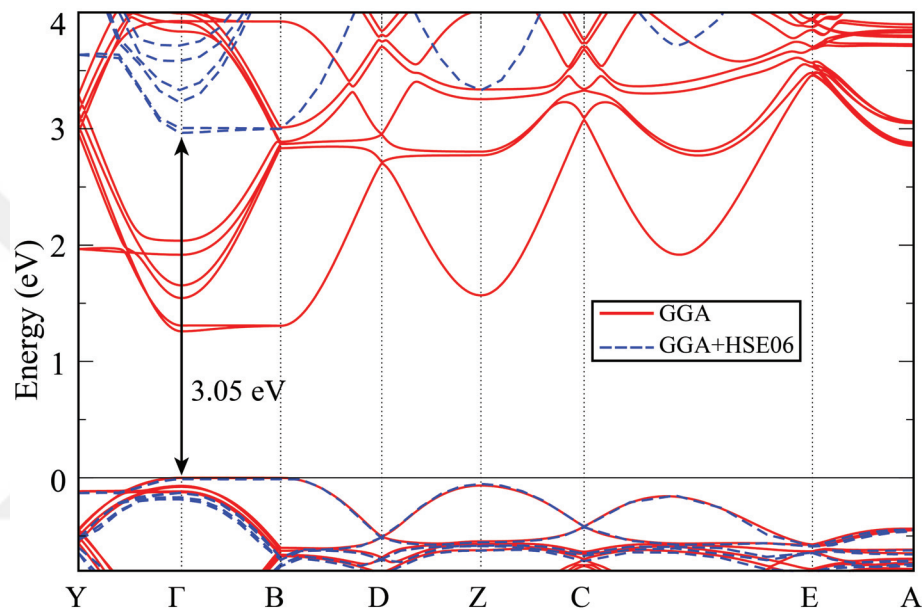


Figure 5.12. The electronic band dispersion of RT- WO_3 . Red lines belong to calculations performed by GGA, and blue lines refer to HSE06 approximation added.

We first calculated the electronic band dispersion curves of RT- WO_3 to confirm the reliability of our method. The results of the calculations are shown in Fig.5.12. The calculations based on GGA show that the crystal produced a direct band gap of 1.29 eV at the Γ point. It is known that bare-GGA based calculations underestimate the experimentally observed band gaps which should be over 3 eV for WO_3 . Therefore we included a correction functional, that is HSE06, in our calculations to obtain more precise electronic band gaps. The hybrid functional calculations including the HSE06 correction yielded a band gap energy of 3.05 eV, which is satisfactorily close to the experimentally observed band gap (Koffyberg et al. (1979); Bringans et al. (1981)).

5.3.2. Vibrational Properties of WO_3

To reveal the nature of the measured Raman modes, we also investigated the vibrational properties of RT-monoclinic WO_3 in detail by DFT based calculations. The phonon band dispersions were calculated using the small-displacement method as implemented in the PHONOPY code. A $2 \times 2 \times 1$ supercell was used for the phonon band structure calculations of the crystal. The calculated Raman modes of the crystal are shown in Fig.5.13 with red vertical lines. As seen in the figure the four calculated prominent Raman active modes are very well compatible with the experimentally observed Raman peaks of RT- WO_3 .

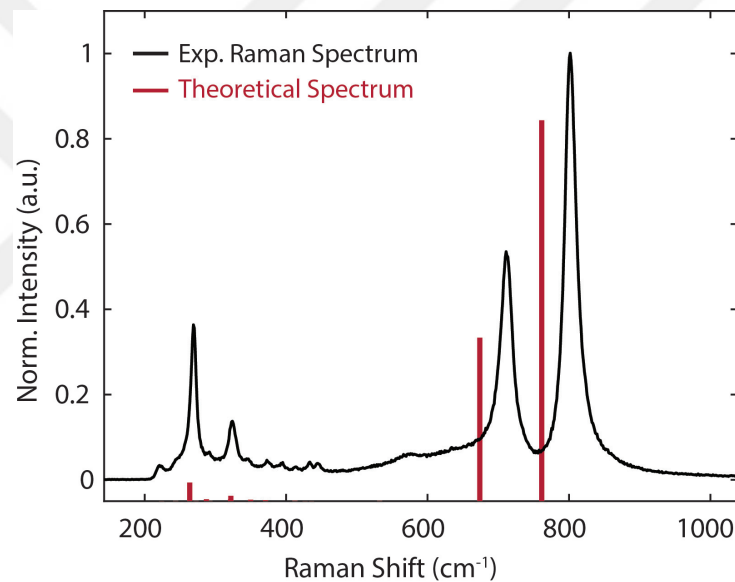


Figure 5.13. Experimental Raman spectrum of RT-monoclinic WO_3 and calculated Raman activities are shown with black and red lines, respectively.

The agreement with the experimental results is almost perfect for the two low energy phonon modes while the method underestimates the position of the high energy Raman modes by about 25 cm^{-1} as seen in Fig.5.13. The reason for this high energy discrepancy in the calculations is most probably due to the fact that while the calculations were carried out for zero K lattice temperature, but the actual Raman measurements were performed at room temperature. It is well known that unharmonic effects become quite important at high energies thus yielding smaller energies for the higher energy vibrational

states than the lower ones. Thus, we can claim that high energy Raman modes are effected more at high temperatures than the low energy ones. Hence, this is the reason of the observed difference.

5.3.3. Structural and Electronic Properties of Oxygen Vacancy in WO_3

Native defects such as host atom vacancies, antisite defects and foreign atoms always exist in all materials to some extent and they affect the electronic and optical properties of the material. Thus, investigation of their effects has importance in many material-based applications, especially for the single photon sources. In RT- WO_3 oxygen vacancy is considered to be energetically much more favorable than other type of point defects. Hence, we wanted to see if oxygen vacancies would indeed yield defect states in the band gap of WO_3 in our calculations. In order to investigate the effect of O vacancies a $2 \times 2 \times 1$ supercell of WO_3 is used. Fully optimized geometric structure of such a supercell of WO_3 crystal in the presence of a single O atom vacancy is shown in Fig.5.14 (a) and (b). The missing O atom is along the \vec{a} direction is shown in Fig.5.14 (a), while it is along the \vec{b} direction in (b). As shown in the figure, the W atoms closest to the removed atom move in the opposite direction away from the vacancy. Compared to the defect-free crystal, when O atom is removed the lattice parameters a and b increase by 0.4% and 3.6%, respectively, whereas the lattice parameter c decreases by 2.9%. Moreover, the β decreases to 90.1.

In order to properly describe the electronic structure of WO_3 with O vacancy defect, the PBE and HSE06 methods are used together. Due to a very high number of atoms for a proper supercell (the supercell with an oxygen vacancy must contain hundreds of atoms to avoid structural changes), electronic energy dispersion curve calculations were not computationally possible. Thus, we carried out calculations only for the electron density of states for the WO_3 crystal with oxygen vacancies. At the right panel in Fig.5.14 the calculated partial density of states of WO_3 crystal with O defect are shown. It is seen that formation of different O vacancy defects in WO_3 leads to several midgap states that are not seen in the defect free calculations. It is calculated that the defect energy levels are located above the VB maximum in the range of 1.74-3.05 eV (712-406 nm) and 1.33-2.7 eV (932-459 nm) for the O vacancy defects positioned along \vec{b} and (b) \vec{a} directions, respectively.

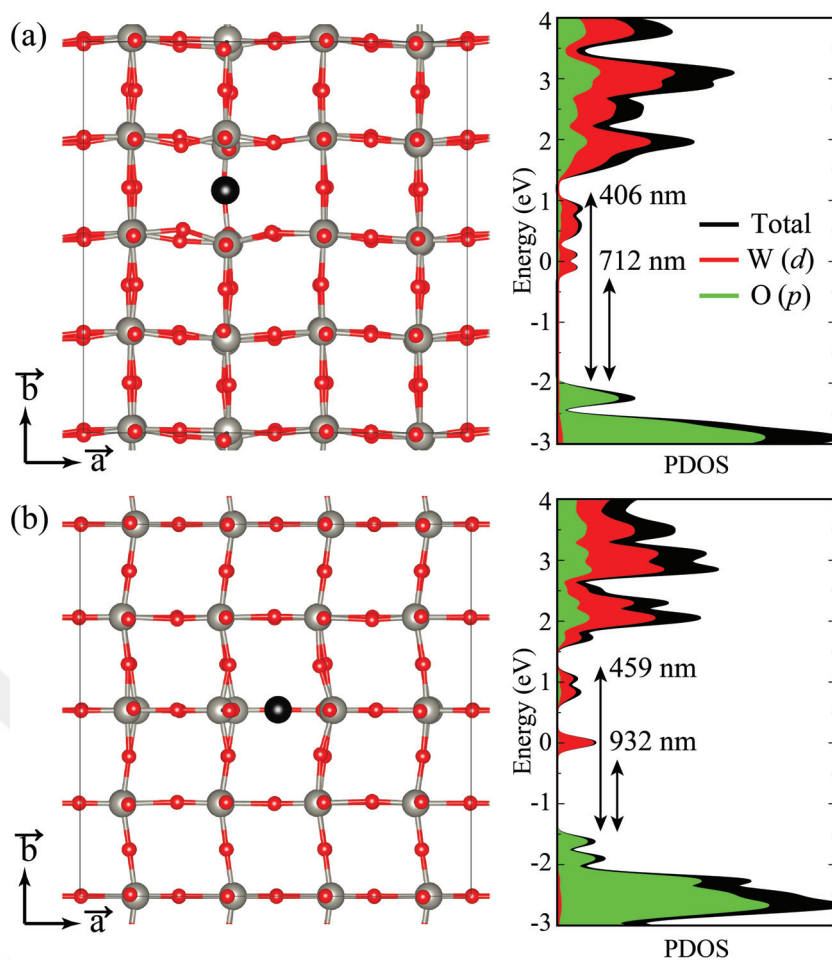


Figure 5.14. On the left, top views of an oxygen vacancy defect structure in $2 \times 2 \times 1$ supercell, and on the right partial density of states (PDOS) of RT- WO_3 with oxygen vacancy defect structures are given. On the left, the structures of (a) O vacancy along \vec{b} and (b) \vec{a} directions are shown. The black atoms are the removed oxygen atoms.

5.4. Low Temperature Optical Characteristics of WO_3

Low temperature optical characteristics of WO_3 and luminescence from defect centers were analyzed in this section. First, phase transition around -140°C of WO_3 was observed by photoluminescence measurements. After that, single photon emission from defect center in WO_3 was analyzed with respect to varied temperatures. Temperature of the samples were varied down to -195°C from room temperature in a Linkam THMS 600E cooling stage (see in Fig.3.3) for the optical measurements which were explained in this section.

5.4.1. Low Temperature Raman Spectroscopy Analyses of WO₃

According to the experimental studies, the reported phases of WO₃ are as follows; monoclinic ϵ -phase from 5 to 278 K, triclinic δ -phase from 248 to 290-300 K, monoclinic γ -phase from 290-300 to 600 K, orthorhombic 600 to 1010 K and tetragonal up to the melting point 1746 K (Cazzanelli et al. (1999a)). Accordingly, energy band structure of

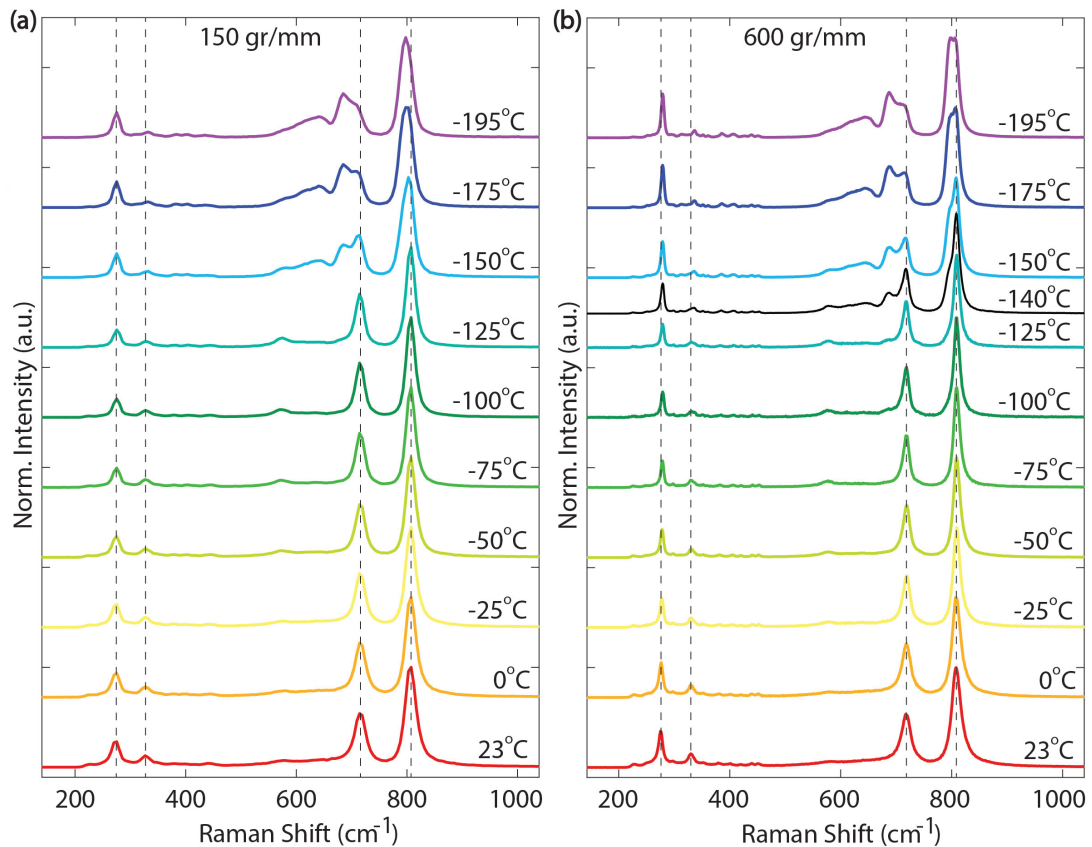


Figure 5.15. Temperature dependent Raman spectra of an annealed WO₃ flake. (a) Raman spectra were recorded by 150 gr/mm and (b) by 600 gr/mm.

WO₃ varies with phase variations with changing temperature which eventually leads to changes in electronic properties. The RT phase is monoclinic with a bandgap of 2.80 eV while the structure becomes the low temperature monoclinic phase under -140 °C with a 3.14 eV bandgap energy which was also calculated using a HSE06 hybrid density functional in the DFT method (Di Valentin et al. (2013)).

Fig.5.15 summarizes our temperature dependent Raman measurements from the

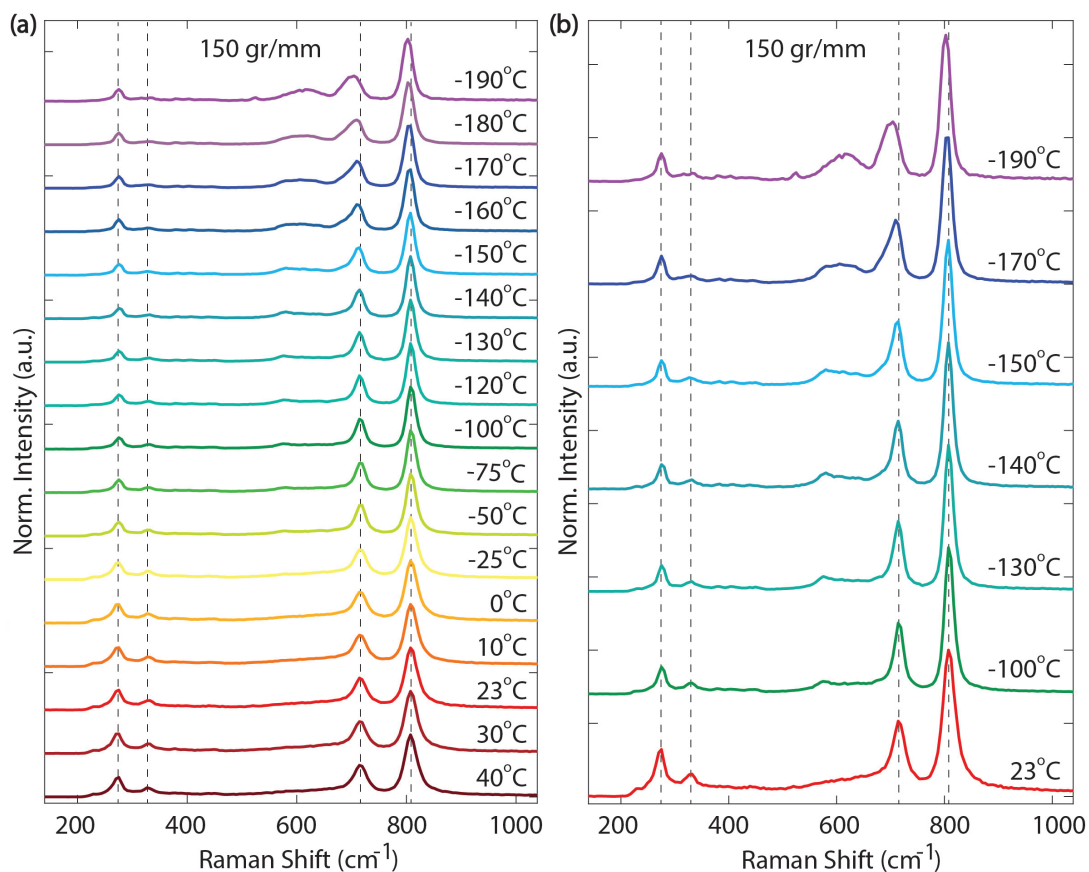


Figure 5.16. Temperature dependent Raman spectra of an annealed WO₃ flake. (a) Raman spectra were recorded by 150 gr/mm and (b) the selected spectra.

annealed WO₃ samples with varying temperatures starting from 23 °C down to -195 °C. Clearly a phase transition at temperatures below -140 °C sets in modifying the observed Raman spectra which indicates a transition to the low temperature monoclinic phase as stated earlier. The Raman peaks observed at 714.3 cm⁻¹ and 807.5 cm⁻¹ originate from antisymmetric and symmetric stretching vibration modes; $\nu(\text{W-O-W})$ and $\nu(\text{O-W-O})$, respectively (Daniel et al. (1987); Xu et al. (2015)). As temperature goes below -140 °C, these peaks split and shift as seen in Fig.5.15. (We note that, the data in Fig.5.15 (a) were recorded using a 150 gr/mm grating while a 600 gr/mm grating was used for those Fig.5.15 (b)). The phase transition at -140 °C is seen more clearly from the black colored spectrum in Fig.5.15 (b). The peak centered at 807.5 cm⁻¹ at RT was shifted down to 797.7 cm⁻¹ when the temperature was cooled down to -195 °C. Also, the measurements performed with the 600 gr/mm grating revealed more detailed features. The peak at 808 cm⁻¹ is split into two components at 805.6 cm⁻¹ and 797.3 cm⁻¹ which

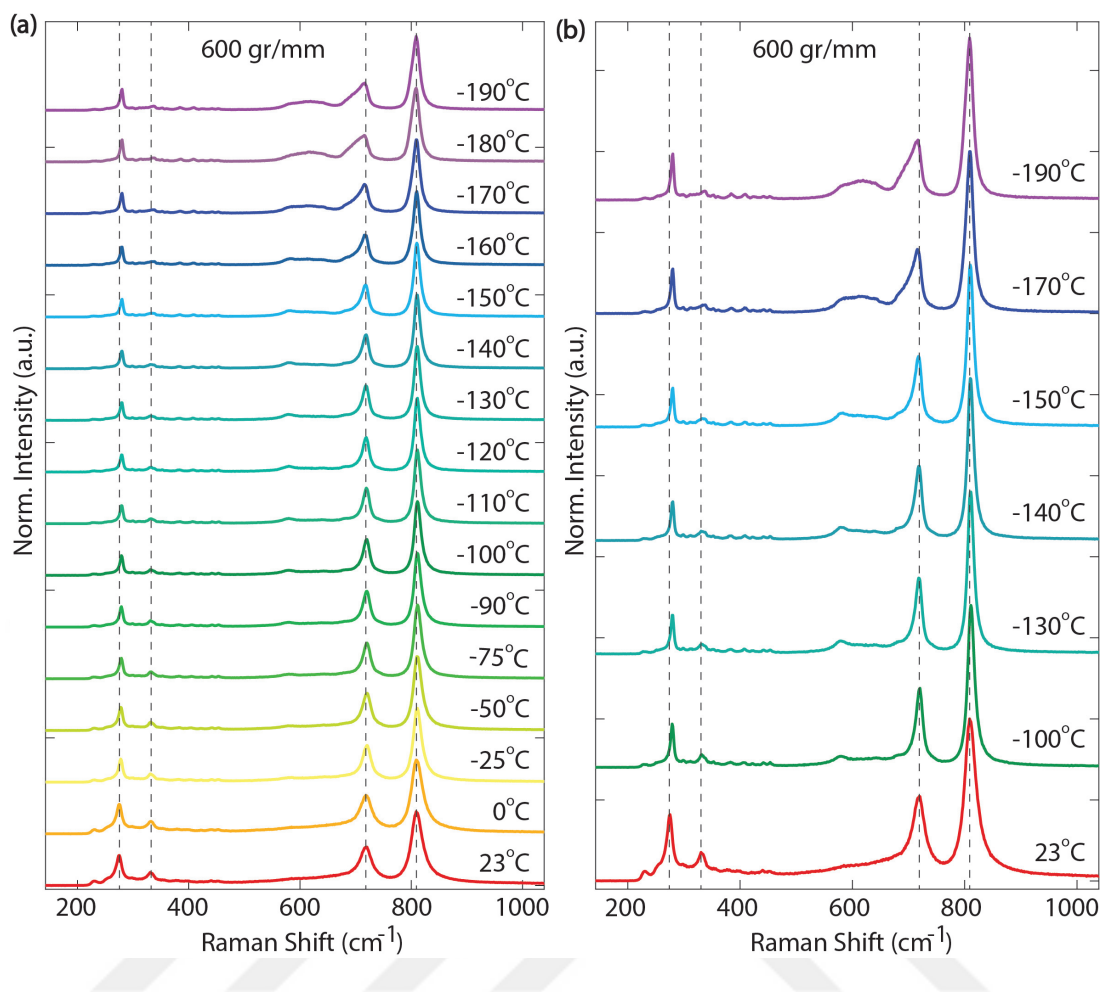


Figure 5.17. Temperature dependent Raman spectra of an annealed WO_3 flake. (a) Raman spectra were recorded by 600 gr/mm and (b) the selected spectra.

was only seen as a broadening in the spectra taken with the 150 gr/mm grating. The peak at 714.3 cm^{-1} was observed at RT by 150 gr/mm, and it split two peaks at 709.4 cm^{-1} and 684.7 cm^{-1} below the transition temperature. However, this peak was observed at 717.4 cm^{-1} (the difference is possibly due to a calibration error in the 150 gr/mm measurements) and it was split into two different peaks at 717.4 cm^{-1} and 687.4 cm^{-1} below the transition temperature. Additionally, a new peak at 640 cm^{-1} was showed up at -195°C . In the 600gr/mm measurements, this peak was observed at 642.8 cm^{-1} . The other two RT Raman active modes observed at 275.2 cm^{-1} and 326.7 cm^{-1} are the bending vibrational modes $\delta(\text{O}-\text{W}-\text{O})$ (Daniel et al. (1987); Xu et al. (2015)). In 150 gr/mm measurements, the peak at 275.2 cm^{-1} does not shift, whereas it shifts to 279 cm^{-1} in 600 gr/mm measurements (Fig.5.15 (b)) below the transition temperature. The bending vibrational mode at 326.7 cm^{-1} shifted to 331.9 cm^{-1} while somewhat losing its intensity

after the phase transition. In 600 gr/mm measurements, this is seen at 330.4 cm^{-1} and shifted to 336.7 cm^{-1} below $-140\text{ }^{\circ}\text{C}$.

At this point, it is important to clarify that the phase transition behavior observed from the Raman measurements strictly depends on the geometry of WO_3 particles in the shapes such as nanoparticles and nanowires, which show different characteristic peaks (Thummavichai et al. (2018)). There are many studies in the literature to understand the phase transition characteristics of different kind of WO_3 nanostructures, which is essential to develop new technologies based on WO_3 nanostructures. Thus, Raman spectroscopy is a very useful technique to reveal the phase transition characteristics of the materials due to high sensitivity to bonding and atomic position changes in the lattice. Fig.5.16 and Fig.5.17 also show temperature dependency of Raman spectra of WO_3 flakes with similar results as those for the spectra in Fig.5.15.

5.4.2. Photoluminescence Analyses of Defects in WO_3 at Low Temperatures

After confirming structural characteristics of WO_3 samples with Raman spectroscopy, single photon emission properties from the defects in WO_3 flakes were studied at various temperatures ranging from room temperature (RT, $23\text{ }^{\circ}\text{C}$) down to $-195\text{ }^{\circ}\text{C}$. All the spectroscopic measurements discussed in this section were performed with the 514 nm laser excitation beam. In Fig.5.18, the excitation polarization dependency of the PL emission from two different defect centers in different WO_3 flakes are shown. The WO_3 flakes are seen as black regions in the optical microscope images as seen on the right. The maximum intensities were observed at 140 and (b) at 80 degree polarization angles. In Fig.5.19, emission spectra from two different defect centers are shown in (a) and (b) as a function of sample temperature. The defect centers were excited at the maximum intensity polarization angles. The weak peak observed at 528 nm is the main Raman phonon mode of the Si substrate.

The emission peaks observed from the defects in WO_3 are very broad compared to those from the other room temperature defect related single photon sources such as those in hBN. To improve the emission characteristics of the SP sources in WO_3 , we carried out measurements at decreasing sample temperature down to $-195\text{ }^{\circ}\text{C}$. As temperature is decreased from RT, the density of phonon will also decrease, hence leading to decreases in the phonon interactions with the defect centers which should eventually improve the

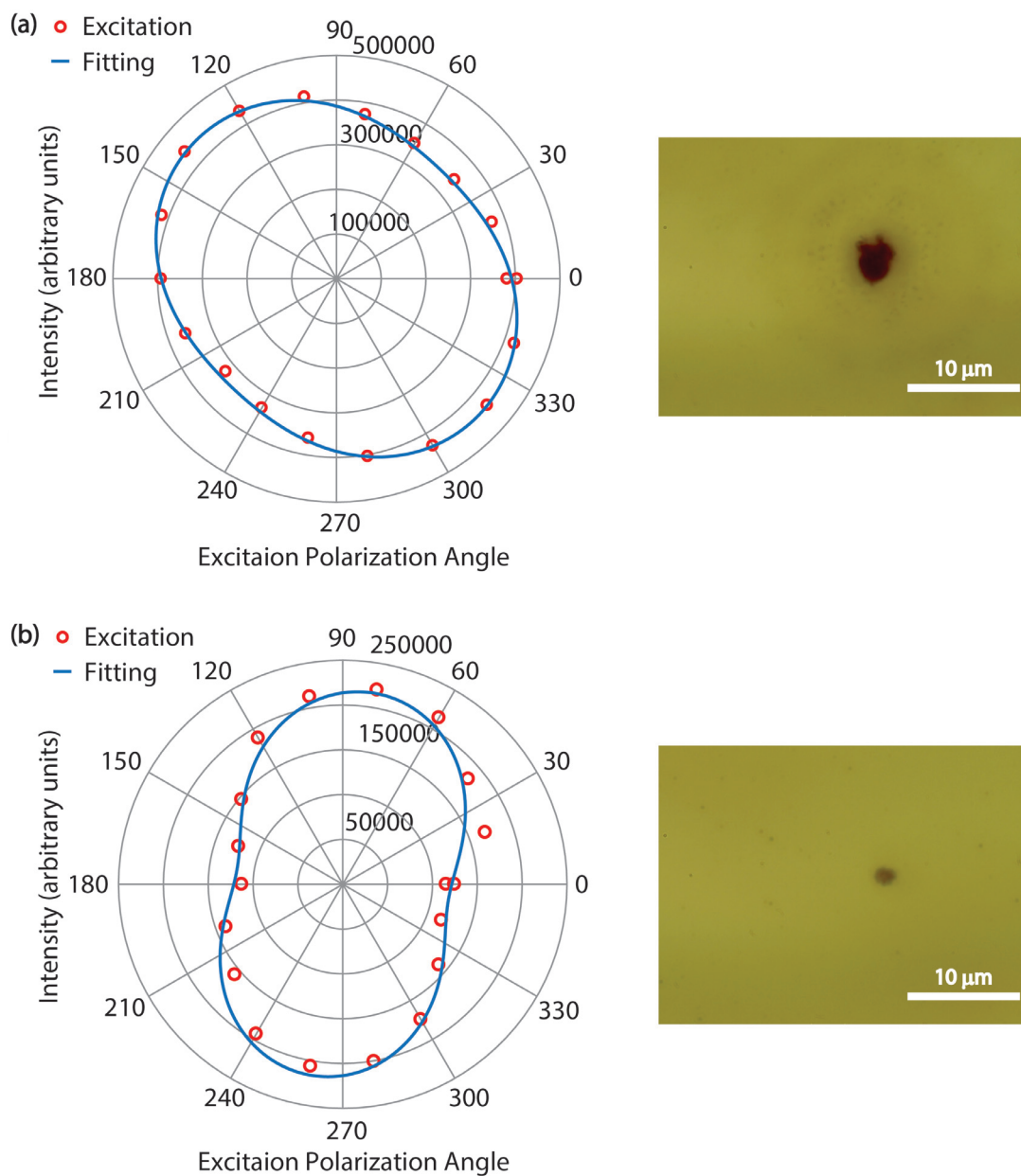


Figure 5.18. Excitation polarization dependent PL intensity from two different defect centers in annealed WO_3 flakes. PL spectra were recorded by 150 gr/mm and 514 nm excitation source. At the right the optical microscope images of the flakes are shown.

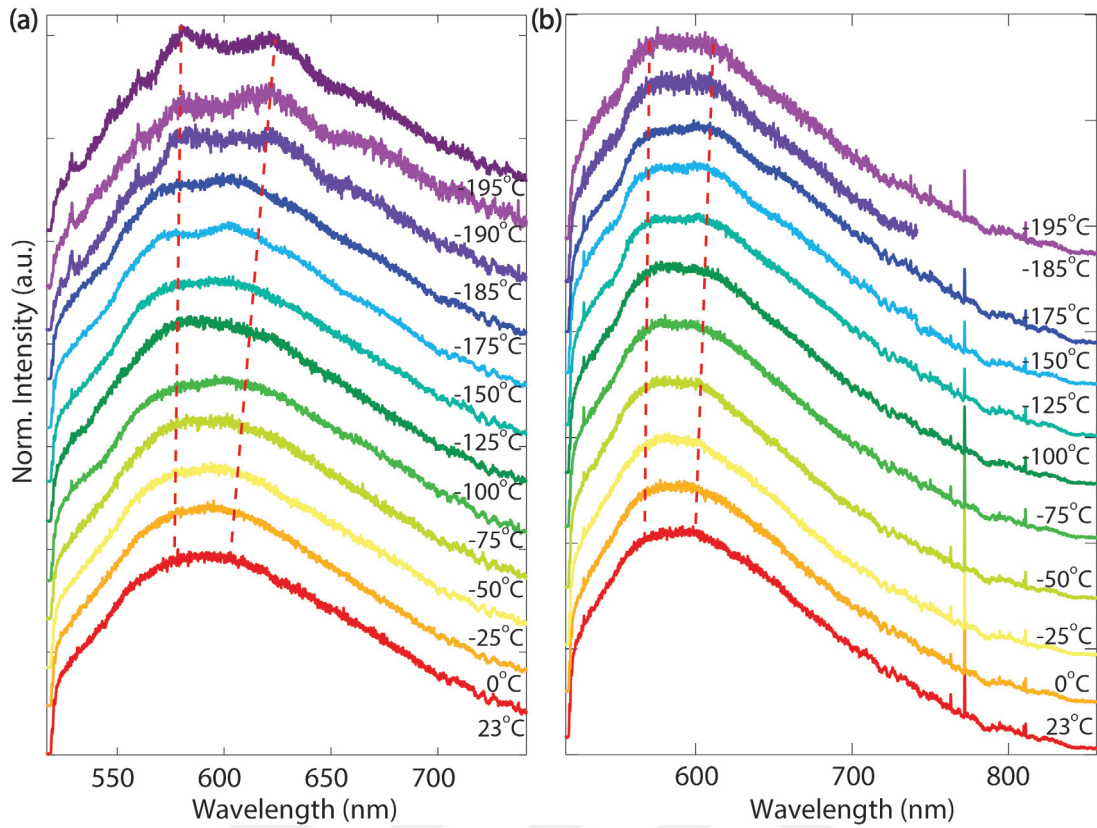


Figure 5.19. Temperature dependent Photoluminescence spectra from two different defect center in annealed WO_3 flakes. PL spectra were recorded by 150 gr/mm and 514 nm excitation source.

intensity and sharpness of the single photon emission peak observed from the defects in WO_3 . As seen in Fig.5.19, the broad peak splits into two or more components with different wavelengths. In (a), the split peaks are 42 nm away from each other, whereas in (b) the difference is 36.4 nm. The reason could be that there are more than one defect center under the beam and recorded spectrum may belong to both of them. The energy differences are about 144 meV and 120 meV for both defects which are more than 99 meV. So they are far away from the ZPL phonon side bands.

5.5. Single Photon Emission Enhancement by Gold Nanoparticles

Another way to improve the single photon emission characteristics from the defect centers in WO_3 are due to their interactions with resonant plasmonic excitation. For that purpose, we introduced gold nanoparticles (NP) on WO_3 flakes on Si substrates. First a

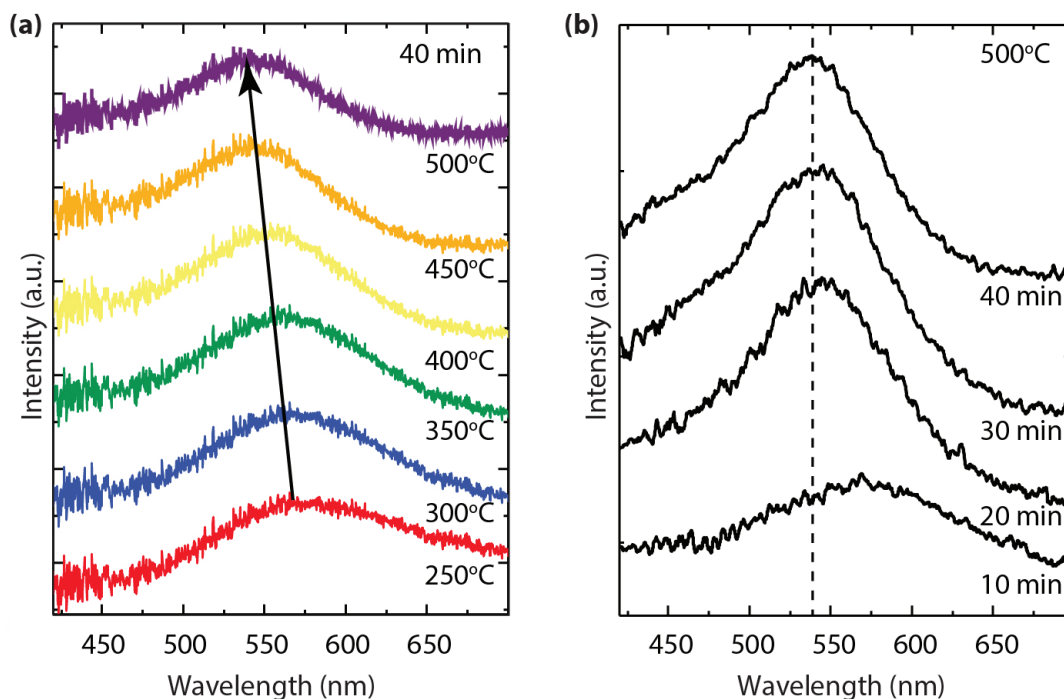


Figure 5.20. Reflection spectra for various annealing (a) temperatures and (b) durations.

4 nm thick gold film was deposited on a Si substrates. Then the samples were annealed at various temperatures and durations. Annealing transforms the gold film into many isolated parts due to dewetting and cohesive forces. After cooling, each parts turns into a particle of a few tens of nanometer in diameter depending on the annealing temperature and duration. The plasma frequency of each gold particle depends on the size of the particle as given in the theoretical section.

In this part of the study, we first examine the effect of annealing conditions on the emission characteristics of the defect centers in WO_3 . Fig.5.20 gives the reflection spectra for various annealing temperatures and durations. As seen from figure (a), the increased annealing temperature, at a fixed 40 min annealing time, shifts the reflection peak from 572 nm to 538 nm which is close to the 514 nm excitation source wavelength. This shift to high energies is due to decrease in the size of the nanoparticles. As the NP plasmonic oscillation frequency gets closer to the frequency of the emission from the defects in WO_3 , the coupling between the defect center and NP plasmons intensifies, leading to resonance enhancement of the single photon emission from the defects. Additionally, as seen in Fig.5.20 (b) the increased annealing time is also useful to obtain the closer resonance frequency to the excitation source. After 30 min there is not a dramatic affect.

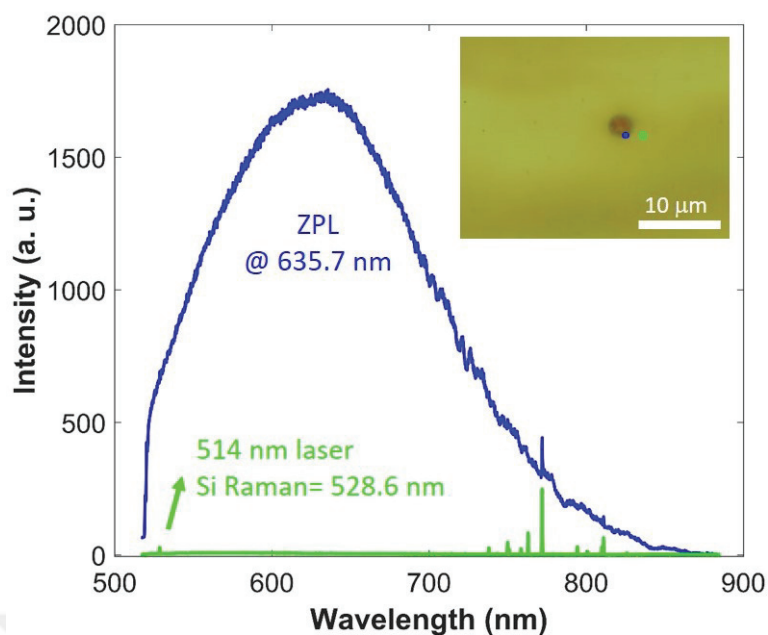


Figure 5.21. PL spectra recorded from a WO_3 flake (blue) and about $1 \mu\text{m}$ distance away from the defect center in WO_3 flake (green) shown in the inset. Intensities of the spectra are for 1 sec exposure counts. The green spectrum is shown to clearly understand that there is no background effect of gold nanoparticles.

After gold nanoparticle deposition, an excitation power dependent emission intensity series were recorded using the 514 nm excitation wavelength of the Ar laser (in Fig.5.22 (a)). All intensity values with respect to excitation laser power were recorded individually as counts per second. As seen in in Fig.5.22 (a), intensity of the emission increases linearly at small excitation powers, then it asymptotically approaches to a saturation value at high excitation powers. This saturation behavior is a clear evidence for the single photon nature of the emission. Incidentally, at high emission powers the nature of the defect center changes a little which causes a downward shift in the emission intensity. To correct for that shift we first chose the intensity data obtained at a definite excitation power in the low power linear regime as a reference. After carrying out each high power measurement the intensity at the reference power was checked. The reduction ratio in the intensity at the reference power was used to obtain the correction factor (inverse of the reduction ratio) for each high power measurement. Fig.5.22 (b) illustrates the reduction in the intensity for the reference power of 0.2 mW after a measurement at the saturation power of 3.1 mW. After this reference power value the reference intensity begun to decrease because of the over excitation by the plasmonic effect. The corrected

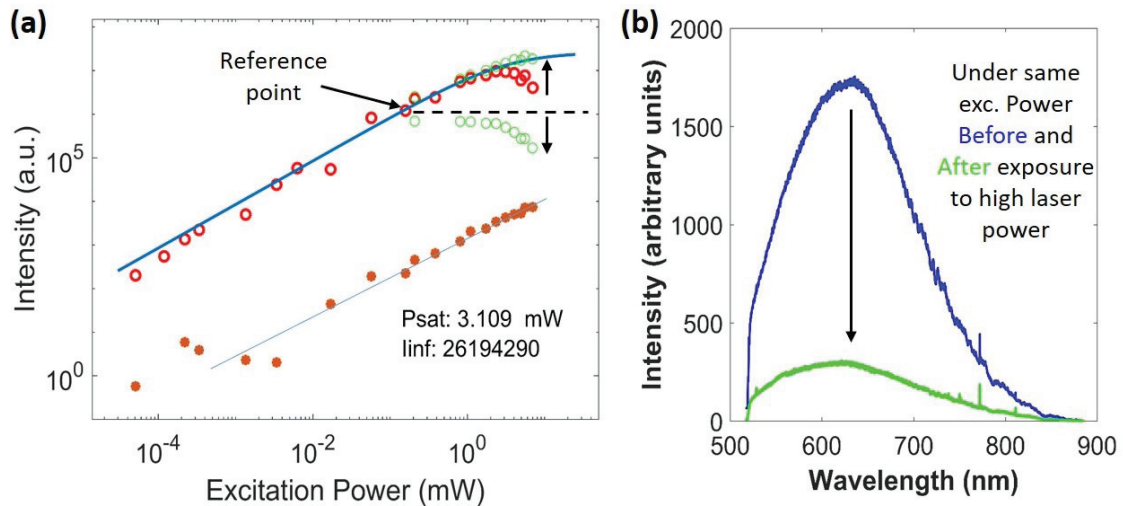


Figure 5.22. (a) After gold nanoparticle deposition, the excitation power dependent intensity variation of an emission. The circles represent the intensities of the emission and the dots are intensities of Si Raman signals extracted from the same spectra. The solid lines are theoretical fits. (b) The low power excited emission intensity decrease after exposure to a high power to obtain the saturation curve of the power series.

data are shown in Fig.5.22 (a) as green dots above the black dashed line while the raw measurements are given with red data points. The theoretical fit was applied after correction for high power measurements in the saturation regime from which the ultimate saturation power value was calculated as 3.1 mW.

5.5.1. Statistical Analyses of Emission Enhancement

It is natural to study the emission of a particular defect center before and after the introduction of gold nanoparticles. However, such an introduction changes the nature of a particular defect modifying its emission characteristics beyond the resonant interaction. Thus, it is very impractical to observe a particular defect center. For that reason, a statistical approach is more appropriate to have a comprehensive understanding of the resonance enhancement from the nanoparticles on the emission characteristics of defects. The resonance enhancement of the emission by plasmonic gold nanoparticles depends on many factors as explained in Chapter 2. In Fig.5.23 (a), the excitation power dependent intensity series before (black) and after the introduction of gold nanoparticles (red) from the defects in a WO_3 flake is shown. The optical image (b) and excitation/emission po-

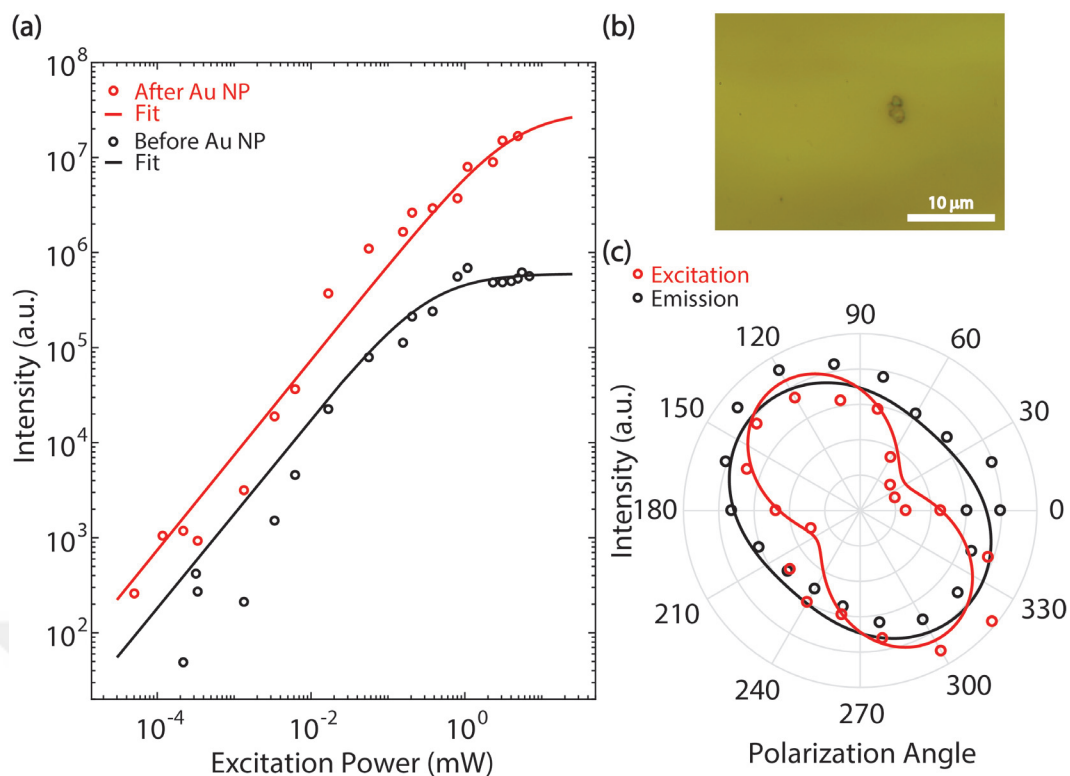


Figure 5.23. (a) Before (black) and after (red) gold nanoparticle deposition, the excitation power dependent intensity variation of the emission from same defect center. The circles represent the intensities of the emission and the solid lines are theoretical fits. (b) the optical image of the WO₃ flake before the gold nanoparticle deposition. (c) Excitation (red) and emission (black) polarization dependent intensity variation of the emission. The solid lines are theoretical fits

larization dependencies (c) are also given. As seen from the power series, the maximum intensity values increase more than 20 folds after the gold nanoparticle deposition. After a series data collection in Fig. 5.24 four different power series of different emission centers were plotted before and after nanoparticle deposition. These series yield an average enhancement factor of more than 20 times.

5.6. Summary

In this chapter, the defects in WO₃ on Si substrates were investigated as room temperature SP sources. The unstable emission from the defect centers in the as grown samples were stabilized after annealing them at about 500 °C for 40 min. Annealing also

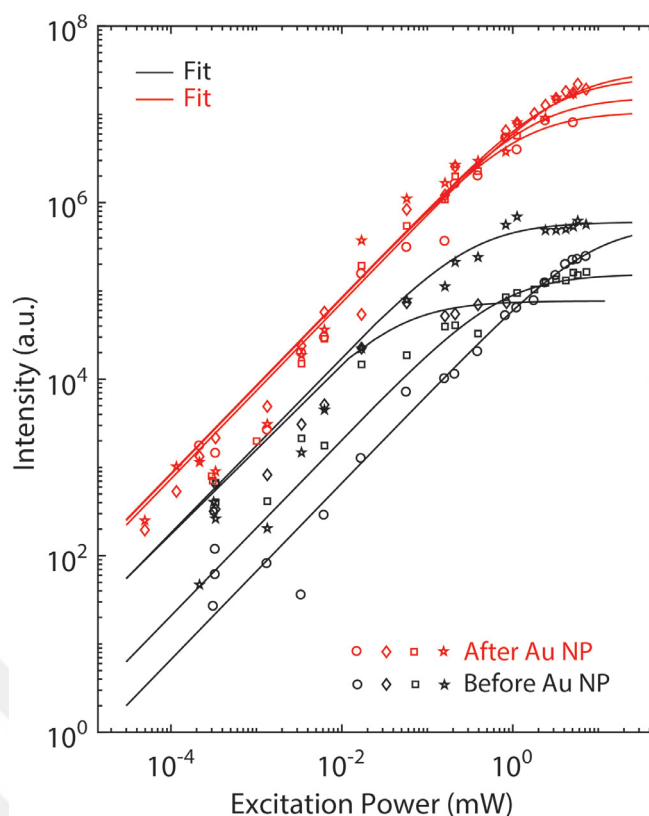


Figure 5.24. (a) Before (black) and after (red) gold nanoparticle deposition, the excitation power dependent intensity variation of the emission are shown. The circles represent the intensities of the emission and the solid lines are theoretical fits.

leads to decrease in the multi-photon emission. It was shown that efficient and stable room temperature luminescence from annealed WO_3 defects centers was obtained. Further analyses of the structural and optical characteristics of these localized emitters were performed in detail. To confirm the observed emission originates from point defect in WO_3 , a density functional theory (DFT) based first principle computational approach was carried out. Hence, we concluded that oxygen vacancies, which yielded mid-gap states, were the most possible cause of the observed single photon emission.

A further study was performed to increase the brightness of the emissions at RT. For that purpose, we introduced gold nanoparticles as plasmonic resonators which exhibits weak coupling with the individual emission centers (Nguyen et al. (2018); Iff et al. (2018); Hoang et al. (2016)). After the introduction of gold nanoparticles near WO_3 flakes, emission intensity enhancement of more than 20 times were clearly observed. These results are promising for future applications of WO_3 based SP emitters, either stan-

alone or inside a TMDC host, in terms of integrated nanophotonics and plasmonic devices. We are confident that our results will contribute to the understanding of the nature of defects as room temperature SP emitters in WO_3 .



CHAPTER 6

ENERGY TRANSFER BETWEEN A SINGLE PHOTON EMITTER IN HBN AND GRAPHENE: QUENCHING EFFECT

Nowadays, one of the most crucial research areas in the development of quantum optics technology is control of single photon (SP) emission at room temperature. A coupled system with graphene based on Förster resonance energy transfer (FRET) mechanism provides a convenient way to modulate the emission. Graphene is 2D and nearly transparent semimetal with honeycomb structure and possesses high carrier mobility (Bolotin et al. (2008)). Furthermore, it exhibits broad absorption across the visible spectral range by exciting electron-hole pairs (Bolotin et al. (2008)). Thus, an emission near field distance to the graphene is quenched with the rate of d^{-4} for 2D materials (Swathi and Sebastian (2009); Kim et al. (2010); Federspiel et al. (2015)). There are variety of reports on FRET-based graphene hybrid nanomaterials such as nanocrystals (Federspiel et al. (2015); Guzelturk and Demir (2016); Yu et al. (2015)), dye molecules (Kim et al. (2010); Treossi et al. (2009)), nitrogen-vacancy centers (NVCs) in diamond (Tisler et al. (2013)). The exceptional fluorescence quenching ability of graphene also widely used in applications such as biosensors (Tang et al. (2010); Wang et al. (2011)), nanoposition sensor (Mazzamuto et al. (2014)) and fluorescence quenching microscopy (Stöhr et al. (2012)).

Furthermore, optoelectronic device applications are under review about reversible control of emission quenching rate by tuning the optical properties of graphene (Wang et al. (2008)). Recently, gate-controlled graphene emitter separation is used to modulate emission from NVCs in nanodiamonds which are SP emitters at 3 K (Reserbat-Plantey et al. (2016)). Additionally, graphene is used to control light emission from quantum dots (QDs) which are used for light-emitting applications (Salihoglu et al. (2016); Lee et al. (2014)). Considering all these reports, emission quenching depends on both the emitter-graphene distance and doping level of graphene that leads Fermi energy shifting and modulates FRET properties.

In this thesis we report, for the first time to our knowledge, a graphene hybrid atom-size level device to reversible control of SP emission at room temperature. Graphene is placed near field distance of the SP emitter in hBN. Additionally, we use ionic liquid

(IL) based electrolyte gating in a large area device to modulate Fermi energy as large as 1.2 eV (Polat and Kocabas (2013)). Indium tin oxide (ITO) is used on the top as a traditional transparent conductive electrode. The designed capacitor leads to switch on/off and gradually modulate SP emission via gate voltage in the visible spectrum.

In this chapter, first the analyses of single photon emission from a defect centers in dropcasted hBN flakes are given. The PL spectrum, excitation and emission polarization dependency and excitation power dependency of the emission intensity are analyzed. Then energy of the single photon emission is non-radiatively transferred to graphene when it is placed close enough to the emitter. In previous sections it is determined that the energy transfer rate depends on the distance between the emitter and graphene as d^{-4} . Thus, first we showed the static quenching of the single photon emission by analyzing the PL spectrum before and after coupling with graphene. To achieve total quenching, additional individual graphene layers will be transfer on the same defects. In that way, the single photon emission was closed off as a reversible switch. Finally, reversible energy transfer by modulating Fermi level of graphene was shown.

6.1. Irreversible Energy Transfer: Static Quenching

Recent works reported that defect centers in hBN are optically active single photon (SP) emitters (Tran et al. (2015, 2016); Martínez et al. (2016)). In contrast to other 2D materials such as MoS₂ and WSe₂, SP emission from defect centers in hBN are observed at room temperature and over a wide energy range that exceeds 500 meV (Jungwirth et al. (2016)). These isolated single atom scale emitters provide new opportunities for applications of 2D materials including quantum information processing technologies, sensing and quantum computing.

Here hBN flakes were dropcasted on the Al₂O₃/Si substrate, as explained in detail in Chapter 4. SP emission from an optically active defect center in hBN was observed and characterized with its dipole properties, such as ZPL spectrum by excitation polarization and power dependencies at room temperature. Afterwards, a single layer of graphene was placed on a pre-analysed hBN as shown in Fig.6.1. As determined in a previously reported study (Balci et al. (2018)), the graphene layers were synthesized by chemical vapor deposition (CVD) method on ultra-smooth copper foils. The single layer graphene was transferred on hBN by a photoresist assisted transfer method which was explained in detail in Chapter 4. After graphene transfer on top of the hBN flakes all the analyses which have been performed before graphene were repeated under the same conditions.

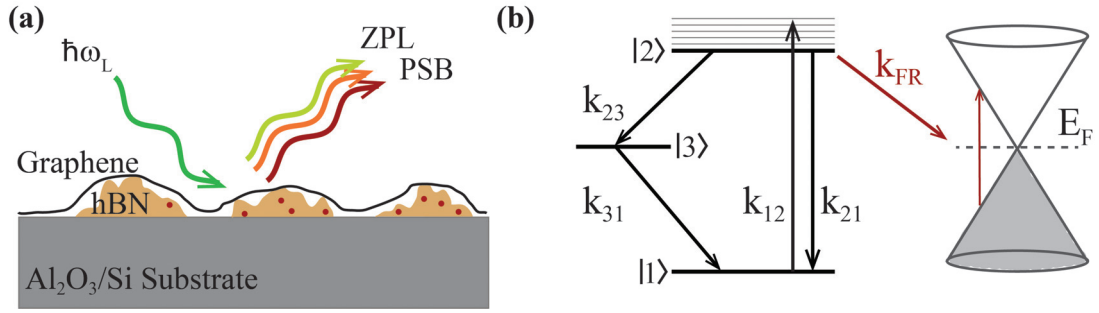


Figure 6.1. (a) Schematic of the studied sample structure is shown with the dropcasted hBN flakes (yellow) and defect centers (red dots). A single layer graphene (black line) is transferred on top. Excitation by a 532 nm CW laser (green) and the emission (colored) in visible spectrum depend on the emission wavelength are shown by arrows. (b) A single defect is illustrated as a three-level system. The non-radiative energy transfer rate is k_{FR} . The band structure of graphene near the K point is seen with Fermi level, E_F .

These before and after graphene transferred analyses results were compared to observe quenching of the single photon emission.

6.1.1. Energy Transfer from a Single Emitter to Single Layer Graphene

A schematic representation of SP emission from a defect center in hBN, drop-casted on $\text{Al}_2\text{O}_3/\text{Si}$ substrate, is shown in Fig. 6.1 (a). Red dots in hBN flakes (yellow) indicate defect centers. Excitation by a 532 nm CW laser is represented by a green arrow and the emission represented by different colored arrows in visible spectrum depend on the emission wavelength. The emission coupled to the graphene which is represented by a black line on top of the hBN flakes. Graphene surface has different distances to the different defects, thus the energy transfer rate varies with the distance between the graphene and the defect center as d^{-4} . Bringing an undoped graphene layer close enough to the emitter activates a non-radiative coupling channel with a rate k_{FR} between the excited state of the emitter and the graphene (Fig.6.1 (b)).

A defect center in hBN shown in Fig.6.2 had been analyzed before and after graphene transfer on top of the hBN. The optical image and its two dimensional PL map are also shown in Fig.6.2 (a). The brightest spot on the map shows a localized emission

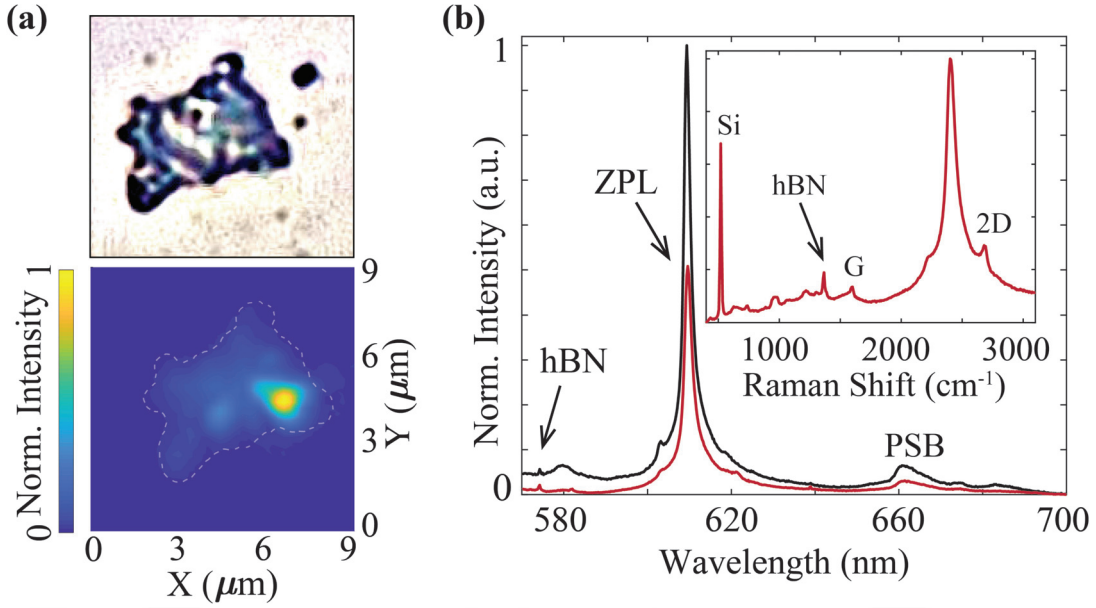


Figure 6.2. (a) Optical microscope image (left) and the PL map of the same bulk hBN with a bright and localized emission from a single defect (right). (b) Room temperature PL spectra of the defect shown in the map before (black) and after (red) graphene transfer.

from a single defect in hBN. The single defect (donor) behaves like a three-level system with the given rates between the energy levels shown in Fig.6.1 (b). Placing a graphene layer (acceptor) close enough to the emitter activates a non-radiative coupling with a rate k_{FR} between the excited state of the emitter and the graphene (Förster-like energy transfer).

A graphene layer in near field (< 50 nm) to the emitter yields nonradiatively coupling between them Reserbat-Plantey et al. (2016); Salihoglu et al. (2016). Nonradiative interaction between the emission from a defect center in hBN and a single layer graphene resulting electron-hole pair excitations (i.e., Förster-like energy transfer) is shown in Fig.6.1 (b). Theoretical (Swathi and Sebastian (2009); Gómez-Santos and Stauber (2011)) and experimental (Gaudreau et al. (2013); Stöhr et al. (2012); Kim et al. (2010); Mazzamuto et al. (2014)) studies are showed that the coupling leads to emission quenching and a shorter lifetime of the emitters in higher decay rates. The emission quenching raises with reducing the distance between the emitter and graphene with the order of d^{-4} (Swathi and Sebastian (2009)). As seen in Fig.6.2 (b), room temperature PL spectra of the defect shown in the map before (black) and after (red) graphene transfer is proved the statically quenching of the emission by graphene. The ZPL emission of the defect is observed at

610 nm. The small peak at 574 nm is the Raman signal of hBN. The ZPL intensity is quenched by a factor of ~ 2 ($\sim 50\%$) while the Raman signal of hBN is not changed. Furthermore, a phonon side band (PSB) doublet around 665 nm and 675 nm is seen in Fig. 6.2 (b). The inset shows a high power spectrum of the defect after graphene transfer which shows all the Raman shifts of Silicon substrate (520 cm^{-1}), hBN (1370 cm^{-1}), graphene G peak (1631 cm^{-1}), and graphene 2D peak (2711 cm^{-1}). The spectra were taken with 532 nm CW laser at the same excitation power and polarization conditions.

Dipole properties of SP emission from the optically active defect center in hBN was also characterized. Its polarization dependency at room temperature, before and after graphene transfer is shown in Fig.6.3. Again the intensity reduction of a factor of ~ 2 after graphene transfer indicates a quenching effect of the emission due to a single layer graphene. The linear transition dipole orientation almost remains unchanged.

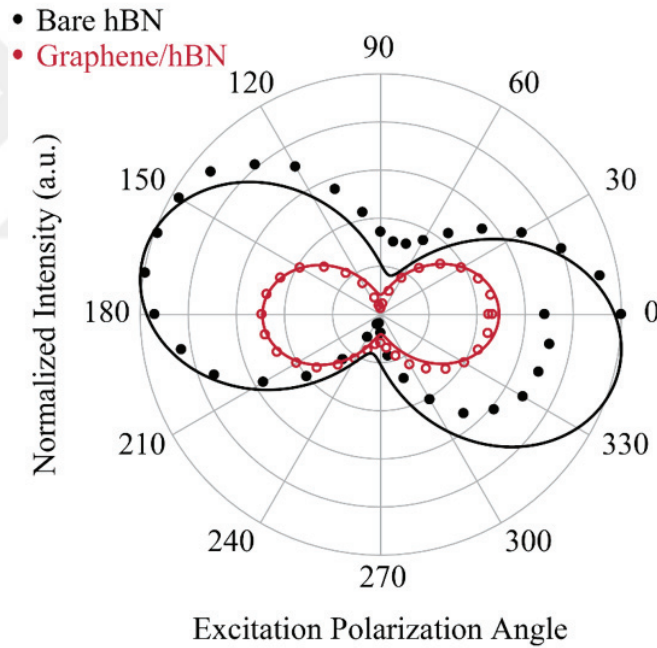


Figure 6.3. The relation between excitation polarization and emission intensity of defect center with before (black) and after (red) graphene transfer shows linearly polarized emission.

The experimental data fit (Fig.6.3, solid lines) relation is

$$I = I_B + I_0 \cos^2(\theta + \theta_{offset}), \quad (6.1)$$

where I_B and $I_B + I_0$ are the minimum and maximum values of the PL intensity, θ corresponds to excitation polarization angle and θ_{offset} is the angle corresponds to the maximum emission intensity. The visibility is defined as polarization degree by the following relation:

$$V = \frac{I_{max} - I_{min}}{I_{max} + I_{min}}, \quad (6.2)$$

where I_{max} and I_{min} are maximum and minimum intensities, respectively. The visibility of SP emission at 610 nm before and after graphene coupling are found as 93% and 90%, respectively. This strong polarization dependency indicates a characteristic single dipole behaviour (Neu et al. (2011)).

Additionally, the same quenching effect is seen from excitation power versus emission intensity saturation relation. It is shown in Fig.6.4, the black dots indicate pre-analysed PL intensities with respect to excitation power and the red dots are the PL intensities of single layer graphene coupled system. The spectra shown in Fig.6.2 (b) and the high power excited spectrum in the inset were extracted from these excitation power and intensity relation series. These series were recorded under the excitation polarization of maximum intensity. Before and after graphene transfer the spectra for each excitation power were recorded from the same point in the hBN flake (shown in Fig.6.2 (a)) by optimizing the XYZ stage position to observe the maximum intensity of the ZPL. The experimental data was fit (solid lines) using the relation, which was described in Chapter 2 detailed,

$$I = I_{\infty} \frac{P}{P_{sat} + P}, \quad (6.3)$$

where I_{∞} , P_{sat} are the emission rate and excitation power at saturation, respectively, although the saturation power of the emission is not influenced, the saturation emission rate of before ($I_{sat,BG}$) to after graphene ($I_{sat,AG}$) is around 2 as expected from the individual spectra intensity quenching rates. Silicon Raman peak intensities were extracted from the same spectra (Fig. 6.4) before (black) and after (red) graphene transfer. The ZPL intensity is quenched by a factor of ~ 2 almost at all excitation powers while the Silicon Raman peak intensity were not quenched after the graphene transfer. This indicates that the quenched ZPL emission is due to the FRET-like energy transfer between the defect and the graphene layer.

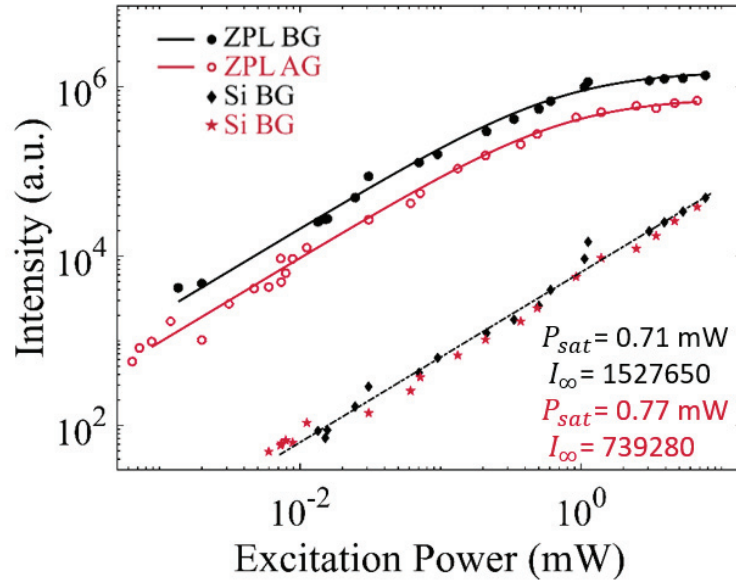


Figure 6.4. Excitation power dependent of ZPL and the Silicon Raman peak intensities extracted from the same spectra before (black) and after (red) graphene transfer for the same defect.

Furthermore, the PL intensity ratio of pre-analysed (black spectrum) and single layer graphene coupled (red spectrum) defect center is around 2 which is defined as $I_{BG}/I_{AG} \cong 2$. Assuming after the coupling the decay rates, $k_{21} \cong k'_{21}$ and $k_{23} \cong k'_{23}$, have been changed very little to be ignored. Then using pre-defined intensity and decay rate relations following intensities can be described in terms of decay rates:

$$I_{BG} \approx \frac{k_{12}\gamma_r}{k_{21} + k_{23}}, \quad (6.4)$$

$$I_{AG} \approx \frac{k_{12}\gamma_r}{k_{21} + k_{23} + k_{FRET}}. \quad (6.5)$$

Hereby, the experimental intensity quenching rate 2 can be used to estimate the k_{FRET} rate as $k_{FRET} = k_{21} + k_{23}$.

To prove the ZPL corresponds to an isolated defect that emits SPs, correlation spectroscopy using a Hanbury Brown and Twiss (HBT) interferometer was used. A measured antibunching curve, $g^{(2)}(\tau)$, recorded from the defect center is shown in Fig.6.5 and

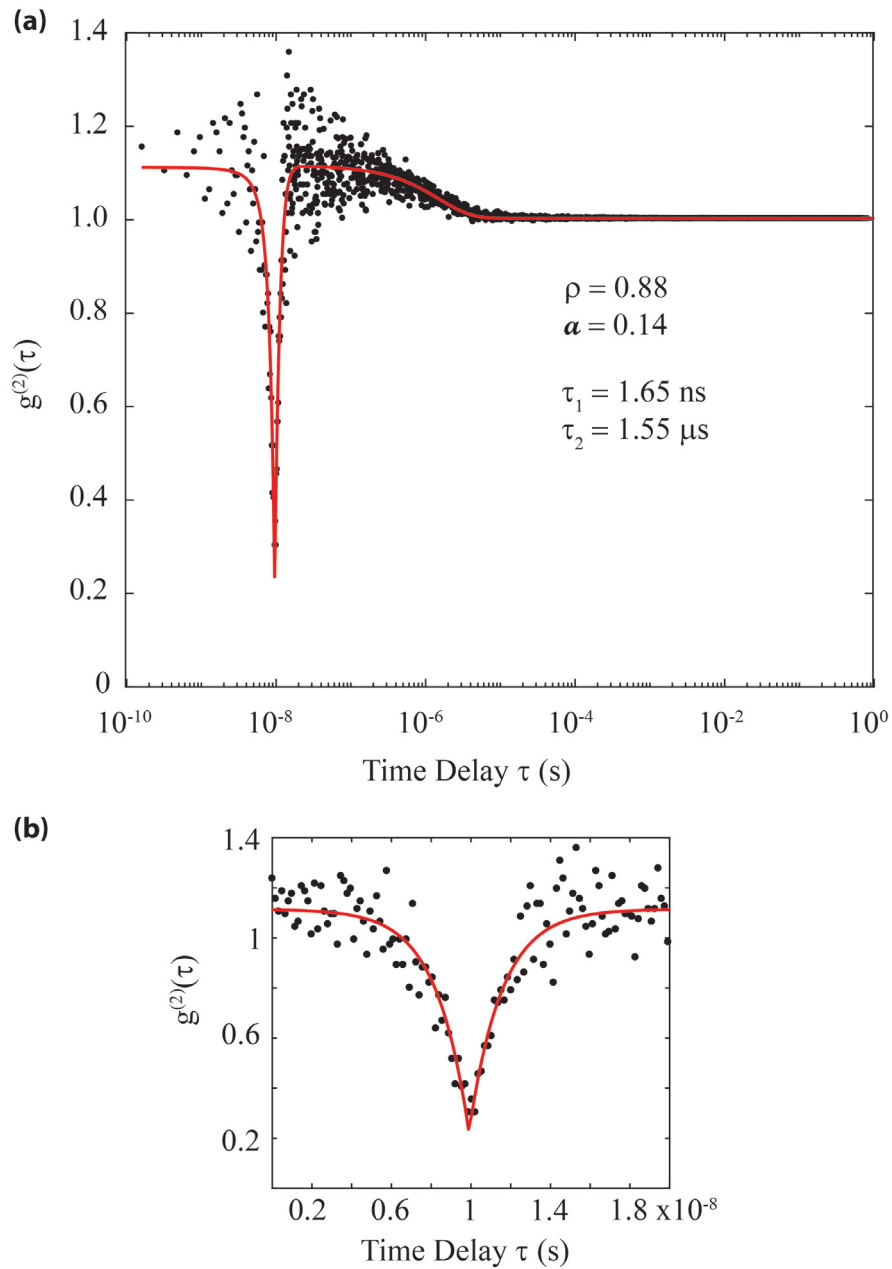


Figure 6.5. To identify the single photon character of the emission observed at 610 nm from a localized point in the hBN the second order photon correlation experiment was performed by HBT setup. (a) The extracted excited state and metastable state lifetimes from the fit are on the order of 1.65 ns and 1.55 μ s. (b) The antibunching dip is seen and it is below the value of 0.5 which is the threshold value to identify a single photon emitter.

fitted by the following three level model relation (Exarhos et al. (2017)):

$$g_m^{(2)}(\tau) = 1 - \rho^2 [(1 + a)e^{-|\tau|/\tau_1} - ae^{-|\tau|/\tau_2}]. \quad (6.6)$$

Three level model includes bunching at $g^{(2)}(\tau) > 1$. The delay time is τ and the calculated photon bunching amplitude, a , is 0.14. The extracted emission lifetime, τ_1 , and metastable state lifetime, τ_2 , from the fit are 1.65 ns and 1.55 μ s, respectively. The Poissonian background arising from optical components, the detector quantum efficiency, metastable states and excitation power affects the overall detection efficiency (Brouri et al. (2000)). Ideally the antibunching at zero delay time is $1 - \frac{1}{n}$ for n emitters. Thus, second order correlation function is between 0 and 0.5 indicates SP emitter, but background causes to increase this limit. The Poissonian background is the value of the signal-to-background ratio, $\rho = S/(S + B)$, extracted from the fit as 0.88. That increases the $g^{(2)}(0)$ threshold from 0.5 to $0.5(1 + \rho^2 a)$ (Exarhos et al. (2017); Brouri et al. (2000)). From photon correlation measurement of the pre-analyzed SP emission at 610 nm (Fig.6.2 (b)), this threshold is calculated as 0.554. The antibunching dip at zero delay time is 0.23 and well below this threshold confirming SP emission characteristics.

6.1.2. Energy Transfer from a Single Emitter to Three Layer Graphene

In this part of our work we studied the effect of various layers of graphene transferred on to SP emitting defect sources in dropcasted hBN flakes. After a graphene transferred onto hBN the distance of point-like defects (red dots) to the graphene (black line) varies, as shown in Fig.6.1(a). Thus the quenching rate also varies from defect to another defect. Another way to increase the quenching rate is increasing transferred energy rate by additional graphene layers (Chen et al. (2010); Guzelturk and Demir (2016); Yu et al. (2015)).

The samples were prepared by the procedure which was explained in Chapter 4. Si substrate was cleaned which has ~ 60 nm Al_2O_3 oxide layer to see the optical contrast of hBN on the substrate (Gorbachev et al. (2011)). Then the hBN flake solution was dropcasted on the substrate and the liquid evaporated itself. First, the optically active defect centers on hBN flakes were analyzed. Their coordinates on the substrate and single

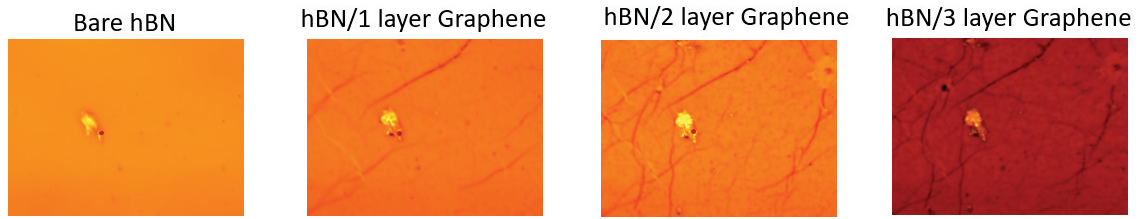


Figure 6.6. Bare, one layer, two layer and three layer graphene transferred onto hBN flake are given respectively. Red dots show the (laser beam) defect center position on the flake.

PL spectrum with the same optical excitation conditions and exposure time were recorded. Optimizing the sample position under laser beam we obtain the ZPL as intense as possible to record the excitation polarization and power dependent intensity series.

After ~ 50 different single photon emitters were analyzed, a thin layer graphene was transferred onto hBN flakes by the transfer procedure explained in Chapter 4. Then the same defect centers were analyzed again with same optical excitation conditions and exposure time by optimizing the position to observe maximum intensity of the peaks. This cycle was repeated after a second and then a third layer graphene were transferred onto the hBN flakes. The optical microscope images of an hBN flake for bare, first layer, second layer and a third layer graphene transferred are shown in Fig.6.6.

Single graphene layers are considered to not interact with one another Castro Neto et al. (2009). Thus each layer is considered individually coupled to the emitter. The effect of graphene layer number on the intensity of ZPL from defect centers in hBN flakes were compared after each layer transfer. However, it is known that the stress of the graphene due to the hBN flake height and thickness leads to break the graphene and causes wrinkles around the flakes. This affects the structural and optical properties of graphene. Another important issue is that the results were compared by normalizing both Si Raman signal and hBN Raman signal. The reason is that after graphene transfer if we assume the position of the defect does not change (the focal distance changes), at the same position the Si and hBN Raman signals should be unaffected. Also, according to the daily calibration differences the intensities should be corrected by a factor which can be ignored. In Fig.6.7, raw data recorded before and after graphene layer transfers are shown on the left. The black arrows show the intensity quenching percentages from bare to one layer-graphene, from one layer to two layer-graphene and from two layer to three layer-graphene transfer. The longest arrow gives the total quenching of the ZPL

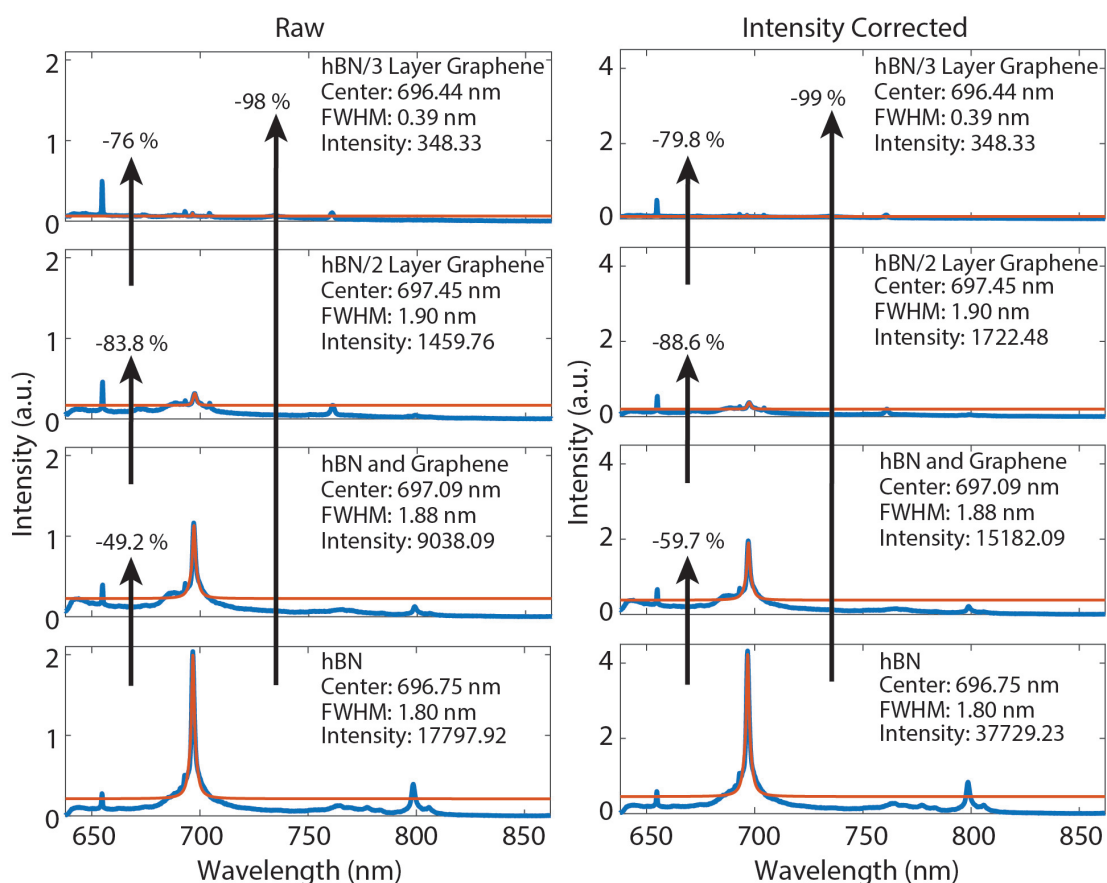


Figure 6.7. A single photon emission at 697 nm is seen from bottom to up bare, one layer, two layer and three layer graphene transferred onto emitter are shown. On the left raw spectra and on the right intensity corrected in terms of Si Raman peak spectra are shown. The orange lines belong to fit curves of the peaks. The calculated FWHM, intensity and shift values are also given in each spectrum. The black arrows show the quenching rates.

intensity by coupling with three individual graphene layers. As seen after each transfer the intensity quenches and three layer is enough totally suppress the emission. There are ignorable changes after intensity normalization with respect to Si Raman peak seen in the right panel of Fig.6.7 as corrected. The black arrows show the intensity quenching percentages. By means of the fitted ZPL curves (orange) the intensity (by subtracting background), FWHM and shifting of the peak centers, which are also written on each graph, can be calculated. To reach the totally quenching of the emission, a second and

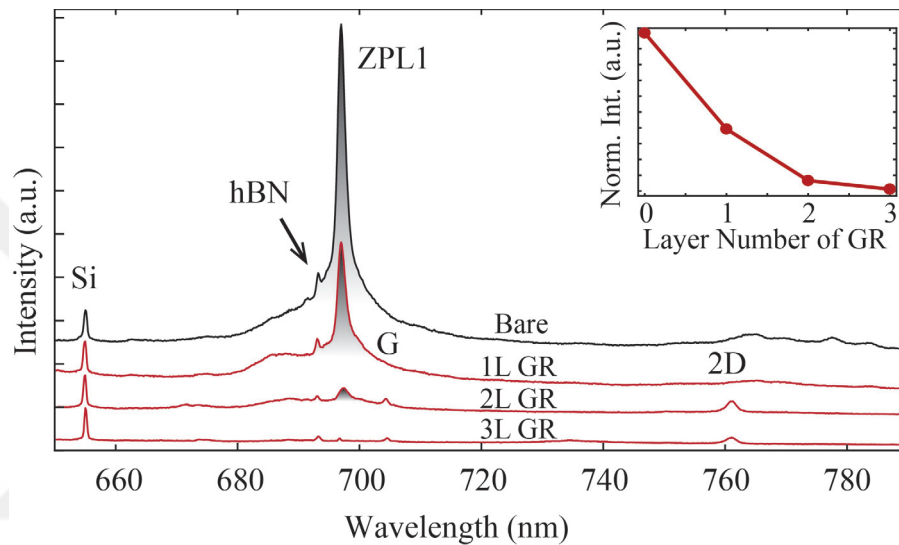


Figure 6.8. A SP emission at 697 nm is corrected by normalizing the Si Raman signal intensity. The inset shows the normalized intensity variation of the emission with respect to the layer number of graphene.

third layers of graphene were placed on the same hBN. In Fig.6.8 the behavior of emission was analyzed after each graphene placement by correcting with respect to Si Raman signal intensity. After the third layer, SP emission was quenched to almost 99 %, as opposed to the Raman peaks which were not influenced by graphene layers. This is an indication of a graphene-hybrid system with a single atom scale can be used to close the single photon emission as an irreversible switch. The spectra were recorded by a CW excitation with 632 nm wavelength. The peak at 656 nm is the Raman shift of the silicon substrate, and the small peak at 693 nm is the Raman shift of hBN. The graphene Raman peaks of G and 2D are also visible. As shown, the intensity of the Raman peaks are almost same while the ZPL emission is quenched completely after the third layer transfer. The inset

shows the normalized intensity of the defect emission dependency to the layer number of graphene.

There were a few ZPLs in our statistical study that correction according to Si or hBN Raman signal give very different results of quenching rate. For example, the raw data quenching percentages from bare to three layer graphene are 20, 15 and 60, respectively and the total quenching is 73%. However, after correction according to Si Raman signal intensity the total quenching increases to 85%. After correction according to hBN Raman peak intensity the total quenching decreases to 28%. As seen to realize the real quenching rates the correction should be made with respect to Si, because the focal distance changes after each graphene layer transfer on top of hBN flake. The hBN Raman signal changes, but the Si Raman signal would not affect as compared to hBN flake. The thickness and the volume of the Si substrate is much larger than hBN flake.

Besides the Raman peak intensity correction factor analysis we also examine the phonon side bands (PSBs). As seen from the Fig.6.9 the exponential y-axis reveals the PSB (right panel). As expected, it can be concluded that graphene on top of the defect center also quenches PSBs. As seen increasing graphene layer number increases the PSB quenching as well.

Placing graphene in close proximity to optically active defects in hBN flakes provides nonradiative energy transfer between defect center and graphene. This results strong changes in the emission characteristics of single photon source. Nonradiative energy transfer from emitter to graphene results electronic transitions in graphene. As a result, quenching of the emission of single photons is observed. The rate of quenching depends on the defect-graphene distance by d^{-4} . Nonradiative energy transfer leads electronic transitions in graphene, which reduces the emission of single photons due to error-graphene distance. In this study, we could not estimate the distance properly. Thus, additional graphene layers were transferred to increase the energy transfer channels and increase the energy transfer rate. To that aim a statistical study has been performed with many different samples. The polarization and power series of all ZPLs were recorded before and after each graphene layer transfer. Generally, three layers of graphene were enough to quench the emission almost completely. In Fig.6.10 (a and c), the optimized PL intensities of before graphene and after each three single layer graphene is placed are shown. Single graphene layers are considered to not interact with one another (Castro Neto et al. (2009)). Thus each layer is considered individually coupled to the emitter.

A defect with a ZPL emission at 656 nm (D656) next to the Si Raman peak at 654.6 nm is observed with 633 nm CW laser excitation in Fig.6.10(a). The hBN Ra-

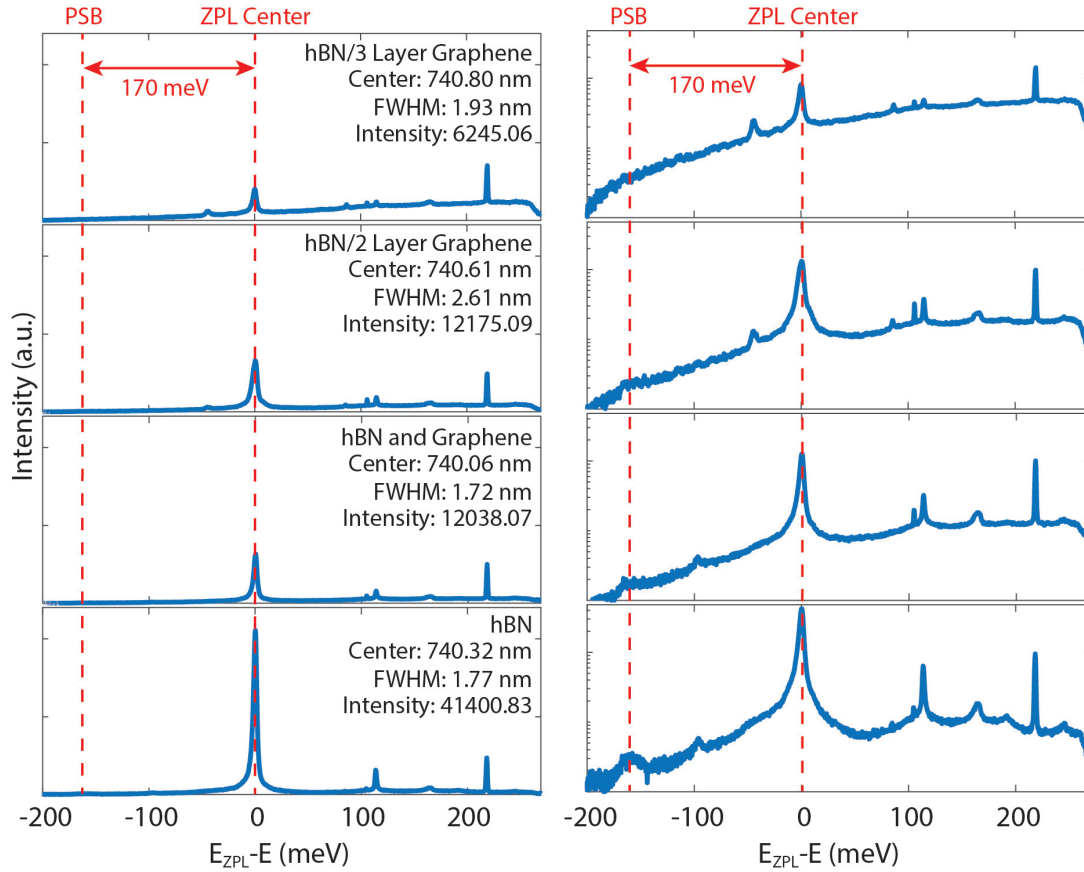


Figure 6.9. A single photon emission at 740 nm is seen from bottom to up bare, one layer, two layer and three layer graphene transferred onto emitter cases are shown. They are corrected with respect to Si Raman signals. On the left the spectra are plotted linearly normalized. On the right the spectra are plotted logarithmically normalized. The orange lines belong to fit curves of the peaks. The calculated FWHM, intensity and shift values are also given in each spectrum. The orange arrows show the quenching percentages. To see clearly the energy difference between PSB and ZPL center, the ZPL center plotted on zero in purpose.

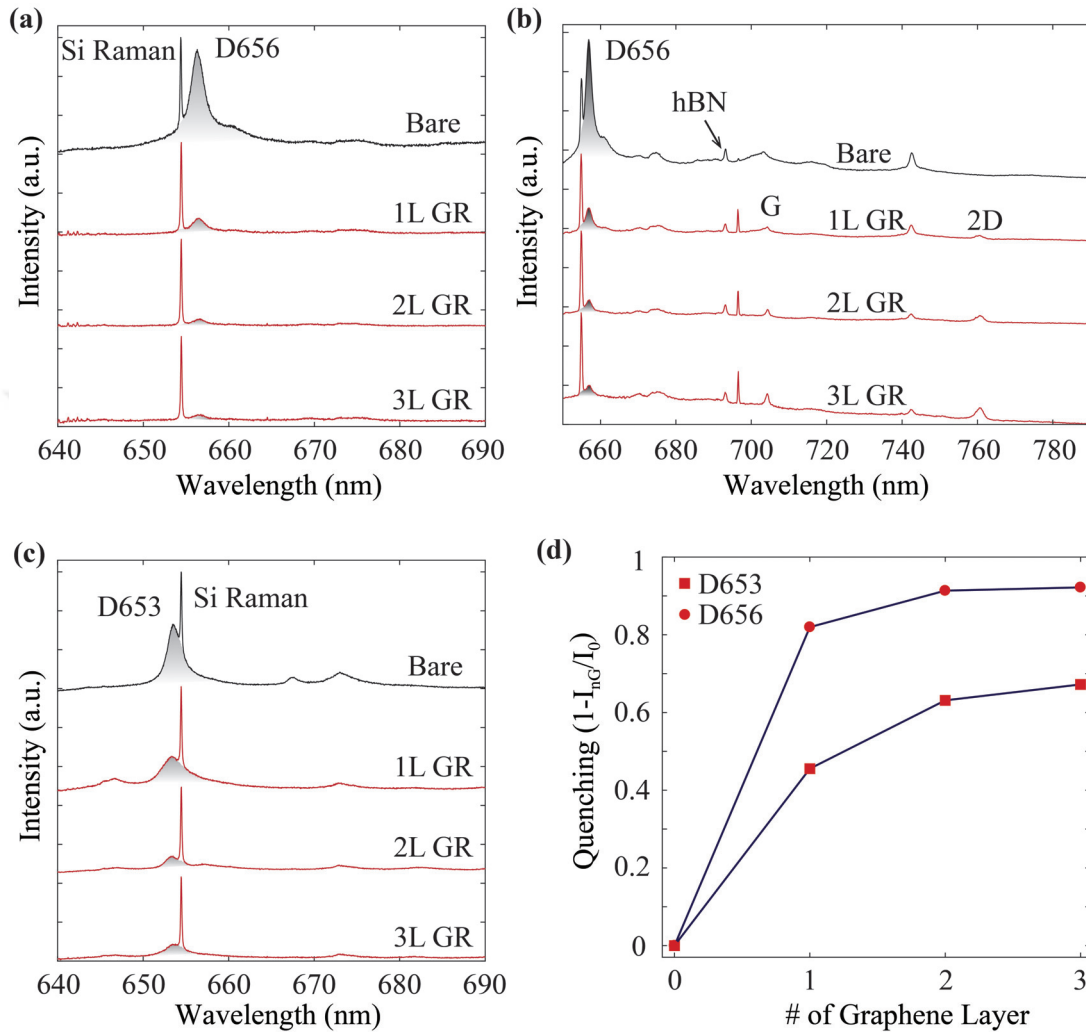


Figure 6.10. (a) A SP emission at 656 nm (D656) next to the Silicon Raman peak at 654.6 nm and its quenching after each graphene layer transfer are observed with 600 gr/mm grating. (b) The PL spectra of D656 are shown by 150 gr/mm with G and 2D bands of graphene. (c) Quenching of another defect emitting at 653 nm (D653) is shown. (d) Quenching rate of both defects as a function of graphene layer.

man signal is at 693 nm. Transferring a single layer of graphene as before shows a clear quenching of the ZPL while the Si Raman peak intensity is almost same. Adding two additional graphene layers further increase the quenching and the ZPL emission is almost completely suppressed. The PL spectra in Fig.6.10(a) were recorded by 600 gr/mm while in Fig.6.10(b) were 150 gr/mm. Thus in (b), the graphene Raman peaks are also visible. The G peak is at 703 nm and the 2D peak is at 761 nm. As seen, the intensity of the Raman peaks are almost same while the ZPL emission is quenched completely after the third layer transfer. Additionally, another defect emitting at 653 nm is shown in Fig.6.10 (c). This defect has a slightly lower quenching rate than D656. We proposed that D656 is closer to the sample surface, and therefore to the graphene, as the quenching rate depends on the distance d^{-4} it quenches more than D653 just after the first graphene layer transfer. Quenching rates of both defects as a function of graphene layer are shown in Fig.6.10 (d).

6.1.3. Influence of Transition Rates

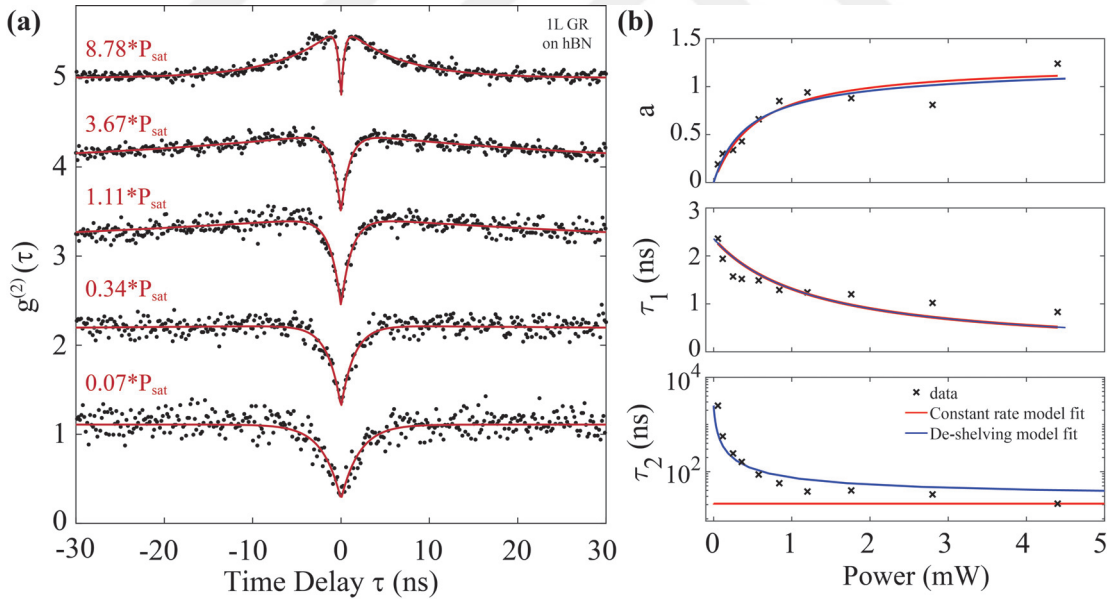


Figure 6.11. (a) Excitation power dependent $g^{(2)}(\tau)$ for the ZPL at 610 nm after graphene layer transfer. (b) The parameters calculated from $g^{(2)}(\tau)$ fits, a , τ_1 and τ_2 .

The population dynamics can be characterized by the effects of transition rates.

This was explained in Chapter 2, detailed by assuming the constant rate coefficient model in Neu (2012) with excitation rate k_{12} of the excited state linearly depends on the excitation laser power. Experimentally, we found that after coupling with graphene the emission intensity quenches also for each power value shown in emission intensity versus excitation power saturation relation in Fig. 6.4, where the black dots indicate pre-analyzed PL intensities with respect to excitation laser power and the red dots are the PL intensities of single layer graphene coupled system. Remember for a three level system, these rate equations were given in Chapter 2 in Eq.2.38, Eq.2.39 and Eq.2.40 and after graphene coupling in Eq.2.76, Eq.2.77 and Eq.2.78. As explained, summation of the differential equations of population changes of the system is equal to 1, but under interaction with graphene the decay rates decreases due to FRET decay rate k_{FRET} as shown in Fig.2.18. We ignored the effect of FRET from k_{23} and k_{31} because they have negligible effects as discussed in Neu (2012):

$$k_{21} \longrightarrow k'_{21} + k_{FRET}, \quad (6.7)$$

$$k_{23} \longrightarrow k'_{23}, \quad (6.8)$$

$$k_{31} \longrightarrow k'_{31}. \quad (6.9)$$

In the case all effects of FRET on decay rates have been taken into account as following:

$$k_{21} \longrightarrow k'_{21} + k_{F21}, \quad (6.10)$$

$$k_{23} \longrightarrow k'_{23} + k_{F23}, \quad (6.11)$$

$$k_{31} \longrightarrow k'_{31} + k_{F31}, \quad (6.12)$$

where k_{F21} , k_{F23} and k_{F31} are the contributions to the k_{FRET} from the each decay rate.

We have been measured power dependent second order correlation functions, $g^{(2)}(\tau)$, after the emitter and a single layer graphene coupling as shown the ZPL at 610 nm in Fig.6.2 (b). According to the second order correlation function for a three level model as given:

$$g^{(2)}(\tau) = 1 - (1 + a)e^{-|\tau|/\tau_1} + ae^{-|\tau|/\tau_2}. \quad (6.13)$$

The parameters of the $g^{(2)}(\tau)$ function are given by

$$\tau_{1,2} = 2/(A \pm \sqrt{A^2 - 4B}), \quad (6.14)$$

$$A = k_{12} + k_{21} + k_{23} + k_{31}, \quad (6.15)$$

$$B = k_{12}k_{23} + k_{12}k_{31} + k_{21}k_{31} + k_{23}k_{31}, \quad (6.16)$$

$$a = \frac{1 - \tau_2 k_{31}}{k_{31}(\tau_2 - \tau_1)}. \quad (6.17)$$

The excitation power dependent $g^{(2)}(\tau)$ functions were fitted (in Fig.6.11 (a)) and these parameters were calculated for each power value (in Fig.6.11 (b)). First, define the a , τ_1 and τ_2 values from the fits of each $g^{(2)}(\tau)$ function according to the experimental data. Using the limiting values of these parameters from the data the rates can be calculated. The extracted data were fitted by the red lines shown in Fig.6.11 (b). As seen the model is not sufficient to fit the τ_2 , especially for the low excitation powers. The relations of rate coefficients according to the three-level constant rate model (Neu (2012)) as following:

$$k_{31} = \frac{1}{(1 + a^\infty)\tau_2^\infty}, \quad (6.18)$$

$$k_{21} = \frac{1}{\tau_1^0} - k_{23}, \quad (6.19)$$

$$k_{23} = k_{31}a^\infty, \quad (6.20)$$

$$k_{21} + k_{23} > k_{31}. \quad (6.21)$$

There is another possibility of defect states, that can be obey de-shelving model rather than constant rate model. As shown in Fig.6.12, the model includes an excitation from the shelving state to higher lying states and returns back to the ground state. To fit the model and the experimental data of τ_2 values the limiting value of $k_{31} = \frac{1}{\tau_2^0}$ is used to take into account the low excitation power values. Additionally, in the model k_{31} depends

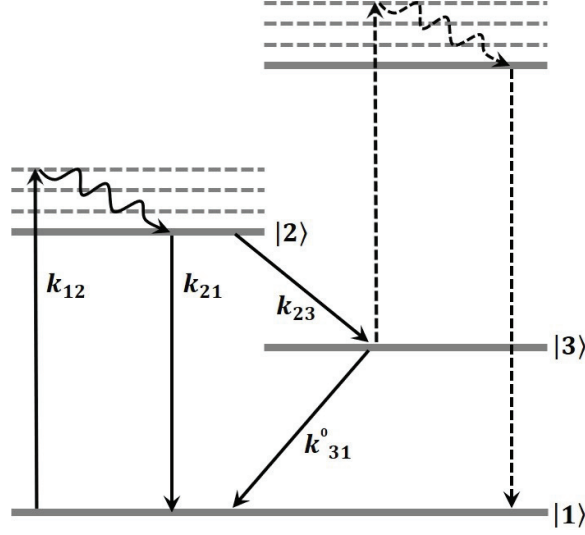


Figure 6.12. Schematic representation of the de-shelving model with higher lying states from the excited states.

on the intensity following a saturation behavior with respect to experimental observations in Neu (2012):

$$k_{31} = \frac{d \cdot P}{P + c} + k_{31}^0, \quad (6.22)$$

where k_{31}^0 is intensity independent rate. Using this rate equation modulation and $k_{21} + k_{23} > k_{31}^0$ for the de-shelving model the other rate relations can be expanded as following:

$$k_{31}^0 = \frac{1}{\tau_2^0}, \quad (6.23)$$

$$k_{21} = \frac{1}{\tau_1^0} - k_{23}, \quad (6.24)$$

$$k_{23} = \frac{1}{\tau_2^\infty} - k_{31}^0 - d, \quad (6.25)$$

$$d = \frac{\frac{1}{\tau_2^\infty} - (1 + a^\infty) \frac{1}{\tau_2^0}}{a^\infty + 1}. \quad (6.26)$$

Using the limiting values from the experimental data the rates were calculated with respect to de-shelving model relations and the experimental data were fitted by blue lines in Fig.6.11 (b). As seen, the model is sufficiently fit the data of τ_2 , as well.

The aim of this analyses in this section is to estimate the rate coefficient of before and after graphene coupling. However, as explained the experimental data of power dependent $g^{(2)}(\tau)$ belong to coupled with graphene conditions. The excitation power dependent intensity relation of before and after graphene coupling was shown in Fig.6.4. As seen, although the saturation power of the emission is not influenced, the saturation emission rate of before ($I_{sat,BG}$) and after graphene ($I_{sat,AG}$) is around 2 as expected from the individual intensity quenching rate. The ZPL intensity is quenched by a factor of 2 almost at all excitation powers after the graphene transfer on the source. Now, using our calculated rates these experimental excitation power series can be fit with respect to constant rate model and de-shelving model. To this aim, in order to calculate the steady state solution of the excited state before the graphene layer, we used the same rate of k_{31} because it has negligible effect. However, k_{21} and k_{23} were reduced by a factor of 2 as observed from the measured data. The extracted rates are given in Table 6.1.

Table 6.1. The extracted rates for before and after graphene coupling with respect to constant rate model (CRM) and de-shelving model (DSM).

	After			Before		
	k_{F21}	k_{F23}	k_{F31}	k_{21}	k_{23}	k_{31}
CRM	k_{21}	k_{23}	0	0.1987	0.0132	0.0106
DSM	k_{21}	k_{23}	0	0.0994	0.0065	0.0002

According to these extracted rates the experimental excitation power dependent intensity series were fit and shown in Fig.6.13. As it is seen, the red solid lines (after graphene coupling) and also black solid lines (before graphene coupling) fit very well with the experimental data.

As summary, the slight effects of two model can be observed at high power values of excitation power series in Fig.6.13. The difference is the distance between the fit lines which are getting closer for the constant rate model, while the lines are getting away from each other for de-shelving model. However, according to our data to correctly fit the τ_2 value, the k_{31} depends on the intensity following a saturation behavior should be taken into account. This assumption affects the extracted values of k_{21} and k_{23} by a factor of 2

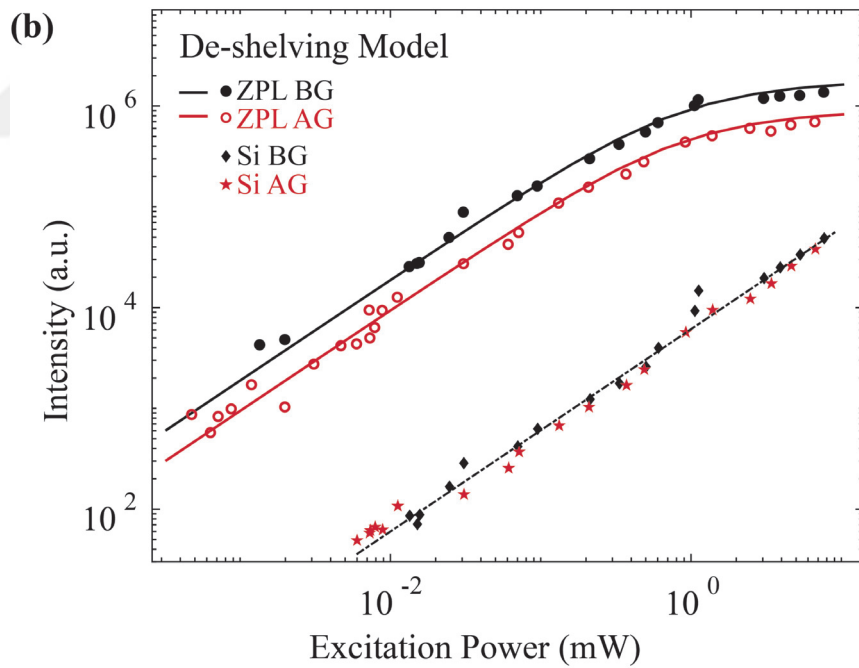
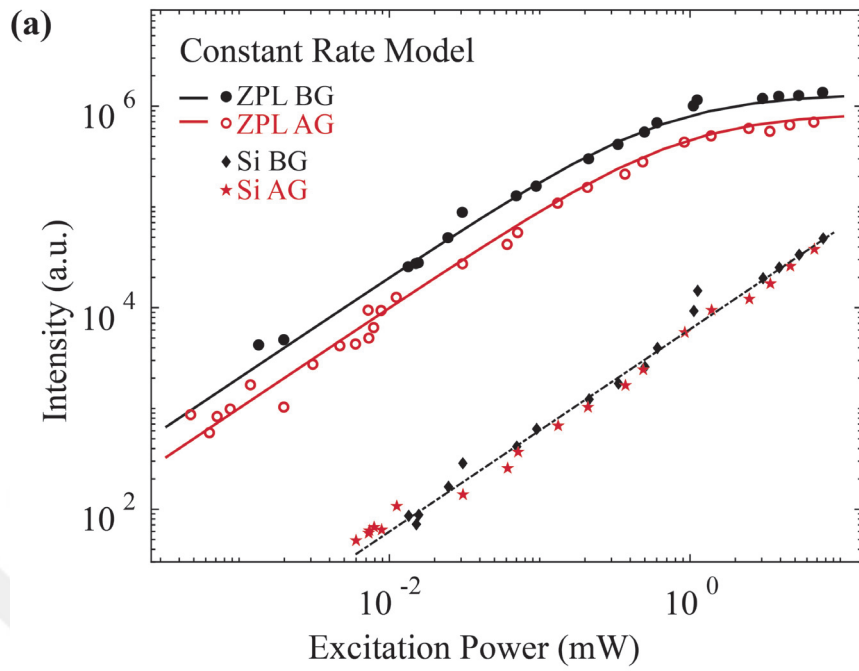


Figure 6.13. (a) The constant rate model and (b) de-shelving model rate equations are used to fit experimental power series of before and after graphene coupling

which is also the quenching rate of the intensities after graphene coupling. However, the value of k_{31} decreased with the assumptions of de-shelving model by a factor of 50, but in both model its effect is very lower than k_{21} and k_{23} .

6.1.4. Lifetime Measurements of Static Quenching

The single layer graphene is transferred on hBN dropcasted $\text{Al}_2\text{O}_3/\text{Si}$ substrate by photoresist assisted transfer method. Placing a graphene layer near field (< 50 nm) to the emitter yields a coupling between them (Reserbat-Plantey et al. (2016); Salihoglu et al. (2016)). Nonradiatively interaction between the emission from a defect center in hBN and a single layer graphene resulting electron-hole pair excitations (i.e., Förster-like energy transfer) is shown in Fig.6.1. Theoretical (Swathi and Sebastian (2009); Gómez-Santos and Stauber (2011)) and experimental (Gaudreau et al. (2013); Stöhr et al. (2012); Kim et al. (2010); Mazzamuto et al. (2014)) studies are showed that the coupling leads to emission quenching and a shorter lifetime of the emitters.

To measure the lifetime, the average decay time of an emitter's excited state, the time difference between the excitation laser pulse and the following detected photon is recorded repeatedly for a sufficient enough time period. These time differences for each count are plotted to obtain a histogram. The $1/e$ width of the exponentially decaying distribution gives the excited state lifetime $\tau = 1/\gamma$. For $\Delta t \rightarrow 0$ the distribution reaches to zero due to the finite response time of the detector. To calculate excited state lifetime, the decay of the plotted histogram can be fit by $e^{-t/\tau}$.

In this study, the excited state lifetime of a SP emission before and after graphene transfer were calculated. As seen in Fig.6.14, for all the measurements the besides PL spectra, optical microscopy image, excitation polarization and excitation power effects were recorded by both 532 nm CW and 483 nm pulsed laser excitation. Than the lifetime measurement was performed by the pulsed laser. As seen, the excited state lifetime is decreased after graphene transfer (red) and corresponding single spectra show intensity quenching when before graphene (black line) and after graphene coupled (red line) spectra.

The single photon emission quenching ratio was increased by addition of individual graphene layers on the top. The quenching of the emission also led to decreased excited state lifetime even after two individual layers of graphene coupling which is shown in Fig.6.15.

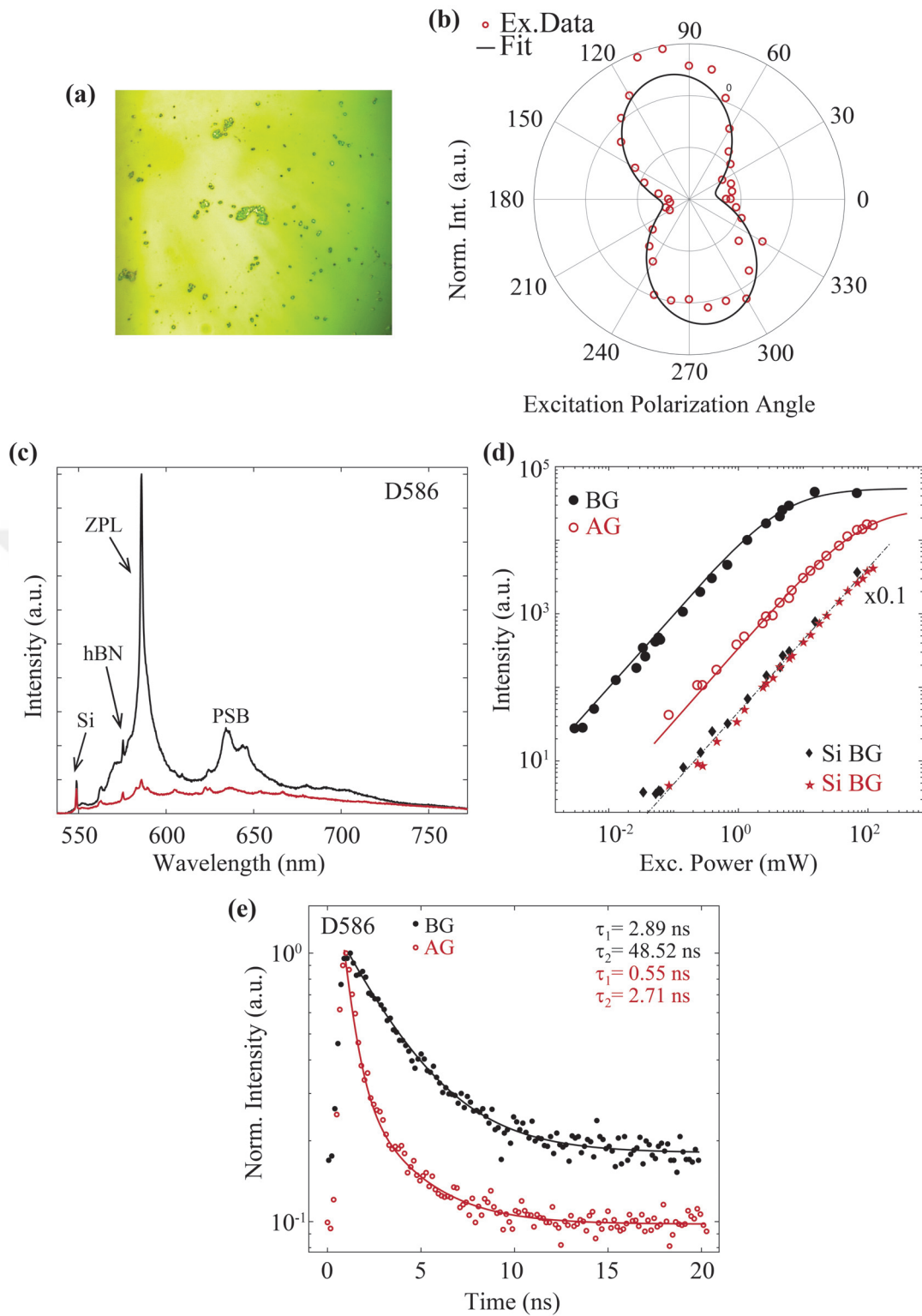


Figure 6.14. (a) Optical microscopy image of the hBN flake cluster. (b) excitation polarization versus emission intensity (c) PL spectra of before (black) and after (red) graphene transfer show emission quenching. (d) Excitation power versus emission intensity. (e) Lifetime measured at 50 MHz frequency. Black dots are the experimental statistics of before graphene and the line is one order fit. The red dots belong to after graphene statistics.

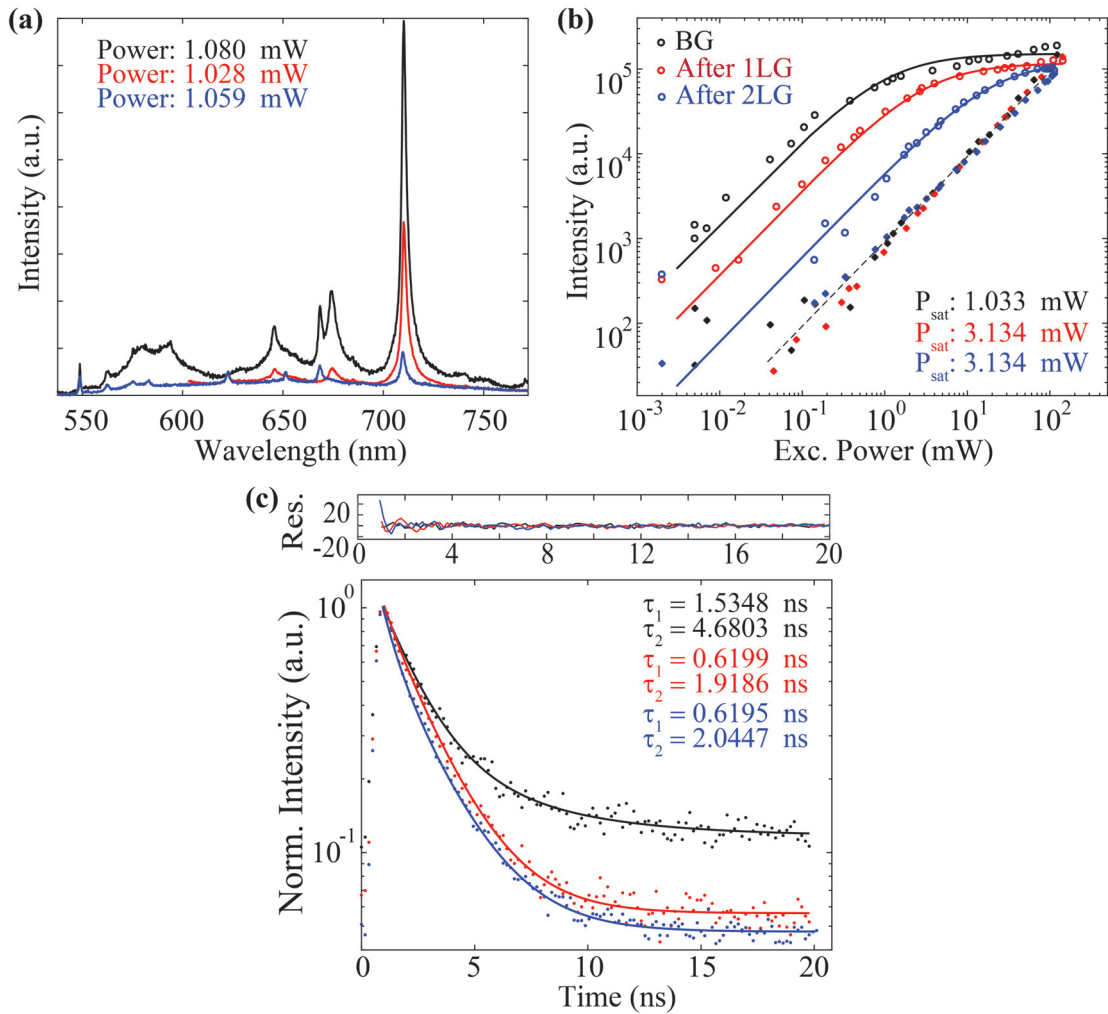


Figure 6.15. (a) Excitation power versus emission intensity. (b) PL spectra of before (black line), after one layer graphene transfer (red line) and after a second layer graphene (blue line) transfer. (c) Lifetime measured at 50 MHz frequency. Black dots are the experimental statistics of before graphene and the line is one order fit. The red dots belong to after 1 layer graphene statistics and the blue dots refer to after a second layer graphene transfer.

6.2. Reversible Energy Transfer: Active Quenching

Graphene has single atom-thick structure and low density of states. These enable electrically tuning of its optical properties by Fermi energy shifting (Wang et al. (2008); Wu et al. (2017)). Electrostatic doping of graphene modulates optical gap of $2E_F$ for interband transitions due to Pauli blocking (Polat and Kocabas (2013)). In Fig.6.16 the Fermi level shifting of graphene with respect to n-type doping and p-type doping are shown.

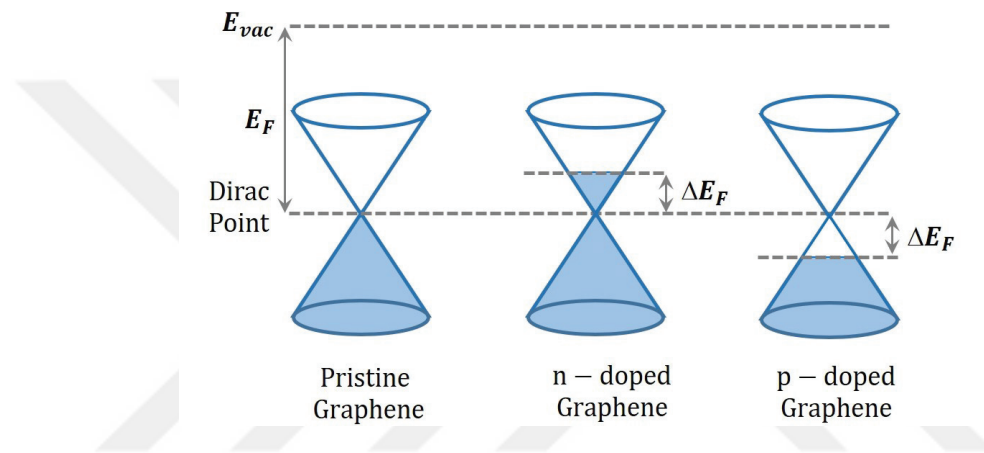


Figure 6.16. Energy band diagrams of the pristine, n-doped and p-doped graphene with their Fermi levels.

There are reports on graphene hybrid optoelectronic devices. Recently, graphene is used to modulate light emission from nitrogen-vacancy centers (NVCs) in nanodiamonds which are single photon emitters at 3 K (Reserbat-Plantey et al. (2016)). In the study, the nanomotion of the graphene on the point defect provided by modest voltages applied to a gate electrodes enables altering the NVC emission intensity. Interaction between emitting point dipole and induced dipoles in graphene effects the excited emitter relaxation rate as $\Gamma_g \propto d^{-4}$ for small separations ($d < 50$ nm) (Reserbat-Plantey et al. (2016); Gaudreau et al. (2013)). According to their results, the emission intensity is strongly reduced with decreasing graphene-emitter separation. In another study, graphene is used to control light emission from QDs which are used for light-emitting applications (Salihoglu et al. (2016)). In this way, emission quenching depends on both the emitter-graphene distance and doping level of graphene.

In present studies reversible fluorescence quenching of single photon emitter in a two dimensional material at room temperature has not been demonstrated. In this study, graphene is placed near field distance of the single photon emitter in hBN. We use hBN flakes in ethanol solution until we prove the transfer of 2D hBN to silicon substrate is achieved.

6.2.1. Device Structure

Reversible quenching can be obtained by shifting Fermi level of graphene to restrict electronic transitions in graphene (Fig.6.17 (a)). In this study, Fermi level was shifted as large as 1.2 eV (Polat and Kocabas (2013)) using ionic liquid (IL) based electrolyte gating in a large area device shown in Fig.6.17 (b) and (c). Schematic representation of the electrolyte-gated device restricts the inter-band electronic transitions in graphene. In that way, fluorescence quenching of single photon emission can be con-

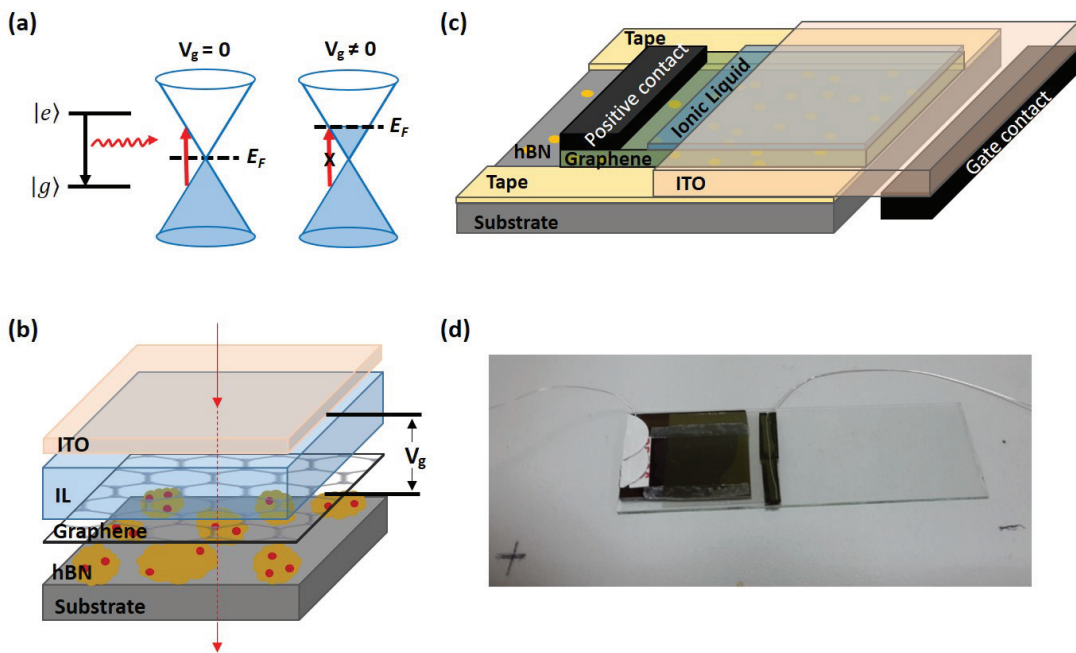


Figure 6.17. (a) Schematic representation of the Fermi level shifting of graphene by gate voltage and energy transfer restriction. (b-c) Schematic representation of the designed device for reversible fluorescence quenching of SPE. (d) The used device in the experiments.

trolled in the visible range of the spectrum, which is shown in Fig.6.17 (b,c).

In Fig.6.17 (b), the designed capacitor compose of Si substrate hBN, graphene, ionic liquid and Indium tin oxide (ITO) as a traditional transparent conductive electrode. Graphene on hBN and ITO are the electrodes. To reach high doping levels, an ionic liquid is used as electrolyte between graphene and ITO that leads to shift Fermi level of graphene up to 1.2 eV. The designed device scheme is shown in Fig.6.17 (b) and its more realistic components are shown in Fig.6.17 (c). Additionally, the constructed large area device image is shown in Fig.6.17 (d) on a microscope slide. The resonance energy transfer from the single photon source to graphene mechanism and modulating the doping level by gate voltage lead to reversible control of emission intensity. To observe this, the PL spectra of a defect center in hBN under a single graphene layer was recorded with respect to varied positive and negative gate voltages.

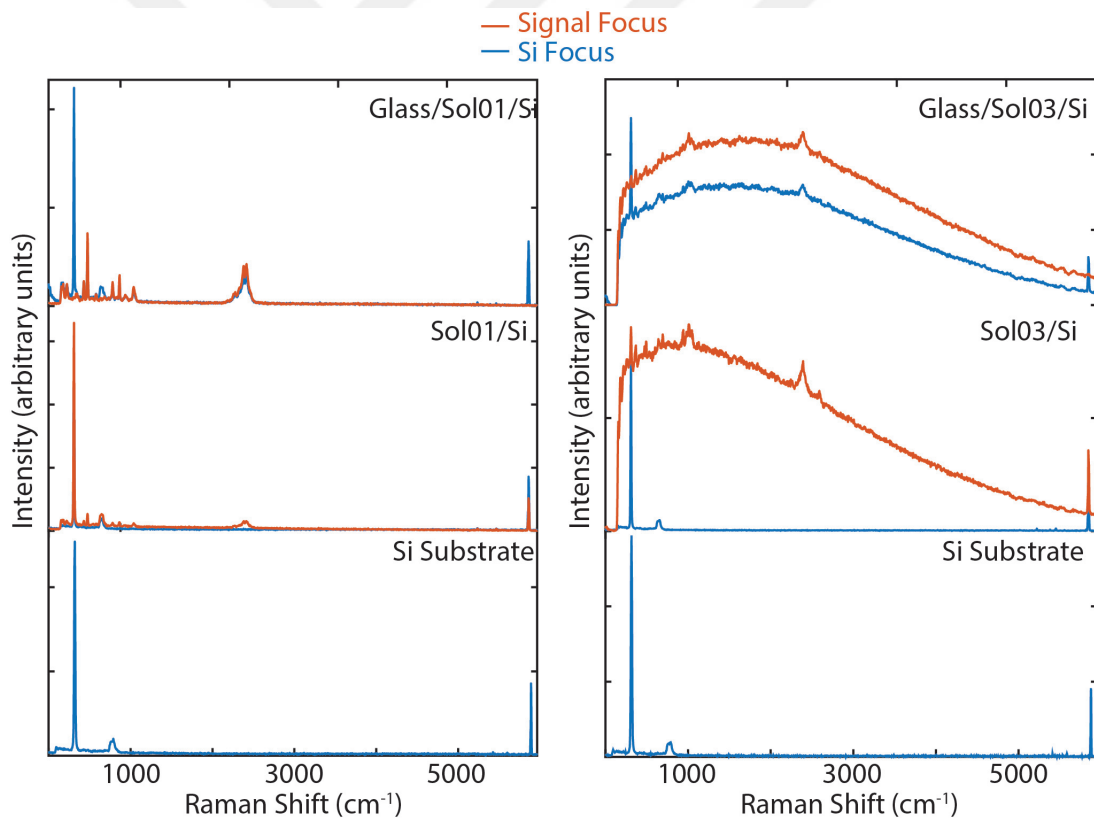


Figure 6.18. The background effect of ionic liquid. The left panel includes the Raman spectra of Si substrate, solution 1 (Sol01)/Si and glass/(Sol01)/Si. The right panel shows the background of another solution (Sol03).

6.2.2. The Effect of Ionic Liquid

The most suitable ionic liquid must have the minimum background effect to observe the proper change on single photon emission. Ten different electrolytes were analyzed by PL to observe their background contributions to the spectrum. As shown in Fig.6.18, there were no background when the laser was focused on Si substrate. However, there is a thickness of the liquid and the hBN flakes with graphene cover were embedded in this liquid. Thus, the laser was focused upward from the substrate and some of the electrolytes give a broad and strong background, seen in right panel of Fig.6.18. After that according to the device structure the measurements of different focus lengths were repeated by using ITO on the top. The solution 01 was chosen to use reversible quenching experiments due to no background observed.

6.2.3. Demonstration of Active Quenching

In the study, static quenching of SP emission from defect center in hBN is demonstrated so far. To integrate optoelectronic systems the quenching rate is controlled dynamically by gate voltage. The schematic illustration of the capacitor structure is shown in Fig.6.17. Graphene on hBN and ITO are the electrodes. To reach high doping levels an ionic liquid is used as electrolyte between graphene and ITO that leads to raise Fermi level of graphene up to 1.2 eV. The PL spectra of a SP emission from a defect center in hBN under coupled with three single graphene layers were recorded with respect to varied gate voltage, shown in Fig.6.19 (a). According to the distance between the graphene and SP source single layer graphene can quench the emission up to a certain rate. As explained before, the additional graphene layers increase the energy transfer rate and the possibility to totally close the emission is increased.

As seen in Fig.6.19 (b), the PL intensity saturates at the threshold voltage value of 1.4 V. The SP emission at 725 nm shows up after 0.5 V and its intensity increases up to 1.4 V. The ZPL at 725 nm (1.7 eV) with a phonon sideband at 805 nm is controlled between ± 2 because of its energy (1.7 eV) it is close to the Fermi level and shows up by low voltage values as 0.5 V. If another ZPL was observed around 600 nm it showed up with the voltage larger than 0.5 V. This clearly indicates that doping increases the Fermi level from infrared to visible region.

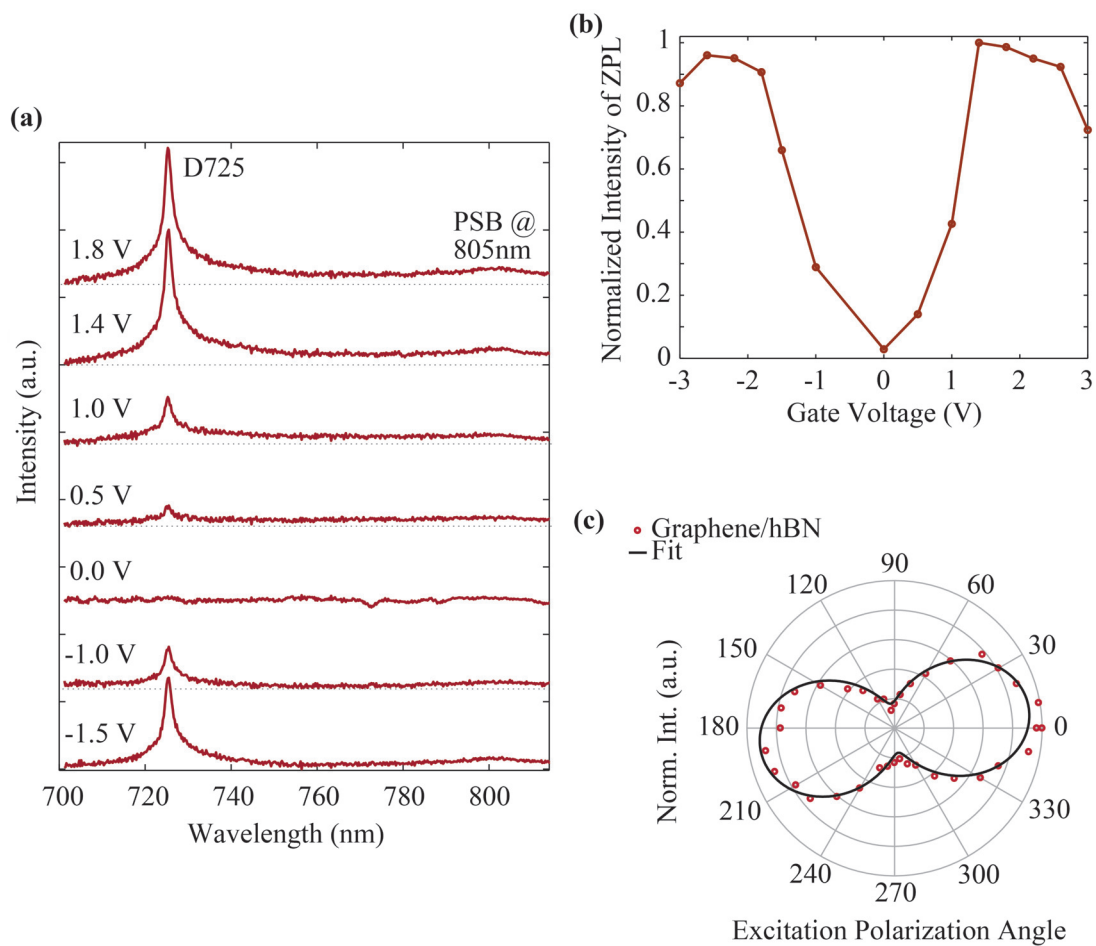


Figure 6.19. (a) After three layer graphene (3 L GR) are placed on hBN individually, PL intensity variation of the SP emission at 725 nm with respect to gate voltages are shown. (b) The effect of alteration of the gate voltage on PL intensity of ZPL at 725 nm. (c) The excitation polarization dependent ZPL emission intensity under 1.4 V gate voltage.

6.2.4. Summary

The fluorescence of the subjected material can be suppressed by graphene. Non-radiative energy transfer between graphene and the emitter is controlled by distance between them (d^{-4}) or graphene layer number (increasing coupling channels). In this study, the distance could not be estimated, thus the emission was quenched by coupling the emitter with graphene layers. We also discussed correction factors with respect to Si and hBN Raman signals. As we thought after graphene transfer on hBN flake the silicon Raman signal from the substrate should not be changed. However, there should be focal length change of the single defect center because of the hBN flake thickness and graphene layer thickness are comparable. Thus, we need to correct the intensities by considering these effects. Additionally, PSB peaks were quenched by graphene layers.

The FRET-like energy transfer between graphene and the defect center can be modulated gradually and reversibly by designing a device structure.

Summarizing, we demonstrated FRET-like energy transfer from a SP emitter in hBN to graphene at room temperature. This non-radiative energy transfer mechanism was observed from PL quenching after graphene transfer. Furthermore, the quenching rate increased by additional graphene layers by opening up new energy transfer channels from the emitter and the graphene. In that way, the SP emission was almost closed statically. After that we demonstrated a device structure with an ionic liquid (IL) electrolyte gating to obtain maximum conductance and Fermi level shifting. Altering gate voltage, reversibly and gradually modulated the SP emission. We reported a graphene based optoelectronic device which is used to modulate the SP emission intensity at nanoscale as an on/off switch.

CHAPTER 7

CONCLUSIONS

This thesis was focused on the experimental studies on room temperature SP sources. In particular, defects in WO_3 and hBN were analysed as bright and stable SP sources. We have investigated emission characteristics of these defects along with manipulation of their properties with nanostructures. The interaction between the emitter and gold nanoparticles revealed an enhancement of the emission by a resonance plasmonic effect. On the other hand, the coupling between the emitter and a graphene sheet provided the quenching of the emission. The quenching was reversible under the action of a bias potential on the graphene sheet.

According to the literature, single-photon emission from TMDCs originates from localized weakly bound excitons at cryogenic temperatures due to the small exciton binding energies. However, room temperature SP emission from WS_2 can be obtained by creating WO_3 defects. As far as we know there is only one recent work in the literature about such an emission. In our studies, we investigated the room temperature single photon emission characteristics directly from the defects in WO_3 , in detail for the first time. 2D PL maps revealed that the emission originated from localized centers in WO_3 . The excitation and emission polarization related intensity measurements showed the linear dipole behavior of the emitter as an indication of the single photon behavior. Additionally, excitation power related intensity saturation confirmed the SP behavior. Density functional theory calculations showed that the source of the emission are probably oxygen vacancy defects. Additionally, we were able to increase the intensity of the single photon emission in WO_3 as much as 20 times due to weak coupling of SP center with plasmonic gold nanoparticles which is very promising for their nano photonic applications.

Furthermore, the optical characteristics of SP emission from defects in hBN were investigated. 2D PL maps indicated that the emission originated from a single localized emitter in an hBN flake. The PL spectrum of the emission showed a high brightness and stability. Photon correlation measurements verified the second order correlation function at zero delay time, $g^{(2)}(0) < 0.5$, and indicated the emission is a stream of SPs. Additionally, the excitation power and the single dipole behavior of the emission were analyzed before and after a single graphene layer placement on the hBN and PL intensity quenching was observed. In that way, fluorescence quenching of SP emission from defect centers

of hBN flakes by Förster-like resonance energy transfer was demonstrated for the first time. In addition to ZPL, phonon side band peaks were also quenched by the nonradiative energy transfer. The quenching rate depends on the distance between the emitter and the graphene layer. In our study, the distance could not be controlled. Thus, second and third graphene layers were introduced to increase the quenching further up to $\sim 99\%$ by addition of energy transfer channels which means the emission signal was almost turned off statically. After the static quenching analyses, active (reversible) control of the quenching rate by an electrically controlled device was demonstrated. Using this device, the Fermi level of a graphene layer covering an hBN defect was increased up to 1 eV by an applied gate voltage. Thus, altering the Fermi level of graphene lead to a reversible and dynamic control (on/off) of the nonradiative quenching channel between the defect in hBN and graphene layer. In summary, the analyses on room temperature SP emission sources are very important for the future technologies in the fields of quantum information, quantum computing, and medical applications. This thesis analyses such SP emission from defects in hBN and WO_3 at room temperature. Additional analyses of their optical properties and modulation of these properties by nanostructures were given. We elucidated our studies and results in fair detail. Finally, we hope that our results will be a useful resource for further quantum optics researches.

REFERENCES

- Aharonovich, I., D. Englund, and M. Toth (2016, sep). Solid-state single-photon emitters. *Nature Photonics* 10(10), 631–641.
- Ajayi, O. A., N. C. Anderson, M. Cotlet, N. Petrone, T. Gu, A. Wolcott, F. Gesuele, J. Hone, J. S. Owen, and C. W. Wong (2014, apr). Time-resolved energy transfer from single chloride-terminated nanocrystals to graphene. *Applied Physics Letters* 104(17), 171101.
- Akhtar, M. B. (2010). *Fluorescence Lifetime Measurement using Time Correlated Single Photon Counting*. Ph. D. thesis, Lund University.
- Attacalite, C., M. Bockstedte, A. Marini, A. Rubio, and L. Wirtz (2011, apr). Coupling of excitons and defect states in boron-nitride nanostructures. *Physical Review B - Condensed Matter and Materials Physics* 83(14), 144115.
- Balci, O., N. Kakenov, E. Karademir, S. Balci, S. Cakmakyapan, E. O. Polat, H. Caglayan, E. Özbay, and C. Kocabas (2018, jan). Supplementary Materials for Electrically switchable metadevices via graphene. *Science Advances* 4(1), eaao1749.
- Benson, O. (2009). Elements of Nanophotonics - Chapter 6: Physics of Single Quantum Emitters. *Elements of Nanophotonics Course Script & Materials(c)*, 181–207.
- Berhane, A. M., K.-Y. Jeong, C. Bradac, M. Walsh, D. Englund, M. Toth, and I. Aharonovich (2018, apr). Photophysics of GaN single-photon emitters in the visible spectral range. *Physical Review B* 97(16), 165202.
- Berkdemir, A., H. R. Gutiérrez, A. R. Botello-Méndez, N. Perea-López, A. L. Elías, C.-I. Chia, B. Wang, V. H. Crespi, F. López-Urías, J.-C. Charlier, H. Terrones, and M. Terrones (2013, dec). Identification of individual and few layers of WS₂ using Raman Spectroscopy. *Scientific Reports* 3(1), 1755.
- Bolotin, K., K. Sikes, Z. Jiang, M. Klima, G. Fudenberg, J. Hone, P. Kim, and H. Stormer (2008, jun). Ultrahigh electron mobility in suspended graphene. *Solid State Communications* 146(9-10), 351–355.

- Born, M. and R. Oppenheimer (1927). Zur Quantentheorie der Molekeln. *Annalen der Physik* 389(20), 457–484.
- Bringans, R. D., H. Höchst, and H. R. Shanks (1981, Sep). Defect states in wo_3 studied with photoelectron spectroscopy. *Phys. Rev. B* 24, 3481–3489.
- Brouri, R., A. Beveratos, J.-P. Poizat, and P. Grangier (2000, sep). Photon antibunching in the fluorescence of individual color centers in diamond. *Optics Letters* 25(17), 1294.
- Brown, R. H. and R. Twiss (1954, jul). LXXIV. A new type of interferometer for use in radio astronomy. *The London, Edinburgh, and Dublin Philosophical Magazine and Journal of Science* 45(366), 663–682.
- Castro Neto, A. H., F. Guinea, N. M. R. Peres, K. S. Novoselov, and A. K. Geim (2009, jan). The electronic properties of graphene. *Reviews of Modern Physics* 81(1), 109–162.
- Cazzanelli, E., C. Vinegoni, G. Mariotto, A. Kuzmin, and J. Purans (1999a, feb). Low-Temperature Polymorphism in Tungsten Trioxide Powders and Its Dependence on Mechanical Treatments. *Journal of Solid State Chemistry* 143(1), 24–32.
- Cazzanelli, E., C. Vinegoni, G. Mariotto, A. Kuzmin, and J. Purans (1999b). Raman study of the phase transitions sequence in pure wo_3 at high temperature and in hxwo_3 with variable hydrogen content. *Solid State Ionics* 123(1), 67 – 74.
- Ceperley, D. M. and B. J. Alder (1980, aug). Ground State of the Electron Gas by a Stochastic Method. *Physical Review Letters* 45(7), 566–569.
- Chakraborty, C., L. Kinnischtzke, K. M. Goodfellow, R. Beams, and A. N. Vamivakas (2015, jun). Voltage-controlled quantum light from an atomically thin semiconductor. *Nature Nanotechnology* 10(6), 507–511.
- Chen, Z., S. Berciaud, C. Nuckolls, T. F. Heinz, and L. E. Brus (2010). Energy Transfer from Individual Semiconductor Nanocrystals to Graphene. *ACS Nano* 4(5), 2964–2968.
- Choi, S., B. C. Johnson, S. Castelletto, C. Ton-That, M. R. Phillips, and I. Aharonovich

- (2014, jun). Single photon emission from ZnO nanoparticles. *Applied Physics Letters* 104(26), 261101.
- Chunlang, W. (2007). *A solid state single photon source based on SiV centers in diamond*. Ph. D. thesis, Ludwig-Maximilians-Universität München.
- Daniel, M., B. Desbat, J. Lassegues, B. Gerand, and M. Figlarz (1987, apr). Infrared and Raman study of WO₃ tungsten trioxides and WO₃·xH₂O tungsten trioxide hydrates. *Journal of Solid State Chemistry* 67(2), 235–247.
- Davies, G. (1981, jul). The Jahn-Teller effect and vibronic coupling at deep levels in diamond. *Reports on Progress in Physics* 44(7), 787–830.
- Di Valentin, C., F. Wang, and G. Pacchioni (2013, nov). Tungsten Oxide in Catalysis and Photocatalysis: Hints from DFT. *Topics in Catalysis* 56(15-17), 1404–1419.
- Diehl, R., G. Brandt, and E. Salje (1978, Apr). The crystal structure of triclinic WO₃. *Acta Crystallographica Section B* 34(4), 1105–1111.
- Djerad, S., L. Tifouti, M. Crocoll, and W. Weisweiler (2004, feb). Effect of vanadia and tungsten loadings on the physical and chemical characteristics of V₂O₅-WO₃/TiO₂ catalysts. *Journal of Molecular Catalysis A: Chemical* 208(1-2), 257–265.
- Dong, J.-W., X.-D. Chen, H. Zhu, Y. Wang, and X. Zhang (2017, mar). Valley photonic crystals for control of spin and topology. *Nature Materials* 16(3), 298–302.
- Exarhos, A. L., D. A. Hopper, R. R. Grote, A. Alkauskas, and L. C. Bassett (2017). Optical Signatures of Quantum Emitters in Suspended Hexagonal Boron Nitride. *ACS Nano* 11(3), 3328–3336.
- Federspiel, F., G. Froehlicher, M. Nasilowski, S. Pedetti, A. Mahmood, B. Doudin, S. Park, J.-O. Lee, D. Halley, B. Dubertret, P. Gilliot, and S. Berciaud (2015, feb). Distance Dependence of the Energy Transfer Rate from a Single Semiconductor Nanostructure to Graphene. *Nano Letters* 15(2), 1252–1258.
- Flores-Mena, J. E., J. Díaz-Reyes, and J. A. Balderas-López (2012). Structural properties of WO₃ dependent of the annealing temperature deposited by hot-filament metal

- oxide deposition. *Revista Mexicana de Fisica* 58(6), 504–509.
- Förster, T. (1948, jan). Zwischenmolekulare Energiewanderung und Fluoreszenz. *Annalen der Physik* 437(1-2), 55–75.
- Forster, T. (1951). *Fluoreszenz organischer Verbindungen*. Göttingen: Vandenhoeck und Ruprecht.
- Fox, M. (2006). *Quantum Optics: An Introduction*. OUP Oxford.
- Gaebel, T., I. Popa, A. Gruber, M. Domhan, F. Jelezko, and J. Wrachtrup (2004, jul). Stable single-photon source in the near infrared. *New Journal of Physics* 6, 98–98.
- Gaudreau, L., K. J. Tielrooij, G. E. D. K. Prawiroatmodjo, J. Osmond, F. J. G. de Abajo, and F. H. L. Koppens (2013, may). Universal Distance-Scaling of Nonradiative Energy Transfer to Graphene. *Nano Letters* 13(5), 2030–2035.
- Gerry, C. and P. Knight (2004). *Introductory Quantum Optics*, Volume 66. Cambridge: Cambridge University Press.
- Gómez-Santos, G. and T. Stauber (2011, oct). Fluorescence quenching in graphene: A fundamental ruler and evidence for transverse plasmons. *Physical Review B* 84(16), 165438.
- González-Borrero, P. P., F. Sato, A. N. Medina, M. L. Baesso, A. C. Bento, G. Baldissera, C. Persson, G. A. Niklasson, C. G. Granqvist, and A. Ferreira da Silva (2010, feb). Optical band-gap determination of nanostructured WO₃ film. *Applied Physics Letters* 96(6), 061909.
- Goodfellow, K. M., C. Chakraborty, K. Sowers, P. Waduge, M. Wanunu, T. Krauss, K. Driscoll, and A. N. Vamivakas (2016). Distance-dependent energy transfer between CdSe/CdS quantum dots and a two-dimensional semiconductor. *Applied Physics Letters* 108(2), 2–6.
- Gorbachev, R. V., I. Riaz, R. R. Nair, R. Jalil, L. Britnell, B. D. Belle, E. W. Hill, K. S. Novoselov, K. Watanabe, T. Taniguchi, A. K. Geim, and P. Blake (2011, feb). Hunting for Monolayer Boron Nitride: Optical and Raman Signatures. *Small* 7(4), 465–468.

- Gordon, L., J. R. Weber, J. B. Varley, A. Janotti, D. D. Awschalom, and C. G. Van de Walle (2013, oct). Quantum computing with defects. *MRS Bulletin* 38(10), 802–807.
- Govorov, A., H. Martínez, P. Ludwig, and H. V. Demir (2016). *Understanding and Modeling Förster-type Resonance Energy Transfer (FRET): introduction to FRET*, Volume 1 of *SpringerBriefs in Applied Sciences and Technology*. Singapore: Springer Singapore.
- Granqvist, C. (2000, jan). Electrochromic tungsten oxide films: Review of progress 1993-1998. *Solar Energy Materials and Solar Cells* 60(3), 201–262.
- Graphene-supermarket (2016). graphene-supermarket.
- Guzelturk, B. and H. V. Demir (2016). Near-Field Energy Transfer Using Nanoemitters For Optoelectronics. *Advanced Functional Materials* 26(45), 8158–8177.
- He, X., N. F. Hartmann, X. Ma, Y. Kim, R. Ihly, J. L. Blackburn, W. Gao, J. Kono, Y. Yomogida, A. Hirano, T. Tanaka, H. Kataura, H. Htoon, and S. K. Doorn (2017). Tunable room-Temperature single-photon emission at telecom wavelengths from sp³ defects in carbon nanotubes. *Nature Photonics* 11(9), 577–582.
- Hoang, T. B., G. M. Akselrod, and M. H. Mikkelsen (2016, jan). Ultrafast Room-Temperature Single Photon Emission from Quantum Dots Coupled to Plasmonic Nanocavities. *Nano Letters* 16(1), 270–275.
- Hodes, G., D. Cahen, and J. Manassen (1976, mar). Tungsten trioxide as a photoanode for a photoelectrochemical cell (PEC). *Nature* 260(5549), 312–313.
- Hohenberg, P. and W. Kohn (1964, nov). Inhomogeneous Electron Gas. *Physical Review* 136(3B), B864–B871.
- Holmes, M. J., K. Choi, S. Kako, M. Arita, and Y. Arakawa (2014, feb). Room-Temperature Triggered Single Photon Emission from a III-Nitride Site-Controlled Nanowire Quantum Dot. *Nano Letters* 14(2), 982–986.
- Iff, O., N. Lundt, S. Betzold, L. N. Tripathi, M. Emmerling, S. Tongay, Y. J. Lee, S.-H. Kwon, S. Höfling, and C. Schneider (2018, oct). Deterministic coupling of quan-

- tum emitters in WSe₂ monolayers to plasmonic nanocavities. *Optics Express* 26(20), 25944.
- Iqbal, M. Z., M. W. Iqbal, S. Siddique, M. F. Khan, and S. M. Ramay (2016, feb). Room temperature spin valve effect in NiFe/WS₂/Co junctions. *Scientific Reports* 6(1), 21038.
- Jackson, J. D. (1998). *Classical electrodynamics* (3 ed.). New York: John Wiley & Sons.
- Jiandong Qiao, J. Q., F. M. Fuhong Mei, and Y. Y. Yu Ye (2019). Single-photon emitters in van der Waals materials. *Chinese Optics Letters* 17(2), 020011.
- Jungwirth, N. R., B. Calderon, Y. Ji, M. G. Spencer, M. E. Flatté, and G. D. Fuchs (2016, oct). Temperature Dependence of Wavelength Selectable Zero-Phonon Emission from Single Defects in Hexagonal Boron Nitride. *Nano Letters* 16(10), 6052–6057.
- Kehl, W. L., R. G. Hay, and D. Wahl (1952). The structure of tetragonal tungsten trioxide. *Journal of Applied Physics* 23(2), 212–215.
- Kim, J., L. J. Cote, F. Kim, and J. Huang (2010, jan). Visualizing Graphene Based Sheets by Fluorescence Quenching Microscopy. *Journal of the American Chemical Society* 132(1), 260–267.
- Kimble, H. J., R. J. Cook, and A. L. Wells (1986, oct). Intermittent atomic fluorescence. *Physical Review A* 34(4), 3190–3195.
- Kimble, H. J., M. Dagenais, and L. Mandel (1977, sep). Photon antibunching in resonance fluorescence. *Physical Review Letters* 39(11), 691–695.
- Koffyberg, F., K. Dwight, and A. Wold (1979). Interband transitions of semiconducting oxides determined from photoelectrolysis spectra. *Solid State Communications* 30(7), 433 – 437.
- Kubota, Y., K. Watanabe, O. Tsuda, and T. Taniguchi (2007, aug). Deep Ultraviolet Light-Emitting Hexagonal Boron Nitride Synthesized at Atmospheric Pressure. *Science* 317(5840), 932–934.

- Kurtsiefer, C., S. Mayer, P. Zarda, and H. Weinfurter (2000, jul). Stable Solid-State Source of Single Photons. *Physical Review Letters* 85(2), 290–293.
- Lee, J., W. Bao, L. Ju, P. J. Schuck, F. Wang, and A. Weber-Bargioni (2014). Switching individual quantum dot emission through electrically controlling resonant energy transfer to graphene. *Nano Letters* 14(12), 7115–7119.
- Link, S. and M. A. El-Sayed (2003, oct). Optical Properties and Ultrafast Dynamics of Metallic Nanocrystals. *Annual Review of Physical Chemistry* 54(1), 331–366.
- Linkam (2016). Linkam Scientific Instruments, U.E.D.M.C.W., Tdworth, Surrey, UK.
- Liu, R.-F. and C. Cheng (2007, jul). Ab initio studies of possible magnetism in a BN sheet by nonmagnetic impurities and vacancies. *Physical Review B* 76(1), 014405.
- Loopstra, B. O. and P. Boldrini (1966, Jul). Neutron diffraction investigation of WO_3 . *Acta Crystallographica* 21(1), 158–162.
- Loudon, R. (2000). *The Quantum Theory of Light*. OUP Oxford.
- Lumerical Solutions, Inc. (2019). FDTD Solutions.
- Luo, Y., N. Liu, X. Li, J. C. Hone, and S. Strauf (2019, may). Single photon emission in WSe₂ up 160 K by quantum yield control. *2D Materials* 6(3), 035017.
- Ma, X., N. F. Hartmann, J. K. S. Baldwin, S. K. Doorn, and H. Htoon (2015, aug). Room-temperature single-photon generation from solitary dopants of carbon nanotubes. *Nature Nanotechnology* 10(8), 671–675.
- Martínez, L. J., T. Pelini, V. Waselowski, J. R. Maze, B. Gil, G. Cassabois, and V. Jacques (2016, sep). Efficient single photon emission from a high-purity hexagonal boron nitride crystal. *Physical Review B* 94(12), 121405.
- Matthias, B. T. and E. A. Wood (1951, Dec). Low temperature polymorphic transformation in WO_3 . *Phys. Rev.* 84, 1255–1255.
- Mazzamuto, G., A. Tabani, S. Pazzagli, S. Rizvi, A. Reserbat-Plantey, K. Schädler,

- G. Navickaite, L. Gaudreau, F. S. Cataliotti, F. Koppens, and C. Toninelli (2014, nov). Single-molecule study for a graphene-based nano-position sensor. *New Journal of Physics* 16(11), 113007.
- Mie, G. (1908). Beiträge zur Optik trüber Medien, speziell kolloidaler Metallösungen. *Annalen der Physik* 330(3), 377–445.
- Misra, P., D. Casimir, R. Garcia-Sanchez, and S. Baliga (2015). Raman spectroscopic characterization of carbon nanotubes & tungsten oxide of relevance to energy storage and gas sensing applications. *NSTI: Advanced Materials - TechConnect Briefs 2015 1*, 55–58.
- MIT OpenCourseWare (2006). Chapter 6 Interaction of Light and Matter.
- Museur, L., E. Feldbach, and A. Kanaev (2008, oct). Defect-related photoluminescence of hexagonal boron nitride. *Physical Review B* 78(15), 155204.
- Nair, R. R., P. Blake, A. N. Grigorenko, K. S. Novoselov, T. J. Booth, T. Stauber, N. M. R. Peres, and A. K. Geim (2008, jun). Fine Structure Constant Defines Visual Transparency of Graphene. *Science* 320(5881), 1308–1308.
- Naydenov, B., R. Kolesov, A. Batalov, J. Meijer, S. Pezzagna, D. Rogalla, F. Jelezko, and J. Wrachtrup (2009, nov). Engineering single photon emitters by ion implantation in diamond. *Applied Physics Letters* 95(18), 181109.
- Neitzke, O., A. Morfa, J. Wolters, A. W. Schell, G. Kewes, and O. Benson (2015, may). Investigation of Line Width Narrowing and Spectral Jumps of Single Stable Defect Centers in ZnO at Cryogenic Temperature. *Nano Letters* 15(5), 3024–3029.
- Neu, E., M. Fischer, S. Gsell, M. Schreck, and C. Becher (2011, nov). Fluorescence and polarization spectroscopy of single silicon vacancy centers in heteroepitaxial nanodiamonds on iridium. *Physical Review B* 84(20), 205211.
- Neu, E. K. (2012). *Silicon vacancy color centers in chemical vapor deposition diamond : new insights into promising solid state single photon sources*. Ph. D. thesis, Universität des Saarlandes.

- Nguyen, M., S. Kim, T. T. Tran, Z.-Q. Xu, M. Kianinia, M. Toth, and I. Aharonovich (2018). Nanoassembly of quantum emitters in hexagonal boron nitride and gold nanospheres. *Nanoscale* 10(5), 2267–2274.
- Nielsen, M. A. (2000). Quantum Computation. *Cambridge University Press, (UK)* 1(1), 1.
- Novoselov, K. S., D. Jiang, F. Schedin, T. J. Booth, V. V. Khotkevich, S. V. Morozov, and A. K. Geim (2005, jul). Two-dimensional atomic crystals. *Proceedings of the National Academy of Sciences* 102(30), 10451–10453.
- Novotny, L. and B. Hecht (2006). *Principles of Nano-Optics*. Cambridge: Cambridge University Press.
- Orellana, W. and H. Chacham (2001, mar). Stability of native defects in hexagonal and cubic boron nitride. *Physical Review B* 63(12), 125205.
- Paul, H. (1982, oct). Photon antibunching. *Reviews of Modern Physics* 54(4), 1061–1102.
- Pecquenard, B., H. Lecacheux, J. Livage, and C. Julien (1998, jan). Orthorhombic WO₃ Formed via a Ti-Stabilized WO₃·13H₂O Phase. *Journal of Solid State Chemistry* 135(1), 159–168.
- Perdew, J. P., K. Burke, and M. Ernzerhof (1996, oct). Generalized Gradient Approximation Made Simple. *Physical Review Letters* 77(18), 3865–3868.
- Perebeinos, V. (2015, jun). Two dimensions and one photon. *Nature Nanotechnology* 10(6), 485–486.
- Polat, E. O., O. Balci, N. Kakenov, H. B. Uzlu, C. Kocabas, and R. Dahiya (2015, dec). Synthesis of Large Area Graphene for High Performance in Flexible Optoelectronic Devices. *Scientific Reports* 5(1), 16744.
- Polat, E. O. and C. Kocabas (2013, dec). Broadband Optical Modulators Based on Graphene Supercapacitors. *Nano Letters* 13(12), 5851–5857.
- Rabeau, J. R., Y. L. Chin, S. Praver, F. Jelezko, T. Gaebel, and J. Wrachtrup (2005,

- mar). Fabrication of single nickel-nitrogen defects in diamond by chemical vapor deposition. *Applied Physics Letters* 86(13), 131926.
- Raj, A. and L. N. Tripathi (2019). Single photon sources from two dimensional materials and their interfacing with plasmonic waveguides. *Arxiv preprint*, 1–16.
- Ramana, C. V., S. Utsunomiya, R. C. Ewing, C. M. Julien, and U. Becker (2006, jun). Structural Stability and Phase Transitions in WO₃ Thin Films. *The Journal of Physical Chemistry B* 110(21), 10430–10435.
- Reserbat-Plantey, A., K. G. Schädler, L. Gaudreau, G. Navickaite, J. Güttinger, D. Chang, C. Toninelli, A. Bachtold, and F. H. L. Koppens (2016, jan). Electromechanical control of nitrogen-vacancy defect emission using graphene NEMS. *Nature Communications* 7, 10218.
- Rosenberger, M. R., C. K. Dass, H.-J. Chuang, S. V. Sivaram, K. M. McCreary, J. R. Hendrickson, and B. T. Jonker (2019, jan). Quantum Calligraphy: Writing Single-Photon Emitters in a Two-Dimensional Materials Platform. *ACS Nano* 13(1), 904–912.
- Salihoglu, O., N. Kakenov, O. Balci, S. Balci, and C. Kocabas (2016, dec). Graphene as a Reversible and Spectrally Selective Fluorescence Quencher. *Scientific Reports* 6(1), 33911.
- Schietinger, S. (2012). *Investigation ,Manipulation and Coupling of Single Nanoscopic and Quantum Emitters*. Ph. D. thesis, Humboldt-Universitat.
- Shi, Y., C. Hamsen, X. Jia, K. K. Kim, A. Reina, M. Hofmann, A. L. Hsu, K. Zhang, H. Li, Z. Y. Juang, M. S. Dresselhaus, L. J. Li, and J. Kong (2010, oct). Synthesis of few-layer hexagonal boron nitride thin film by chemical vapor deposition. *Nano Letters* 10(10), 4134–4139.
- Song, L., L. Ci, H. Lu, P. B. Sorokin, C. Jin, J. Ni, A. G. Kvashnin, D. G. Kvashnin, J. Lou, B. I. Yakobson, and P. M. Ajayan (2010, aug). Large Scale Growth and Characterization of Atomic Hexagonal Boron Nitride Layers. *Nano Letters* 10(8), 3209–3215.

- Sontheimer, B., M. Braun, N. Nikolay, N. Sadzak, I. Aharonovich, and O. Benson (2017, sep). Photodynamics of quantum emitters in hexagonal boron nitride revealed by low-temperature spectroscopy. *Physical Review B* 96(12), 121202.
- Srivastava, A., M. Sidler, A. V. Allain, D. S. Lembke, A. Kis, and A. Imamoğlu (2015, jun). Optically active quantum dots in monolayer WSe₂. *Nature Nanotechnology* 10(6), 491–496.
- Stöhr, R. J., R. Kolesov, K. Xia, R. Reuter, J. Meijer, G. Logvenov, and J. Wrachtrup (2012, oct). Super-resolution Fluorescence Quenching Microscopy of Graphene. *ACS Nano* 6(10), 9175–9181.
- Swathi, R. S. and K. L. Sebastian (2009, feb). Long range resonance energy transfer from a dye molecule to graphene has d^{-4} dependence. *The Journal of Chemical Physics* 130(8), 086101.
- Tabernig, S. W. (2018). *MSc Physics Förster resonance energy transfer from PbS quantum dots to silicon : The missing link towards singlet fission solar cells* by. Ph. D. thesis, University of Amsterdam.
- Tang, Z., H. Wu, J. R. Cort, G. W. Buchko, Y. Zhang, Y. Shao, I. A. Aksay, J. Liu, and Y. Lin (2010, jun). Constraint of DNA on Functionalized Graphene Improves its Biostability and Specificity. *Small* 6(11), 1205–1209.
- Thummavichai, K., N. Wang, F. Xu, G. Rance, Y. Xia, and Y. Zhu (2018, apr). In situ investigations of the phase change behaviour of tungsten oxide nanostructures. *Royal Society Open Science* 5(4), 171932.
- Tisler, J., T. Oeckinghaus, R. J. Stöhr, R. Kolesov, R. Reuter, F. Reinhard, and J. Wrachtrup (2013). Single defect center scanning near-field optical microscopy on graphene. *Nano Letters* 13(7), 3152–3156.
- Tonndorf, P., R. Schmidt, R. Schneider, J. Kern, M. Buscema, G. A. Steele, A. Castellanos-Gomez, H. S. J. van der Zant, S. Michaelis de Vasconcellos, and R. Bratschitsch (2015, apr). Single-photon emission from localized excitons in an atomically thin semiconductor. *Optica* 2(4), 347.

- Tran, T. T., K. Bray, M. J. Ford, M. Toth, and I. Aharonovich (2015, oct). Quantum emission from hexagonal boron nitride monolayers. *Nature Nanotechnology* 11(1), 37–41.
- Tran, T. T., S. Choi, J. A. Scott, Z.-q. Xu, C. Zheng, G. Seniutinas, A. Bendavid, M. S. Fuhrer, M. Toth, and I. Aharonovich (2017, mar). Room-Temperature Single-Photon Emission from Oxidized Tungsten Disulfide Multilayers. *Advanced Optical Materials* 5(5), 1600939.
- Tran, T. T., C. Elbadawi, D. Totonjian, C. J. Lobo, G. Grosso, H. Moon, D. R. Englund, M. J. Ford, I. Aharonovich, and M. Toth (2016, aug). Robust Multicolor Single Photon Emission from Point Defects in Hexagonal Boron Nitride. *ACS Nano* 10(8), 7331–7338.
- Treossi, E., M. Melucci, A. Liscio, M. Gazzano, P. Samori, and V. Palermo (2009, nov). High-Contrast Visualization of Graphene Oxide on Dye-Sensitized Glass, Quartz, and Silicon by Fluorescence Quenching. *Journal of the American Chemical Society* 131(43), 15576–15577.
- Utzat, H., W. Sun, A. E. K. Kaplan, F. Krieg, M. Ginterseder, B. Spokoyny, N. D. Klein, K. E. Shulenberger, C. F. Perkinson, M. V. Kovalenko, and M. G. Bawendi (2019, mar). Coherent single-photon emission from colloidal lead halide perovskite quantum dots. *Science* 363(6431), 1068–1072.
- Walker, J. (1979, oct). Optical absorption and luminescence in diamond. *Reports on Progress in Physics* 42(10), 1605–1659.
- Wang, F., C. Di Valentin, and G. Pacchioni (2011, apr). Electronic and Structural Properties of WO₃ : A Systematic Hybrid DFT Study. *The Journal of Physical Chemistry C* 115(16), 8345–8353.
- Wang, F., Y. Zhang, C. Tian, C. Girit, A. Zettl, M. Crommie, and Y. R. Shen (2008, apr). Gate-Variable Optical Transitions in Graphene. *Science* 320(5873), 206–209.
- Wang, Y., Z. Li, J. Wang, J. Li, and Y. Lin (2011, may). Graphene and graphene oxide: biofunctionalization and applications in biotechnology. *Trends in Biotechnol-*

ogy 29(5), 205–212.

Watanabe, K., T. Taniguchi, and H. Kanda (2004, sep). Ultraviolet luminescence spectra of boron nitride single crystals grown under high pressure and high temperature. *Physica Status Solidi (a)* 201(11), 2561–2565.

Watanabe, K., T. Taniguchi, T. Kuroda, and H. Kanda (2006, oct). Effects of deformation on band-edge luminescence of hexagonal boron nitride single crystals. *Applied Physics Letters* 89(14), 141902.

Wolber, P. and B. Hudson (1979, nov). An analytic solution to the Förster energy transfer problem in two dimensions. *Biophysical Journal* 28(2), 197–210.

Wong, D., J. Velasco, L. Ju, J. Lee, S. Kahn, H.-Z. Tsai, C. Germany, T. Taniguchi, K. Watanabe, A. Zettl, F. Wang, and M. F. Crommie (2015, nov). Characterization and manipulation of individual defects in insulating hexagonal boron nitride using scanning tunnelling microscopy. *Nature Nanotechnology* 10(11), 949–953.

Wu, G., X. Tang, M. Meyyappan, and K. W. C. Lai (2017). Doping effects of surface functionalization on graphene with aromatic molecule and organic solvents. *Applied Surface Science* 425, 713–721.

Wysin, G. (2011). Quantization of the Free Electromagnetic Field: Photons and Operators.

Xu, L., M.-L. Yin, and S. (Frank) Liu (2015, may). Agx@WO₃ core-shell nanostructure for LSP enhanced chemical sensors. *Scientific Reports* 4(1), 6745.

Yamamoto, Y. and A. Imamoglu (1999). *Mesoscopic quantum optics*. John Wiley.

Yu, Y.-J., K. S. Kim, J. Nam, S. R. Kwon, H. Byun, K. Lee, J.-H. Ryou, R. D. Dupuis, J. Kim, G. Ahn, S. Ryu, M.-Y. Ryu, and J. S. Kim (2015, feb). Temperature-Dependent Resonance Energy Transfer from Semiconductor Quantum Wells to Graphene. *Nano Letters* 15(2), 896–902.

Zhao, S., J. Lavie, L. Rondin, L. Orcin-Chaix, C. Diederichs, P. Roussignol, Y. Chassagneux, C. Voisin, K. Müllen, A. Narita, S. Campidelli, and J.-S. Lauret (2018, dec).

Single photon emission from graphene quantum dots at room temperature. *Nature Communications* 9(1), 3470.



VITA

Date and Place of Birth: 19.12.1987, Eskişehir-TURKEY

EDUCATION

2013 - 2019 Doctor of Philosophy in Department of Materials Science and Engineering

Graduate School of Engineering and Sciences, İzmir Institute of Technology
İzmir -Turkey

Thesis Title: Single-photon Generation from Defects and Manipulation with Nanostructures

Supervisor: Assist. Prof. Dr. Enver TARHAN

2011 - 2013 Master of Science in Physics

Graduate School of Engineering and Sciences, İzmir Institute of Technology
İzmir -Turkey

Thesis Title: Influence of Ni Thin Film Structural Properties over Graphene Growth by CVD

Supervisor: Assoc. Prof. Dr. Yusuf SELAMET

2005 - 2010 Bachelor of Physics Education

Department of Physics Education, Faculty of Education, Dokuz Eylül University
İzmir - Turkey

PROFESSIONAL EXPERIENCE

2012 - 2019 Research Assistant

Department of Physics, İzmir Institute of Technology,
İzmir -Turkey